STUDY OF A PROTOTYPE MODULE OF A PRECISION TIME-OF-FLIGHT DETECTOR FOR PARTICLE IDENTIFICATION AT LOW MOMENTUM

PAR

Lucía CASTILLO GARCÍA

acceptée sur proposition du jury:

Prof. V. Savona, président du jury
Prof. T. Nakada, directeur de thèse
Dr R. Forty, rapporteur
Prof. P. Krizan, rapporteur
Dr J.-B. Mosset, rapporteur

EPFL

ÉCOLE POLYTECHNIQUE
FÉDÉRALE DE LAUSANNE

Suisse
2016

*To my family, specially
to my father who left us during
the last year of this research work.*

*The science of today is
the technology of tomorrow.*
— Edward Teller

Acknowledgements

The first words in this space are dedicated to my CERN supervisor Thierry Gys. I would like to thank him wholeheartedly for his continuous support and professional guidance throughout my PhD studies, for his patience and effort in training me to a high research standard. His role has been essential for the completion and success of this work. Un grand merci de tout coeur pour ton travail, ton soutien et ton humanité.

I would like to express my sincere gratitude to my thesis director Tatsuya Nakada for his interest in supporting this thesis and for his useful and constructive recommendations during the development of this research work.

I would also like to thank the jury members of my PhD examination, Prof. Vincenzo Savona, Dr. Roger Forty, Prof. Peter Križan and Dr. Jean-Baptiste Mosset for reading and examining this thesis and for providing valuable comments and suggestions.

I wish to express my gratefulness to Didier Piedigrossi for the essential and regular support in mechanical and optical aspects for running this research work. My grateful thanks are also extended to Christoph Frei for his valuable technical support on this project. Merci pour votre soutien pendant ces années.

I would like to express my very great appreciation to the TORCH collaboration, specially to Neville Harnew and Roger Forty for giving me the opportunity to participate in this interesting project.

I also wish to thank Rui Gao for his help and the many fruitful discussions we had about electronics, David Cussans for providing an electronics test board and helping with the initial tests and Ana Ros García for helping with the collection of beam test data and the electronics calibrations in the laboratory.

My special thanks are extended to Tom Conneely and James Milnes for their collaboration in the TORCH project and their guidance in the testing of custom photon detectors and the electronics calibrations.

I would like to thank Roberta Cardinale and Jibo He for helping with data analysis software.

Acknowledgements

Advice given by Olav Ullaland and Klaus Föhl has been a great help in the writing of this thesis.

I would also like to extend my thanks to the LHCb members, specially the VELO team for helping in running the beam test activities.

I would like to thank the secretaries of the LHCb collaboration, Véronique Wedlake of EP-DT group at CERN, Erika Lüthi and Esther Hofmann of the LPHE at EPFL and Anh Eymann of the Physics Doctoral School for your friendliness and for doing administrative tasks much easier.

This work has been made possible with the vital support and encouragement from my family and specially my husband who has been my fellow traveller in this experience, Happy birthday!

Lausanne, 30th March 2016   L. C. G.

Abstract

In this thesis, Time Of internally Reflected Cherenkov light detector (TORCH), proposed for the LHCb Upgrade to perform three-sigma separation between kaon and pion up to 10 GeV/c, was studied. TORCH is designed to add significant particle identification capability to the existing LHCb system based on two gas Ring Imaging Cherenkov detectors. TORCH would be placed at ~10 m from the interaction point, where the flight time difference between a primary pion and kaon is 37.5 ps. TORCH will give a pion-kaon separation of three sigma at 10 GeV/c from the flight time using the Cherenkov photons generated by the charged particle in a 1 cm-thick quartz plate. In order to calculate accurately the flight time in a busy LHCb environment, Cherenkov angle and photon detection time information, as well as the momentum information from the tracking detector are included in the analysis. For the required TORCH performance, the flight time difference must be measured with a resolution of better than 70 ps for a single Cherenkov photon.

In order to demonstrate the required performance, the intrinsic time resolution of the photon detector and electronics jitter have been investigated, firstly with commercially available Micro-Channel Plate Photo Multiplier Tubes (MCP-PMT) and electronics, then custom-made Multi-Channel MCP-PMT with custom-made electronics, which are designed for the TORCH R&D. The Multi-Channel MCP-PMT has been developed in collaboration with industry. For the custom electronics, NINO, an ASIC chip developed for the Time of Flight detector of the ALICE experiment was used as well as the HPTDC ASIC chip, which is being used by the ATLAS, CMS and ALICE experiments. Important characteristics such as the linearity and time walk have been carefully analysed and a method to correct biases introduced by those characteristics has been developed.

TORCH optics must propagate the Cherenkov photons to the photocathode of the Multi-channel MCPMT with minimum loss. On the other hand, spectra of photons reaching the photocathode should not be too wide in order to limit the chromatic error. All the optical components have been tested with a stand-alone system and results are compared with simulation studies. A small scale TORCH prototype has been constructed to test the system with a charged-particle beam and results are being analysed.

_____

Résumé

Dans cette thèse, le détecteur «Time Of internally Reflected Cherenkov light» (TORCH), proposé pour la future version améliorée de LHCb pour effectuer la séparation de trois sigmas entre kaon et pion jusqu'à 10 GeV/c, a été étudié. TORCH est conçu pour compléter les capacités d'identification des particules du système existant dans LHCb basé sur deux détecteurs à gaz à lumière Cherenkov. TORCH serait placé à ~10 m du point d'interaction, où la différence de temps de vol entre un pion et un kaon primaires est de 37.5 ps. TORCH donnera une séparation pion-kaon de trois sigmas à 10 GeV/c du temps de vol en exploitant les photons Cherenkov générés par la particule chargée dans une plaque de quartz de 1cm d'épaisseur. Afin de calculer avec précision le temps de vol dans un environnement LHCb encombré, les informations de l'angle Cherenkov et du temps de détection des photons, ainsi que les informations sur l'impulsion de la particule du détecteur de trajectoires sont incluses dans l'analyse. Pour la performance requise par TORCH, la différence de temps de vol doit être mesurée avec une résolution meilleure que 70 ps pour un photon Cherenkov unique.

Afin de démontrer les performances requises, la résolution temporelle intrinsèque du détecteur de photons et l'électronique ont été étudiés, tout d'abord avec des photo-détecteurs à galette de micro-canaux et de l'électronique disponibles dans le commerce, puis avec des photo-détecteurs et une électronique customisés, qui sont conçus dans le cadre des études R&D du TORCH. Les photo-détecteurs à multi-anode ont été développés en collaboration avec l'industrie. L'électronique customisée a utilisé la puce NINO développée pour le détecteur de temps de vol de l'expérience ALICE, ainsi que la puce HPTDC exploitée dans les expériences ATLAS, CMS et ALICE. Des caractéristiques importantes telles que la linéarité et le temps de marche des signaux ont été analysés avec soin et une méthode pour corriger les distorsions introduites par ces caractéristiques a été développée.

L'optique du TORCH doit propager les photons Cherenkov jusqu'à la photocathode du photo-détecteur multi-anode avec une perte minimale. D'un autre côté, les spectres des photons atteignant la photocathode ne doit pas être trop larges afin de limiter l'erreur chromatique. Tous les composants optiques ont été testés avec un système autonome et les résultats sont comparés avec des études de simulation. Un module prototype TORCH à échelle réduite a été construit pour tester le système dans un faisceau de particules chargées et les résultats sont en cours d'analyse.

Résumé

Table of Contents

Table of Contents

List of Figures

List of Tables

Introduction

Particle identification (PID) of charged hadrons (π, K, p) is vital for the physics programme of the LHCb experiment. Currently, PID is provided by two gas Ring Imaging Cherenkov (RICH) detectors. In the LHCb Upgrade scenario, where the data collection rate will be increased by a factor of 10, a degradation in performance at low momentum is expected.

The TORCH detector has been proposed to perform 3σ separation between kaons and pions up to 10 GeV/c and has been designed to add significant PID capability to the existing RICH system in LHCb. TORCH combines Time-Of-Flight and RICH detection techniques to measure the flight time of charged particles by timing the arrival of Cherenkov photons generated when these particles cross a 1 cm-thick quartz plate. At 10 GeV/c, the difference in time-of-flight between a kaon and a pion over a ~10 m path is 37.5 ps. This requires the use of fast photon detectors and readout electronics.

As part of the TORCH R&D studies, Micro-Channel Plate Photo Multiplier Tubes (MCP-PMT) with extended lifetime (Phase I) and fine segmented anode (Phase II) have been manufactured in collaboration with industry. Dedicated multi-channel front-end electronics are also developed using existing fast amplifier with Time-Over-Threshold discriminator, NINO, and time digitization conversion, HPTDC, ASIC chips. A small-scale TORCH prototype consisting of a quartz plate coupled to a focusing block has been built.

This thesis covers the experimental work carried out during an R&D programme aiming to achieve the challenging TORCH requirements. This manuscript is structured in seven chapters:

Chapter 1: Two particle identification techniques, Time-Of-Flight and Ring Imaging Cherenkov, that are used to measure the particle velocity in high energy physics experiments are presented. The concept and design of a novel PID detector, TORCH, which combines these two techniques are introduced. The TORCH R&D project is also presented.

Chapter 2: The principles and characteristics of the photon detectors that have been investigated in this thesis are described.

Chapter 3: The characterization of various commercial photon detectors with different designs is reported. The impact of the photon detector input gap on the timing performance is

discussed. The performance of the Phase I MCP-PMT prototypes for TORCH is also presented.

Chapter 4: The first version of customized readout electronics is characterized together with a commercial multi-anode photon detector. The procedure to apply off-line corrections to raw data is detailed. The efficiency of the electronics system in detecting the MCP-PMT signal from single photons is estimated. Spatial aspects are studied.

Chapter 5: The second version of customized readout electronics is characterized together with a Phase II MCP-PMT prototype. Photon charge distribution and spatial resolution are studied with emphasis on electronics calibrations.

Chapter 6: Laboratory tests of the light transmission in glass and glue samples for the choice of a glue material suitable for the coupling of the TORCH optical components are reported. Simulation studies of the optical quality of TORCH optics are presented.

Chapter 7: Charged-particle beam tests of a small-scale TORCH prototype are described. Preliminary results are presented.

1 Particle Identification in High Energy Physics

Particle Identification (PID) is crucial in most of particle physics experiments and fundamental to heavy ion, hadron and flavour physics and CP violation studies. There are two major PID applications: the identification of beam particles and the decay products such as pions, kaons, protons, electrons and muons.

A particle is identified by its electric charge q and by its mass m as given by

$$m = \frac{p}{c\beta\gamma} \tag{1.1}$$

where p is its momentum, β is its velocity (v/c) and γ is the Lorentz factor $\gamma = 1/\sqrt{1-\beta^2}$. The particle mass is inferred from measuring two out of the three following variables: the momentum, the kinetic energy and the velocity.

High energy physics detectors measure the particle momentum by means of tracking and magnetic spectrometers from the radius of curvature r of the particle track trajectory in the magnetic field B as $p = rqB$. A second observable is needed to identify the particle type. There is a large variety of techniques to identify particles. This chapter focuses on two techniques to determine the particle velocity: the time-of-flight (TOF) and the Cherenkov radiation imaging methods and is inspired from [1–4]. From the knowledge of the particle momentum and velocity then the mass can be calculated as given by Equation (1.1) and in such a way the particle can be identified.

1.1 Time-of-Flight technique

In a time-of-flight detector, the particle velocity is determined by measuring the time that it takes to travel a defined distance L between two detectors (start and stop counters), $\beta = L/ct$. The track flight path and the particle momentum p are provided by the tracking system of the experiment. Particles with different masses m_1 and m_2 but same momentum p will have different time-of-flight over the same path length. From the momentum and the measured

time-of-flight the mass of the particle can be determined as given by Equation (1.1).

The flight time difference, Δt_{TOF}, over a path length L between the two particles is given by

$$\Delta t_{TOF} = |t_{TOF1} - t_{TOF2}| = \left| \frac{L}{\beta_1 c} - \frac{L}{\beta_2 c} \right| = \frac{L}{c} \left| \sqrt{1 + \frac{m_1^2 c^2}{p^2}} - \sqrt{1 + \frac{m_2^2 c^2}{p^2}} \right|. \tag{1.2}$$
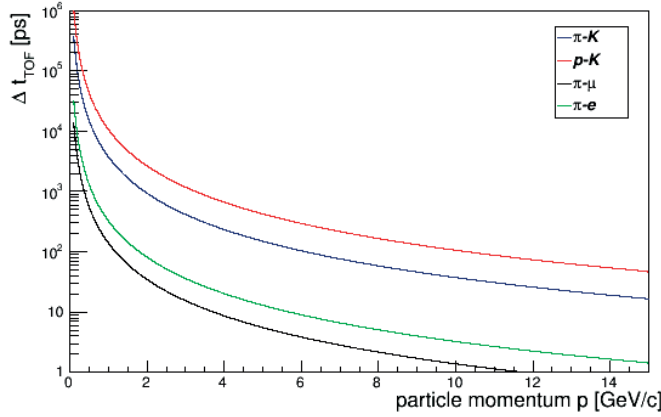
Figure 1.1: Time-of-flight difference between particles as a function of momentum for a path length of 9.5 m.

For $p \gg mc$, the TOF performance in terms of separation power in units of Gaussian standard deviations becomes

$$N_{\sigma_{TOF}} = \frac{|t_{TOF1} - t_{TOF2}|}{\sigma_{TOF}} \approx \frac{Lc}{2p^2 \sigma_{TOF}} |m_1^2 - m_2^2| \tag{1.3}$$

where σ_{TOF} is the time resolution of the TOF detector.

In the case of Equation (1.3), at very high momentum $|t_{TOF1} - t_{TOF2}|$ is too small and becomes comparable to the detector resolution, so particle misidentification occurs. This technique is consequently suited to identify hadrons at low momentum. The identification of charged particles for momenta larger than 1 GeV/c, requires however very good time resolution and a long path length.

The TOF resolution σ_{TOF} has two contributions, that from the event start time t_0 and that from the stop time measured by the TOF detector itself. The error on the stop time measurement is affected by contributions such as the photon detector transit time spread (TTS) σ_{TTS}, the readout electronics noise σ_{elec}, the precision of the particle path. The first two factors contribute significantly to the performance of the TOF detector. The error on the particle mass

is given by

$$\frac{\sigma_m}{m} = \sqrt{\gamma^4 \left(\frac{\sigma_t}{t} + \frac{\sigma_L}{L}\right)^2 + \left(\frac{\sigma_p}{p}\right)^2}. \qquad (1.4)$$

Since typically $\gamma \gg 1$, the mass resolution is dominated by the time resolution and the accuracy in the path length measurement.

1.1.1 ALICE TOF detector

The ALICE experiment [5] is one of the four large experiments at the Large Hadron Collider (LHC) [6] at CERN [7]. PID is an important feature of the experiment with a large-area TOF detector and other sub-systems dedicated to identify particles. The ALICE TOF detector [8, 9] aims at a π/K/p separation for momenta below 5 GeV/c with a design σ_{TOF} to reach better than 100 ps. It is based on gaseous detectors, Multigap Resistive Plate Chambers (MRPCs) [10], covering 150 m^2. A fast amplifier and time-over-threshold discriminator (NINO ASIC) [11] was designed and developed to match the requirements for the ALICE TOF detector. A high performance time-to-digital converter (HPTDC ASIC) [12, 13] for measuring the arrival time of both the leading and trailing edges of the NINO output pulse was also developed. As shown in Figure 1.2 a time resolution of 80 ps is achieved providing π-K separation up to ~2.5 GeV/c. MRPCs are excellent TOF detectors however they suffer from rate capability issues with a maximum of ~1 kHz cm^{-2}. This makes them not good candidates for high rate environments.
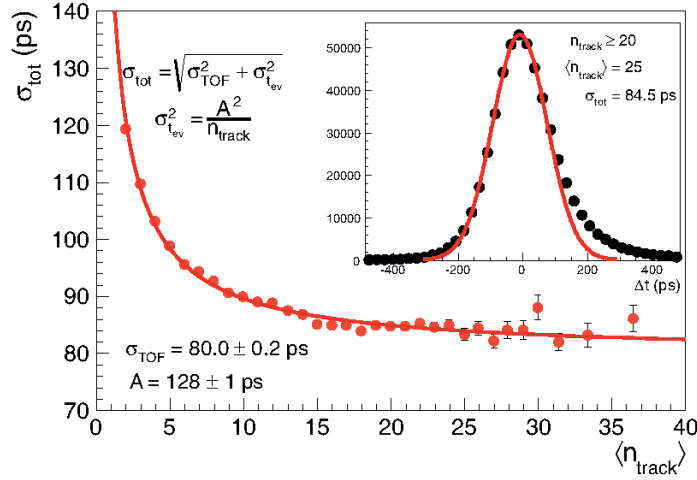
Figure 1.2: Total time resolution of the ALICE TOF for pion tracks with 0.95 GeV/c < p < 1.05 GeV/c as a function of the number of tracks used to define the TOF event time. Data refer to p-Pb collisions. The inset shows the original distribution for a track multiplicity on TOF > 20 which corresponds to an average of 25 [14].

5

1.2 Cherenkov radiation imaging

The phase velocity v_p is defined as the speed of light in an optical medium with refractive index n and is given by

$$v_p = \frac{c}{n} \tag{1.5}$$

The refractive index varies with the photon wavelength, λ, and for glasses can be described by the Sellmeier equation [15]:

$$n^2(\lambda) = 1 + \frac{B_1 \lambda^2}{\lambda^2 - C_1} + \frac{B_2 \lambda^2}{\lambda^2 - C_2} + \frac{B_3 \lambda^2}{\lambda^2 - C_3} \tag{1.6}$$

where λ is in micrometres and $B_{1,2,3}$ and $C_{1,2,3}$ are the Sellmeier coefficients. This dependence in wavelength causes chromatic dispersion in media.

In dispersive media, photons propagate at the group velocity $v_g = c/n_g$. The relationship between n and n_g as a function of the photon wavelength is a non-linear function that depends on the medium but obeys:

$$n_g(\lambda) = n(\lambda) - \lambda \frac{\mathrm{d}n(\lambda)}{\mathrm{d}\lambda} \tag{1.7}$$

Figure 1.3 shows the variation of phase and group refractive indices with photon wavelength in fused silica.
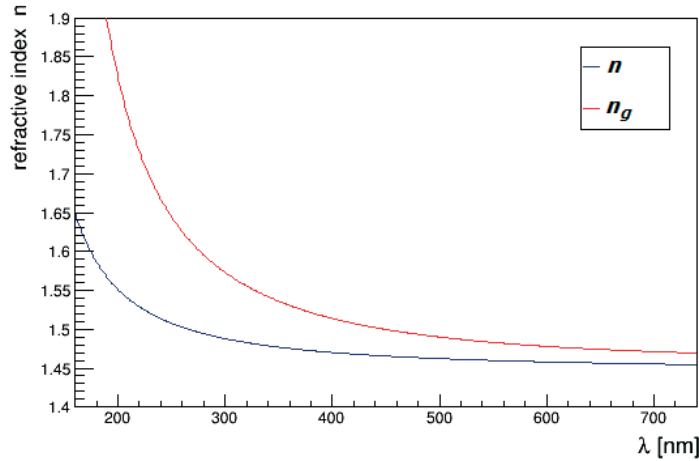
Figure 1.3: Phase and group refractive indices versus wavelength λ in fused silica.

1.2.1 Cherenkov effect

A charged particle traversing a dielectric medium at a velocity larger than the phase velocity loses a feeble part of its energy via radiation. This radiation is linked to a polarisation effect in the medium due to the electric field created by the particle charge [16]. As shown in Figure 1.4, if the particle velocity is smaller than v_p, it induces dipoles isotropically arranged around its path. At a certain distance there is a no net dipole moment as a result of this polarization and thus no emission of Cherenkov radiation. On the contrary, if the particle is ultrafast, $v > v_p$, the isotropy is broken as the particle moves faster than the electromagnetic waves. The result from the polarization and depolarization of the medium is the emission of Cherenkov photons in the perpendicular direction with respect to the particle wavefront. The Cherenkov effect was first observed and validated in 1934 by P.A. Cherenkov [17].
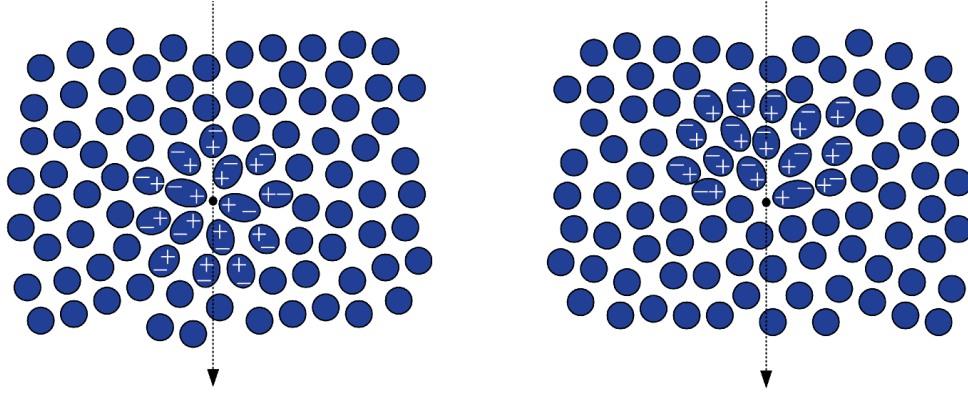
Figure 1.4: Behaviour of matter in the vicinity of the charged particle. Dipole distribution symmetric for $v < v_p$ (left) and not symmetric for $v > v_p$ (right) [18].

From Huygens' principle (see Figure 1.5), one deduces that Cherenkov light is emitted with a defined angle θ_C, with respect to the trajectory of the charged particle. Cherenkov light propagates perpendicularly to the surface of the cone of opening angle $\frac{\pi}{2} - \theta_C$. In a time interval t, Cherenkov radiation propagates over a distance ct/n whereas the charged particle travels a distance βct. One can then geometrically derive the following relation

$$\cos \theta_C = \frac{1}{n(\lambda)\beta} \tag{1.8}$$

considering the general case of n varying with wavelength.

As the mass is given by Equation (1.1) and $\beta = \frac{1}{n(\lambda)\cos\theta_C}$, a solution for m is obtained by measuring the Cherenkov angle and the momentum of the charged particle. There are two distinct solutions for the Cherenkov angle relation (Equation (1.8)):

- Since $|\cos\theta_c| \leq 1$, charged particles do not generate Cherenkov photons below a threshold velocity, corresponding to $\beta_{th} = \frac{1}{n}$. The solution for the threshold momentum is
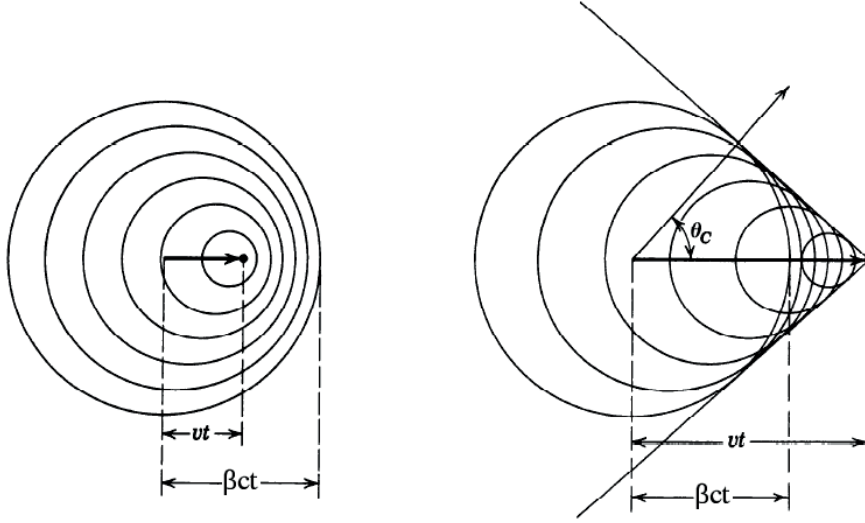
Figure 1.5: Cherenkov radiation geometry. Spherical wavelets of fields of a particle travelling at $v < v_p$ (left) and for $v > v_p$ (right) [19].

$$p_{th} = m\gamma_{th}\beta_{th}c = \frac{mc\beta_{th}}{\sqrt{1-\beta_{th}^2}} = \frac{mc}{\sqrt{n^2(\lambda)-1}} \tag{1.9}$$

- When $\beta \sim 1$, the Cherenkov angle converges to its maximum angle

$$\theta_{Cmax} = \arccos\left(\frac{1}{n(\lambda)}\right) \tag{1.10}$$

In 1937 I.M. Frank and I.E. Tamm fully explained the Cherenkov effect using Maxwell's equations [20]. The Nobel Prize in Physics 1958 was jointly awarded to both together with P.A. Cherenkov for the discovery and the interpretation of the Cherenkov effect [21]. The number of Cherenkov photons produced by a charged particle along its path, L, through a material is given by the following formula

$$N_{prod} = 2\pi\alpha Z^2 L \int \frac{\sin^2\theta_C(\lambda)}{\lambda^2}\,\mathrm{d}\lambda = \frac{\alpha}{\hbar c}Z^2 L \int \sin^2\theta_C(E_{ph})\,\mathrm{d}E_{ph} \tag{1.11}$$

where $\frac{\alpha}{\hbar c} = 370\,\mathrm{eV}^{-1}\mathrm{cm}^{-1}$ and $E_{ph} = \frac{hc}{\lambda}$. The photon spectrum expands over all wavelengths satisfying $n(\lambda)\beta > 1$. The medium dispersion fixes an upper bound to the emitted wavelengths. Figure 1.6 reproduces the Cherenkov spectrum for the case of saturated tracks $\beta = 1$ in 1 cm-thick quartz radiator.

However, not all generated photons are detected, most of them are lost due to the different processes they undergo in a detector. If the photons are reflected off a mirror with reflectivity $R(E_{ph})$, transmitted in an optical window $T(E_{ph})$ and then converted to a photoelectron in a
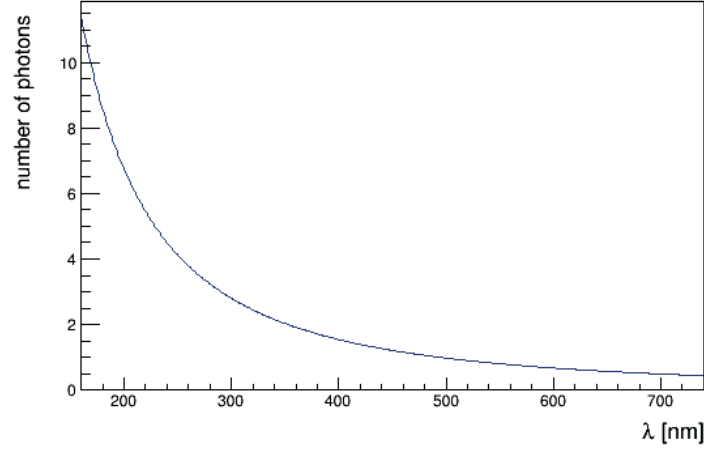
Figure 1.6: Calculated number of Cherenkov photons produced by a saturated particle track in 1 cm-thick quartz radiator as a function of wavelength using Equation (1.11).

photocathode with quantum efficiency $QE(E_{ph})$, the previous equation becomes

$$N_{det} = \frac{\alpha}{\hbar c} Z^2 L \int R(E_{ph}) T(E_{ph}) QE(E_{ph}) \sin^2 \theta_C(E_{ph}) \, dE_{ph} \tag{1.12}$$

As the typical variation of refractive index as a function of photon energy is modest, the number of detected photoelectrons is given by

$$N_{det} \approx N_0 L \langle \sin^2 \theta_C \rangle \tag{1.13}$$

where N_0 is defined as the Cherenkov detector quality factor and depends on the quality of the optical components, transmission in the optical medium and the photon detection efficiency.

From Equations (1.6) and (1.8), one deduces that photons with different wavelengths generated by the same charged particle track have different Cherenkov angles. This spread results in a chromatic error when measuring the average θ_C angle. In order to reduce the chromatic error, one can filter out low wavelengths before light is detected or choose an appropriate radiator.

1.2.2   Threshold Cherenkov counter detectors

The simplest application of the Cherenkov effect is in the form of threshold counter detectors [22]. A photomultiplier tube (PMT) collects all Cherenkov light produced in a radiator with known refractive index (Figure 1.7). Only signals produced from those particles with a velocity $v > \beta_{th}$ are detected. The refractive index is chosen such that some of the particles with the same momentum will generate Cherenkov signal. Using the number of photoelectrons one can discriminate between particles.
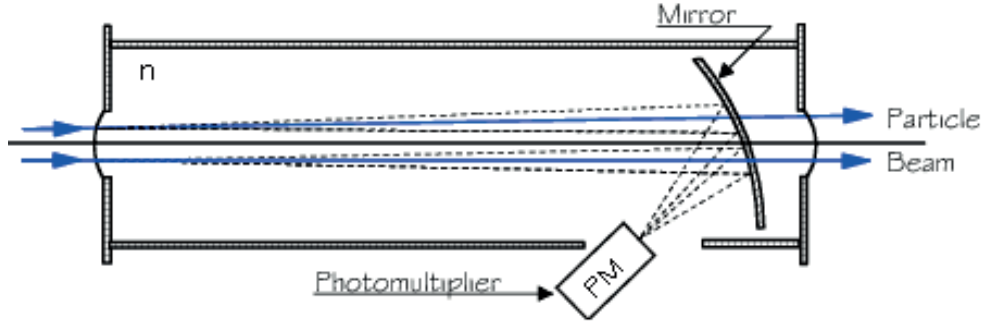
Figure 1.7: Typical optical system used in a threshold Cherenkov counter [22].

A common configuration is to use two such threshold Cherenkov counters in series containing gas radiators with different refractive indices, for example n_1=1.000135 (Ar-Ne) and n_2=1.00037 (Ar-CO_2). Equation (1.9) is used to calculate the momentum threshold at which each particle will *not* generate Cherenkov light for each radiator and the values are shown in Figure 1.8. The separation of π, K and p is performed up to 57.1 GeV/c. Cherenkov light detected in both radiators for a particle with a momentum between 8.5 and 30 GeV/c will identify a pion, light only detected in the second radiator between 18.1 and 30 GeV/c will identify a kaon and no light in both radiators will identify a proton. Between 34.5 and 57.1 GeV/c a proton is identified when light is detected only in the second radiator and distinguished from pions and kaons.
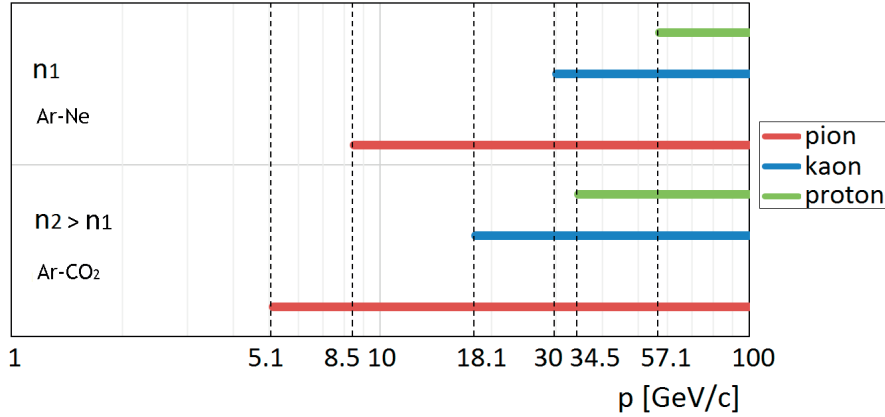
Figure 1.8: Momentum threshold in two gas radiators, Ar-Ne and Ar-CO_2, for pions, kaons and protons. They can be separated below 57.1 GeV/c.

1.2.3 Ring Imaging Cherenkov detectors

The principle of Ring Imaging Cherenkov (RICH) detectors [23] allows to measure the particle velocity by using both the Cherenkov angle and the number of detected photoelectrons. This PID technique can be used with position-sensitive photon detectors capable to detect single photons.

Cherenkov photons emitted along the particle trajectory with an angle θ_C are focused by means of spherical or parabolic mirrors and form a ring-shaped image at the photon detector plane. From its radius r, together with the knowledge of the optics geometry, in this case considering a spherical mirror with radius R_S, the Cherenkov angle can be extracted as

$$\theta_C = \frac{2r}{R_S} \tag{1.14}$$

and the particle velocity can be obtained from Equation (1.8) giving

$$\beta = \frac{1}{n(\lambda)\cos\left(\frac{2r}{R_S}\right)} \tag{1.15}$$

Combining Equations (1.1) and (1.15), the mass of the charged particle is determined as

$$m = \frac{p}{c}\sqrt{n^2(\lambda)\cos^2\theta_C - 1} \tag{1.16}$$

The velocity resolution is given by [24]

$$\frac{\sigma_\beta}{\beta} = \tan\theta_C\,\sigma_{\theta_C} \tag{1.17}$$

where

$$\sigma_{\theta_C}^2 = \left(\frac{<\sigma_{\theta_i}>}{\sqrt{N_{ph}}}\right)^2 + \sigma_{other}^2 \tag{1.18}$$

with $<\sigma_{\theta_i}>$ is the mean Cherenkov angle measurement resolution per single photoelectron in a ring including the contribution from the emission point, the chromatic dispersion and the pixelisation errors. The term σ_{other} is the error contribution from alignment, hit reconstruction, etc.

Two particles with masses m_1 and m_2 with momentum p generate Cherenkov photons in a medium at an angle θ_{C1} and θ_{C2}, respectively. The angle resolution plays an important role in the determination of the momentum range over which the two particles can be distinguished, since θ_C saturates and the ring radii become very similar. The separation power for velocities $\beta \sim 1$ is approximated as

$$N_{\sigma_{\theta_C}} \approx \frac{c^2|m_1^2 - m_2^2|}{2p^2\sigma_{\theta_C}\sqrt{n^2(\lambda) - 1}} \tag{1.19}$$

Equation (1.19) is similar to Equation (1.3) established for TOF detectors. The factor $\frac{1}{\sqrt{n^2-1}}$ allows RICH detectors to cover higher momenta with a suitable radiator medium. In order to design a RICH detector and achieve the best performance over the required momentum range, one can adjust the different parameters to maximize the quality factor N_0 with the smallest angular resolution per single photoelectron σ_{θ_i}.

RICH detector at the LHCb experiment

LHCb [25] is one of the other three major experiments at the LHC, dedicated to the search for New Physics (NP) in CP violation and rare decays of heavy flavours. It is a forward spectrometer with an horizontal angular acceptance of 10-300 mrad operating in p-p collider mode. It is located in one of the four points where the two beams cross and produce a variety of particles resulting from the decay of B mesons.

In the LHCb experiment, particle identification of charged hadrons (π, K, p) is provided by two RICH detectors [26] equipped with three radiators: silica aerogel and gaseous C_4F_{10} radiators in RICH 1 (upstream of the magnet) and gaseous CF_4 radiator in RICH 2 (downstream of the magnet) [27–30] covering a momentum range from 2 GeV/c up to 100 GeV/c. Cherenkov
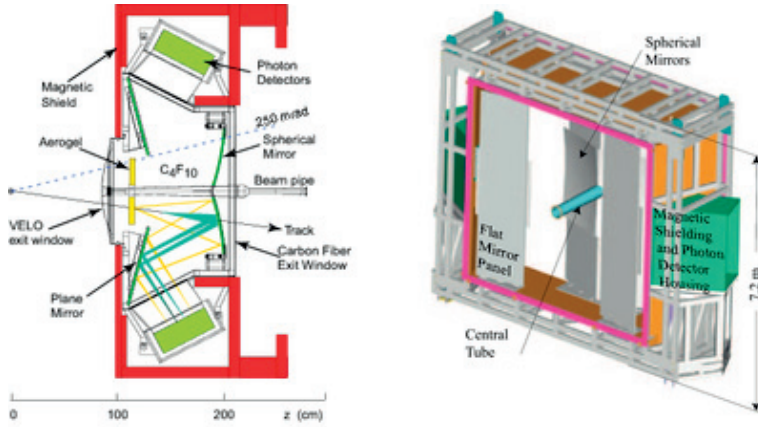
Figure 1.9: Side view schematic layout of RICH 1 (left) and RICH 2 (right) detectors [25].

photons generated by charged particles passing through the three radiators are reflected off a set of spherical [31] and flat mirrors and collected by hybrid photon detectors (HPD) [32], where photoelectrons are accelerated and detected with a silicon pixel array [33]. These vacuum-based photon detectors have a uniform gain of typical value 5000 e^-/e^- and small noise ($<$200 e^- rms) which is suitable for single photon detection [34].

The position of photons that hit the HPD pixels is reconstructed on the HPD plane. From the photon hits the ring images are built up using pattern recognition and maximum-likelihood algorithms [35]. Generally, the reconstructed Cherenkov rings overlap with other rings. However, about 2% of the tracks in 2011 data are isolated corresponding to rings which do not overlap with others formed from the same radiator [36]. In the meantime, the aerogel radiator was removed. The RICH 1 performance using isolated tracks in the C_4F_{10} gaseous radiator is illustrated in Figure 1.10. Kaons do not produce Cherenkov photons in C_4F_{10} below 9.3 GeV/c and pions and kaons are efficiently separated between 2 and 30 GeV/c.
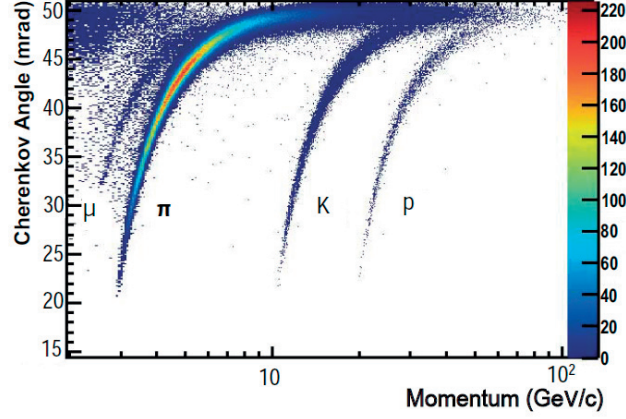
Figure 1.10: Reconstructed Cherenkov angle versus particle momentum for the LHCb-RICH 1 detector using a C_4F_{10} gaseous radiator [36].

1.2.4 Detection of Internally Reflected Cherenkov light

The principle of a Detection of Internally Reflected Cherenkov light (DIRC) detector [37] is based on the detection of Cherenkov light trapped by total internal reflection in a solid radiator (Figure 1.11).
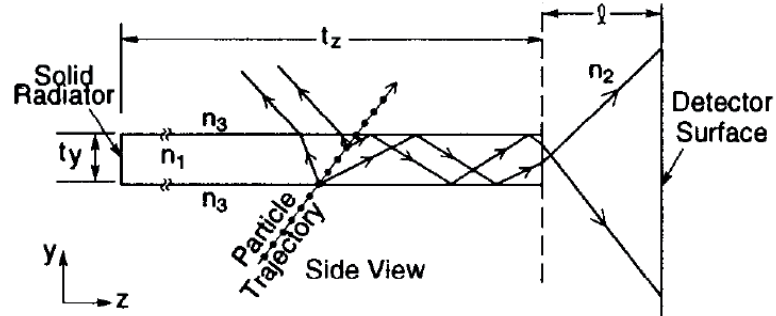
Figure 1.11: Schematic side view of Cherenkov light production and image formation in a radiator bar of the BaBar DIRC counter [37].

The DIRC at the BaBar spectrometer [38] uses as Cherenkov radiator and light guide 4.9 m long, rectangular bars made from synthetic fused silica. The bars are only instrumented with photon detectors on one end and a mirror placed at the other end reflects photons to the instrumented end. Photon detectors provide the measurement of the Cherenkov angle θ_C and the arrival time t_γ of the photon. The arrival time gives the time-of-propagation (TOP),

$$t_\gamma = \frac{l_\gamma n_g(\lambda)}{c} \tag{1.20}$$

where l_γ is the photon path length.

This is used to estimate the photon wavelengths and correct for the chromatic error. After computing $n(\lambda)$ from Equation (1.7), the mass of the particle can be extracted using Equation (1.16). Figure 1.12 shows the Cherenkov angle as a function of momentum for a sample of tracks from multi-hadron events and illustrates that pions, kaons and protons are efficiently separated below 3 GeV/c.
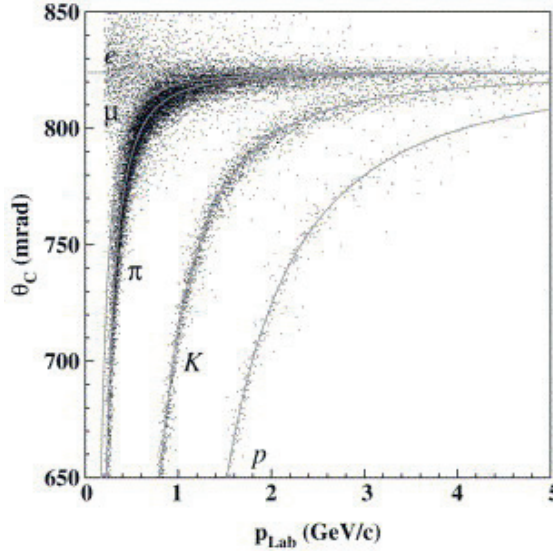
Figure 1.12: Cherenkov angle, θ_C, versus the momentum of tracks from an inclusive sample of multi-hadron events in BaBar DIRC. The grey lines are the predicted values of θ_C for the different particle species [38].

Time-of-Propagation counters

A time-of-propagation counter is a DIRC-like detector measuring the arrival time and position of Cherenkov photons at the exit of a quartz radiator with an array of fast photon detectors. In this case the required time precision is of order ~50 ps. Currently the best choice of photon detectors is the micro-channel plate photomultiplier tubes (MCP-PMTs). Chapter 2 will describe in detail this type of vacuum-based photon detectors. A TOP counter is being built and commissioned for the Belle II experiment [39, 40]. The PANDA Collaboration [41] is also considering a similar device type. DIRC-like detectors can derive their particle separation capability not only from the measurement of the Cherenkov angle, as in RICH detectors, but they can also separate particles as a time-of-flight counter as explained in the next section.

1.3 TORCH detector

Within the LHCb upgrade framework [42], a new PID system to cover the momentum range below 10 GeV/c has been proposed to achieve positive $\pi/K/p$ separation at a ≥3σ level.

1.3.1 The TORCH concept

Time Of internally Reflected CHerenkov light (TORCH) is an innovative DIRC-like detector that combines TOF and RICH detection techniques [43]. It consists of a 1 cm-thick rectangular plate made of quartz (amorphous fused silica) with focusing elements and photon detectors along the top and bottom edges. The dimensions of the radiator plate are imposed by the LHCb angular acceptance, ±300 mrad in the horizontal direction and ±250 mrad in the vertical direction, leading to a surface 6×5 m^2 at the proposed location of about 10 m downstream of the interaction point.

Charged-particle tracks crossing the quartz plate generate Cherenkov photons. Some of them are trapped in the plate and propagate by total internal reflection to the edges. Subsequently, they are focused onto an array of MCP-PMT photon detectors where their arrival is precisely timed (Figure 1.13). Angular information of the photon direction has been preserved when the photon comes out at the end of the quartz plate, since it is total internally reflected while propagating through the quartz plate. The focusing element uses a cylindrical mirror which allows to accurately convert the propagation angle of the photon, θ_z, from the vertical position of the photon in the photon detector array plane. This element has been designed to cover θ_z angles in the range 0.45 to 0.85 rad. Figure 1.14 shows the trajectory of photons through the quartz plane (x,y). The propagation angle of the photon projected on the quartz plane, θ_x, is determined from its emission point on the track path in quartz and the detection point in the photon detector array plane. By measuring both propagation angles the trajectory of the Cherenkov photons in the quartz can be reconstructed.

Modular layout

The TORCH design has evolved to a modular layout being more realistic for the LHCb application [44]. The single quartz plate is now segmented in 18 identical modules of dimensions of $66 \times 250 \times 1$ cm^3, each instrumented with 11 MCP photon detectors (Figure 1.15).

This modular layout reduces the number of tracks that contribute to the signal in a given module. However, the additional reflections of Cherenkov photons off the lower edge and sides of the module introduce extra ambiguities in the reconstruction.

TORCH requirements

The TORCH collaboration (Bristol and Oxford Universities and CERN) has launched an R&D programme aiming to deliver a TORCH prototype module of dimensions of $66 \times 250 \times 1$ cm^3 instrumented with 10 custom-made photon detectors and suitable radiator and focusing optics [45]. The project is funded by the European Research Council [46]. The proof-of-principle of TORCH should be demonstrated in laboratory and beam tests.

The R&D programme is focused mainly in the development of custom-made photon detectors
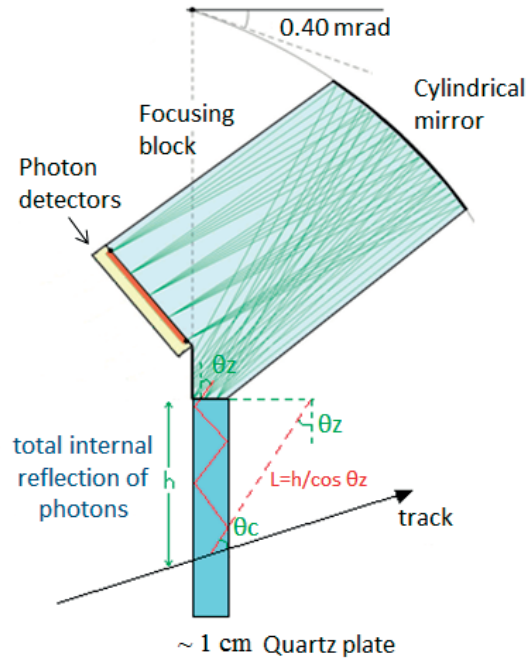
Figure 1.13: Schematic principle of the TORCH detector. Cross-section through focusing element, attached to the edge of the quartz plate. The photon propagation angle θ_z is defined as the angle between the photon direction at the exit of the radiator and its vertical axis. The focusing of photons is indicated for five illustrative photon angles between 0.45 and 0.85 rad, emerging at different points across the edge of the plate [43].
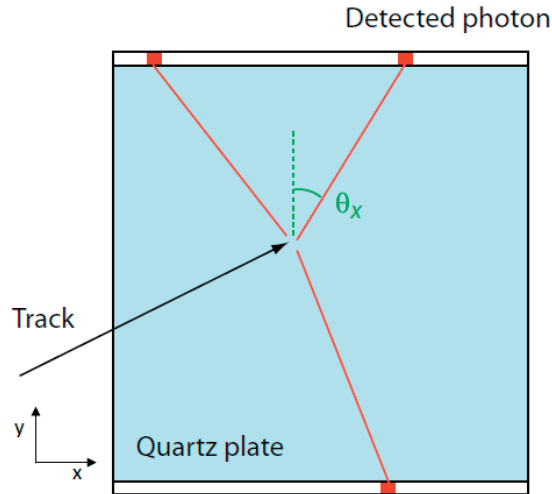
Figure 1.14: Schematic view of the reconstruction of the photon trajectory in the transverse projection (x,y). The photon propagation angle θ_x is defined as the angle between the photon direction and the y-axis [44].
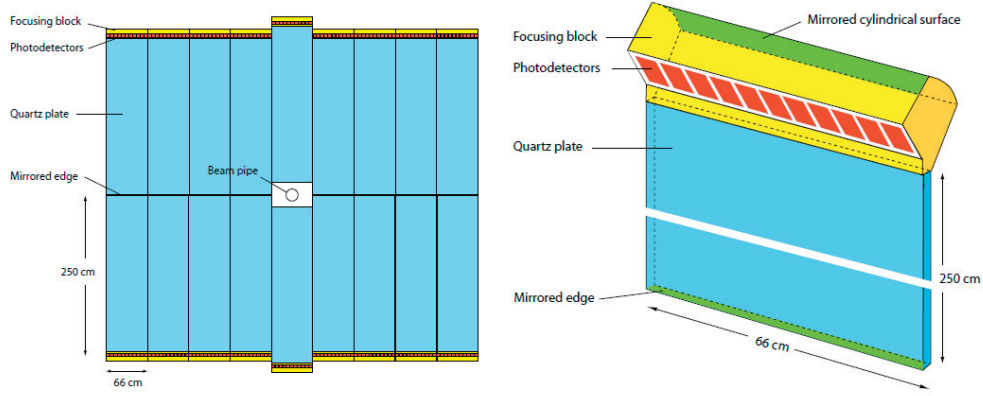
Figure 1.15: Schematic modular layout (front view) of the TORCH detector (left). Isometric view of a single TORCH module, showing the 1 cm-thick quartz radiator plate coupled to the focusing block (right) [44].

suitable for the final TORCH prototype module. These devices require the use of dedicated multi-channel electronics that will be developed and characterized. In parallel with these activities, the TORCH performance will be simulated and the design of the optical components will be investigated.

The high multiplicity events of order 100 tracks every 25 ns at the LHCb upgraded luminosity is a challenge. The detected average photon rate, γ_{rate}, at TORCH is expected to be at least 10 MHz cm^{-2} and is calculated as:

$$\gamma_{rate} = \frac{c_{rate} \times n_{tracks} \times n_{photons}}{n_{modules} \times n_{MCP} \times s_{MCP}} \tag{1.21}$$

where c_{rate} is the collision rate, n_{tracks} is the number of tracks, $n_{photons}$ is the expected number of detected Cherenkov photons, $n_{modules}$ is the number of modules in TORCH, n_{MCP} is the number of MCP photon detectors in each module and s_{MCP} is the active surface of a MCP photon detector.

The MCP devices will need to survive several years in a high occupancy environment with an accumulated anode charge per year of 1-10 C cm^{-2} for a modest operating gain of 5×10^5. The spectral response of the MCP tubes needs also to be optimized for Cherenkov light, which is a flat distribution as a function of photon energy. The Quantum Efficiency (QE) should be better than 15% in the range 200-600 nm.

From simulation, a dynamic range of 0.4 rad in the fine direction and a 128-channel segmentation was found to correspond to an uncertainty of 0.96 mrad on θ_z [43]. The projected propagation angle θ_x needs also to be measured with a ~1 mrad precision given the long lever arm of ~2 m. The use of a square photon detector with finely segmented anode of 8×128 pads of dimensions of 6.6×0.4 mm^2, respectively, is assumed. The spatial precision in the fine direction should be better than $0.4/\sqrt{12}$=0.12 mm.

Currently, a commercially-available MCP photon detector with the highest granularity is the XP85022 Planacon from Burle-Photonis[1]. This device with physical dimensions of 59×59 mm^2 consists of an array of 32×32 pads in a 53×53 mm^2 active area. The anode structure can in principle be adjusted according to TORCH needs, but it requires collaboration with industry.
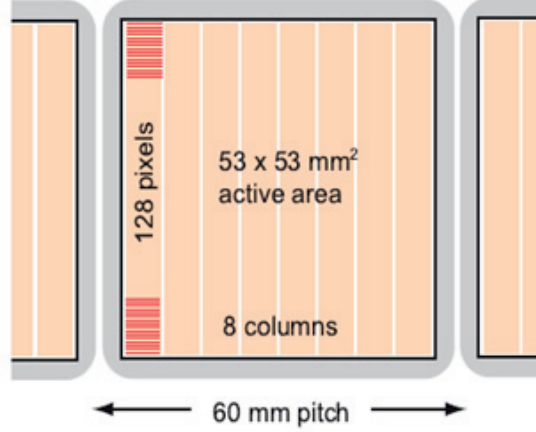
Figure 1.16: Schematic of the photon detector layout for TORCH, with Planacon-sized MCPs placed side-by-side, with pixellization adjusted to be fine in one direction and coarse in the other [44].

In the case of the LHCb application, the TORCH detector will measure the time-of-flight of kaons and pions. The TOF difference over a path length L between both particles given by Equation (1.2), if $m^2 c^2 \ll p^2$, is approximated as

$$\Delta t_{TOF}(\pi - K) = t_K - t_\pi \sim \frac{Lc}{2p^2}(m_K^2 - m_\pi^2) \tag{1.22}$$

where t_K and t_π are the times-of-flight and m_K and m_π are the masses of a kaon and a pion, respectively. In Figure 1.1, blue coloured line corresponds to the TOF difference between kaons and pions over a distance of 9.5 m. For 3σ separation, the per-track resolution, σ_t, should be better than

$$\sigma_t < \frac{1}{3} \frac{Lc}{2p^2}(m_K^2 - m_\pi^2) \tag{1.23}$$

Distinguishing between the two particles at 10 GeV/c is a challenge, where $\Delta t_{TOF}(\pi\text{-}K)$=37.5 ps. Hence, 3σ separation between kaons and pions and proton positive separation requires a per-track resolution of σ_t = 12.5 ps. Assuming a QE of the photon detector optimized for the photon wavelength range of 200-600 nm and for a 1 cm thickness of quartz, the expected number of detected Cherenkov photons per track is ~30. The product $\sigma_t \times \sqrt{30}$ leads to an overall required resolution per detected photon of ~70 ps.

[1]Burle-Photonis, Lancaster, PA17601-5688, USA: http://www.photonis.com

The arrival time measurement resolution should be better than 50 ps for single photons which includes the transit time spread (TTS) of the MCP photon detector and the readout electronics jitter. A time resolution better than 50 ps has already been demonstrated with commercially-available MCP devices[2] with coarse pad size of ~6 mm and using commercial single-channel electronics to read out the charge signal from a single pad [47].

The time-of-propagation of Cherenkov photons in the quartz plate needs to be measured with a precision of 50 ps. The propagation time depends on the particle type that generates Cherenkov photons. Different particle velocities give different Cherenkov angles and therefore different photon path lengths. The chromatic dispersion effect in the quartz spreads the time-of-propagation due to the different photon paths and needs to be corrected for. This is achieved by accurately measuring the Cherenkov angle, θ_C, which depends on the phase refractive index. The time-of-propagation also varies with photon wavelength as it depends on the group refractive index in quartz as given by Equation (1.20).

The combination in quadrature of the intrinsic time resolution and the time-of-propagation in the quartz plate leads to an overall resolution per detected photon of ~70 ps as required. The overall resolution on the photon propagation time is dominated by the uncertainty on the θ_z angle coming from the pixelization of the photon detector.

High-quality polishing of the optical components, whilst maintaining the surfaces parallel, is essential to preserve the angular precision after multiple internal reflections. The quartz plate thickness is also a crucial parameter, compromising between the photon yield and the uncertainty on the position of the photon emission point. The coupling between the quartz plate and the focusing optics is also crucial, as is the mechanical mounting.

Table 1.1: Summary table with some of the TORCH requirements.

TORCH requirements	
accumulated anode charge	1-10 C/cm^2/year
precision of photon propagation angles θ_x and θ_z	1 mrad
spatial resolution in fine direction	0.4/$\sqrt{12}$=0.12 mm
track resolution at 10 GeV/c	12.5 ps
overall time resolution per detected photon	70 ps
precision of the time of propagation	50 ps
MCP TTS and electronics jitter	50 ps
quartz plate surface roughness	1-2 nm

Reconstruction and pattern recognition

The TORCH detector combines RICH, TOF and TOP techniques in an elegant way measuring the time-of-flight of charged-particle tracks over a given distance, as well as the angles of

---

[2]XP85012-A1 Planacon with 8×8 pads, Burle-Photonis, Lancaster, PA17601-5688, USA

Cherenkov photons [43, 44]. From the time-of-flight measured by the difference between the time the track left the primary vertex (PV) and that when the Cherenkov photon is emitted, the velocity of the particle can be determined. By combining this velocity with the momentum measured by the LHCb spectrometer, the mass of the particle can be obtained as given by Equation (1.1) and so the particle can be identified.

The arrival time of Cherenkov photons at the photon detectors is the sum of the time that the track left the PV, the time-of-flight of the charged-particle track and the time-of-propagation of Cherenkov photons in the quartz:

$$t_{photon\ arrival} = t_0 + t_{TOF} + t_\gamma = t_0 + \frac{L}{c}\sqrt{1 + \left(\frac{mc}{p}\right)^2} + \frac{l_\gamma n_g(\lambda)}{c} \qquad (1.24)$$

where for a given track t_0 and t_{TOF} are fixed for all photons and t_γ varies per photon wavelength, and $n_g(\lambda)$ may be determined from Equation (1.7) where

$$n(\lambda) = \frac{1}{\beta\cos\theta_C} = \frac{\sqrt{m^2c^4 + p^2c^2}}{p\cos\theta_C} \qquad (1.25)$$

From the photon position in the photon detector plane the propagation angles, θ_z and θ_x, are inferred. The trajectory of a Cherenkov photon is then calculated by assuming that it was emitted at the midpoint in z of the charged track path through the quartz plate. By the combination of the θ_z angle with the knowledge of the track direction the Cherenkov angle of the photons, θ_C, is directly determined. With all this information the mass of the particle can be extracted from $t_{TOF}+t_\gamma$.

TORCH acts as a *stop counter* and in order to perform TOF measurements it needs a *start time*. In LHCb the production time of the particle, t_0, can be precisely determined from other particle tracks produced at the same PV in the interaction. These such tracks are mostly pions, so assuming that all of them are pions the time $t_{TOF}+t_\gamma$ is calculated. Subtracting this from the arrival time of the photons measured by TORCH, $t_{photon\ arrival}$, gives a measurement of the track *start time*, t_0, with precision of typically a few ps. This resolution is smaller than the per-track resolution by roughly $\sqrt{N_\pi}$, where N_π is the number of reconstructed pion tracks.

The spatial and timing information of the detected Cherenkov photons would help to associate signals to a track. The propagation time of photons in the quartz is calculated with respect to a track position at the plate. Photons belonging to that track will peak at the true time whereas photons from other tracks will be spread out. The photon wavelength calculated from the Cherenkov angle, θ_C, is limited in the range to which the photon detector is sensitive. Photon wavelengths outside this range are rejected.

Simulation and performance

A simple simulation of the TORCH detector interfacing to the full Monte Carlo simulation of events in the LHCb spectrometer has been studied within the GEANT4 framework [44, 48, 49]. A simple conceptual design of a single quartz plate with a central hole around the beam pipe has been assumed. The tracks that would cross TORCH are determined, and the emission, propagation and detection of Cherenkov photons in TORCH are simulated with a stand-alone program. Reconstruction and pattern recognition as explained in the previous subsection are applied.

The performance in terms of PID efficiencies for those kaon and pion tracks crossing the TORCH detector is characterized. The TORCH PID efficiencies and misidentification fractions for kaons and pions as a function of track momentum are shown in Figure 1.17. The figure compares events simulated at two luminosities: 2×10^{32} cm^{-2} s^{-1} and 2×10^{33} cm^{-2} s^{-1}, corresponding to the nominal and upgraded luminosities of the LHCb experiment. Good π-K separation is achieved up to 10 GeV/c as required even at the high luminosity of the LHCb upgrade.
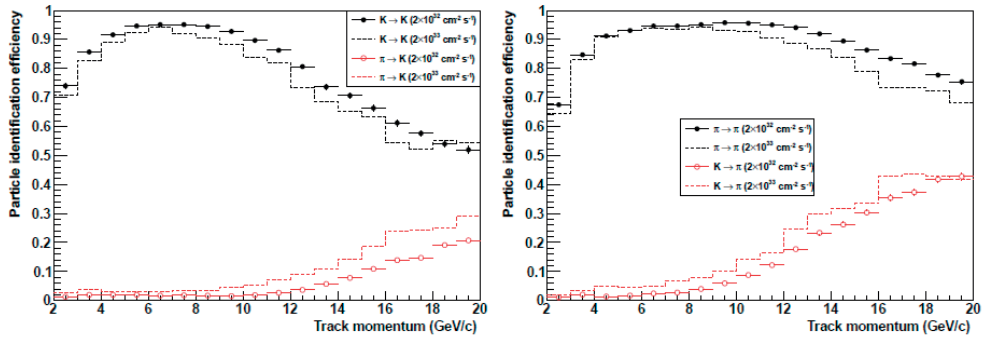
Figure 1.17: TORCH identification efficiency for a subset of well-measured, truth-matched charged tracks in the simulation which are matched to a primary vertex. The plots show the efficiency for a kaon (left) or pion (right) track to be identified correctly (black, upper points) or incorrectly (red, lower points). The ID and mis-ID efficiencies are shown for two different luminosities, 2×10^{32} cm^{-2} s^{-1} (points) and 2×10^{33} cm^{-2} s^{-1} (dotted histograms). Tracks are assigned as pions or kaons depending on which hypothesis maximizes the likelihood, ignoring other mass hypotheses [44].

The performance of a combination of the TORCH and LHCb-RICH system for isolated tracks is calculated in terms of the significance (in number of Gaussian standard deviation) for π-K separation as a function of track momentum and is shown in Figure 1.18. The resolution per photon and photon yields per track are (70 ps, 1.6 mrad, 0.7 mrad) and (30,16,12) for TORCH, RICH 1 and RICH 2, respectively [44].

Initial simulation studies of the TORCH modular layout are in progress and the performance is expected to be maintained.
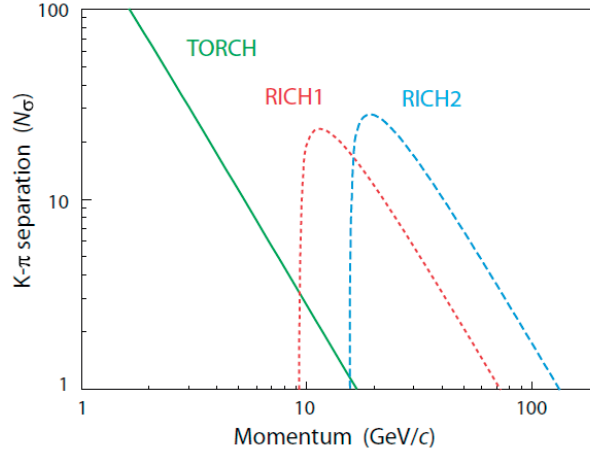
Figure 1.18: Calculated performance in terms of power separation (in number of Gaussian standard deviation) of the different components of the LHCb PID system for π-K separation as a function of momentum, for isolated tracks [44].

1.3.2 TORCH R&D project

Photon detector development

Custom-made MCP-PMT photon detectors are manufactured in collaboration with an industrial partner[3]. This development is divided into three phases:

- First phase: manufacture and delivery of circular-shape single-channel MCP-PMT prototypes with extended lifetime. The characterization of these tubes will be described in Chapter 3.

- Second phase: manufacture and delivery of circular-shape multi-channel MCP-PMT prototypes with the required spatial precision suited for TORCH. These tubes will be described and their characterization will be detailed in Chapters 5 and 7.

- Third phase: manufacture and delivery of square-shape multi-channel MCP-PMT prototypes with extended lifetime and with the timing and the granularity as required by TORCH.

Readout electronics

The readout electronic system is based on both the NINO and HPTDC chips already introduced in Subsection 1.1.1. The NINO front-end chip [11] amplifies and discriminates the MCP-PMT signals using time-over-threshold approach allowing for time walk corrections. The time hits for the leading and trailing edges of the NINO output pulses are digitised by the HPTDC chip [12, 13].

---

[3]Photek, St Leonards-on-Sea, TN38 9NS, United Kingdom: http://www.photek.com

A first version of multi-layer printed circuit boards (PCB) incorporates two 8-channel NINO and two HPTDC chips [50]. The performance of a commercial photon detector instrumented with a single such board is reported in Chapter 4. For the final 1024-channel MCP-PMTs, a single device would need sixteen 64-channel NINO chips. Due to the higher channel count and density of new MCP-PMTs this electronics modularity requires additional study. New 64-channel front-end boards using 32-channel NINO chips are being developed [51]. This new version will be coupled to custom-made photon detectors and their performance will be investigated in detail and is covered in Chapters 5 and 7.

TORCH prototype module development

During this 4-year R&D, optical components of the TORCH prototype module will be manufactured by industry. The ability to polish the quartz surface over a large area, in order to maintain less than a 1 mrad angular uncertainty after multiple internal reflections will also be investigated. The mechanical mounting of the quartz is crucial as well as its optical coupling, where an adequate gluing material is required. Transmission properties of various glass and optical glues will be studied in Chapter 6. The prototyping will be a multi-stage process, eventually culminating in a full-scale module.

Simulation

The R&D programme is also focused on the extension of the current TORCH simulation framework by updating to the new modular detector design. The integration of the TORCH simulation within a full GEANT4 framework is also foreseen. Detailed studies introducing multiple scattering effects that smear the track angle and more realistic track timing and propagation through the magnetic field will be evaluated. The performance using various photon detectors in beam tests will be also investigated. Simulation studies are described in more detail in the PhD dissertation of M. van Dijk at the University of Bristol [52]. Highlighted results on the reconstruction of beam test data will be reported in Chapter 7.

2 Micro-channel plate photon detectors

Vacuum photon detectors are extensively used in many high energy physics experiments especially those having a subsystem based on the detection of Cherenkov radiation. Precision timing of vacuum photon detectors is of particular importance for some of these applications since they have to deal with low-light level signals at the single-photon regime. To be specific, micro-channel plate photomultipliers (MCP-PMTs) are currently the best choice for fast timing of single photons. These devices give measurements down to the picosecond level and tubes with segmented anode are capable to measure the position of photons with high precision.

2.1 Principle of operation

A MCP-PMT consists of an optical window, a photocathode, a MCP electron multiplier and an anode. The light transmitted through the optical window is detected at the photocathode which emits electrons by the photoelectric effect [53]. The Nobel Prize in Physics 1921 was awarded to A. Einstein for his contributions to Theoretical Physics, and especially for his interpretation of the photoelectric effect [54]. The released photoelectrons are electrostatically accelerated onto an electron multiplier. Typically, MCP-PMTs comprise a dual MCP in place of the conventional discrete dynode structure of the classical PMTs [55]. On an impact of each electron on the inner wall of a channel, a number of secondary electrons are emitted. Being accelerated by the electric field created by the voltage applied across both ends of the MCP, these secondary electrons bombard the channel wall again to produce additional secondary electrons. This process is repeated many times along the channel and as a result, a large number of electrons are released from the output end and collected at the anode. Figure 2.1 shows the cross section of a typical MCP-PMT. The applied voltages are typically 200 V for the input and output gaps and 2000 V across the MCPs for an overall gain of 10^6 electrons [56].
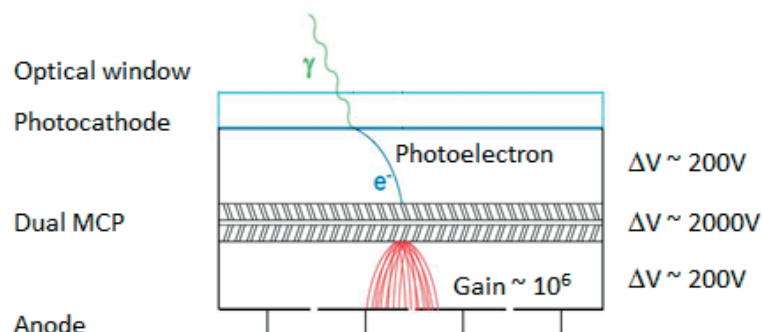
Figure 2.1: Cross section layout of a typical MCP-PMT describing its principle of operation [56].

2.2 Optical window

The transmission properties of the optical window exerts influence on the light spectrum reaching the photocathode. The choice of the window material is especially significant when detecting ultraviolet light (UV), as is the case for Cherenkov radiation. The light transmission in the UV region in the case of TORCH needs to be optimized and is a compromise between light yield and chromatic effects. This aspect will be examined thoroughly in Chapter 6 .

The following common window materials are used in the manufacturing of vacuum tubes:

- borosilicate glass: suitable for incident light of wavelength greater than 300 nm.

- uv glass: transmits down to 185 nm.

- quartz: made from fused silica its sensitivity can extend down to 160 nm and has the additional advantage of low radioactive background.

- sapphire (Al_2O_3): it has good UV transmission and low background.

2.3 Photocathode

The photocathode is deposited as a semitransparent layer directly on the inside surface of the optical window. Ideally, a photon entering a photocathode always releases an electron, but in reality this incident photon can be reflected, transmitted or absorbed [57] as shown in Figure 2.2. Some absorbed photons will yield free electrons but these are not always emitted into the vacuum. Those free electrons which are not emitted into the vacuum can undergo several processes:

- electrons may lose energy by electron-phonon scattering in the crystal lattice

- electrons may lose energy by inelastic electron-electron scattering

- electrons may get to the photocathode-vacuum interface without sufficient energy to overcome the potential barrier at the surface (due to the high work function, ϕ, of the photocathode)
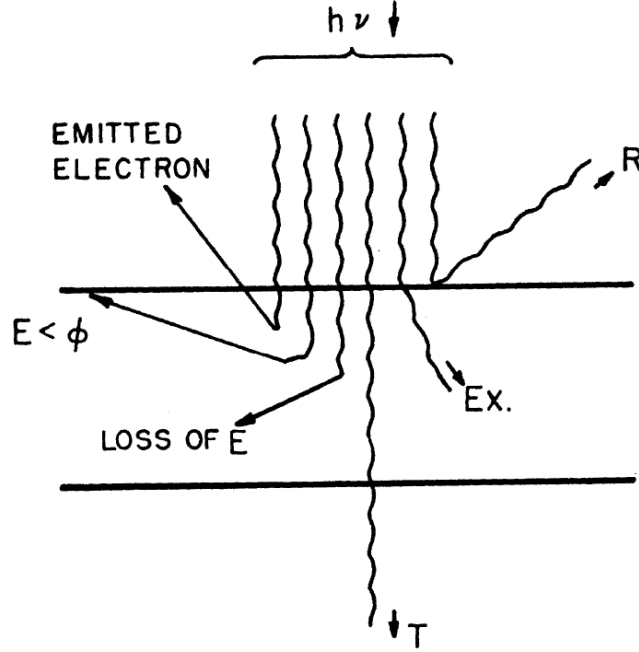
Figure 2.2: Schematic of the several processes an incident photon on a reflective photocathode can undergo [57].

2.3.1 Photocathode sensitivity

The photoemission process was described in terms of optical absorption length, l_a, and electron scattering processes as well as work function of the photocathode material by the Spicer Three-Step model [58]. The photocathode sensitivity describes the conversion efficiency for photons into photoelectrons. The spectral response is the relation between photocathode sensitivity and wavelength. The average photoelectric yield per incident photon is the quantum efficiency (QE) and is usually expressed as a percentage. It is the most essential quantity bearing on the performance of a photon detector. Other fundamental factors such as time resolution, signal-to-noise ratio and detection efficiency are all correlated to QE. The quantum yield (QY) was derived as a function of photon energy in [59] and is given by the following formula:

$$QY = \frac{number\ of\ electrons\ emitted}{number\ of\ absorbed\ photons} = \frac{\frac{\alpha_{PE}}{\alpha} P_E}{1 + \frac{l_a}{L}} \tag{2.1}$$

where α is the photon absorption coefficient of the material, $\frac{\alpha_{PE}}{\alpha}$ is the fraction of electrons excited above the vacuum level, P_E is the electron escape probability for reaching the surface

with sufficient energy to escape into the vacuum and $\frac{l_a}{L}$ is the ratio of absorption length to scattering length, L. All parameters are functions of the photon energy.

From Equation 2.1, one can show how the various parameters determine the QE. A higher QE implies large P_E and $\frac{\alpha_{PE}}{\alpha}$ and small $\frac{l_a}{L}$. Photon absorption should take place over a distance smaller or closer to the scattering length, so that a large amount of the excited electrons will escape and contribute to increase the QE. To obtain $L > l_a$ electrons should escape without undergoing electron-electron scattering. The term $\frac{\alpha_{PE}}{\alpha}$ will get larger by reducing the electron affinity, E_A, the difference between the vacuum level and the conduction band minimum. Typical values of this ratio are in the range of 0.1 to 1.

2.3.2 Photocathode materials

Photocathodes can be fabricated from a variety of components and each photocathode type will have a characteristic spectral response. The choice of a particular photocathode is mainly governed by the wavelength distribution of the photons to be detected.

Semiconductors are much better photoemitters than metals, they have an energy window twice the energy gap, E_g, where electrons have sufficient energy to escape from the material without interacting with other electrons. This is seen in Figure 2.3. Consequently, the dominating mode of scattering is the electron-phonon interaction which may orientate electrons in the right direction to escape from the material into the vacuum.
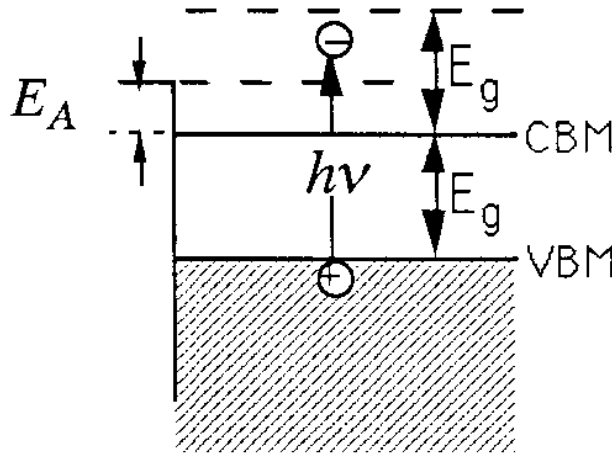
Figure 2.3: Electron-electron scattering in semiconductors. Electrons excited in the energy window $<2E_g$ escape into the vacuum without interacting with other electrons [59].

In alkaline photocathodes, in order to emit a photoelectron, the incident photon energy should be enough to let the electron reach the vacuum level from the valence band. This means that for a photon with energy $h\nu$=3 eV, an electron will be emitted if $\phi = E_g + E_A$ is smaller than 3 eV. Alkali metals have low work function, in particular Cs is the element with the lowest work

function and has been used in combination with other materials to form a highly efficient semiconductor [57]. The most used photocathodes in the production of MCP-PMTs are the following:

- bialkali (SbKCs): it has mostly replaced one of the earliest photocathodes, the S11 (SbCs), providing better sensitivity in the blue region and lower dark current. Recently, new bialkali photocathodes with much higher QE have been developed by Hamamatsu [60].

- S20, trialkali or multialkali (NaKSbCs): its response extends from UV to the near infra-red. It has higher light level capability but may require cooling to reduce dark current. It is one of the latest photocathodes, accidentally discovered by Sommer in 1956 [57].

2.4 The micro-channel plate electron multiplier

MCP electron multipliers were mainly developed for night vision applications as image intensifiers [61]. Over the last years, several particle identification and time-of-flight detectors considering the employment of this technology for fast timing are under study or development as part of new or existing high energy physics experiments [62]. Some of these detectors have been introduced in Chapter 1.

The MCP is a planar element consisting of an array of millions of parallel micro-channels usually manufactured from lead glass as shown in Figure 2.4. The MCP manufacturing process is covered in [63, 64]. The glass structure is treated in such a way as to optimize the secondary emission properties of the channel walls. Hence, each channel is considered as a continuous dynode acting as its own resistor chain. Input and output electrodes deposited on each face of this glass structure are made of Nickel-Chromium alloy. When electrodes are evaporated a fraction of the metallic coating remains in each channel and is referred to as "end spoiling" [65]. The depth of the electrode penetration into the MCP channel is within the range of 0.5 to 3 in units of channel diameters, d (see Section 2.6 for details).
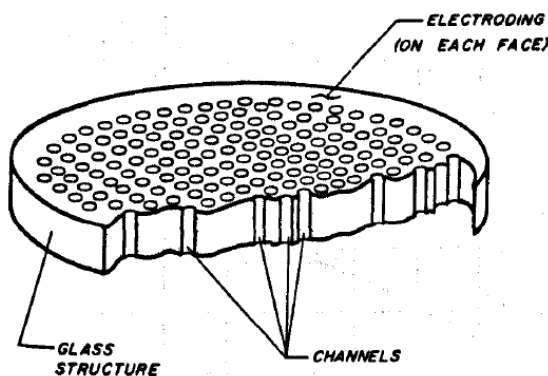
Figure 2.4: Cutaway view of a micro-channel plate electron multiplier [63].

The typical diameter of a channel is in the range 6-100 μm and the MCP thickness is of order 1 mm. A fundamental parameter on the electrical performance of the MCP electron multiplier is the ratio of channel length, l, to channel diameter defined by $\alpha = l/d$, which is typically between 40 and 100 [63]. Reduced pore size decreases the channel length for the same photoelectron amplification, reducing the transit time. To achieve optimal timing performance it is desirable to have small channels, a minimum value of α and a high electric field across the MCP.

2.4.1 Types of MCP electron multiplier structures

Channel axes are typically normal to or form a small angle with respect to the MCP input surface. For straight channels ions of residual gas molecules and gas molecules adsorbed by the input surface of the MCP can drift back to the channel input and produce after pulses. These ions can also bombard the photocathode and damage it, thereby reducing the photon detector lifetime. The optimal bias angle is typically in the range 5-15 °. A bias angle increases transit time and photoelectron amplification; α can be reduced while increasing the bias angle to keep the same timing properties but improving the photon detector lifetime. A commonly used mechanism of impeding positive ions produced at the output of the rear plate from reaching the input of the front plate is the chevron configuration where two MCPs are stacked and the bias angle of the channels is staggered as seen in Figure 2.1. The plates are typically separated by 50-150 μm and individually operated at gains of ~10^3 electrons. Devices with three MCPs staggered, known as Z-stack configuration, are also feasible [64]. In general the various structures are a compromise between physical dimension and electrical performance, especially regarding gain, timing properties and robustness against external magnetic fields.

2.4.2 Gain

MCP amplification is accountable for the anode rise time. Secondary electron trajectories result in fluctuations in the time between strikes at the channel walls. A typical secondary yield is 2. The number of strikes depends on the velocity of individual secondary electrons, and for $\alpha = 40$ there are typically 10 strikes. This leads to a gain of ~10^3 electrons for a single MCP plate with a quasi-negative exponential as pulse height spectrum (PHS).

The channel gain is limited by the space charge density which is defined by the channel geometry and the overall applied voltage. The maximum gain is proportional to the channel diameter. In the case of a chevron configuration, the voltage between the two MCPs has an effect on the output PHS, on the spreading of the electron cloud. The parameter α sets the gain assuming the same applied electric field.

2.4.3 Open Area Ratio

The Open Area Ratio (OAR) is the geometrical ratio between the total open area and the full effective area of an MCP and is typically about 60%. In the case of a MCP with a channel pitch of 32 μm and a channel diameter of 25 μm, the OAR is 55%.

2.5 The photocathode - MCP gap

Photoelectrons emitted by the photocathode into the vacuum are accelerated onto the input surface of the MCP by an electric field. Transit time spread (TTS) originates from the variation in photoelectron velocity and angle at emission, an effect that gets worse at larger incident photon energies. Smaller physical gap dimensions and/or an increase of the applied voltage will reduce this effect resulting in a smaller transit time, and therefore TTS.

The released photoelectrons have different energies and may escape into the vacuum with a velocity v at different emission angles, δ, with respect to the normal of the photocathode surface. From second Newton's law, one can obtain the photoelectron's trajectory as follows:

$$F = 0 = m_e \ddot{x}_1 \rightarrow \dot{x}_1 = constant \rightarrow x_1 = v \sin\delta\, t + x_0$$

$$F = eE = m_e \ddot{y}_1 \rightarrow \dot{y}_1 = \frac{eE}{m_e} t + v\cos\delta \rightarrow y_1 = \frac{eE}{2m_e} t^2 + v\cos\delta\, t + y_0 \tag{2.2}$$

Consequently, from Equation 2.2 one calculates the transit time difference between the time a photoelectron with 0 eV initial kinetic energy and a photoelectron with 1.5 eV initial kinetic energy take to reach the MCP input surface, at $y_1 = h$. This difference is given by:

$$\Delta t_{transit} = t_{0eV} - t_{1.5eV} = \sqrt{\frac{2m_e}{eV/h}} h - \frac{-\frac{2m_e}{eV/h} v\cos\delta + \sqrt{\left(\frac{2m_e}{eV/h} v\cos\delta\right)^2 + 4\frac{2m_e}{eV/h} h}}{2} \tag{2.3}$$

where m$_e$ is the electron mass, the electric field is $E = V/h$, V is the voltage difference between the photocathode and the MCP input and h is the gap distance between the photocathode and the MCP. Figure 2.5 (left) shows the transverse spatial displacement indicated as x_1 in Figure 2.6 and Figure 2.5 (right) the transit time difference, both as a function of δ for four MCP-PMTs which have different input gaps. The largest input gap is represented by the red coloured line. The largest values of x_1 correspond to δ=90° while the largest transit time differences correspond to δ=0.

2.5.1 Back-scattering effects

The design of the MCP glass structure implies dead space between channels as shown in Figure 2.4. Photoelectrons can undergo back-scattering effects at the MCP input surface by
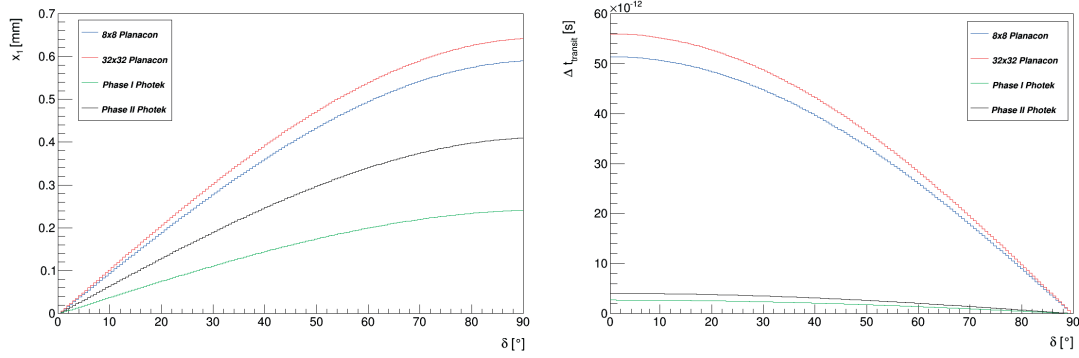
Figure 2.5: Transverse position and transit time difference at the photocathode-MCP gap where (350 V, 4.9 mm, red line), (350 V, 4.5 mm, blue line), (200 V, 0.2 mm, black line) and (175 V, 0.12 mm, green line) are the applied voltage and the input gap values for various MCP-PMTs studied for TORCH.

hitting this dead area, being reflected with a velocity v' at an angle, β, with respect to the MCP input surface and slowed down by the electric field. Some of these photoelectrons are re-accelerated and hit back the entrance of a channel. Figure 2.6 shows a typical event for a photoelectron suffering back-scattering effect at the MCP-PMT input gap.
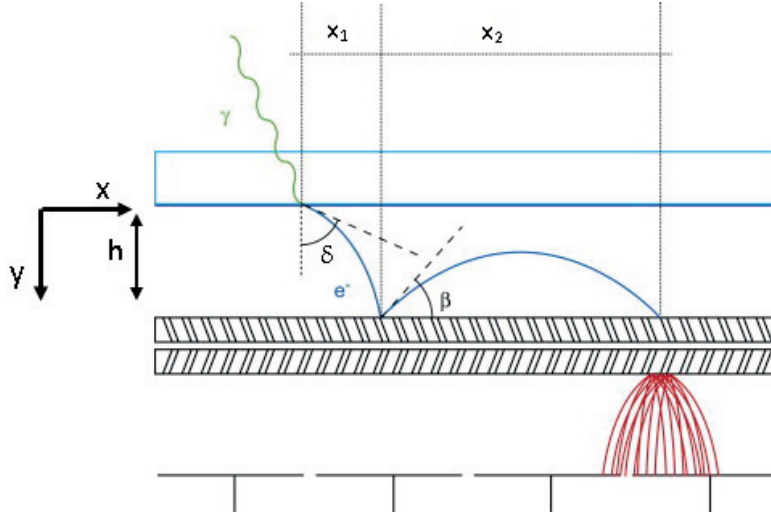
Figure 2.6: Back-scattered photoelectron leading to a signal at the MCP-PMT anode [56].

From second Newton's law, one can obtain the photoelectron's trajectory as follows:

$$F = 0 = m_e \ddot{x}_2 \rightarrow \dot{x}_2 = constant \rightarrow x_2 = v' \cos\beta t + x_1$$

$$F = \frac{eV}{h} = -m_e \ddot{y}_2 \rightarrow \dot{y}_2 = -\frac{eV}{m_e h} t + v' \sin\beta \rightarrow y_2 = -\frac{eV}{2m_e h} t^2 + v' \sin\beta t + y_1 \tag{2.4}$$

From Equation 2.4 and with the knowledge that $y_2=y_1$, the time that a photoelectron takes to hit back the input surface of the MCP after being back-scattered is calculated as

$$t_{back-scattering} = \frac{2 m_e v' \sin\beta}{eV/h} \tag{2.5}$$

Back-scattered photoelectrons can travel a maximum distance from its initial strike of twice the gap distance. This maximum spatial range corresponds to a photoelectron elastically back-scattered at an angle of 45 ° with respect to the MCP input surface. In terms of timing, a photoelectron elastically back-scattered at an angle of 90 ° with respect to the MCP input surface will result in a maximum time value corresponding to twice the initial transit time. This is graphically reproduced in Figure 2.7 which shows the spatial and timing range of back-scattered photoelectrons at the input gap for various MCP-PMTs.
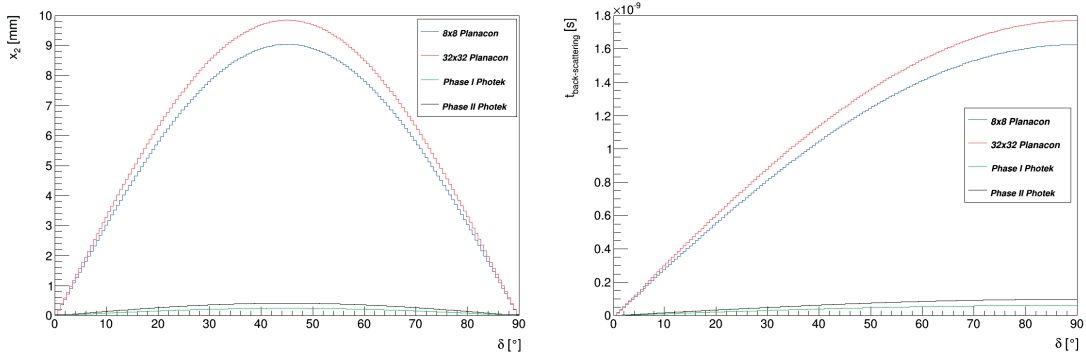
Figure 2.7: Transverse position and time of back-scattered photoelectrons at the MCP input surface where (350 V, 4.9 mm, red line), (350 V, 4.5 mm, blue line), (200 V, 0.204 mm, black line) and (175 V, 0.12 mm, green line) are the applied voltage and the input gap values for various MCP-PMTs studied for TORCH. In the calculation it is assumed that the initial kinetic energy of a photoelectron at the exit of the photocathode is 1.5 eV with an emission angle δ=0.

Late pulses occurring in MCP-PMTs and visible in their TTS distributions as long tails after the main peak are attributed to back-scattered photoelectrons. Late pulses are a feature of vacuum photon detectors. Back-scattered photoelectrons affect not only the timing response of the tube but also its spatial resolution. The detection efficiency of these photoelectrons is also reduced.

2.6 The MCP - anode gap

In the MCP-anode gap region of an MCP-PMT, the transit time spread is the variation in velocity of secondary electrons at the output of the MCP after the amplification process. It is dominated by the location of their emission point in the MCP and is also affected by the transverse momentum of secondary electrons. Similarly to the photocathode-MCP gap, the

reduction of the output gap physical dimensions or the increased voltage reduce the transit time and the effects of the transverse momentum of secondary electrons. The MCP input and output gaps can be varied and adapted to different applications.

Notably, end spoiling has an impact on the spread of the output electron cloud. In applications requiring high spatial resolution the depth is preferably larger resulting in a collimated output electron cloud however producing less gain. Figure 2.8 shows the effect on the electron cloud for two depths of electrode penetration. The signal quality at the anode may also be affected by the capacitance and inductance between the two electrodes.
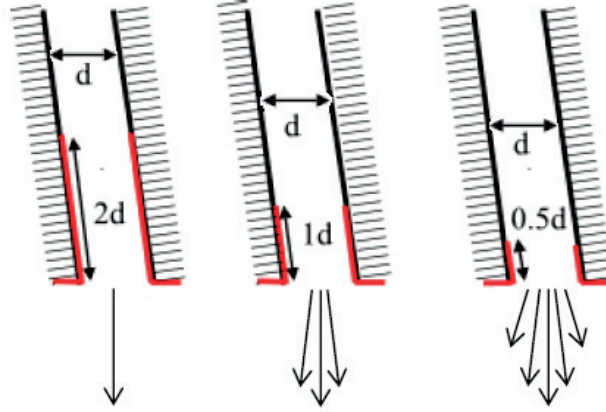
Figure 2.8: Schematic showing the depth of the electrode penetration in units of channel diameters at the output of the channels in an MCP. Larger depth results in a collimated output electron cloud and smaller gain [65].

2.7   Ion-feedback and ageing

It is important to differentiate between late pulses resulting from back-scattering effects and after pulses caused by ions drifting back to the photocathode. They are well known as ion-feedback pulses and their delay time from the main pulses is typically from hundreds of nanoseconds to dozens of microseconds.

When increasing the tube gain the probability to have ions in the high charge density region, the output of the MCP channels, is higher and the quality of the vacuum is degraded. Consequently, the MCP lifetime is affected by the change in the secondary emission coefficient due to electron bombardment in the channel walls.

Good lifetime for the photon detectors in TORCH (see Subsection 1.3.2) is also essential to ensure given that they will be operated in a high photon environment up to the 10 MHz/cm^2 level.

Many recent improvements in photon detector lifetime have been achieved. The Belle-II Col-

laboration used a thin film as ion barrier which was placed between the two MCPs preventing ions drifting back to the input gap and hitting the photocathode [66]. With the complement of a ceramic insulator for preventing chemical reactions and ensuring stable QE response up to an integrated anode charge of 3 C/cm^2 was achieved [67]. The most innovative technology is the Atomic Layer Deposition (ALD) technique [68]. It is a chemical process where the MCPs are coated in three steps with a resistive layer, a secondary emission layer and an electrode layer. The main advantage of this technique is to achieve the same gain with significantly lower operating voltage across the MCP due to the higher secondary electron yield compared to the standard MCP glass. Since the operating voltage is lower, the secondary electron energy is lower and this results in a drop of the probability to produce an ion. Consequently, the damage of the photocathode due to ion bombardment is reduced. This film coating technology has been successfully applied in MCP-PMTs by the PANDA Collaboration showing a stable QE beyond the 5 C/cm^2 [69, 70]. TORCH also requires extended lifetime photon detectors [71]. MCP-PMT prototypes manufactured with ALD technology are described in Chapter 3.

2.8 Timing limitations

The main factors that affect the timing performance are:

- intensity level of operation

- detected QE

- electron optics and amplification

- signal processing and readout electronics

Since TORCH will detect single photoelectrons a low noise and very fast amplifier is essential. An efficient photocathode together with an optimal secondary emission yield for the initial strike into the channel wall would help to maximize the QE which also depends on the collection efficiency. Reducing the MCP input and output gaps decreases the transit time of photoelectrons resulting in better timing. Larger electron amplification may result in larger gain improving the timing performance, however the lifetime of the photon detector would be affected.

3 | Characterization of MCP photon detectors using commercial electronics

3.1 Commercial devices

In this section, commercial MCP-PMTs that have been characterized at CERN are described. The performance of single-anode and multi-anode devices read out using commercially-available single-channel electronics is presented. The multi-anode device has also been characterized with custom-made multi-channel electronics. This will be thoroughly discussed in Chapter 4.

3.1.1 Single-channel MCP photon detectors

The present subsection reports on the characterization of two commercially-available single-channel MCP tubes[1] [72]. They have a 18 mm diameter dual MCP in chevron configuration and a 25 mm active diameter for the quartz input window. The bleeder chain is encapsulated in the tube outer case. The photocathode is of the type S20. The QE curves provided by the manufacturer are reproduced in Figure 3.2. Both devices have similar spectral response. The MCP channel diameter is 6 μm with an α parameter of 50. The photocathode-MCP gap is 120 μm and the MCP-anode gap is 1 mm. This tube design provides immunity against magnetic field, a fast response and very low time jitter.

Experimental set-up

The light source is a pulsed laser diode[2] emitting at 405 nm. The laser pulse width is 21 ps full width at half maximum (FWHM) for an optimal laser tune setting of 60%. The light is attenuated through a digital variable attenuator[3] and neutral density (ND) filters[4] [73] to reach

---

[1]Single-channel MCP device model PP0365G from Photonis-DEP B. V., Roden, The Netherlands.

[2]Optical head model PiL040, digital control unit EIG1000D from PiLas, D-12489, Berlin, Germany.

[3]Digital variable attenuator model DA-100-3S-405-3/125-S-40 from OZ Optics Limited, 219 Westbrook Rd, Ottawa, ON, Canada.

[4]WRATTEN Neutral Density Filters No 96, Kodak.
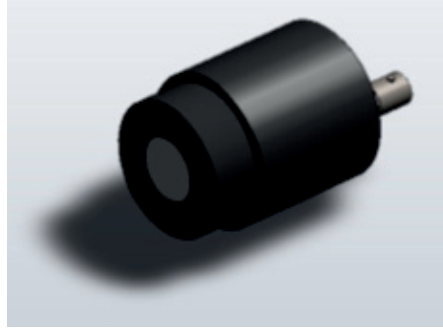
Figure 3.1: Single-channel MCP device model PP0365G from Photonis-DEP.
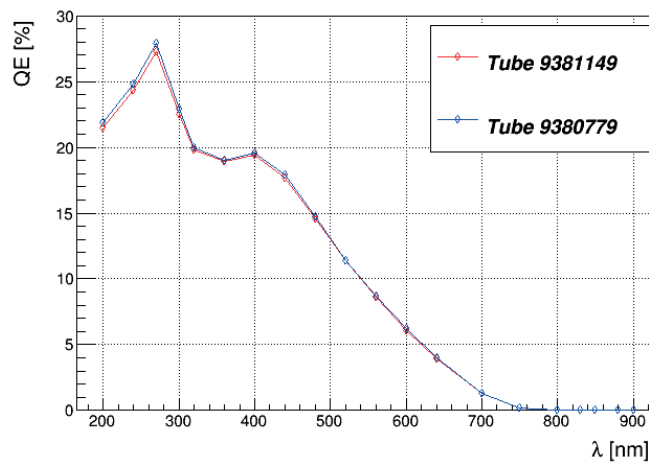
Figure 3.2: QE versus wavelength, λ, curves for both single-channel MCP devices model PP0365G from Photonis-DEP.

the single photon regime. The light is focused with a microfocus lens[5] and a collimator[6]. The best spot size achieved was 200 μm FWHM at a distance of 27.3 mm [47]. Single-channel electronics is used to read out the output signal from the tubes. Data are registered in a multi-channel analyser[7] (MCA). An RC filter is used for noise reduction from the high voltage supply and the bleeder chain configuration for both tubes is 1:10:3 where one unit corresponds to a 0.5 MΩ resistor value. A total voltage of 2.93 kV is applied (1.95 kV across the dual MCP).

Laser light level and MCP gain calibrations

The light intensity and the MCP gain are calibrated. The measurements are carried out using a charge pre-amplifier[8] [74] connected to a spectroscopy shaping amplifier[9] with a shaping

---

[5]Microfocus lens model PIL040MFS-30 from PiLas, D-12489, Berlin, Germany.

[6]Optics collimator model PIL040-FC-6.16 from PiLas, D-12489, Berlin, Germany.

[7]Multi-channel analyser model ADCAM 926 MCA (8192 channels) from ORTEC, Oak Ridge, TN37831-0895, USA.

[8]Charge pre-amplifier model 142 A from ORTEC, Oak Ridge, TN37831-0895, USA.

[9]Spectroscopy shaping amplifier model 672 from ORTEC, Oak Ridge, TN37831-0895, USA.

time of 0.5 μs [75]. The experimental set-up is shown in Figure 3.3 and a typical Pulse Height Spectrum (PHS) in single photon regime is shown in Figure 3.4.
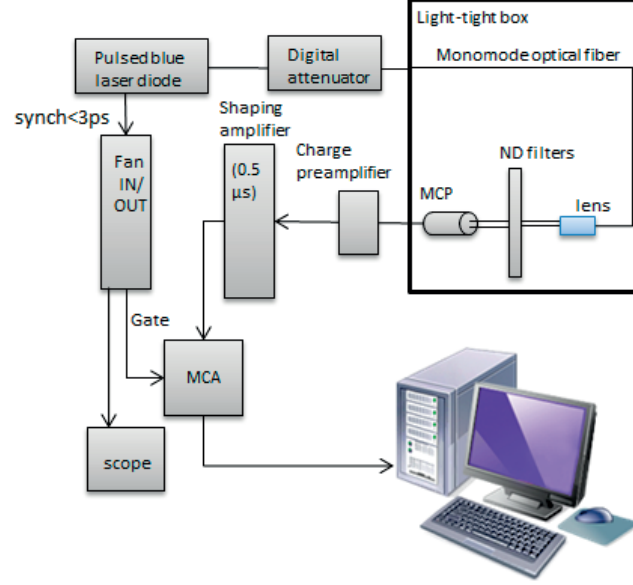
Figure 3.3: Experimental set-up used for the laser light level and MCP gain calibrations.
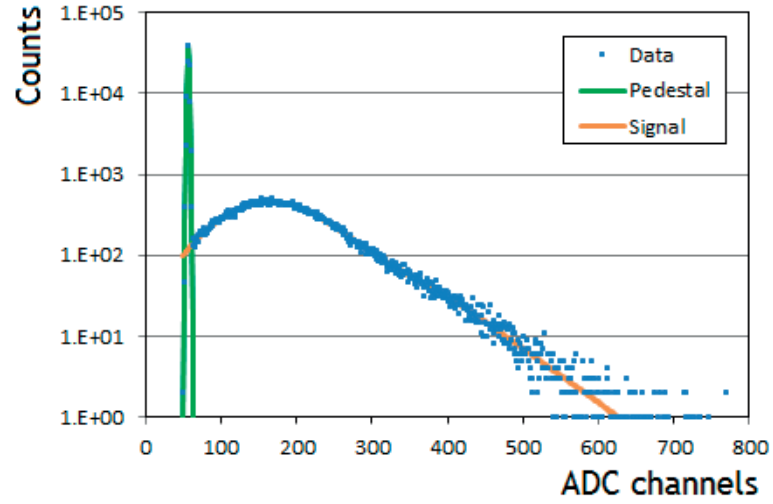
Figure 3.4: Pulse height spectrum in single photon regime (vertical logarithmic scale) for tube 9381149. Experimental data is fitted with a Poisson distribution model.

A standard Poisson distribution is used to fit the spectrum and is in very good agreement with the data. The light source fluctuation is given by:

$$P_\mu(N) = \frac{e^{-\mu}\mu^N}{N!} \tag{3.1}$$

where N is the number of photoelectrons per pulse and μ the average number of photoelectrons. The pedestal is fitted with a Gaussian with standard deviation σ_0 and the full PHS is fitted with the following equation:

$$f_{PHS}(x) = S \times \left(\sum_{N=0}^{\infty} P_\mu(N) \times Gaussian(x, x_N, \sigma_N) \right) \tag{3.2}$$

where S is a normalization parameter and $Gaussian(x, x_N, \sigma_N)$ is a Gaussian function which takes into account the MCP gain fluctuation. The model assumes that the N-photoelectron peak width, σ_N, scales as

$$\sigma_N = \sigma_1 \sqrt{N} \tag{3.3}$$

where σ_1 is the width of the 1-photoelectron peak and the position of the N-photoelectron peak is calculated as $x_N = x_0 + N \times (x_1 - x_0)$. The first impact of a photoelectron at the MCP channel wall dominates in the amplification process, similarly to the first dynode in PMTs. The secondary electron yield at first impact, ϵ, can be estimated as

$$\epsilon \sim \left(\frac{x_1 - x_0}{\sigma_1} \right)^2 \tag{3.4}$$

The value of μ is inferred from the counts in the pedestal normalized to the total number of counts equivalent to the probability to have zero photoelectrons, P(0). In Figure 3.4, μ is 0.52±0.06. The fraction of two photoelectrons contaminating the 1-photoelectron peak is

$$\frac{P_{0.52}(2)}{P_{0.52}(1)} = \frac{\mu}{2} = \frac{0.52}{2} = 26\% \tag{3.5}$$

The tube response is essentially assessed for single photoelectrons. The light level calibration requires a compromise between the contamination of two photoelectrons and the optimization of data taking time.

The tube gain is estimated from the position of the 1-photoelectron peak with respect to the pedestal position in Figure 3.4. The conversion factor from ADC channels into charge is estimated from the injection of a test pulse of variable amplitude into the charge preamplifier (Figure 3.5) and measuring the peak position of the pedestal in ADC channels. the conversion factor corresponds to

$$1\,fC = 4.9 \pm 0.4\, ADC\, channel \tag{3.6}$$

Then, dividing by the electron charge 1.602×10^{-19} C, the MCP gain is determined.

By modifying the digital attenuator settings a set of PHS measurements at different light intensities is performed. The photon yield and the MCP gain are estimated for each light intensity value. The resulting data for both tubes are tabulated in Tables 3.1 and 3.2.
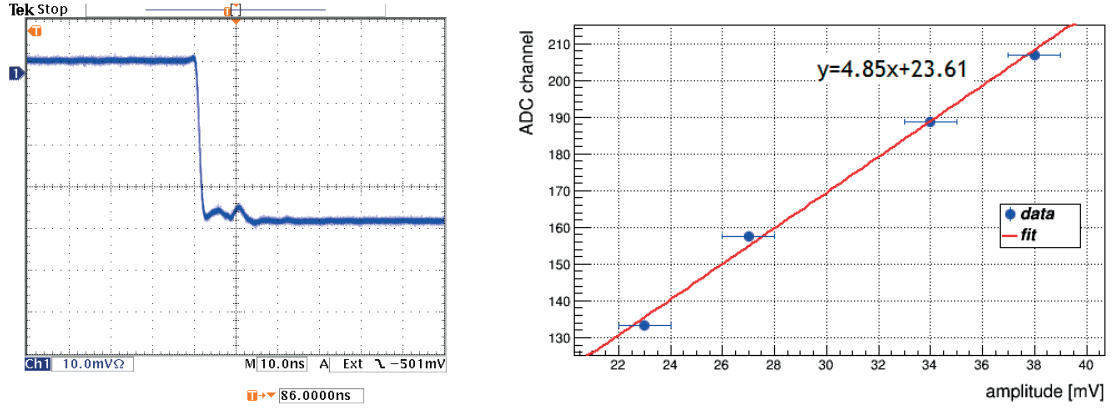
Figure 3.5: Scope display of a test pulse injected through a 1 pF capacitor into the charge pre-amplifier to perform the calibration of the MCA (left). Pedestal peak position in ADC channels as a function of the amplitude of a test pulse injected into the charge pre-amplifier (right).

Table 3.1: Average number of photoelectrons and MCP gain estimate for tube 9381149.

tube 9381149								
Average number of photoelectrons	0.1	0.25	0.56	0.86	1.06	2.06	2.52	3.9	6.8
Gain [10^5 e$^-$]	1.2	1.2	1.1	1.1	1.1	1	1	1	1

Table 3.2: Average number of photoelectrons and MCP gain estimate for tube 9380779.

tube 9380779					
Average number of photoelectrons	0.2	0.4	1.97	4	8
Gain [10^5 e$^-$]	2	1.9	1.8	1.6	1.5

The overall gain for tube 9381149 is in the range $(1\text{-}1.2) \times 10^5$ electrons and for tube 9380779 in the range $(1.5\text{-}2) \times 10^5$ electrons for the same total voltage applied of -2930 V. For both tubes the gain decreases as the average number of photoelectrons increases. This is attributed to the MCP rate capability: with a spot size of 200 μm, a laser rate of 1 kHz and for an average number of photoelectrons of 1 the corresponding rate is 2.5 MHz/cm^2.

The PHS recorded at different light intensities are reproduced in Figure 3.6. For small μ values the first photoelectron peak is clearly visible and leads to small gain fluctuations. The secondary electron yield at first impact is estimated to be ϵ=2.6.

Signal time derivation characteristics

In electronics systems without noise and signal amplitude variations, a leading-edge discriminator would precisely measure the arrival time of analogue pulses [76]. However, in systems with a non-negligible electronics noise level this noise induces a jitter in the leading-edge time
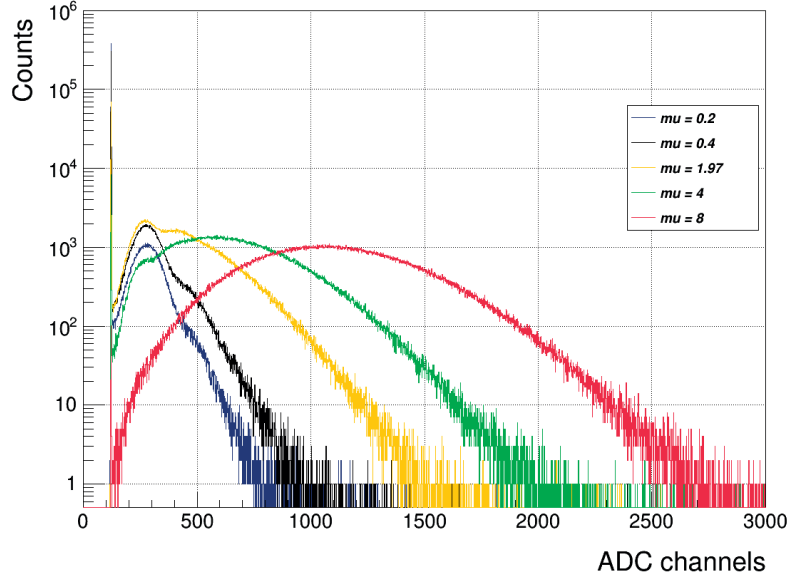
Figure 3.6: Pulse height spectra (vertical logarithmic scale) at different light intensities and a laser tune setting of 60% for tube 9380779.

derivation (Figure 3.7 (left)). The noise contributes to the time jitter, σ_j, as

$$\sigma_j = \frac{\sigma_n}{\mathrm{d}V/\mathrm{d}t} \tag{3.7}$$

where σ_n is the voltage amplitude of the noise and dV/dt is the slope of the signal at the discriminator threshold level.

In the case of MCP-PMTs, their output analogue signals vary in amplitude due to gain fluctuations. Large amplitudes cross the discriminator threshold earlier than small amplitudes which results in a time walk (Figure 3.7 (right)). In an ideal system, the discrimination time should be the same independently of the signal amplitude. Since the slope of the signal varies depending on the number of photoelectrons, the contribution to the time resolution from the MCP will be modelled with the following function:

$$\sigma_{MCP}^2 = \frac{\sigma_{TTS}^2}{\mu} \tag{3.8}$$

where σ_{TTS} is the time resolution from the single photoelectron TTS.

Time walk corrections may be performed by a Constant Fraction Discriminator (CFD). The constant fraction discrimination approach originates from the observation of scintillation detectors and PMT signals. The timing of their leading edge was optimal at a specific fraction of their amplitude, usually 10-15%. Devices using this technique produce accurate timing information from analogue signals of varying amplitudes but the same rise time with the elimination of time walk [77]. The principle of a CFD is based on zero-crossing techniques
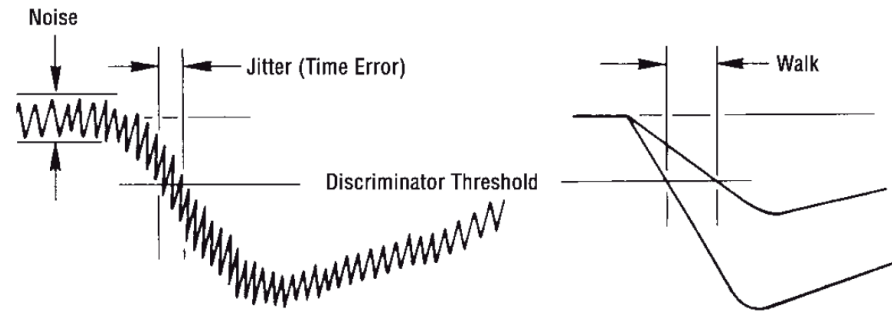
Figure 3.7: Jitter and walk in leading-edge time derivation [76].

and consists of:

- splitting the input signal in two

- attenuating half of it and delaying the other half

- and feeding the two halves into a fast comparator with the delayed input inverted.

The amount of attenuation is determined by the particular fraction of the input amplitude, usually 0.2, desired in a CFD. The delay is chosen in such a way that the CFD fires where the maximum of the attenuated signal crosses the delayed signal, corresponding to a constant fraction of the delayed signal amplitude. The resulting Constant-Fraction signal is illustrated in Figure 3.8.

Timing performance

Timing properties of the tubes have been studied at the same operating conditions as for the gain measurements. Time jitter measurements are performed with a 1 GHz fast timing amplifier with CFD[10] [76, 78]. The threshold discriminator level is adjusted in such a way to be above the noise. The threshold setting value corresponds to a voltage amplitude, V, and is applied after the amplification of the input pulse (Figure 3.9 (left)). The fine tuning of a walk setting allows to minimize the time walk as a function of input pulse amplitude. The effect of the walk setting on the signal time derivation is illustrated in Figure 3.9 (right). Large amplitudes are detected later than small amplitudes for a negative walk setting and earlier than small amplitudes for a positive walk setting.

The start time reference is provided by the laser synchronization signal with <3 ps jitter[11] as specified by the manufacturer, and the stop time by the output signal from the CFD. Both start and stop signals are input into a Time-to-Amplitude Converter[12] (TAC) [79] and data

---

[10]Fast timing amplifier and CFD model 9327 from ORTEC, Oak Ridge, TN37831-0895, USA.

[11]Laser diode data sheets from PiLas, D-12489, Berlin, Germany.

[12]Time-to-amplitude converter model 566 from ORTEC, Oak Ridge, TN37831-0895, USA.
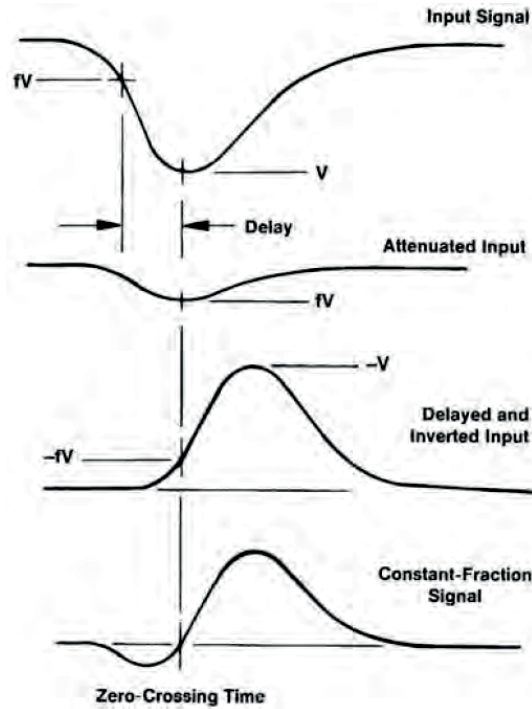
Figure 3.8: Formation of the Constant-Fraction signal [76].
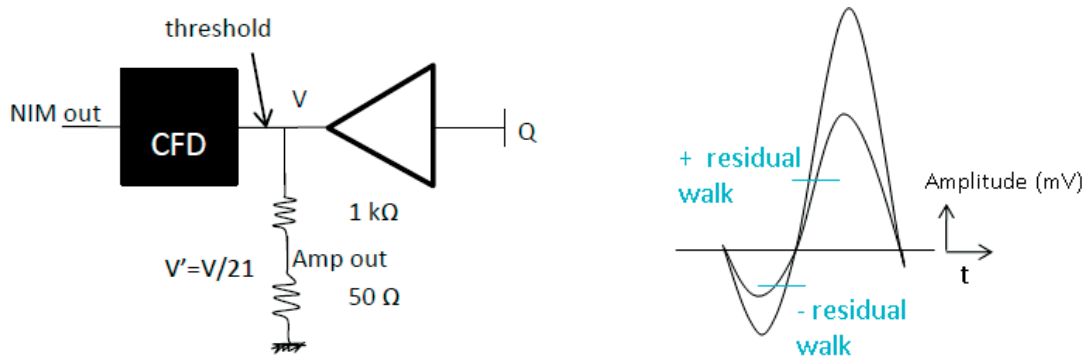
Figure 3.9: CFD schematics (left). Walk setting example (right).

are registered with a MCA with time bin precision of 6.25 ps. The experimental set-up for timing measurements is shown in Figure 3.10. A typical time jitter distribution (TJD) in single photoelectron regime (μ=0.52 from Figure 3.4) is reproduced in Figure 3.11.

The time distribution in single photoelectron regime for these tubes essentially consists of two parts (from left to right): a main prompt peak and a shoulder on the right of it. The main peak represents the MCP intrinsic time response and the shoulder is attributed to a combination of photoelectron back-scattering effects at the MCP input surface and the influence of the laser tune setting. A secondary pulse is seen after ~150 ps which is consistent with the laser
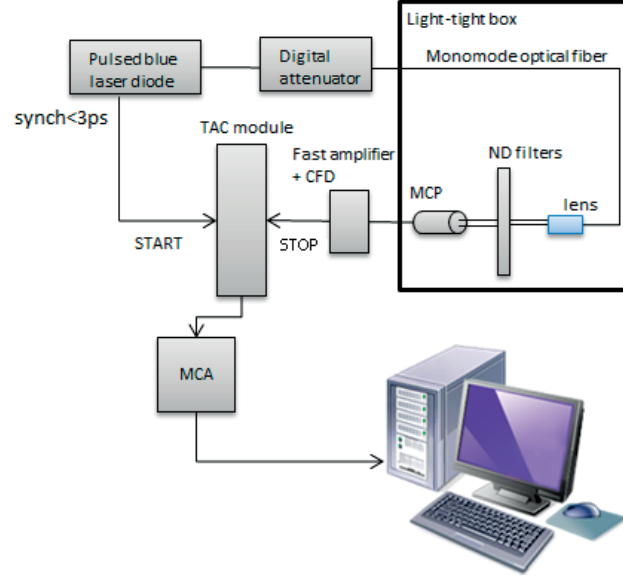
Figure 3.10: Experimental set-up used for the systematic studies of the single-channel MCP timing performance.
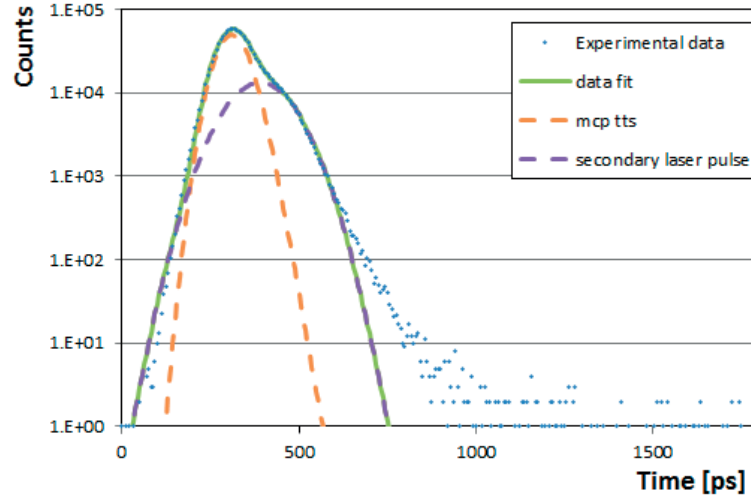
Figure 3.11: Time distribution in single photoelectron regime (vertical logarithmic scale) at a laser tune setting of 60%, with a MCP intrinsic time resolution of 38.9 ps.

relaxation pulse from the manufacturer's data reproduced in Figure 3.12 which shows the laser pulses measured with a streak camera at 100 kHz. The pulse width for the optimal laser tune setting of 60% is 21 ps FWHM and at a tune setting of 30% the corresponding width is 35 ps. This width is larger but not dominant. Due to the rather small MCP input gap of 120 μm, the maximum time for a back-scattered photoelectron as calculated using Equation 2.5 is ~60 ps. To account for this effect and the resulting peak asymmetry the main peak is fitted with an
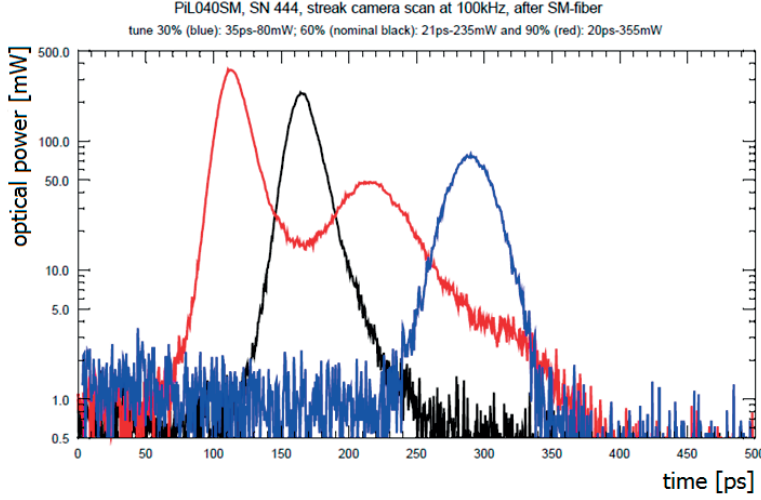
Figure 3.12: Laser pulse measurements with streak camera at 100 kHz for laser tune settings of 30%, 60% and 90% (PiLas data sheets).

exponentially-modified Gaussian distribution [80]

$$f_{peak}(t) = \frac{A}{\tau} \times \left(0.5 \, erf \left(\frac{\frac{t - t_c}{\sigma_g} - \frac{\sigma_g}{\tau}}{\sqrt{2}} \right) + 0.5 \right) \exp \left(0.5 \left(\frac{\sigma_g}{\tau} \right)^2 - \frac{t - t_c}{\tau} \right) \tag{3.9}$$

where t is the time, A is an amplitude, t_c is the centroid at maximum height of the unmodified Gaussian, σ_g is the standard deviation of the unmodified Gaussian, τ is the time constant of exponential decay used to modify the Gaussian and $erf(z) = 2/\sqrt{\pi} \int_0^z e^{-t^2} \, dt$ is the error function. The laser relaxation pulse is fitted with a Gaussian. The time resolution value is defined as the standard deviation of the unmodified Gaussian, σ_g. In Figure 3.11 a time resolution of 38.9 ps is achieved for single photoelectrons. These experimental results have been achieved operating the MCP at a low gain of $\sim 10^5$ electrons.

Probability studies of late photoelectrons

The shoulder in the time distribution is populated by late photoelectrons. Only those late photoelectrons from back-scattering effects will affect the TORCH performance and a precise estimate of this fraction is key. The CFD reacts on the first prompt photoelectron that gets amplified and reaches the MCP anode. Consequently, for a given light pulse, the right-hand part of the time distribution is populated only in the case where all photoelectrons are late [81]. Denoting the probability that one photoelectron is late by p_{late}, the probability that N photoelectrons are late in a given event is:

$$p_\mu^{late}(N) = \frac{e^{-\mu} \mu^N p_{late}^N}{N!} \tag{3.10}$$

Consequently, the probability that at least one photoelectron is prompt in a given event is:

$$p_\mu^{prompt}(N) = \frac{e^{-\mu}\mu^N\left(1 - p_{late}^N\right)}{N!} \tag{3.11}$$

Considering all values for N, the previous expressions become:

$$\sum_{N=1}^{\infty}\frac{e^{-\mu}\mu^N p_{late}^N}{N!} = e^{-\mu}\left(e^{\mu p_{late}} - 1\right) \tag{3.12}$$

and

$$\sum_{N=1}^{\infty}\frac{e^{-\mu}\mu^N\left(1 - p_{late}^N\right)}{N!} = e^{-\mu}\left(e^{\mu} - e^{\mu p_{late}}\right) \tag{3.13}$$

Dividing both series,

$$\frac{e^{\mu p_{late}} - 1}{e^{\mu} - e^{\mu p_{late}}} = \frac{s_{late}}{s_{prompt}} \tag{3.14}$$

which corresponds to the ratio between the number of late events, s_{late}, over the number of prompt events, s_{prompt}. The latter is represented with the exponentially-modified Gaussian fit of the time distribution.

Now, since $s_{late}=s\text{-}s_{prompt}$, the ratio between prompt events over the total number of events, s, is given by

$$\frac{s_{prompt}}{s} = \frac{e^{\mu} - e^{\mu p_{late}}}{e^{\mu} - 1} \tag{3.15}$$

The limit of this expression when $\mu \to 0$ is $1\text{-}p_{late}$.

Time distributions recorded at different light intensities are reproduced in Figures 3.13 and 3.14. Data are fitted using Equation 3.9. Therefore, the standard deviation of the unmodified Gaussians are inferred from the fit and are tabulated in Tables 3.3 and 3.4. The time resolution values are expected to be reduced as the average number of photoelectrons increases.

Table 3.3: Estimated time resolution values at a laser tune setting of 60% for tube 9381149.

laser tune setting of 60%	tube 9381149				
Average number of photoelectrons	0.1	0.25	0.56	0.86	1.06
Time resolution (Eq. 3.9) [ps]	43.3	41.7	42.0	44.5	43.8
Time resolution (Eq. 3.9 + Gaussian) [ps]	40.6	39.2	40.2	40.6	39.9

laser tune setting of 60%	tube 9381149			
Average number of photoelectrons	2.06	2.52	3.9	6.8
Time resolution (Eq. 3.9) [ps]	38.9	31.5	30.4	29.7
Time resolution (Eq. 3.9 + Gaussian) [ps]	33.1	29.5	28.3	26.0
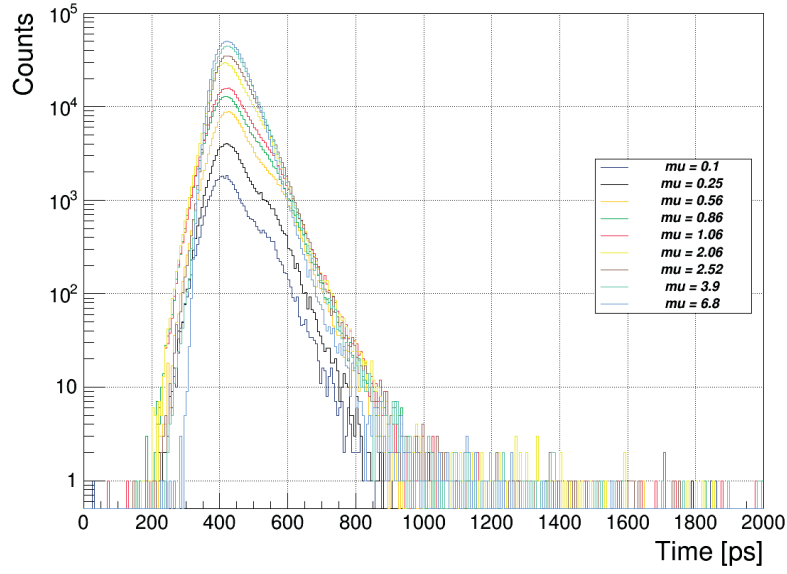
Figure 3.13: Time distributions (vertical logarithmic scale) at different light intensities and a laser tune setting of 60% for tube 9381149.
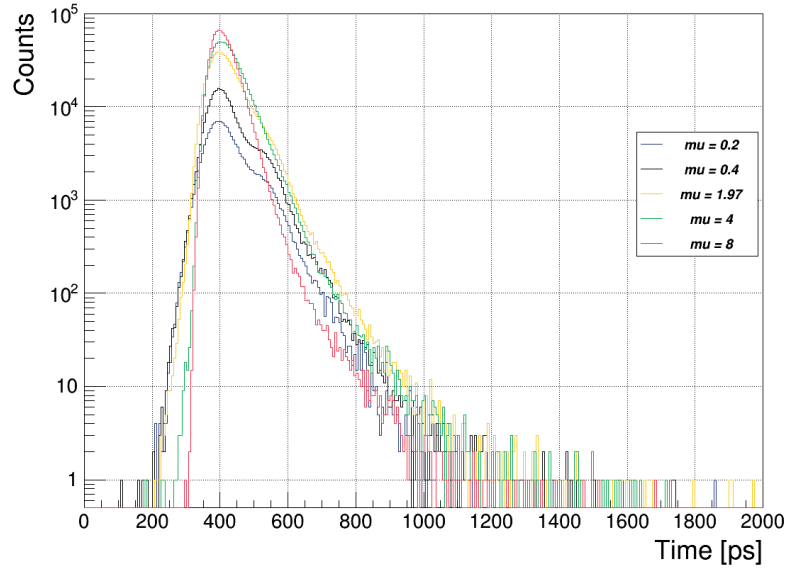
Figure 3.14: Time distributions (vertical logarithmic scale) at different light intensities and a laser tune setting of 60% for tube 9380779.

Table 3.4: Estimated time resolution values at a laser tune setting of 60% for tube 9380779.

laser tune setting of 60%	tube 9380779				
Average number of photoelectrons	0.2	0.4	1.97	4	8
Time resolution (Eq. 3.9) [ps]	36	29.7	27.7	24.3	21
Time resolution (Eq. 3.9 + Gaussian) [ps]	34.9	31.3	26.6	19.2	17.8

The prompt peak of the MCP time response and its asymmetry for large values of μ are well described by Equation 3.9. The time resolution is improved when including a Gaussian in the fitting model accounting for the laser shoulder. These tubes feature a time resolution of 26.0 ps and 17.8 ps in multi-photon regime (μ>6). As expected, better resolutions are achieved for larger values of light intensity.

The following effects contribute to the overall measured time resolution:

- MCP intrinsic TTS

- laser pulse width (21 ps at laser tune setting of 60%)

- laser synchronization pulse of <3 ps

- slope signal $\propto$ number of photoelectrons

- CFD: time jitter + residual walk

- MCA time bin precision of 6.25 ps

- photon energy (photoelectron emission velocity spectrum)

The time resolution values are fitted with the following analytical model:

$$\sigma = \sqrt{\sigma_{MCP}^2 + \sigma_{other}^2} = \sigma_{TTS} \times \sqrt{\frac{1}{\mu} + \frac{\sigma_{other}^2}{\sigma_{TTS}^2}} = A \times \sqrt{\frac{1}{\mu} + B} \qquad (3.16)$$

From the resulting fitting parameters of the experimental data in Figure 3.15 for tube 9380779 using Equation 3.16 a value for σ_{TTS}=12.3±1.4 ps is obtained. The parameter B is 3.5±1.1, and a resolution of 23±4 ps including other contributions is inferred.

Subsequently, the ratios of the prompt events normalized to the total number of events, s_{prompt}/s, are calculated. Data are represented in Figures 3.16 and 3.17 for both MCP tubes at different light intensities and fitted with Equation 3.15 from which the probability p_{late} is inferred.

The probability for a photoelectron to be late because of back-scattering effects or the laser relaxation pulse is 15.7%±1.3% for tube 9380779 and 14.9%±0.9% for tube 9381149 at a laser tune setting of 60%. The asymmetry in the main peak includes effects from the CFD and back-scattering and are difficult to disentangle. Given the small gap between the photocathode and the MCP input a fraction of back-scattered photoelectrons populates the main peak and part of both back-scattering effects and the laser relaxation pulse are superposed in the shoulder. In order to disentangle the two contributions, a new set of timing measurements on tube 9380779 has been performed. By reducing the laser tune setting, from 60% to 30% and 20%, the amplitude of the laser relaxation pulse is decreased. Time distributions recorded
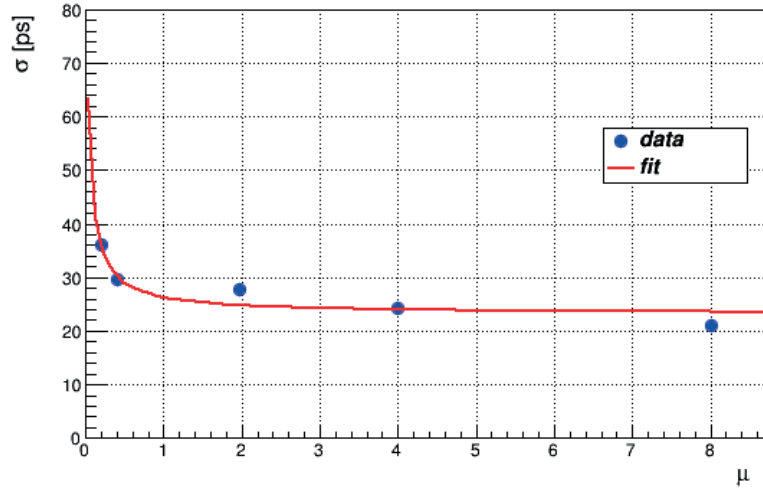
Figure 3.15: Time resolution values as a function of the average number of photoelectrons at laser tune setting of 60% for tube 9380779.
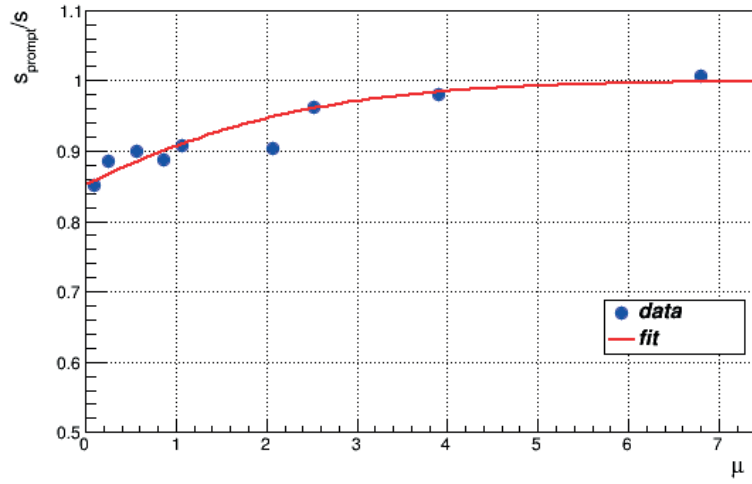
Figure 3.16: Experimental data fitted with Equation 3.15 at different light intensities and a laser tune setting of 60% for tube 9381149. A value for p_{late} of 14.9%±0.9% is inferred.

at different light intensities are reproduced in Figures 3.18 and 3.19. As previously, the main peak on the timing spectra is fitted using Equation 3.9. The standard deviation values are tabulated in Tables 3.5 and 3.6. The surface ratios are then calculated and data are represented in Figures 3.20 and 3.21. The corresponding probabilities are inferred.

Table 3.5: Estimated time resolution values at a laser tune setting of 30% for tube 9380779.

laser tune setting of 30%	tube 9380779					
Average number of photoelectrons	0.25	0.53	1.13	2.02	4.52	8.67
Time resolution (Eq. 3.9) [ps]	35.9	34.3	35.6	25.8	17.7	12.2
Time resolution (Eq. 3.9 + Gaussian) [ps]	34.7	34.6	34.3	25.4	15.3	10.4
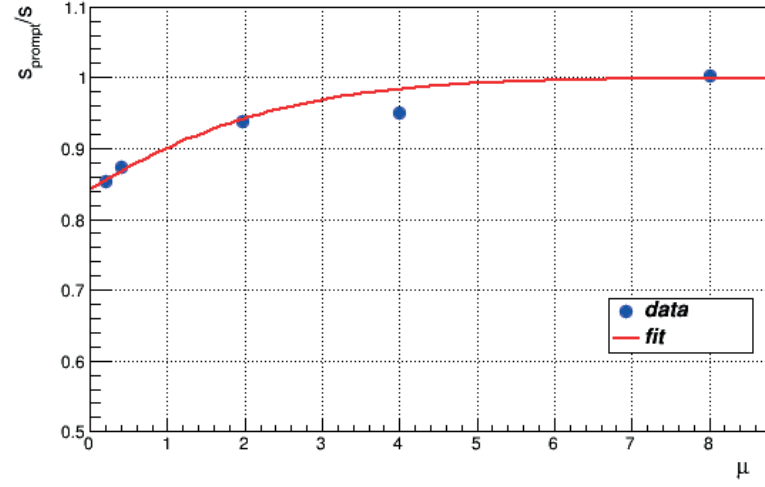
Figure 3.17: Experimental data fitted with Equation 3.15 at different light intensities and a laser tune setting of 60% for tube 9380779. A value for p_{late} of 15.7%±1.3% is inferred.
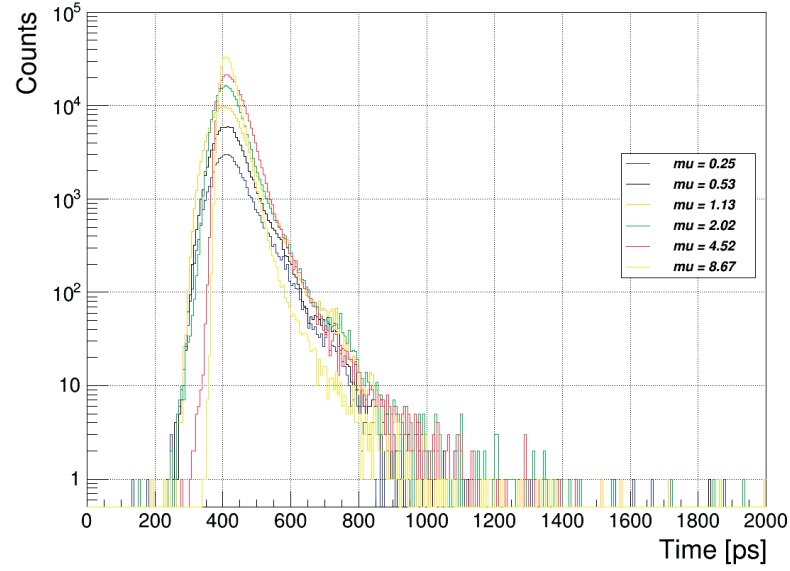
Figure 3.18: Time distributions (vertical logarithmic scale) at different light intensities and a laser tune setting of 30% for tube 9380779.

Table 3.6: Estimated time resolution values at a laser tune setting of 20% for tube 9380779.

laser tune setting of 20%	tube 9380779					
Average number of photoelectrons	0.15	0.33	0.63	1.41	2.96	6.4
Time resolution (Eq. 3.9) [ps]	37.5	39.3	37	28.4	29.5	15.3
Time resolution (Eq. 3.9 + Gaussian) [ps]	34.9	34.8	35.6	27.8	29.3	12.9

At a laser tune setting of 20% the influence of the laser is clearly reduced and consequently
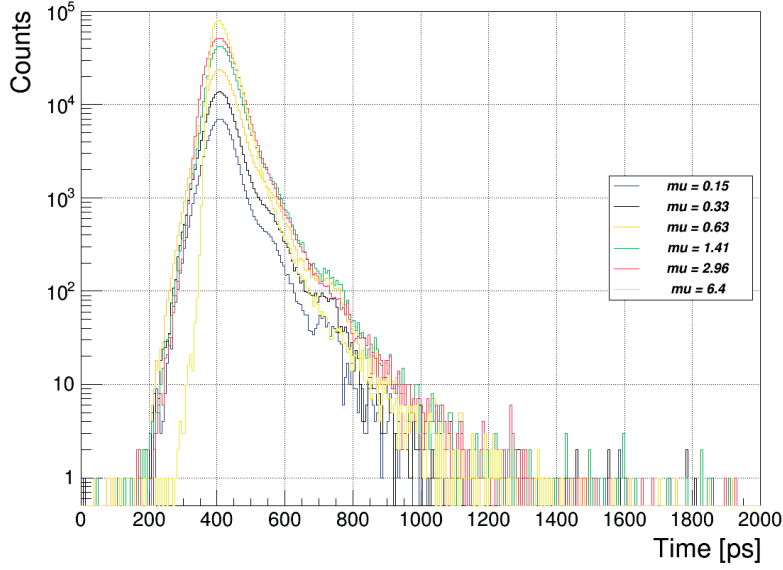
Figure 3.19: Time distributions (vertical logarithmic scale) at different light intensities and a laser tune setting of 20% for tube 9380779. Note that the laser peak visibility is better for μ=0.15 for a laser tune setting of 20% than for μ=0.25 for a laser tune setting 30%.
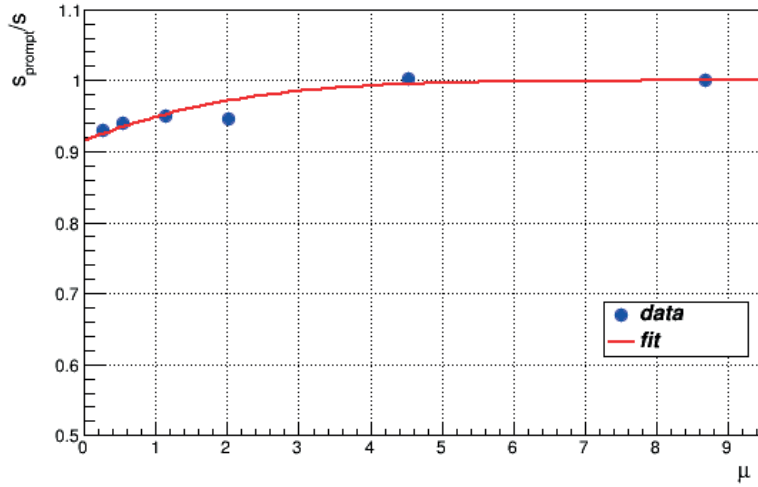
Figure 3.20: Experimental data fitted with Equation 3.15 at different light intensities and a laser tune setting of 30% for tube 9380779. A value for p_{late} of 8.6%±0.9% is inferred.

the late events are less affected. This study results in a probability of 5.3%±0.4% for a photo-electron to be late due to back-scattering effects. Though, the complement of back-scattered photoelectrons populates the main peak given the small photocathode-MCP gap in these devices. A time resolution of 12-15 ps in multi-photon regime is achieved when using a laser tune setting of 20%.
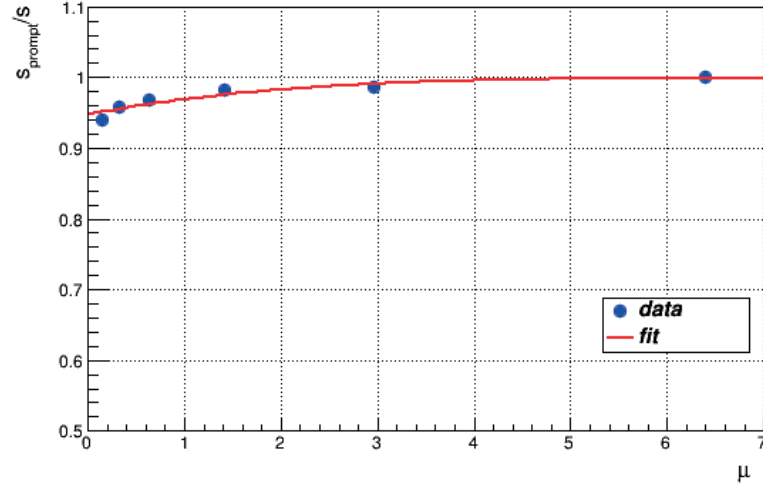
Figure 3.21: Experimental data fitted with Equation 3.15 at different light intensities and a laser tune setting of 20% for tube 9380779. A value for p_{late} of 5.3%±0.4% is inferred.

Spatial scans

PHS and TJD measurements at different positions of the laser spot with respect to the tube axis have been performed. Since the active diameter is 18 mm, 7 mm offsets from the axis have been chosen (Figure 3.22). Two light intensity settings, μ=0.55 and 2.1 photoelectrons, have been considered. Figure 3.23 (left) reproduces the PHS at all laser spot positions and Figure 3.23 (right) reproduces the TJD at all laser spot positions. The average number of photoelectrons does not vary significantly when illuminating a different part of the optical window of the MCP tube. On the other hand, the peak position in the time distributions shifted with respect to that when the laser illuminates at the centre of the optical window. The offsets between the various peaks are attributed to signal propagation time on the metallic anode surface. Signals at the edges of the sensitive surface tend to be delayed [56]. However, similar time resolution values have been measured and are tabulated in Table 3.7.
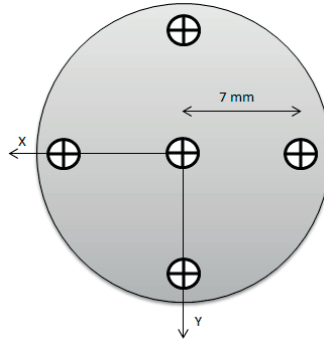
Figure 3.22: Schematic front-view of single channel MCP tube showing the different laser spot positions.
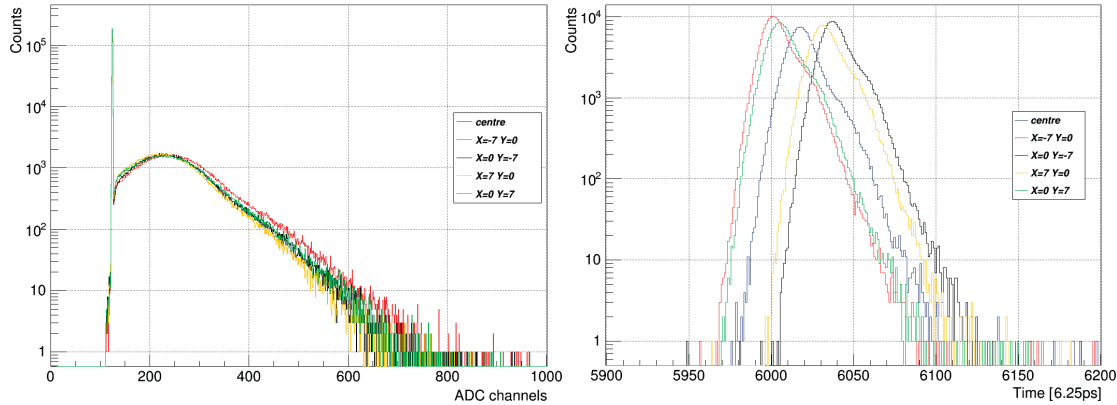
Figure 3.23: Pulse height spectra (left) and time distributions (right) for all laser spot positions (both in vertical logarithmic scale).

Table 3.7: Average number of photoelectrons and time resolution values for the different laser spot positions at a laser tune setting of 60% for tube 9381149.

tube 9381149

Laser position [mm]	Average number of photoelectrons	Time resolution [ps]
(x,y) = (0,0)	0.52	42.3
(x,y) = (7,0)	0.52	40.6
(x,y) = (0,7)	0.55	42.0
(x,y) = (-7,0)	0.56	38.4
(x,y) = (0,-7)	0.55	39.3
(x,y) = (0,0)	2.00	37.5
(x,y) = (7,0)	2.00	38.8
(x,y) = (0,7)	2.12	38.7
(x,y) = (-7,0)	2.15	37.1
(x,y) = (0,-7)	2.10	37.5

3.1.2 8×8 pads Planacon MCP photon detector

To get closer to TORCH requirements a commercial segmented MCP has been investigated with emphasis on the single pad response. The Planacon MCP photon detector[13] consists of an array of 8×8 pads of dimensions 5.9×5.9 mm^2 and a pitch of 6.5 mm. A sealed square vacuum envelope of 53×53 mm^2 active area with physical dimensions of 59×59 mm^2 houses a dual MCP electron multiplier in chevron configuration. The MCP channel diameter is 25 μm with a value of α=40. The optical window made of quartz is 2 mm-thick and the photocathode is bi-alkali. The spectral sensitivity range is 200-650 nm with a typical peak QE of 22% at 380 nm. The photocathode-MCP gap is 4.5 mm and the MCP-anode gap is 3.5 mm. The full data sheet is reproduced in Appendix A. The square shape of this photon detector allows to tile several units together to form larger detection surfaces and is consequently particularly

---

[13]Planacon MCP-PMT device model XP85012-A1 from Burle-Photonis, Lancaster, PA17601-5688, USA.

suited for TORCH.
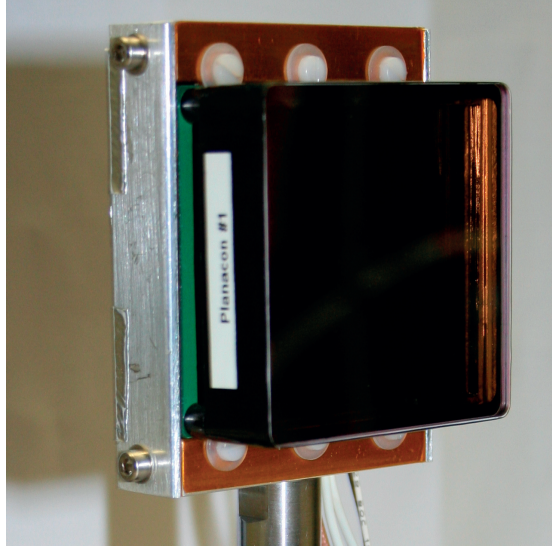
Figure 3.24: 8×8 pads Planacon MCP device model XP85012-A1 from Burle-Photonis.

During a 2010-2011 R&D phase 8×8 Planacons have already been characterized [47]. The response of a single pad was investigated using single-channel commercial electronics while all other pads were connected to ground. The experimental set-up was similar to the one used for the single-channel MCP tubes and described in the previous section (Figures 3.3 and 3.10). The bleeder chain configuration for the tube was 2:10:2 where 2 units correspond to a 1 MΩ resistor value. An overall voltage of 2.45 kV was applied (1.75 kV across the MCP). Data recorded at the time have been revisited [72]. In particular, since the Planacons have larger input gap than the single-channel MCPs the time distributions will be more affected by photoelectron back-scattering effects which can be detrimental for the TORCH performance.

Laser light level and MCP gain calibrations

A pulse height spectrum in single photoelectron regime is shown in Figure 3.25. This tube shows good charge resolution and an exponential behaviour between the pedestal and 1-photoelectron peaks. Data are fitted using Equation 3.2 and an additional negative exponential which accounts for small-amplitude events corresponding to photoelectrons that are not fully amplified and/or collected at the anode. Part of these small-amplitude events is correlated to late photoelectrons through back-scattering effects [81]. The fitting function is in very good agreement up to three photoelectrons with the experimental data points. It deviates at large signals which are attributed to ion-feedback. A value of μ=0.51±0.05 is inferred. The secondary electron yield at first impact is estimated to be ϵ=4.1.
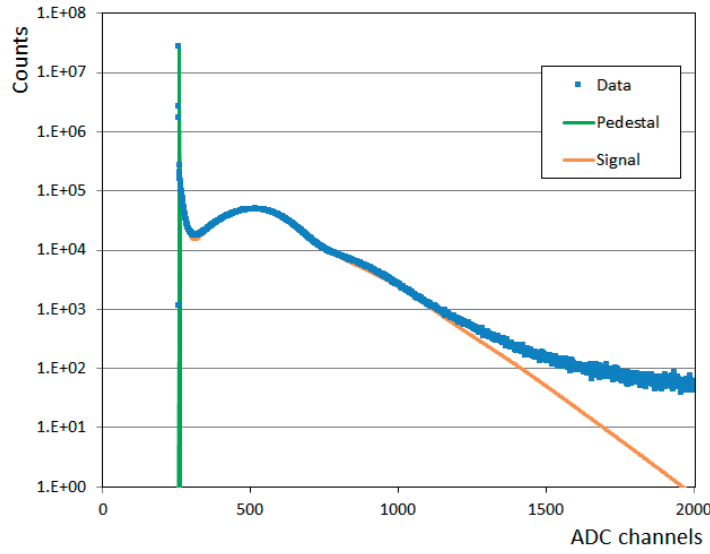
Figure 3.25: Pulse height spectrum in single photoelectron regime (vertical logarithmic scale) fitted with a Poisson distribution model from a single pad of the 8×8 pads Planacon.

The conversion factor from ADC channels into charge was

$$1 fC = 2.21 \, ADC \, channel \tag{3.17}$$

The light level was modified by combining different ND filters and a set of PHS measurements was performed at different light intensities (Figure 3.26). The Planacon gain at the centre of a single anode pad has been estimated. Given the point spread function (PSF) at the anode level was found to be ~1 mm FWHM [47] the collected charge on one pad is assumed to be the full charge (see further studies in Subsection 4.3.6). Table 3.8 reproduces the resulting data at a laser tune setting of 60%.

Table 3.8: Gain estimate from a single pad of the 8×8 pads Planacon.

laser tune setting of 60%	tube 9000906					
Average number of photoelectrons	0.52	1.39	2.96	4.13	5.72	7.55
Gain [10^5 e$^-$]	6.9	6.6	5.7	5.3	5.2	5.0

The overall gain for a single pad is in the range (5-6.9)×10^5 electrons. The gain decreases as μ increases, similarly to the behaviour for the single-channel MCPs.

Timing performance

Timing measurements were performed at the same operating conditions. A time distribution in single photoelectron regime is reproduced in Figure 3.27.
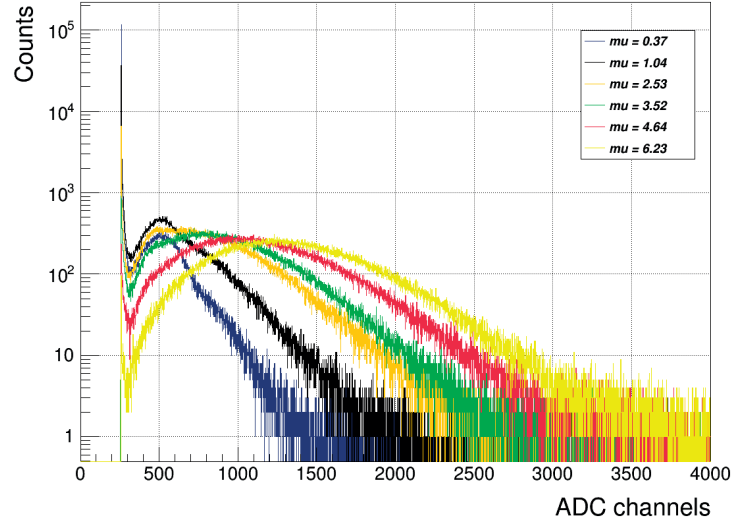
Figure 3.26: Pulse height spectra (vertical logarithmic scale) at different light intensities and a laser tune setting of 60% from a single pad of the 8×8 pads Planacon.
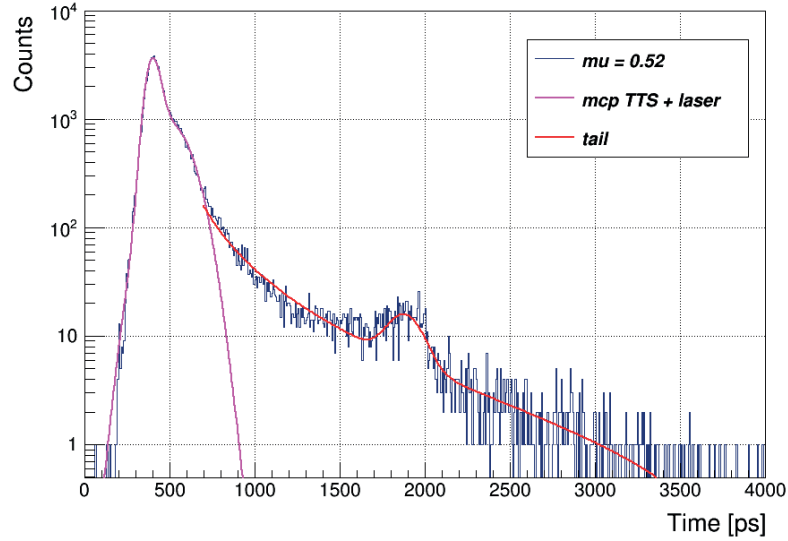
Figure 3.27: Time distribution in single photoelectron regime with μ=0.52 (vertical logarithmic scale) from a single pad of the 8×8 pads Planacon. Prompt signal with a time resolution of 35.9±0.4 ps, shoulder due to the laser relaxation pulse and tail due to backscattered photoelectrons. The fit range for the main peak and shoulder is 0-750 ps and for the tail is 700-4000 ps.

It consists of three parts (from left to right): a main prompt peak, a shoulder on the right of it, and a long tail. The main peak represents the MCP intrinsic time response, the shoulder is due to the laser relaxation pulse, and the long tail results essentially from photoelectron back-scattering effects at the MCP input surface and extends to ~1.5 ns from the main peak. This measured value corresponds to a photoelectron elastically backscattered at an angle of 90° with respect to the MCP input surface. It is consistent with the time value estimated from

the photocathode-MCP input gap of 4.5 mm and the voltage difference of 350 V as shown in the right plot in Figure 2.7. Given the large gap of the Planacon, a small fraction of back-scattered photoelectrons populates the main peak and both the laser and back-scattering effects are clearly distinguished in the distribution. As previously, the main peak is fitted using Equation 3.9 and the laser shoulder is fitted with a single Gaussian. The back-scattering tail is fitted using a model which takes into account the various components to the secondary electron yield [82, 83]:

$$f_{tail}(t) = \frac{a}{(t - t_c)^2} + b + c \times A \times \exp\left(-\frac{1}{2} \times \left(\frac{t - (t_c + d)}{e \times \sigma_g}\right)^2\right) \tag{3.18}$$

where t_c, A and σ_g are the parameters obtained from the exponentially-modified Gaussian fit and c, d and e are the fit parameters. The first term is related to the true secondary electrons, b is a constant term describing inelastically back-scattered electrons and the last term describes the elastically back-scattered electrons.

These Planacon tubes feature a time resolution of 35.9 ps in single photoelectron regime from the readout of a single pad with commercial electronics. These results have been achieved operating the MCP with a rather modest gain of 5×10^5 electrons.

Probability studies of late photoelectrons

The procedure described in the previous section is now applied to calculate the probability of a photoelectron to be late, p_{late}, for the Planacon tube. Time distributions recorded at different light intensities and at laser tune settings of 60%, 40% and 20% are reproduced in Figures 3.28, 3.31 and 3.33, respectively. Equation 3.9 is used to fit the data with and without the Gaussian fit accounting for the laser relaxation pulse. Therefore, the standard deviation of the unmodified Gaussians are obtained and tabulated in Tables 3.9, 3.10 and 3.11. The time resolution values are reduced as the average number of photoelectrons increases and are improved when including a Gaussian in the fitting function. The ratios of the prompt events normalized to the total number of events, s_{prompt}/s, are calculated and represented in Figures 3.29, 3.32 and 3.34.

Table 3.9: Estimated time resolution values at a laser tune setting of 60% from a single pad of the Planacon.

laser tune setting of 60%	tube 9000906					
Average number of photoelectrons	0.52	1.39	2.96	4.13	5.72	7.55
Time resolution (Eq. 3.9) [ps]	45.8	34.5	31.1	28.5	28.1	28.8
Time resolution (Eq. 3.9 + Gaussian) [ps]	35.9	32.4	28.2	27.7	24.6	25.0

The time resolution values are fitted using Equation 3.16 (Figure 3.30). A value for σ_{TTS}=19.6±1.9 ps is obtained. The fit parameter B is 1.6±0.4, and a resolution of 25±4 ps including other contri-
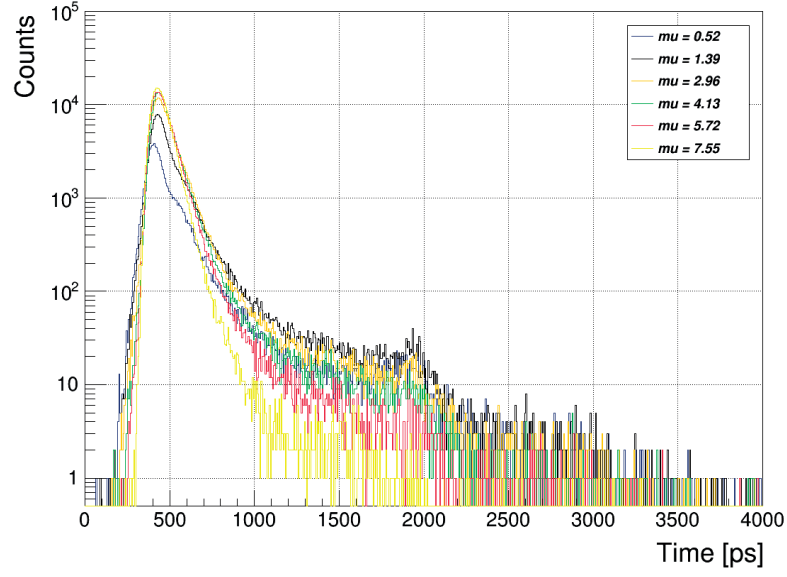
Figure 3.28: Time distributions (vertical logarithmic scale) at different light intensities and a laser tune setting of 60% from a single pad of the Planacon.
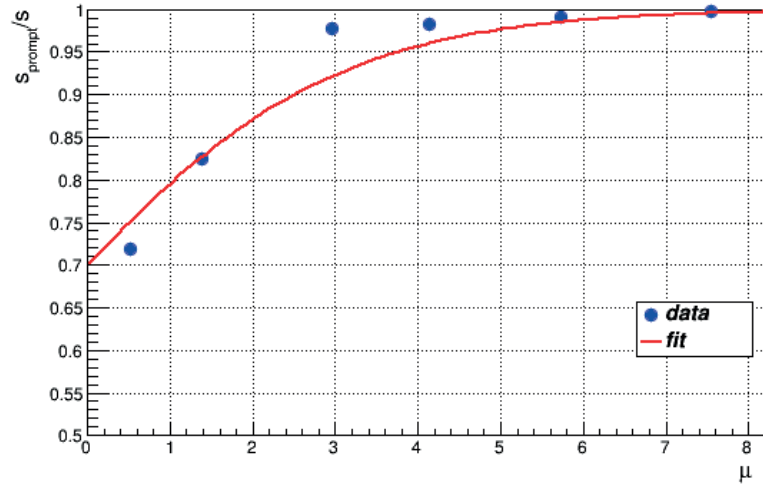
Figure 3.29: Experimental data fitted with Equation 3.15 at different light intensities and a laser tune setting of 60% from a single pad of the Planacon. A value for p_{late} of 30.3%±2.5% is inferred.

butions is inferred.

The probability for a photoelectron to be late is 30.3%±2.5% at a laser tune setting of 60%. This set of measurements shows that at this laser tune setting the effect of the laser operating mode is clearly seen on time distributions. By reducing the laser tune setting to 20% the number of late events is less dependent on this effect.

Since this tube has a large photocathode-MCP input gap, the tail in the time distributions is
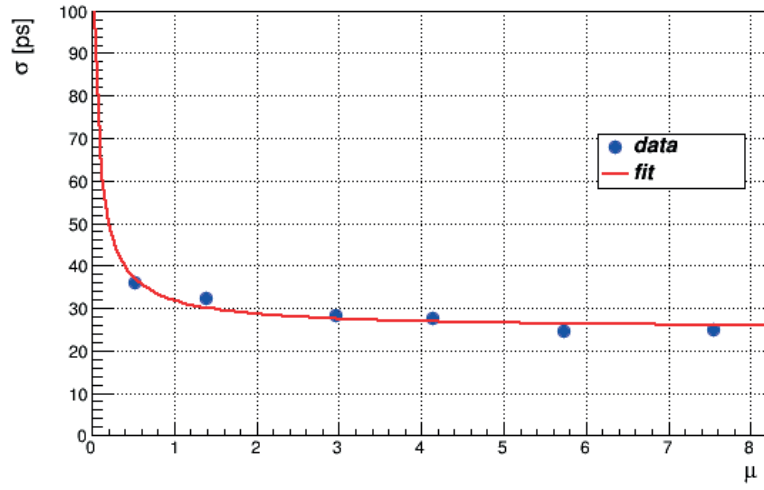
Figure 3.30: Time resolution as a function of average number of photoelectrons at a laser tune setting of 60% from a single pad of the Planacon.
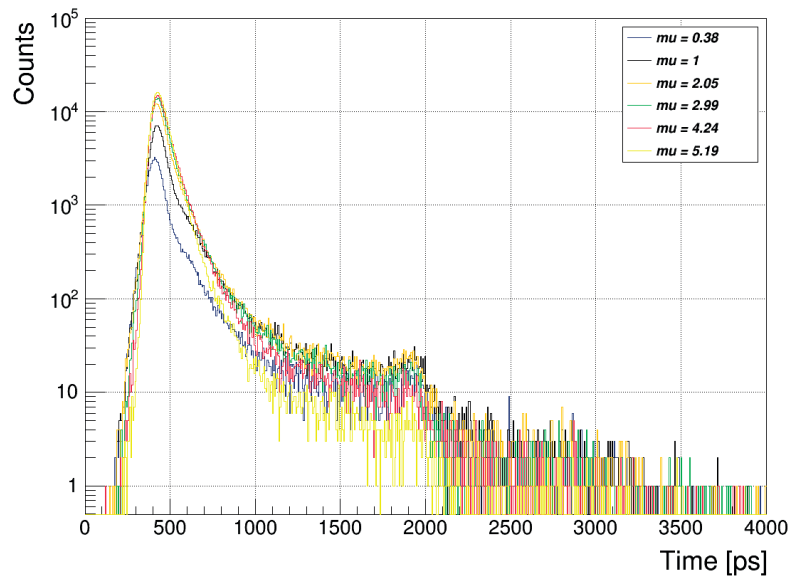
Figure 3.31: Time distributions (vertical logarithmic scale) at different light intensities and a laser tune setting of 40% from a single pad of the Planacon.

Table 3.10: Estimated time resolution values at a laser tune setting of 40% from a single pad of the Planacon.

laser tune setting of 40%	tube 9000906					
Average number of photoelectrons	0.38	1.00	2.05	2.99	4.24	5.19
Time resolution (Eq. 3.9) [ps]	43.8	39.9	32.4	29.5	26.8	26.1
Time resolution (Eq. 3.9 + Gaussian) [ps]	39.1	33.2	25.3	25.9	26.2	25.7
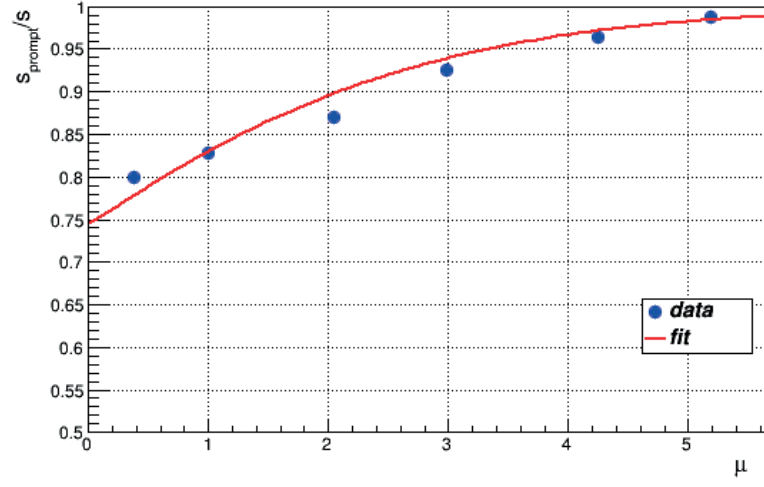
Figure 3.32: Experimental data fitted with Equation 3.15 at different light intensities and a laser tune setting of 40% from a single pad of the 8×8 pads Planacon MCP. A value for p_{late} of 25.8%±1.3% is inferred.
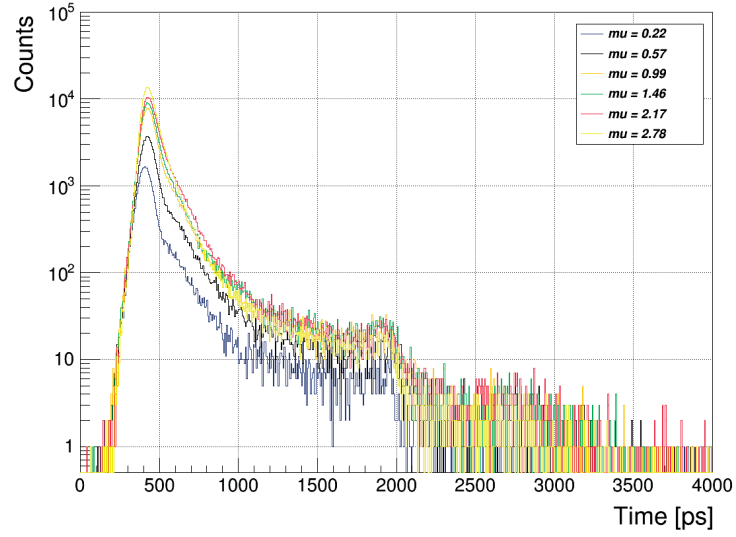
Figure 3.33: Time distributions (vertical logarithmic scale) at different light intensities and a laser tune setting of 20% from a single pad of the Planacon.

Table 3.11: Estimated time resolution values at a laser tune setting of 20% from a single pad of the Planacon.

laser tune setting of 20%	tube 9000906					
Average number of photoelectrons	0.22	0.57	0.99	1.46	2.17	2.78
Time resolution (Eq. 3.9) [ps]	46.2	42.1	38.7	37.5	32.8	29.9
Time resolution (Eq. 3.9 + Gaussian) [ps]	41.4	39.4	35.2	33.0	31.6	28.9
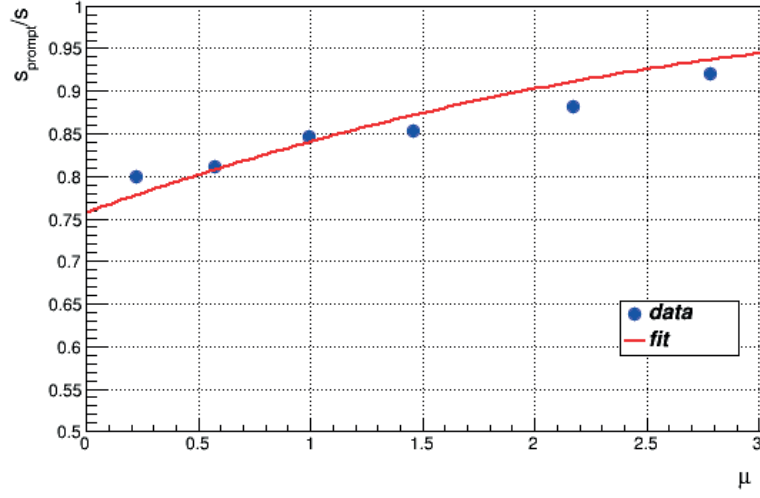
Figure 3.34: Experimental data fitted with Equation 3.15 at different light intensities and a laser tune setting of 20% from a single pad of the 8×8 pads Planacon MCP. A value for p_{late} of 24.3%±1.1% is inferred.

essentially attributed to back-scattered photoelectrons. This study results in a probability for a photoelectron to be late due to back-scattering and seen in the tail of 24.3%±1.1%. However, if there is still a small residual contribution of the laser tune setting this value of 24.3%±1.1% is an upper limit.

3.1.3 Summary

In TORCH, those photoelectrons detected beyond the range defined by the standard deviation of the main peak in the time distribution will not be exploited for the photon reconstruction. From the study of late photoelectrons in the time distribution for two photon detectors with different photocathode-MCP gap, the probability of a photoelectron being back-scattered and seen late in the time distribution, p_{late}, is estimated. For the Planacon tube which has an input gap of 4.5 mm, p_{late} is 24% whereas in the case of the single-channel MCP device which has an input gap of 0.120 mm, p_{late} is 5%.

The back-scattering coefficient for the typical electrode material (Ni-Cr) used in MCP-PMTs is 40%. The calculated values differ from the 40% because:

- Not all back-scattered photoelectrons are recollected and amplified

- Some back-scattered photoelectrons are spatially displaced (can travel a distance up to twice the input gap) and in the case of Planacon which is a multi-anode device they are detected on adjacent channels (see Subsection 4.3.6)

- Some back-scattered photoelectrons populate the main timing peak (can take up to twice the transit time to hit back the MCP entrance)

Phase III MCP-PMT prototypes for TORCH will be square tubes and will have a large input gap of ~1.6 mm which would result in a p_{late}>5%.

3.2 Custom-made devices

The work carried out for the systematic tests of commercial MCP photon detectors has been essential for the understanding of the experimental set-up, the electronics performance and the operation and performance of MCPs. A protocol has been established to perform the measurements in the laboratory and the results have been described using analytical models which are used in other applications. The thorough characterization of commercial devices has been fundamental for the preparation of testing custom-made MCP devices.

As introduced in Section 1.3, the development of suitable photon detectors for TORCH detector focuses on the manufacturing of long-life devices with finely segmented anode. Each phase of the R&D programme aims to the production of intermediate MCP-PMT prototypes incorporating some of the requirements. Phase I tubes with extended lifetime and Phase II tubes with the required segmentation have already been completed and the performance of both MCP-PMT prototypes has been thoroughly investigated in the laboratory. Phase II tubes have in addition been characterized in a charged-particle beam (Chapter 7).

3.2.1 Phase I: Extended lifetime MCP-PMT prototypes

During the first R&D phase, our industrial partner, Photek, has fabricated five circular-shaped single-anode MCP-PMT prototypes with extended lifetime (Figure 3.35). They comprise an S20 photocathode deposited on a quartz window. These devices were manufactured with two MCPs in chevron configuration. The MCPs have 25 mm diameter active area with 10 μm pores and are coated using ALD technique. Of these five tubes, four have standard Photek scrubbing on the MCPs and one has modified scrub recommended by the ALD suppliers.

All five devices have been characterized in the company for the following aspects [71]:

- photocathode response

- MCP gain vs operating voltage

- Output pulse shape

- Timing resolution

- Output linearity

Figure 3.35: Custom-made extended lifetime MCP-PMT prototype model PMT225 from Photek.

In all aspects except for MCP gain, these Photek MCP-PMTs perform as a standard MCP-PMT would. The gain of the ALD-coated MCPs is larger than that for an un-coated MCP operated at the same voltage.

The MCP-PMT prototypes have been tested at CERN [84]. The experimental set-up is the same as the one described in previous subsections (Figures 3.3 and 3.10). The bleeder chain configuration for 4 tubes is reproduced in Table 3.12. The values of the resistor divider chain are measured with a multimeter, with a precision of 0.001 MΩ. All tube supply voltages are accessible and allow dedicated measurements such as the QE (photocurrent) and ageing effects (anode current).

Table 3.12: Measured values of the resistor divider chain for four of the Phase I MCP-PMT prototypes.

	R (MΩ)			
	G1130510	B1130419	G1130614	G2130510
Cathode to MCPin	0.958	0.946	0.949	0.951
MCPin to MCPint	3.291	3.286	3.260	3.274
MCPint to MCPout	3.281	3.268	3.265	3.265
MCPout to anode	4.620	4.660	4.600	4.640
total sum	12.150	12.160	12.074	12.130
total measured	12.160	12.190	12.040	12.150

Laser light level and MCP gain calibrations

PHS for all five tubes are shown in Figure 3.36. The average number of photoelectrons is inferred from Poisson statistics. All tests were performed in single photoelectron regime with a μ in the range 0.3-0.7 and at a gain in the range $(3\text{-}5) \times 10^5$ electrons.
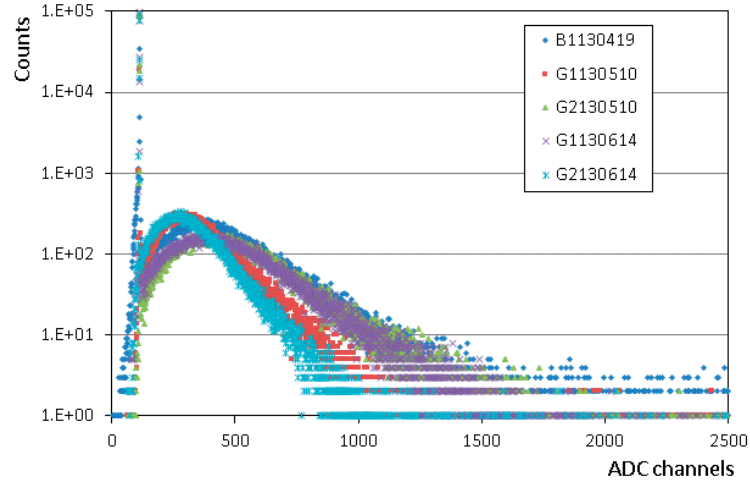
Figure 3.36: Pulse height spectra in single photoelectron regime for all five Phase I MCP prototypes (vertical logarithmic scale).

A characteristic gain versus voltage curve is shown in Figure 3.37 for the five Phase I MCP-PMT prototypes. Tube B1130419 has been tested at lower voltage due to its high level of dark counts. The MCP gain for the other tubes follow a similar behaviour.
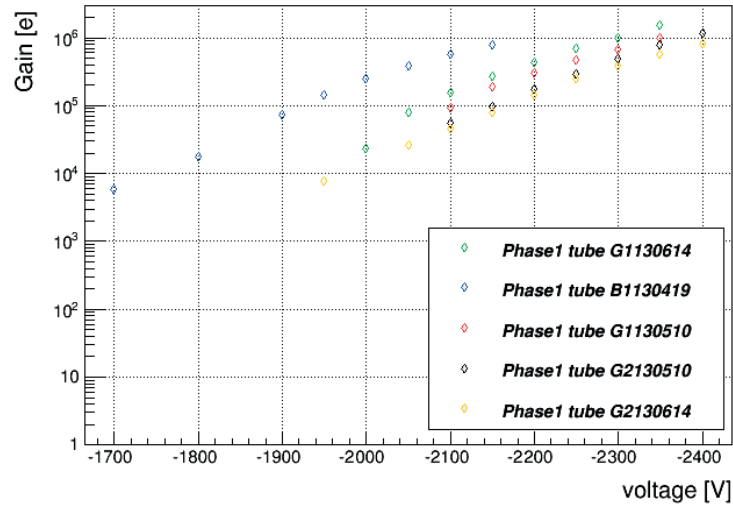
Figure 3.37: MCP gain as a function of the overall applied voltage for the five PMT225 tubes.

Dark count rate

The dark count rate of the four PMT225s with standard scrubbing has been estimated. For this purpose, a PHS is recorded for each tube without laser illumination and is reproduced in Figure 3.38. The MCA was operated in *coincidence off* and the MCA threshold was adjusted to be above the pedestal noise. The counts registered by the MCA normalized to the live time

of the measurement gives the dark count rate of the device. The main peak in Figure 3.38 corresponds to the signal from dark counts and the tail on the right part of the distribution is attributed to ion feedback. Tube B1130419 is the tube with higher dark count rate of 230 kHz. The other tubes, G1130510, G1130614 and G2130510, have dark count rates of 3.3 kHz, 8.8 kHz and 850 Hz, respectively.
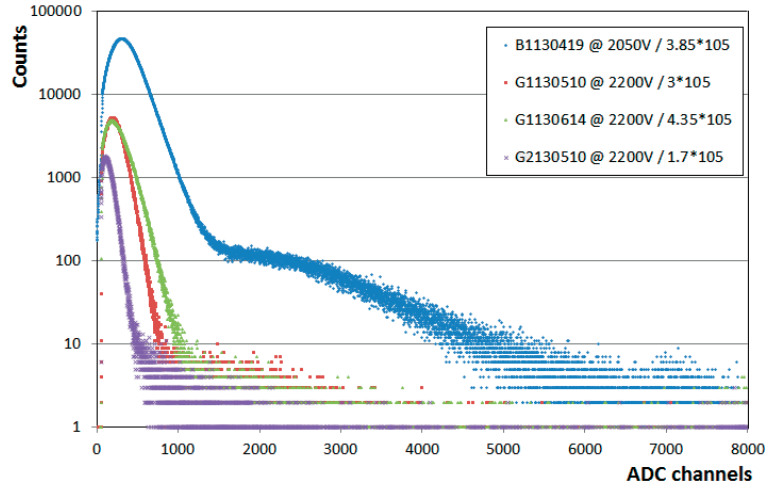
Figure 3.38: Pulse height spectra (vertical logarithmic scale) showing the dark counts when no laser light is used for four PMT225 tubes.

Timing performance

All five PMT225 tubes show good time resolution in the range 21-29 ps. Figure 3.39 shows the time distribution of PMT225/SN G2130510 tube. Due to the small input gap of 200 μm between photocathode and MCP input face almost all back-scattered photoelectrons populate the main peak where the maximum time for the elastically back-scattered photoelectrons is ~100 ps. The resulting peak asymmetry is modelled using Equation 3.9. The shoulder corresponds to the laser relaxation pulse and is fitted with a single Gaussian.

Table 3.13: Data values of the operating voltages, the average number of photoelectrons and the time resolution for the five Phase I MCP prototypes.

PMT225 tube	Operating voltage [V]	μ	Time resolution [ps]
B1130419	-2050	0.73	23.5
G1130510	-2200	0.35	22.8
G2130510	-2300	0.29	21.0
G1130614	-2200	0.30	29.4
G2130614	-2250	0.33	27.3
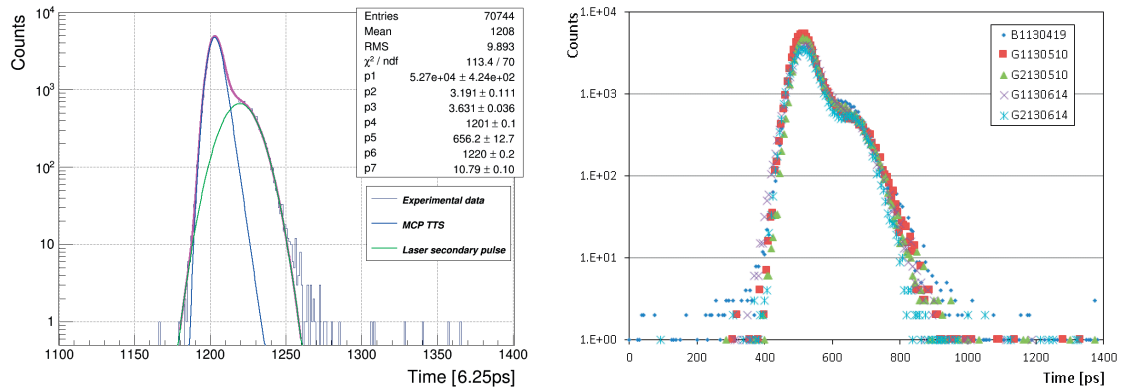
Figure 3.39: Time distribution in single photoelectron regime (vertical logarithmic scale) at a laser tune setting of 60% for a PMT225 device (left). A time resolution of 22.7±0.2 ps is obtained from the fit model (parameter p3). Time distributions in single photoelectron regime at a laser tune setting of 60% for all five PMT225 devices (right).

Ageing tests

The ageing of the photon detectors is one of the main issues in the TORCH detector. The photon detectors will need to survive a number of years with an accumulated charge of 1-10 C/cm^2 per year. The inital QE curves for the five PMT225s provided by the company are shown in Figure 3.40.
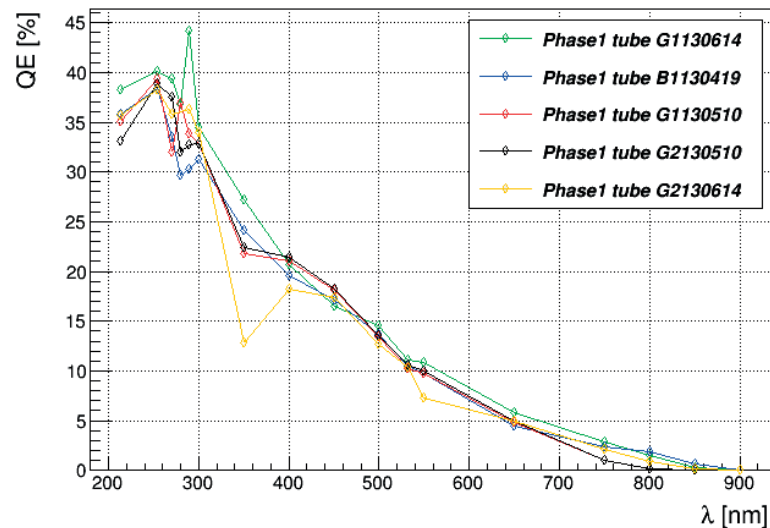
Figure 3.40: QE curves for the five Phase I MCP prototypes as measured by Photek.

Photek kept one PMT225 device which has modified scrub ALD coated for performing an

accelerated lifetime testing. They also performed a lifetime test on an additional tube without ALD coating for comparison. The nominal MCP gain was 10^6 electrons. Below 0.5 C/cm^2 the anode current of the tube with un-coated MCPs dropped to zero, whereas the tube with coated MCPs reached the expected target value of 5 C/cm^2 with acceptable degradation in performance [71]. The gain drop can be compensated by increasing the operating voltage. One of the other four PMT225 tubes is currently under ageing tests at CERN with monthly
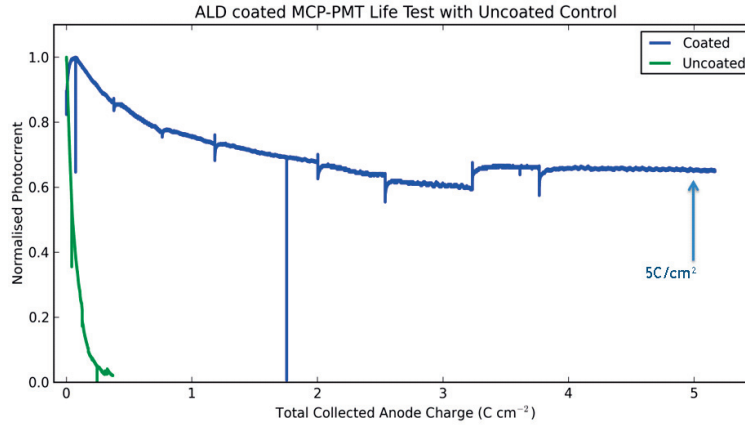
Figure 3.41: Normalised anode current as a function of the integrated anode charge as measured by the tube manufacturer [71].

interruptions to monitor the QE and the MCP gain [84]. This tube will reach the target 5 C/cm^2 after 24 months of testing.

4 Characterization of a Planacon MCP-PMT using custom-made electronics

The high granularity of the MCP photon detectors for TORCH requires the development of dedicated multi-channel readout electronics. The minimization of the electronics noise and corrections for time walk effects are essential. These electronics are designed and produced at the University of Oxford, one of the institutes collaborating in the TORCH project. The development has been divided in stages delivering two prototype versions. The first generation is based on the 8-channel NINO ASIC [11] and the new generation is based on the 32-channel NINO ASIC [85]. In both cases the 32-channel HPTDC ASIC [12, 13] is used. Both electronics systems have been tested at CERN. The 8×8 pads Planacon MCP photon detector already has the required segmentation for TORCH in one direction whereas in the other direction and is used for prototyping the first stage of electronics development. The present chapter covers the characterization of the Planacon using the 8-channel customized readout electronics previously used in beam tests [86–88].

4.1 8-channel custom-made readout electronics

The first generation of readout electronics is designed as a single front-end (FE) board and a readout board.

4.1.1 Front-end NINO-HPTDC board

The front-end board incorporates two 8-channel NINO chips and two 32-channel HPTDC chips. The 8-channel NINO chip has a differential input. The analogue signals from the MCP-PMT are amplified and discriminated by the NINO chips. Using the Time-Over-Threshold (TOT) technique the width of the NINO output pulse is measured as the difference between the trailing and leading edges digitized by the HPTDC.

Figure 4.1(top) illustrates the TOT technique for two signal amplitudes. The leading edge for a large amplitude is detected earlier than that for a small amplitude, $T_1 < T_1'$. The trailing edge for a large amplitude is detected later than that for a small amplitude, $T_2 > T_2'$. Consequently,

T_2-T_1>T_2'-T_1'. The bottom plot in Figure 4.1 shows an ideal, linear correlation curve of the pulse width as a function of the leading edge time. The measurement of the pulse width allows correcting for the time drift of the leading edge due to the discriminator time walk. Since the width of the output pulse depends on the input charge, the pulse width information is not only used to correct for time walk effects but also to measure the amount of negative charge below a given discrimination threshold.
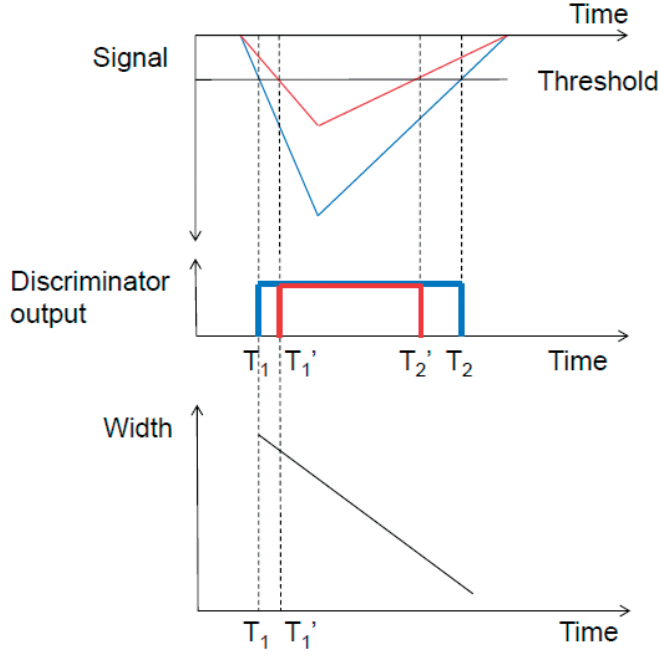
Figure 4.1: Diagram showing the Time-Over-Threshold principle together with a correlation plot of pulse width with leading edge [89].

The design NINO threshold adjustment is in the range 10-100 fC. In the ALICE TOF the signals are in a large dynamic range from 100 fC to 2 pC. TORCH will detect single photons and small charges of typically ~100 fC gain, so it spans the low-end operating range of the NINO. The digital output pulse of each NINO channel is a low-voltage differential signal (LVDS) that matches the input requirements of the HPTDC chips. The pulse width of the NINO varies between 2 ns and 7 ns. A stretch functionality extends this width by 10 ns. This ensures that the HPTDC can time-digitise both the leading and trailing edges a feature requiring a minimum width of 6 ns.

In this electronics version, the HPTDCs are operated in Very High Resolution Mode (VHRM) offering a 25 ps time bin precision. In this mode, an on-chip high resolution interpolation is performed to compress the time measurements from four TDC channels that are connected by a Resistor-Capacitor (R-C) delay line, into a single Very High Resolution time measurement [13]. Therefore, a 32-channel HPTDC only provides 8 channels corresponding to TDC channels 0, 4, 8, 12, 16, 20, 24 and 28.

An on-board Field-Programmable Gate Array (FPGA) controls and configures both NINO and HPTDC chips [50]. The buffering of the HPTDC data and their transmission to the readout board are controlled by the FPGA. Data formatting is also performed in the firmware of the FPGA. Labview-based DAQ software is used to provide data transmission, control and configuration functions. The control of the bias levels of the NINOs is implemented in the firmware and is achieved through a SPI DAC on the FE board. The threshold and stretch settings of NINO chips can be independently adjusted via the LabVIEW interface.

The FE board also includes a test input LEMO connector which will be used to inject a time reference signal. The incoming test pulse can be injected either to all channels of both NINOs or to a specific channel. This selection is done via a jumper.

A fully assembled FE board is shown in Figure 4.2.
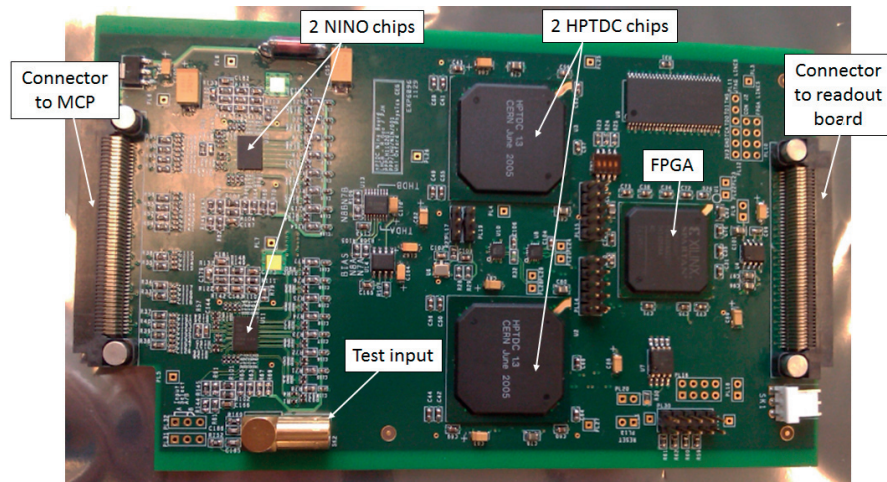
Figure 4.2: Photograph of the front-end board incorporating two 8-channel NINO chips and two 32-channel HPTDC chips operated in Very High Resolution Mode. The chips are controlled by a Field-Programmable Gate Array (FPGA). A test input LEMO connector is also available to allow the injection of a time reference signal [50].

HPTDC data structure

The HPTDC data are decoded to extract the channel number that has been hit and the time hits for the leading and trailing edges of the TOT signal provided by the NINO chip. The HPTDC data are structured in words of 32 bits [13]. The first four bits give the word type in the event and the next four bits indicate the corresponding TDC ID. Every time a trigger is sent to the TORCH electronics it should be detected and a header (first four bits = 2) opens the event data structure. A TDC header contains the information from the trigger, the event ID (an increasing counter that rolls over every 4096) and the bunch ID (trigger time tag). The next information is the time hits, the leading (first four bits = 4) and trailing (first four bits = 5) edges measurements. They contain the TDC ID, the hit channel number and the time information.

Figure 4.3 shows the typical data structure in High Resolution Mode (HRM) (100 ps time bin precision). In the case of VHRM (25 ps time bin precision) the hit channel number is given by bits 21-23 and the edge time is given by bits 0-18 and bits 19-20 are the least significant bits. The event data structure is closed with a trailer (first four bits = 3) containing the event ID and the word count in the full event including header and trailer.

TDC header: Event header from TDC (master and slaves)

31	30	29	28	27	26	25	24	23	22	21	20	19	18	17	16	15	14	13	12	11	10	9	8	7	6	5	4	3	2	1	0
0	0	1	0		TDC							Event ID												Bunch ID							

TDC:	Programmed ID of TDC.
Event ID:	Event ID from event counter.
Bunch ID:	Bunch ID of trigger (trigger time tag).

Leading measurement:

Single edge

31	30	29	28	27	26	25	24	23	22	21	20	19	18	17	16	15	14	13	12	11	10	9	8	7	6	5	4	3	2	1	0
0	1	0	0		TDC				Channel			Leading time																			

TDC:	Programmed ID of TDC.
Channel	TDC channel number.
Leading:	Leading edge measurement in programmed resolution

Trailing measurement:

31	30	29	28	27	26	25	24	23	22	21	20	19	18	17	16	15	14	13	12	11	10	9	8	7	6	5	4	3	2	1	0
0	1	0	1		TDC				Channel			Trailing time																			

TDC:	Programmed ID of TDC.
Channel	TDC channel number.
Trailing:	Trailing edge measurement in programmed resolution

TDC trailer: Event trailer from TDC (master and slaves)

31	30	29	28	27	26	25	24	23	22	21	20	19	18	17	16	15	14	13	12	11	10	9	8	7	6	5	4	3	2	1	0
0	0	1	1		TDC							Event ID												Word count							

TDC:	Programmed ID of TDC.
Event ID:	Event ID from event counter.
Word count:	Number of words from TDC (incl. headers and trailers).

Figure 4.3: Data structure of a typical event in HRM (100 ps bin precision) [13].

Non-linearity in time-to-digital converters

A time-to-digital converter (TDC) provides digital representation of small time differences between two signals. An ideal TDC is characterized by its Least Significant Bit (LSB) and dynamic range. The LSB is the smallest delay that can be converted and the dynamic range is the largest delay that can be measured [90]. Figure 4.4 (left) shows the ideal transfer characteristics of

a 3-bit TDC. The input is a continuous time signal and the output is a digital code. The real transfer curve deviates from the ideal curve due to the influence of the path delay mismatches and the noise [91].

This non-ideal behaviour of a TDC is usually characterized by the Differential and Integral Non Linearity (DNL and INL) as illustrated in Figure 4.4 (right). The DNL is the deviation of output bin size from its ideal LSB value. The INL is the deviation of the input/output curve from the ideal transfer characteristic, which is a straight line that best fits the curve. Corrections for this non-ideal behaviour will be detailed in Subsection 4.3.1.
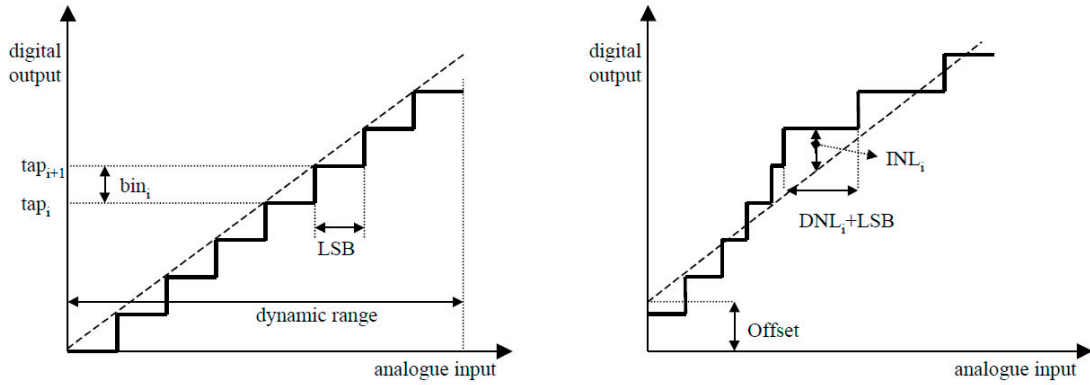
Figure 4.4: Ideal transfer characteristic of a 3-bit time-to-digital converter (left). Example of a time-to-digital converter transfer function illustrating the DNL and INL metrics (right) [90].

4.1.2   Readout board

The readout system is implemented on a Xilinx SP605 development board along with a customized PCB to provide a physical interface to four FE boards [50]. The interface board provides the supply of power to the FE boards using two on-board regulators. The electronics is controlled from a DAQ PC using Giga-bit Ethernet.

4.1.3   Characterization of the NINO-HPTDC board with test pulses

A pulse generator[1], with Root Mean Square (RMS) jitter of 0.01%+15 ps, is used to send electrical pulses via the test input on the FE board (FE-4) and routed to a single NINO channel. A 1.5 ns-long double pulse with an amplitude of -200 mV and a rise time of 0.8 ns is generated. The second pulse is delayed by 80 ns from the first pulse. A 40 MHz external clock[2] is used. A 20 ns-long, 1 kHz trigger is provided by the pulse generator. Clock and trigger signals are synchronized through standard NIM modules and then input to the readout board.

---

[1]Pulse/pattern generator mainframe model 81110A from Agilent. Output module 330 MHz for 81110A model 81112A from Agilent.

[2]2.05 GHz synthesized clock generator model CG635 from Stanford Research Systems.
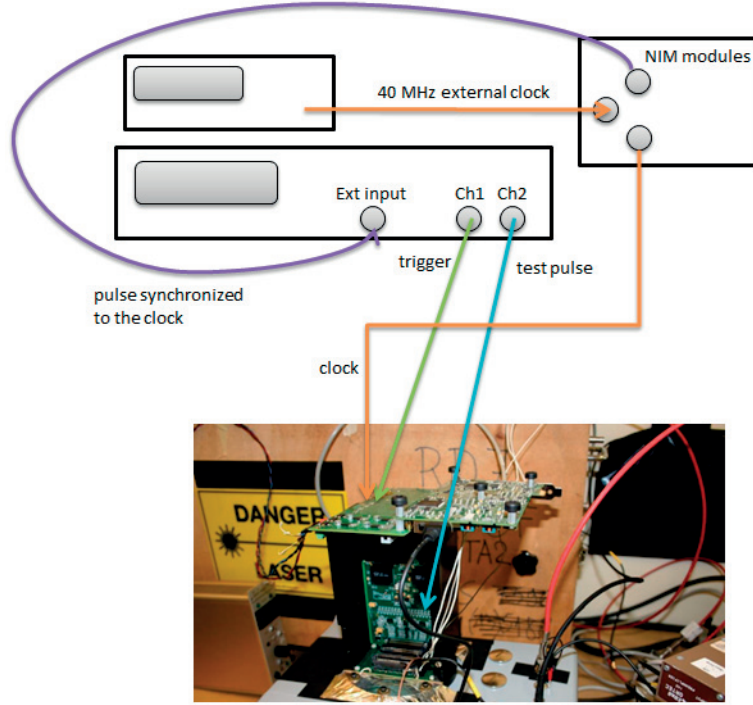
Figure 4.5: Experimental set-up for the characterization of the front-end NINO-HPTDC board with test pulses.

The NINO threshold setting is set at 0 V. These electronics had for the first time been tested in a particle-beam and the original analysis software in [88] is used for data decoding and analysis. The time resolution is measured from the difference between the leading edge of the first pulse and that of the second pulse. The distribution is fitted with a single Gaussian. The time resolution is defined as the standard deviation of the Gaussian and a value of $44.7/\sqrt{2}$=31.6 ps is inferred. Test pulses give very good time resolution values since they are less affected by time walk effects; two pulses with the same amplitude are compared and there is practically no fluctuation in amount of signal.

4.2 Reference measurements with single-channel commercial electronics

The Planacon is coupled to an interface board which has four high bandwidth connectors on the back side to allow assembly of front-end boards [50]. The tube is partially instrumented with one FE NINO-HPTDC board reading out the two bottom rows (16 pads). All other pads are connected to ground except one pad read out with commercial single-channel electronics for calibration purposes (Figure 4.6).

The intensity level is estimated by using commercial single-channel electronics on the calibration pad. For timing measurements in the laboratory with the NINO-HPTDC electronics the

Figure 4.6: Layout of the Planacon MCP anode pads. Only the two bottom rows of pads are instrumented with readout electronics.

time reference signal was intended to be provided by the laser synchronization signal (TTL) and input into the test channel of the NINO-HPTDC electronics. A power divider[3], a passive pulse inverter[4] and several attenuators[5] were used to meet the input requirements on the FE board. However, the time resolution obtained using this method was found to be 85 ps worse than when using the output signal from a single-channel MCP[6] coupled to the CFD and input into the test channel of the NINO-HPTDC electronics. This worse time response is attributed to the low bandwidth of the pulse inverter. Since commercial single-channel MCP devices have shown an intrinsic time resolution of 20 ps in multi-photon regime (see Chapter 3), one of these tubes will provide the time reference.

4.2.1 Laser light level and MCP gain calibrations

The performance of the Planacon MCP is assessed in single-photon regime and the single-channel MCP tube which provides a fast time reference signal is operated in multi-photon regime. Laser light propagates through monomode fibers and is divided by an asymmetric splitter[7], 4% and 96%, to illuminate both the Planacon tube and the single-channel MCP tube, respectively. ND filters are used to attenuate the light to the level of interest. The splitter arm that illuminates the Planacon is remotely controlled by translation stages[8] to position the laser spot on the calibration pad of the Planacon. A charge pre-amplifier[9] is used to read out the

---

[3]BNC resistive power divider Leistungsteiler model 4901.01.A 50Ω 6 dB 1 W 2 GHz from Huber-Suhner.

[4]BNC inverting transformer 400 MHz model IT100 from ORTEC.

[5]BNC attenuator model 6820.01.A 20 dB and model 6830.01.A 30 dB DC-4 GHz 50 Ω from Huber-Suhner.

[6]Single-channel MCP device model PP0365G from Photonis.

[7]Fiber Optic Beamsplitter model FOBS-12P-111-3/125-SSS-405-95/5-40-3S3S3S-1-1 from OZ Optics Limited, 219 Westbrook Rd, Ottawa, ON, Canada.

[8]Positioning controller series SMC-basic/X/XS from MICOS. Vexta clean damper model D4CL-5.0 from Oriental Motor Co. Ltd.

[9]Charge pre-amplifier model 142 A from ORTEC, Oak Ridge, TN37831-0895, USA.

signal from either the calibration pad on the Planacon or the single-channel MCP (Figure 4.7).
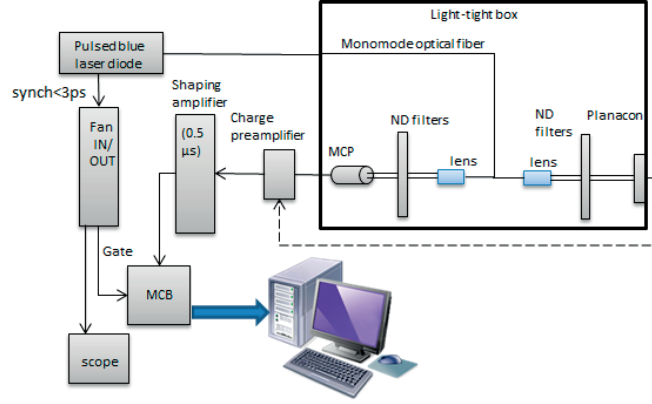
Figure 4.7: Laboratory set-up for light level and MCP gain calibrations.

Pulse height spectra (PHS) are recorded for each photon detector and are reproduced in Figure 4.8. The intensity levels are evaluated from the resulting distributions. The procedure follows that already described in Chapter 3. Data are fitted using Equation 3.2. The left plot shows the resulting distribution from the single-channel MCP device. The average number of photoelectrons is 7.5±0.4. From Poisson statistics, the probability to have zero photoelectrons is

$$P(0) = e^{-\mu} = e^{-7.5} = 0.06\% \tag{4.1}$$

This is verified by the ratio between the counts on the pedestal and the total number of events. The gain of the single-channel MCP device is measured to be 1.5×10^5 at -2930 V.

The right plot in Figure 4.8 shows the distribution from the calibration pad of the Planacon. In this case, the average number of photoelectrons is 0.37±0.02 and the 1-photoelectron signal contamination from two photoelectrons is

$$\frac{P_{0.37}(2)}{P_{0.37}(1)} = \frac{\mu}{2} = \frac{0.37}{2} = 18.5\% \tag{4.2}$$

The gain of the Planacon measured on the calibration pad is found to be 6×10^5 at -2450 V and is assumed to be uniform over the full active surface. This value will be used as the overall MCP gain, assuming that all laser light is collected on the calibration pad since the pad size is 5.9×5.9 mm^2. Despite this large pad size, a fraction of electrons undergo back-scattering effects due to the large input and output gaps of the device and can be detected by other pads (See Section 4.3.6 for details).

These calibrations require a stable laser illumination. The testing room is air conditioned to minimize changes in temperature. A variation on the light level was noticed due to temper-
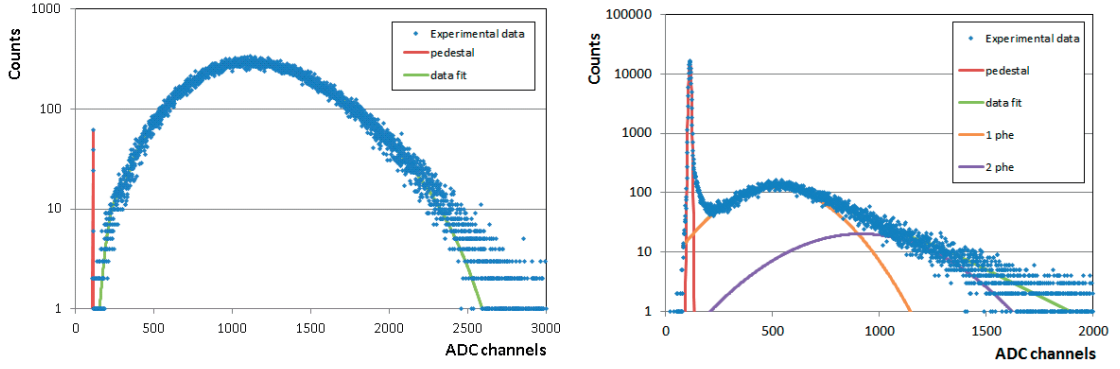
Figure 4.8: Pulse height spectra from single-channel MCP device operated in multi-photon regime (left) and from the calibration pad of the Planacon operated in single-photon regime (right).

ature fluctuations of the laser head during the starting phase of a measurement campaign. Following this observation, a systematic methodology is followed. The laser diode is powered in advance for stability. For every new set of measurements with the NINO-HPTDC electronics is performed, PHS are recorded and the light level is evaluated for both photon detectors.

4.2.2 Time response

As part of this systematic methodology, timing measurements are also performed on both photon detectors using commercial single-channel electronics (Figure 4.9) and are used as reference measurements. The time resolution measured for the calibration pad of the Planacon indicates the best performance that can be achieved.
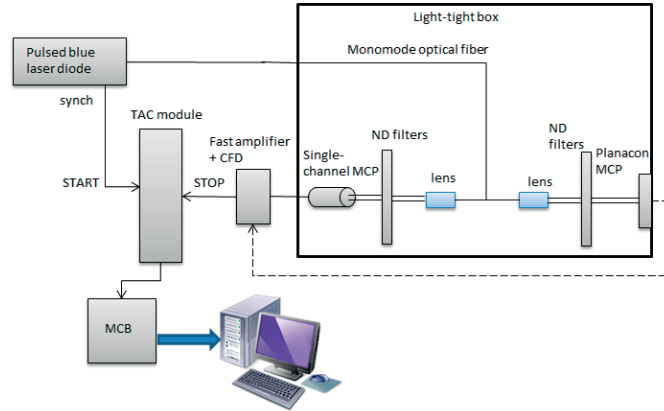
Figure 4.9: Laboratory set-up for timing reference measurements using commercial single-channel electronics.

Time distributions are reproduced in Figure 4.10. The single-channel MCP device gives 18.3 ps

resolution and the calibration pad of the Planacon gives 36.5 ps resolution. The different shape between the two distributions is explained mainly by the photon detector layout. The Planacon has larger input and output gaps (4.5 mm and 3.5 mm) than the single-channel MCP device (120 μm and 1 mm), which results in a long tail due to back-scattered photoelectrons. The maximum time for an elastically back-scattered photoelectron at an angle of 90 ° with respect to the MCP input surface is 1.5 ns at an operating voltage of 350 V for the Planacon and 60 ps at an operating voltage of 200 V for the single-channel MCP. In TORCH it is desired to have MCP photon detectors with small gaps, however this is difficult to achieve for square tubes. Photoelectrons detected late in time will not be exploited for the TORCH timing reconstruction. In addition, the laser effect is not seen in the left plot given that the single-channel MCP device is operated in multi-photon regime and the CFD reacts on the prompt photoelectrons. The residual asymmetry of the peak is attributed to the CFD discrimination process.
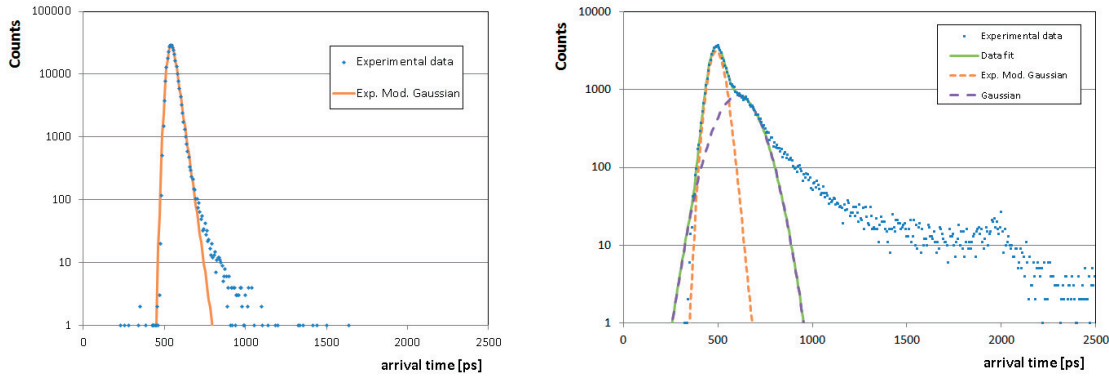
Figure 4.10: Time distributions from the reference single-channel MCP operated in multi-photon regime (left) and from the calibration pad of the Planacon operated in single-photon regime (right).

4.3   Performance using the 8-channel NINO-HPTDC electronics

The experimental set-up is shown in Figure 4.11. The reference signal from the single-channel MCP coupled to the CFD is input into the test channel of the NINO-HPTDC electronics. The test input circuitry has been investigated and verified in the laboratory. This is described in Appendix B. The right arm fibre and collimating optics of the splitter are moved with translation stages and the laser spot is positioned at the centre of a pad located in row 1 (Figure 4.6). For these measurements, it is assumed that the photocathode response is uniform over the full photon detector active area and is similar to that for the calibration pad.

The time jitter distribution is measured from the difference between the leading edge of the reference signal on the test channel and that from the pad illuminated with the laser and is reproduced in Figure 4.12. The back-scattered tail is clearly seen and extends up to <1.5 ns away from the main peak. The visibility of the laser relaxation pulse is degraded by

Figure 4.11: Laboratory set-up used for the systematic studies of the timing performance of the Planacon using the 8-channel NINO-HPTDC electronics.

the HPTDC binning. The main peak is fitted with a double Gaussian function[10]. The first Gaussian describes the MCP intrinsic response and the second Gaussian accounts for the laser relaxation pulse. The peak position of the second Gaussian is constrained from that in Figure 4.10 (right). A time resolution of 88 ps is inferred without time walk correction of the NINOs and a fine calibration of the HPTDC chips [87]. Data need to be first corrected for the non-linearity of the HPTDCs and subsequently corrected for time walk effects.
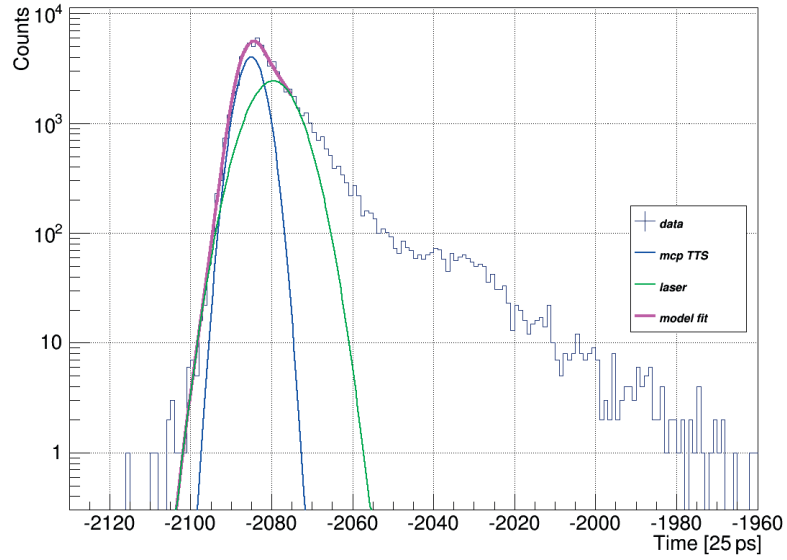
Figure 4.12: Single photoelectron time distribution from a Planacon pad using the 8-channel NINO-HPTDC electronics (vertical logarithmic scale). Prompt signal with a time resolution of 88 ps [87].

---

[10]For these measurements and for historical reasons, the fitting model for the description of the prompt peak is a standard Gaussian and not an exponentially-modified Gaussian.

4.3.1 INL calibration of the HPTDC chips in VHRM (25 ps time bin precision)

The HPTDC chip exhibits non-linearity in the time bins due to the following three effects [92]:

- unequal bin widths in the R-C tapped delay lines, periodic over 4 bins

- unequal bin widths in the Delay Locked Loop (DLL), periodic over 32 bins

- noise coupling from the logic clock network within the chip into the sampling clock network, periodic over 1024 bins

The latter source of non-linearity is what dominates. A detailed procedure to determine the DNL and INL metrics of the HPTDC is described.

The non-linearity of the HPTDC is studied by using statistical methods such as a Code Density Test (CDT) [93] also known as the histogram-based technique. The CDT statistical method is used to determine the residual size of each time bin. The procedure works as follows. For a specific laser position, the centre of a pad, a high statistics data sample is recorded. The INL is periodic over a 25 ns interval. In VHRM the 25 ns time scale corresponds to 1024 bins with a bin size of ~25 ps. In this operating mode, the fine time is defined as the bottom 10-bits of the time hits for the leading and trailing edges of the signals measured by the HPTDCs and is in the range 0-1023. A histogram using the fine time information is built. This is done for the leading and trailing edges hits separately. If the laser and electronics clocks are not correlated, these distributions should be flat since the HPTDC sampling-time is in this case randomly distributed. In reality, due to the non-linear time response of the HPTDC bins within this 25 ns period the number of counts in each time bin, N_i, varies. This requires INL calibration and the subsequent off-line corrections of the HPTDC data. For this purpose to obtain the INL correction factor, INL_i, a CDT is applied [94, 95]. The first step is to compare N_i and the expected value of counts in a time bin, N_{exp}. The weighted number of counts per time bin is known as the DNL and is calculated as:

$$DNL_i = \frac{N_i - N_{exp}}{N_{exp}} \tag{4.3}$$

where N_{exp} is the total number of entries of the histogram divided by the number of time bins, 1024. Figure 4.13 (left) reproduces the DNL weighted count per time bin in a 25 ns period. The largest time bins which contain more counts correspond to time bin 27 plus multiples of 32. These time bins are generated from the end of a DLL delay element to the beginning of the next DLL delay element and have a tendency to be large [13].

The INL correction factor for a given time bin is calculated as:

$$INL_j = \sum_{i=1}^{j} DNL_i \tag{4.4}$$

The INL_j value indicates the deviation from the ideal time bin size. These values are input into a look-up table and are used to correct the raw time hits, $time_{raw}$, as given by:

$$time_{corrected} = time_{raw} + INL_{time} \tag{4.5}$$

where $time_{raw}$ is an integer number and INL_{time} is a real number.

The calibration is performed on all channels including the test channel. Figure 4.13 (right) shows the resulting INL curve (blue coloured curve) for a single HPTDC channel. The correction factor can reach up to 10 time bins in this resolution mode. The green coloured curve represents the INL correction factor if a CDT is applied to the already corrected time hits. It shows that the bin size has been homogenized but there is still a small residual contribution. This is better seen in Figure 4.14 which shows the projection of the INL values onto the vertical axis for blue (left) and green (right) curves. On the left plot the RMS is 2.27 time bins which contributes as 56 ps to the time resolution if raw data remain uncorrected. On the right plot the RMS is 0.56 time bins, resulting in a well-defined peak centred about zero. The residual non-linearity contribution to the time resolution, $\sigma_{res\,INL}$, is 14 ps.
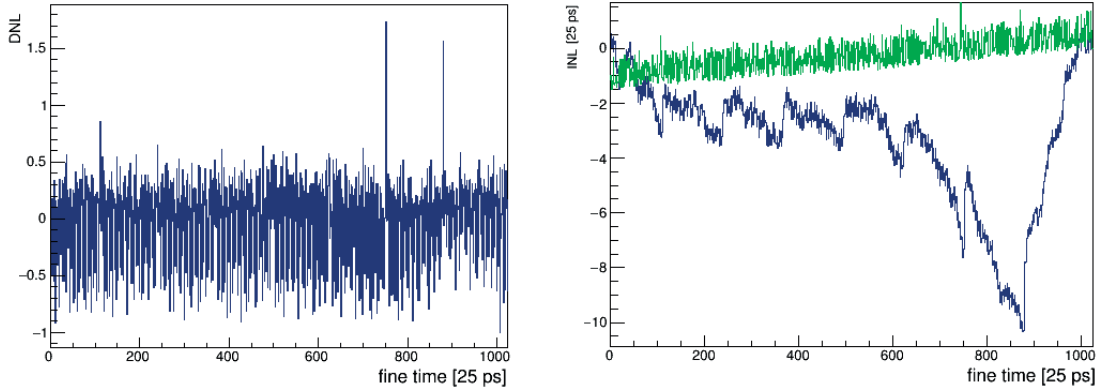
Figure 4.13: DNL distribution (left). Raw and corrected INL distributions (right).
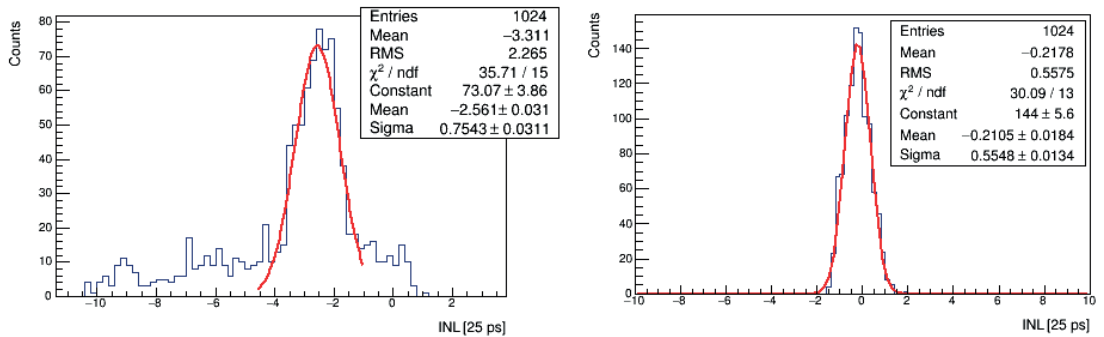
Figure 4.14: INL cumulative plots before correction (left) and after correction (right).

4.3.2 Time walk calibration of the 8-channel NINO chips

Once the time hits of the leading and trailing edges of the signal are corrected for the non-linearity of the HPTDCs, the next step is to correct them for time walk effects of the NINOs. The INL-corrected data are used to build a 2D histogram of the NINO output pulse width (TOT), w, against the arrival time as shown in Figure 4.15 (left). The z-axis is in logarithmic scale and both horizontal and vertical axes are in units of 25 ps. The projection onto the horizontal axis corresponds to the time distribution. The time walk calibration curve is determined as follows. The vertical axis is divided in slices of 1 ns, corresponding to 40 time bins. For each slice, its projection onto the horizontal axis is fitted with a single Gaussian (Figure 4.16). The
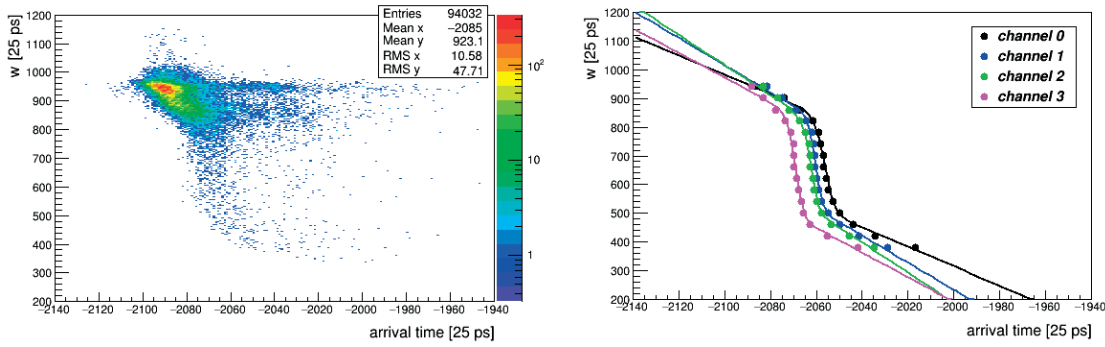
Figure 4.15: 2D scatter plot of pulse width as a function of arrival time (left). Calibration curves of pulse width as a function of the arrival time of photons for four NINO channels (right).
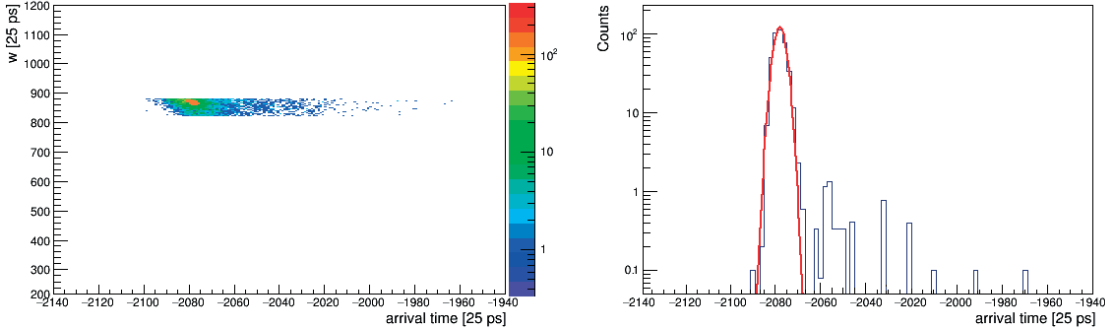
Figure 4.16: A single slice on the 2D scatter plot of pulse width as a function of arrival time (left). Arrival time distribution of a single slice (right).

positions of the Gaussians and the values of the pulse width are plotted in Figure 4.15 (right). The pulse width of each slice is defined as the mid point of the slice range. This calibration is performed on four NINO channels of chip A (see Figure 4.6). The time offsets in Figure 4.15 (right) represent different time delays between channels. The calibration points are fitted with a five-parameter logistic function [96] and an additional linear function:

$$w = p_0 + \frac{p_1 - p_0}{\left(1 + \exp(-s(t - t_c))\right)^{p_4}} + p_5 \times (t - t_c) + 1 \tag{4.6}$$

where p_0 is the minimum asymptote value, p_1 is the maximum asymptote value, s is the hill slope, t_c is the arrival time at 50% of the value p_1 and p_4 is the asymmetrical curvature in the sigmoidal response curve. The resulting fitting function for each channel is superposed to the data points of the calibration curve.

In order to apply the TOT correction, a reference arrival time is required. For a given NINO channel, the largest pulse width value of the calibration points is chosen and the associated arrival time, t_a, is used to correct the discrimination time of the leading edge as:

$$l_{corrected} = l_{INL} - (t' - t_a) \tag{4.7}$$

where l_{INL} is the leading edge time already corrected for non-linearity of the HPTDC and t' is the arrival time inferred using the inverse function of Equation (4.6).

Raw data recorded using the 8-channel NINO-HPTDC electronics are now corrected for non-linearity of the HPTDCs and time walk effect of the NINOs. Figure 4.17 reproduces the raw (blue coloured line) and corrected (green coloured line) time distributions. The corrected distribution is fitted using Equation (3.9) and a single Gaussian. The main peak gets narrower after corrections and the time resolution improves from 88 ps to 68 ps. This resolution includes the contribution of $\sigma_{res\,INL}$.
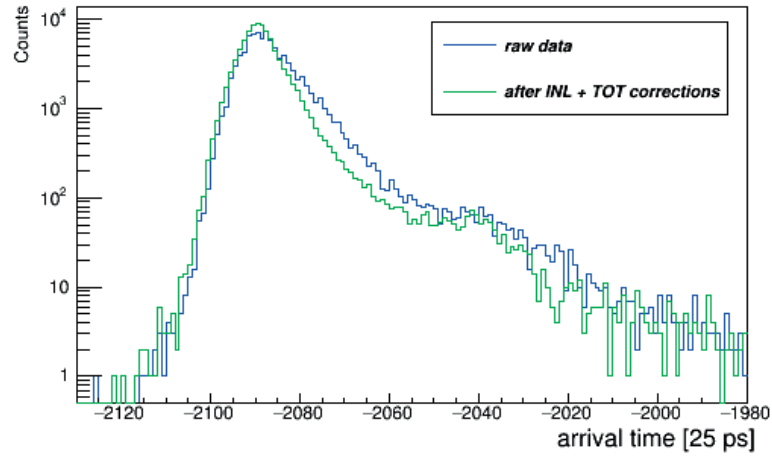
Figure 4.17: Time distributions before (blue) and after (red) off-line corrections from a single pad of the Planacon.

4.3.3 Electronics detection efficiency

Due to the operating regime with single photoelectrons in TORCH, the procedure to determine how efficient the electronics system is in detecting the MCP-PMT signal from single photo-electrons is of particular interest. A set of measurements applying different NINO thresholds is performed. From the counts collected on a pad and detected by a NINO channel at a set

threshold, c_{NINO}, and using Poisson statistics the electronics detection efficiency (EDE) is estimated. The EDE is defined as the ratio between the detected hits over the total signals to be detected and is given by:

$$EDE = \frac{c_{NINO}}{c_{trigger} \times (1 - P(0))} \tag{4.8}$$

where $c_{trigger}$ is the number of sent triggers and amounts to 3×10^5 for this set of measurements. The ratio $c_{NINO}/c_{trigger}$ is corrected for the probability to have signal, 1-P(0), in order to infer the value for EDE.

A value of μ=0.37 for the light level was obtained in Section 4.2.1. From Poisson Statistics, the probability to have zero photoelectrons is

$$P(0) = e^{-\mu} = e^{-0.37} = 69\% \tag{4.9}$$

For the set of measurements at different NINO thresholds the EDE for the full distribution ($N \geq 1$) is obtained and tabulated in Table 4.1.

Table 4.1: Electronics detection efficiency values at different NINO threshold settings.

NINO threshold setting [V]	EDE [%]
0	82.6
0.1	81.3
0.14	81.3
0.5	80.9
1	78.9
2	77.9

Given the current electronics layout on the PCB, the NINO threshold is not the minimal value that can be applied and it dominates in the resulting efficiency. In addition, the Planacon is operated at low gain to comply with the lifetime requirements.

The EDE is also estimated at different light levels for the minimum NINO threshold setting (Table 4.2). There is a compromise between the contamination of two photoelectrons and the efficiency. At low values of μ the probability to have signal is small, 11%. As μ increases the contamination from two photoelectrons also increases and EDE tends to reach 100%. There is a discrepancy between the value of 82.6% in Table 4.1 and the expected value for μ=0.37 from Table 4.2. Systematic errors are introduced from operating the set-up on different days.

4.3.4 8-channel NINO threshold calibration

The NINO threshold control is achieved through the SPI DAC on the FE board. A 12-bit voltage value is in the range 0-2.5 V and a hexadecimal DAC command is sent to the FE board to set the bias voltages THRESHOLD-ADJA/B for chips A and B, respectively. These voltages can be

Table 4.2: Electronics detection efficiency values at different light levels for a set NINO threshold setting.

μ	1-P(0)	$c_{NINO}/c_{trigger}$	EDE [%]
0.12	0.11	0.074	67.3
0.16	0.15	0.117	78
0.28	0.24	0.223	92.9
0.43	0.35	0.326	93.1
0.68	0.49	0.487	99.4

measured on the capacitors C179 and C180 (Figure 4.18). These voltage settings are not the bias voltages directly applied to the NINOs, THRESHPA/B, which are set through a voltage divider as shown in Figure 4.18. The negative bias THRESHNA/B are permanently connected to 1.667 V. Using this voltage divider, the absolute bias level on THRESHPA/B is determined as follows. The example of chip A is chosen. The same procedure also applies to chip B .
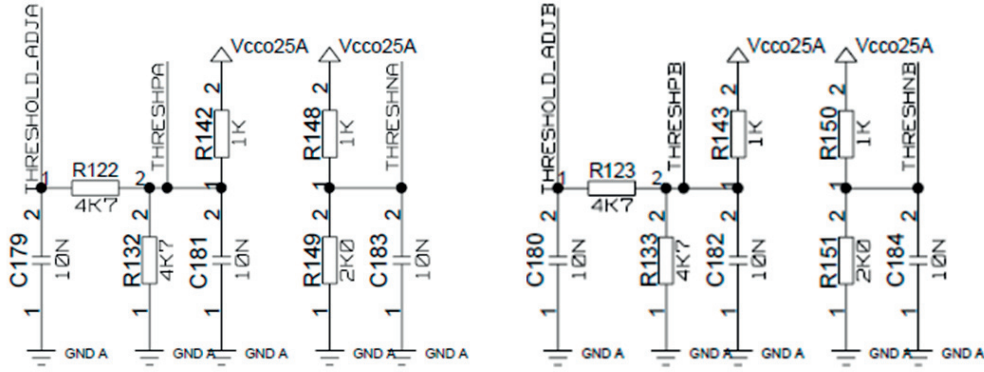
Figure 4.18: Circuitry layout for the 8-channel NINO bias voltage adjustment.

$$\Delta V = (I_2 - I_1) \times 4.7 \rightarrow I_2 = \frac{\Delta V}{4.7} + I_1 \tag{4.10}$$

where THRESHPA is denoted as ΔV and I_1 and I_2 refer to the electric current passing through resistors R122 and R132, respectively.

$$2.5 - \Delta V = (I_1 + I_2) \times 1 + I_1 \times 4.7 \tag{4.11}$$

and by inserting I_2 in the previous equation:

$$I_1 = \left(2.5 - \Delta V - \frac{\Delta V}{4.7}\right) \times \frac{1}{6.7} \tag{4.12}$$

Both electric currents I_1 and I_2 are calculated for seven values of ΔV, and the corresponding

threshold value THRESHPA is determined as given by

$$\text{THRESHPA} = 2.5 - (I_1 + I_2) \times 1 - 1.667 \tag{4.13}$$

The calculated values for the currents and the actual value of the NINO thresholds are tabulated in Table 4.3 for various ΔV values.

Table 4.3: Calculated actual NINO thresholds for various ΔV values.

ΔV [V]	I_1 [A]	I_2 [A]	Actual NINO threshold setting [mV]
0	0.373	0.373	84
0.1	0.355	0.376	99
0.14	0.348	0.378	104
0.5	0.283	0.389	158
0.7	0.246	0.395	189
1	0.192	0.405	233
2	0.011	0.437	382

Assuming the Planacon response is uniform over the full active surface, from the PHS in Figure 4.8 (right) and using the EDE values in Table 4.1, the NINO threshold is estimated in units of charge. A cut on the PHS is applied and the ratio between the counts above threshold over the total counts of the histogram is calculated. The value of this ratio is adjusted to match the EDE values in Table 4.1. In this way the position of the threshold in the histogram is determined and converted into charge. The estimated threshold values are tabulated in Table 4.4 and the EDE for single photoelectrons is determined by calculating the loss fraction in the 1-photoelectron signal. Figure 4.19 reproduces the PHS and the minimum and maximum threshold cuts. The loss in the full signal from two photoelectrons is 1.5-2.5%.
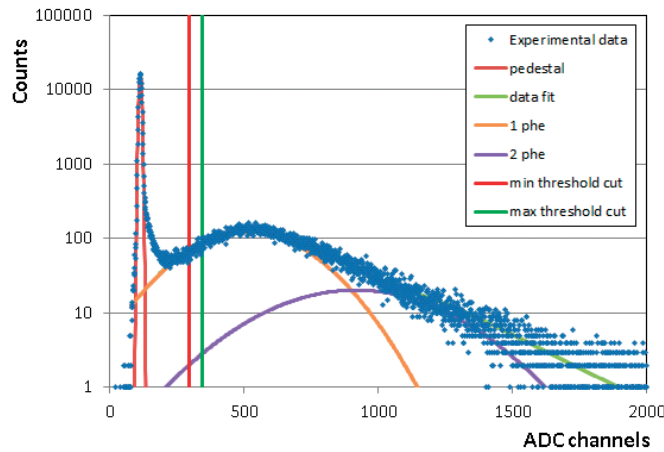
Figure 4.19: Pulse height spectrum from the calibration pad of the Planacon MCP device operated in single photoelectron regime. The estimated minimum and maximum thresholds are used to determine the electronics detection efficiency for single photoelectrons.

Table 4.4: NINO threshold estimate in amount of charge and the corresponding electronics detection efficiency values for single photoelectrons.

ΔV [V]	Threshold [fC]	EDE for single photoelectrons [%]
0	51.8	78.4
0.1	56.7	76.7
0.14	56.7	76.7
0.5	58.1	76.1
1	64.4	73.5
2	67.9	72.2

4.3.5 Efficiency of the time reference signal

The efficiency on the reference signal is also important, since ideally, a time reference signal should be available for each event. If this is not the case, the time difference between leading edge of the hit and that of the reference signal for that particular event cannot be assessed. The study of this efficiency is performed at three different threshold settings of the CFD: -100, -150 and -300 mV. The output signal from the fast amplifier is connected to the oscilloscope. Figure 4.20 shows an oscilloscope display in persistence mode of the NIM (waveform 1) and the amplifier (waveform 2) output signals from the ORTEC CFD device at -100 mV threshold setting. At this threshold setting, MCP signals are not detected above V'=-4.5 mV. The amplitude values measured on the oscilloscope, V', for the other threshold settings are: -7 and -14 mV. These values correspond to input signals of -5.25, -8.17 and -16.3 mV before a ×18 amplification (Figure 3.9 (left)).
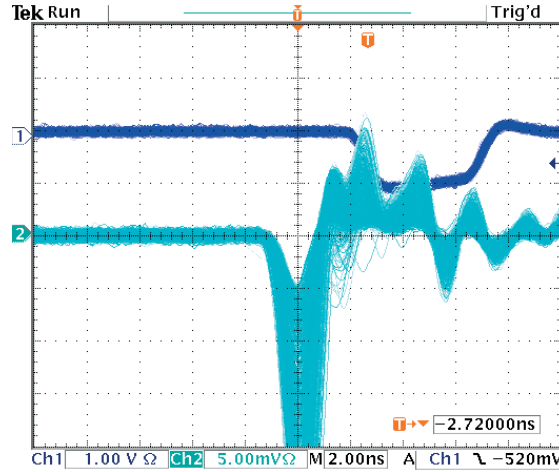
Figure 4.20: Oscilloscope display in persistence mode showing the NIM ouput signal from the CFD (waveform 1) and the MCP signals amplified and discriminated by the CFD (waveform 2). MCP signals above -4.5 mV are not detected at a -100 mV threshold setting of the CFD.

For these measurements, $c_{trigger}$ is 3×10^5 and 1-P(0)=0.996. The efficiency is calculated in three ways:

- First method: using the test channel on the 8-channel NINO-HPTDC electronics and applying Equation (4.8)

- Second method: using a scaler counter which registers the sent triggers and the number of output signals from the CFD

- Third method: by the ratio of counts on the time distribution over the counts on the pulse height spectrum

The resulting efficiencies are tabulated in Table 4.5. The small discrepancy between the result from the third method and that from the other two would be explained by the settings used for the multi-channel analyser and the decay time constant of the shaping amplifier.

Table 4.5: Efficiency values of the reference signal from the single-channel MCP read out by the CFD estimated using three methods.

CFD threshold setting	NINO-HPTDC electronics [%]	Scaler [%]	ORTEC electronics [%]
-100mV	94	94	92
-150mV	87	86	83
-300mV	50	50	40

4.3.6 Spatial scans

The response uniformity of a MCP photon detector over its active surface as well as crosstalk between individual pads are two important aspects [97, 98]. To study these properties as a function of the laser spot position the Planacon is illuminated in steps of 0.2 mm in the horizontal direction while the vertical position (central axis of a pad) is fixed. The response of each pad in the two bottom rows (0 and 1) is recorded for each laser spot position. Figure 4.21 shows the hit counts collected on individual pads when the laser spot is positioned at their centre. Two electronics channels with coordinates (0,1) and (6,1) are seen to be non functional.

The results of such 1D scans are shown in Figures 4.22 and 4.23 where the counts on individual pads in each row as a function of the laser position are plotted. Both figures show a good homogeneity of the Planacon MCP device along a row. In Figure 4.23 the count level is reduced by ~30 %. This is attributed to a lower QE of the photocathode at the tube boundary. Also from these figures, crosstalk between pads is visible. Adjacent pads respond when a given pad is illuminated. This crosstalk is partially attributed to back-scattered photoelectrons whose maximum range for a MCP input gap of 4.5 mm is 9 mm beyond the pad boundary. In addition, for a laser spot position in the range 10-20 mm where a dead channel is located an additional crosstalk of electronics nature is suspected.
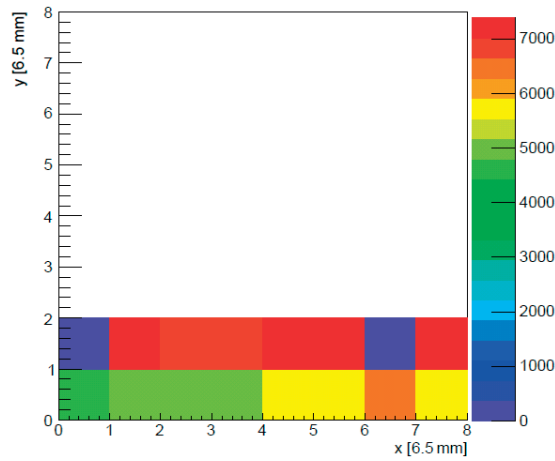
Figure 4.21: Hit map of 16 pads of the Planacon read out by the 8-channel NINO-HPTDC electronics.
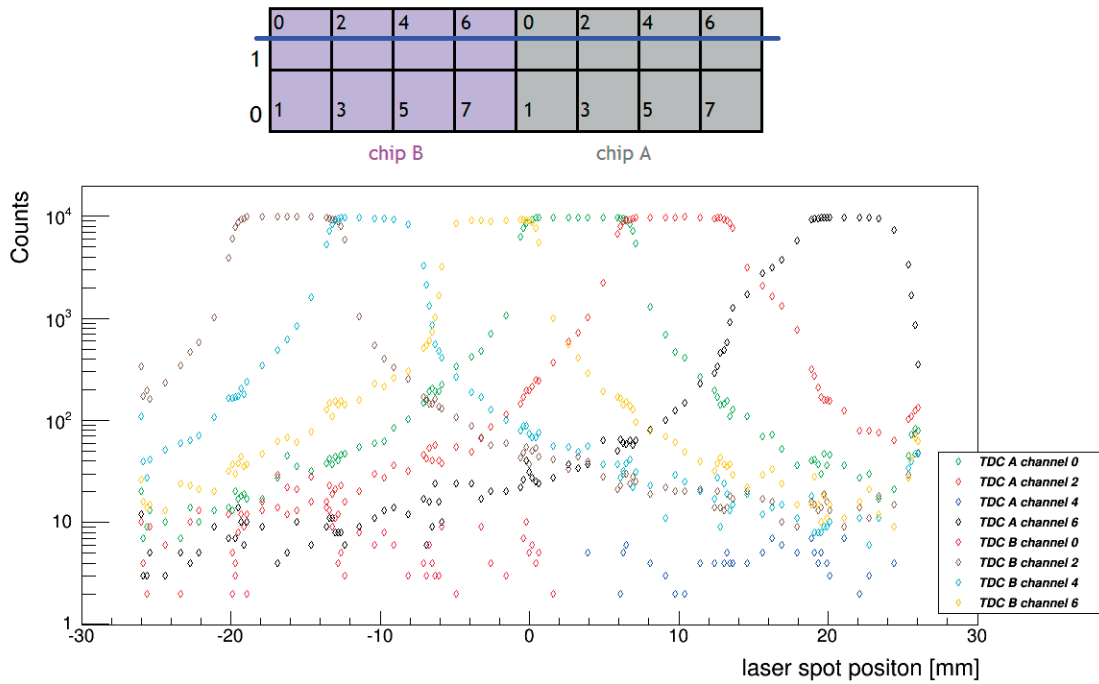
Figure 4.22: Individual pad count rates as a function of the laser position across 8 channels in row 1 (vertical logarithmic scale).

Point spread function

From the response of two adjacent pads, when the laser spot is displaced from centre-to-centre, the PSF is estimated. First, the fraction of counts that a pad (chip A channel 0) collects

89
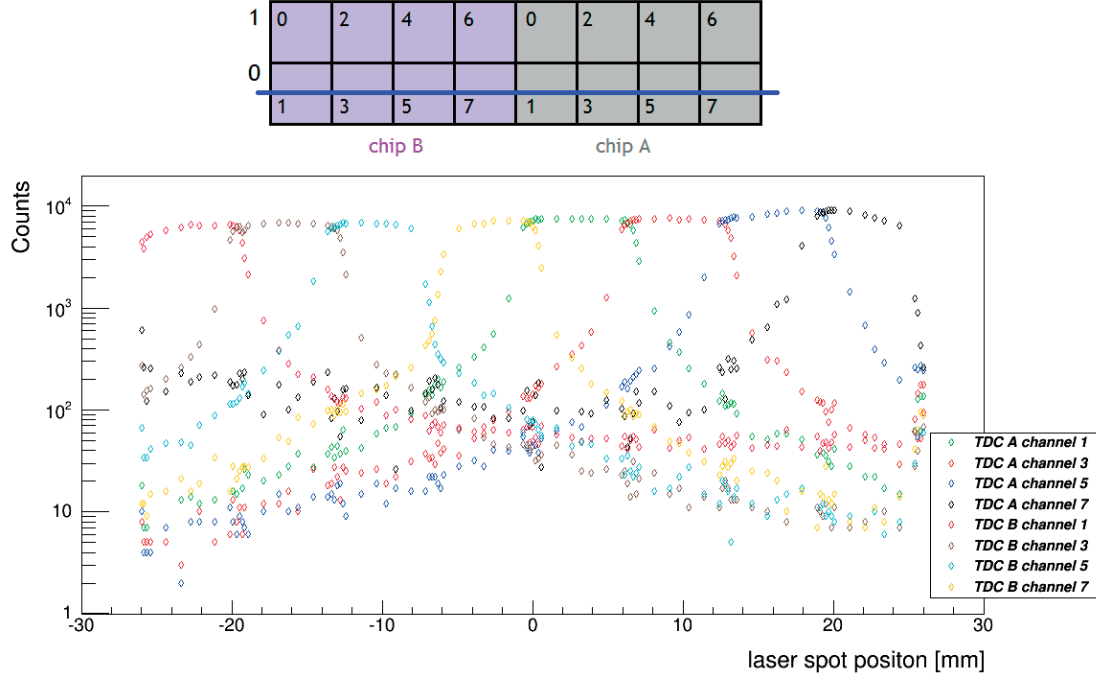
Figure 4.23: Individual pad count rates as a function of the laser position across 8 channels in row 0 (vertical logarithmic scale).

is

$$\text{count fraction} = \frac{c_{channel\ 0}}{c_{channel\ 0} + c_{channel\ 2}} \tag{4.14}$$

where $c_{channel\ 0}$ and $c_{channel\ 2}$ are the counts detected by channel 0 and 2, respectively.

Figure 4.24 illustrates the fractional counts for channel 0 as a function of the laser position. The considered scan range is from the centre of channel 0 to the centre of the adjacent pad (chip A channel 2). Data (black points) are fitted using Equation (4.6). A count fraction of 2% accounting for the back-scattering effects in the adjacent pad is inferred. All other adjacent pads could detect these back-scattered photoelectrons resulting in a halo with a radius of 9 mm. Charge-sharing occurs at the boundary between the two pads. The blue histogram corresponds to the derivative and is calculated as the difference in fraction of counts in a step interval. The histogram is fitted with a single Gaussian and the PSF at the anode level is defined as the standard deviation of the Gaussian, 0.8 mm. This value is compatible with the TORCH requirements if charge-sharing is used. In this case, the spatial resolution can be improved by calculating the centroid position using the TOT information (see Subsection 5.6.5). The width of this distribution can be improved by reducing the gap distance between the MCP output plane and the anode and/or increasing the voltage.

In [47], the PSF was evaluated from the response of the calibration pad using commercial single-channel electronics. Consequently, the obtained value of ~0.4 mm was underestimated.

This difference is attributed to the different readout systems (analogue versus binary).
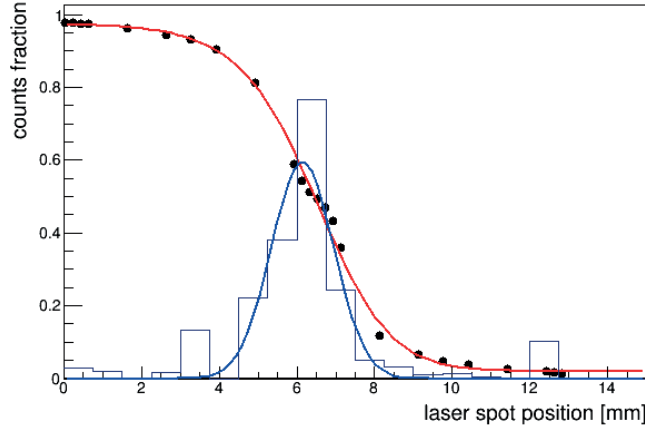
Figure 4.24: Normalized count rate as a function of laser spot position for the left pad with the boundary between pads at 6.5 mm.

Two additional spatial scans have been performed. The first scan consists of a vertical displacement of the laser between two adjacent pads while the horizontal position (central axis of a pad) is fixed. Figure 4.25 (left) illustrates the scan diagram from boundary to boundary of both pads and the counts collected on each pad as a function of the laser position. For the second scan the laser is moved along the diagonal direction of a pad. Figure 4.25 (right) illustrates the scan diagram from centre to centre of both pads and the counts collected on each pad as a function of the laser position for the four adjacent pads. From these results, the tube response is seen to be lower at the tube boundary as clearly observed in the response of channel 1. At the corner of a pad, the charge is shared over the four adjacent pads with a EDE drop as expected [47].

A PHS is recorded on the calibration pad at three specific laser positions: the pad centre, edge and corner. The charge estimated from each PHS can be used together with the pulse width measured using the multi-channel electronics for the same specific positions to perform the charge-to-width calibration. The resulting data are plotted in Figure 4.26 and are fitted using Equation (5.8) which will be discussed in the next chapter. Charge-sharing and the charge-to-width calibration can be used to improve the position resolution (see Subsection 5.6.5 for details).

4.3.7 Summary

The performance of an 8×8 pads Planacon MCP-PMT is assessed with customized 8-channel NINO-HPTDC electronics. A time resolution of 68 ps is achieved after corrections for non-linearity and time walk effects. The residual contribution from INL is estimated to be $\sigma_{res\ INL}=$ 14 ps. Time walk corrections are applied using the Time-Over-Threshold technique from the width information of the NINO pulses. The definition of a time reference point is key
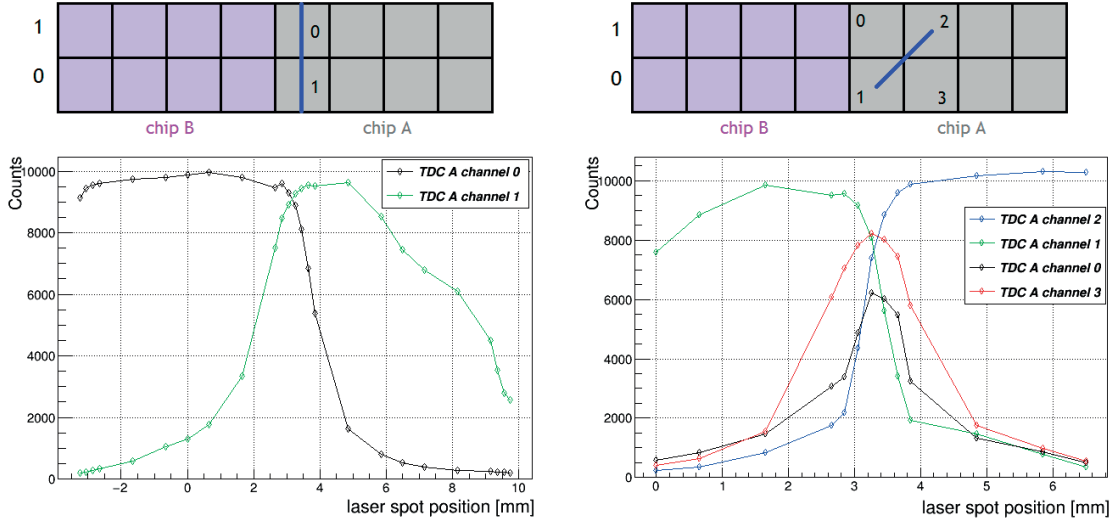
Figure 4.25: Individual pad count rates as a function of laser position across 2 channels in linear scale. Full vertical scan from boundary of channel 0 to boundary of channel 1 at the bottom edge of the tube (left). Individual pad count rates as a function of laser position across 2 channels in linear scale. Diagonal scan from centre of channel 2 to centre of channel 1 (right).
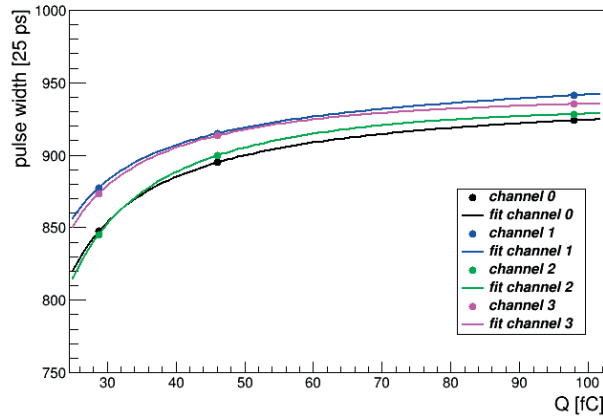
Figure 4.26: Charge-to-width calibration curves for four NINO channels. The charge values are estimated from the PHS recorded on the calibration pad at the corresponding three specific laser positions. The pulse width values are measured by the NINO-HPTDC electronics for four channels at the same laser positions.

for this correction and should in principle be the same for all channels. In practice, a time offset between the calibration curves exists and is explained by the signal time delay between channels.

The electronics detection efficiency is estimated to be close to 80% for single photons when a Planacon device is operated at a low gain of ~5×10^5 electrons.

The time reference signal is provided by a single-channel MCP device illuminated with a fraction of the same laser pulse as for the Planacon. This fraction of light is attenuated to reach a multi-photon regime and results in a time resolution of ~20 ps.

Spatial scans have been performed. Due to the large photocathode-MCP gap of 4.5 mm back-scattered photoelectrons are detected at a maximum distance from the laser position of 9 mm. The intensity level attributed to back-scattered photoelectrons measured on an adjacent Planacon pad is found to be 2%. A point spread function of σ=0.8 mm is measured at the pixel boundaries. This value is compatible with the TORCH requirements if a charge-sharing technique is used.

5 Characterization of Phase II custom-made MCP-PMT prototypes

This chapter describes the Phase II custom-made MCP-PMT prototypes with the spatial precision required for TORCH. In comparison to the 8×8 pads Planacon, these prototype tubes require four times more electronics channels and larger readout bandwidth. The performance of the second generation of custom electronics is assessed and the required calibrations of the NINO and HPTDC chips are evaluated.

5.1   Phase II: MCP prototypes with the required spatial precision

During the second R&D phase, five circular-shaped segmented MCP-PMT prototypes have been fabricated. They are equipped with a 9 mm-thick quartz window on which a S20 photocathode is deposited. These devices were manufactured with three un-coated MCPs in Z-stack configuration. The photocathode-MCP gap is 200 μm and the MCP-to-anode gap is 4.5 mm. Four devices have an electrode penetration depth of 2d at the output of the MCP channels and one device has an electrode penetration depth of 0.5d.

The Phase II MCP-PMT prototypes (Figure 5.1) use a structured multi-layer ceramic readout anode, which is a hybrid between a multi-anode detector with direct connection (DC) from the vacuum envelope to outside of the detector and a charge-sharing imaging MCP device [99]. The signal from the MCP electron cloud is collected on a resistive layer inside the vacuum and is capacitively coupled to anode pads embedded in the ceramic structure. This hybrid anode design allows the use of charge-sharing techniques. The anode is in a 32×32 pad array in a 26.5×26.5 mm^2 active area within a 40 mm diameter circular tube envelope. This design matches the pad size of 0.728 mm and pitch of 0.828 mm of the 64×64 square pattern for the final device and is a quarter size of the final anode for TORCH.

The anode output metallic pads are connected to an interface PCB using Anisotropic Conductive Film (ACF) [100]. The housing for the Phase II devices applies similar even pressure to the ACF but also allows room for the connections to the readout electronics. The interface board merges pads by groups of 8 in the horizontal direction, giving a 4×32 readout channels
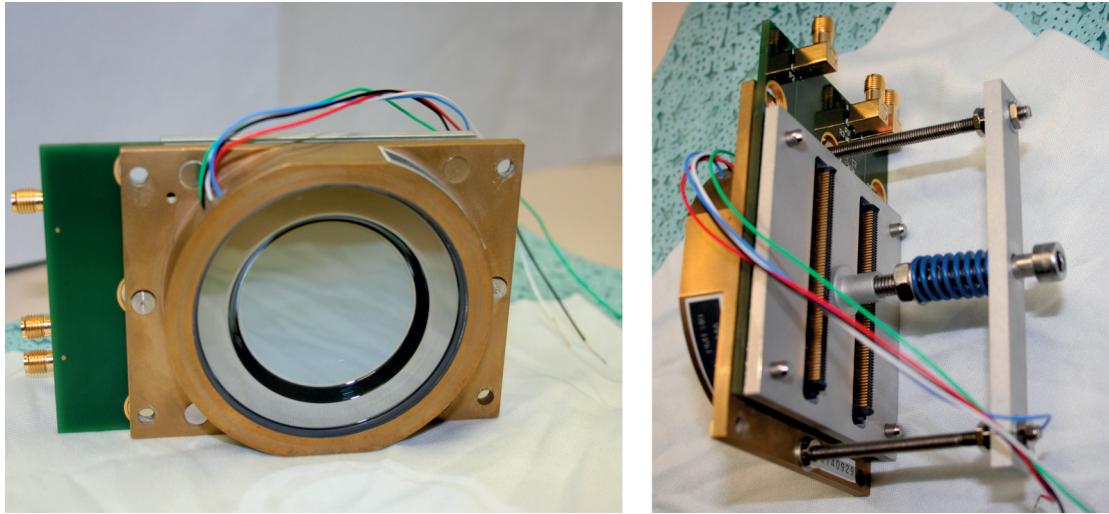
Figure 5.1: A front-view (left) and rear-view (right) photograph of a Phase II MCP-PMT proto-type from Photek Ltd.

of dimensions 6.624×0.828 mm^2 (Figure 5.2). Two high-bandwidth[1] connectors (J1 and J2) at the rear side of the interface board allow assembly of electronics boards, with 64 readout channels each. It also incorporates one SMA connector for the injection of a time reference signal and two SMA connectors for calibration inputs. The study of the test input circuitry used for time reference can be found in Appendix C.
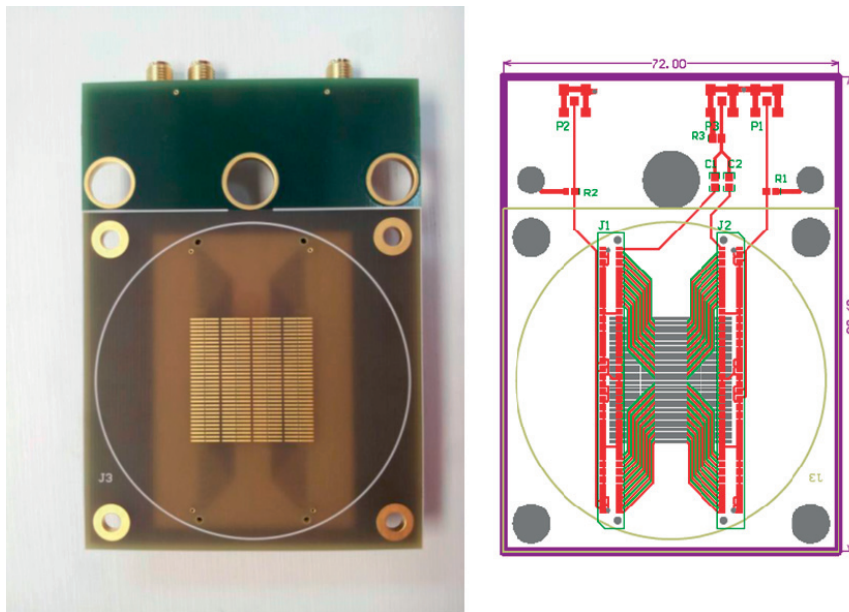
Figure 5.2: Front-view (left) and rear-view schematics (right) of the interface board for the Phase II MCP-PMT prototypes.

---

[1] High-bandwidth connector model ERM8-070 from Samtec.

The resolution of 0.4 mm required for TORCH will be achieved using charge-sharing between pads in the fine direction. This will improve the spatial resolution beyond the pitch of the anode pads and the total channel count will be halved and therefore the required number of NINO and HPTDC chips. The spatial resolution in the fine direction using charge-sharing technique has been simulated and shows a strong dependence on the NINO threshold and MCP gain [99, 101, 102]. These studies result in a requirement of a 10^6 or higher MCP gain, which must be balanced against the requirements on photon detector lifetime. Charge-sharing has been also simulated resulting in a PSF of 1.6 mm FWHM.

Table 5.1 shows the dark count rate values for the five Phase II MCP-PMT prototypes provided by the company. The operating voltages to run the tubes at a gain of 10^7 electrons are also tabulated. Note that the photocathode is at ground while the anode (resistive layer) is at high voltage. The QE curves for the five Phase II MCP-PMT prototypes provided by the company are shown in Figure 5.3.

Table 5.1: Dark count rate values and operating voltages for a gain of 10^7 electrons provided by Photek.

Device	G2140929	23140827	21140827	G3140910	22140827
Dark Count Rate [cps]	1800	3400	2300	<2000	<4400
Total applied voltage [V]	+4100	+4100	+4300	+4400	+4350
Photocathode (blue) [V]	0	0	0	0	0
MCP in (red) [V]	+221	+197	+227	+200	+226
MCP intermediate (white) [V]	+984	+931	+1043	+1009	+1064
MCP out (black) [V]	+2588	+2456	+2751	+2713	+2808
Anode (green) [V]	+4100	+4100	+4300	+4400	+4350
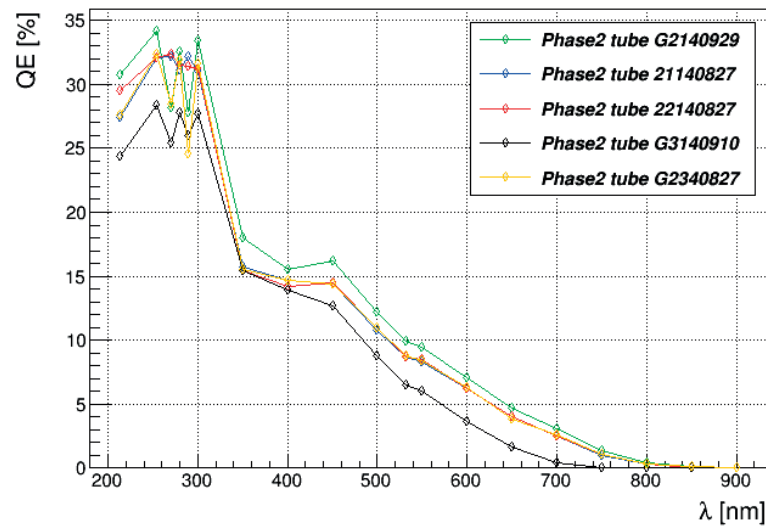
Figure 5.3: QE versus wavelength, λ, curves for the five Phase II MCP-PMT prototypes.

Phase II MCP-PMT prototypes have been characterized in the laboratory using various read-out systems [103]: with an analogue board connected to an oscilloscope or to commercial electronics and with the 32-channel NINO-HPTDC electronics chain. The testing of these MCP prototype tubes has required a detailed study of the electronics schematics and the connectivity of the MCP interface board. A channel mapping that associates a MCP anode pad with a electronics channel has been created for each electronics system. These mapping tables are attached in Appendix D.

5.2   Laser alignment procedure

The experimental set-up is similar to that already introduced in previous chapters where the laser source was pre-aligned for the testing of the 8×8 Planacon which has a 2 mm-thick quartz window. The focal point is at the photocathode. Since the custom MCP-PMT prototypes have an optical window of 9 mm thickness, the laser alignment is then adapted to this new configuration. The procedure is described as follows.

A focused laser source is simulated using a ray tracing software [104]. The laser light wavelength is chosen to be 405 nm, corresponding to that used in the laboratory. A fused silica window of 9 mm thickness is also simulated. The initial simulated configuration considers the laser light focused at the entrance surface of the MCP optical window (Figure 5.4). The distance between the focusing lens output and the optical window corresponds to 27.3 mm, the distance at which the smallest laser spot of 200 μm was achieved [47]. After alignment, the laser is focused on the photocathode plane at the exit surface of the MCP optical window (Figure 5.5). The light wavelength in both cases is 405 nm and the red colour is chosen for graphical comparison. The red colour rays indicate the laser focal point if the optical window would not be present. The blue colour rays take into account the light refraction due to the change in refractive index from air to fused silica. Consequently, the laser will be moved closer to the photon detector a distance, x. The distance between the laser and the optical window for the optimal alignment will be 27.3 mm-x.

In order to determine by how much the laser should be moved, the half-angle of the incoming light cone, θ_i, is varied in the range 0-30 °. The angle of refraction, θ_r, is also calculated using Snell's law [105]:

$$n_{air} \sin\theta_i = n_{fused\ silica} \sin\theta_r \tag{5.1}$$

where n_{air} is the refractive index of air and $n_{fused\ silica}$=1.47 is the refractive index of fused silica at 405 nm.

The distance in the y-axis, s, between the crossing points of the light rays with the input and output surfaces of the optical window is calculated for each θ_r value using the following
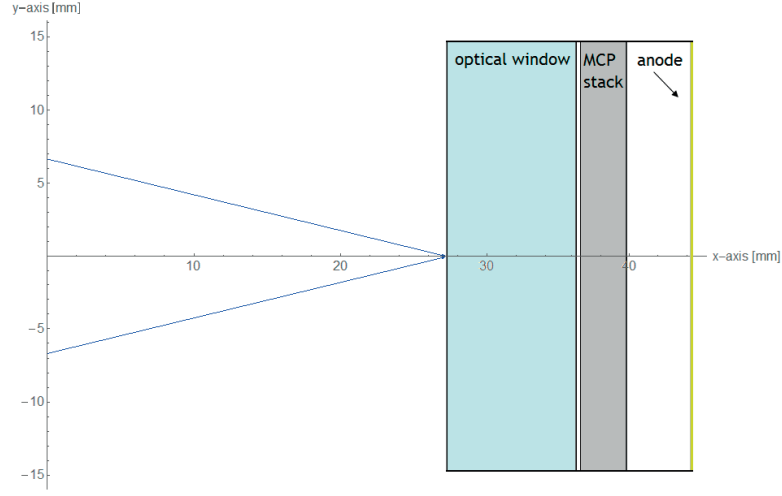
Figure 5.4: Schematics of the initial laser alignment at the entrance surface of the MCP optical window simulated using a ray tracing software.
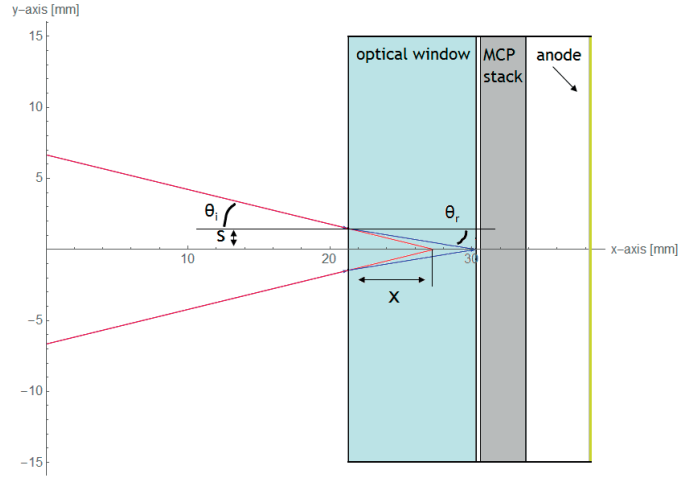
Figure 5.5: Schematics of the desired laser alignment (blue rays) at the exit surface of the MCP optical window simulated using a ray tracing software. The light wavelength in both cases is 405 nm and the red colour is chosen for graphical comparison.

trigonometric relation:

$$\tan\theta_r = \frac{s}{d_{window}} \tag{5.2}$$

where d_{window} is the optical window thickness of 9 mm. The relation between s and x is given by:

$$\tan\theta_i = \frac{s}{x} \tag{5.3}$$

and substituting Equation (5.2) in the previous equation:

$$x = d_{window} \times \frac{\tan\theta_r}{\tan\theta_i} \tag{5.4}$$

As a result, the laser is moved a distance of 6.06±0.04 mm closer to the tube.

5.3 MCP-PMT prototype performance using an analogue board

An analogue board has been designed and manufactured at the University of Bristol for testing the Phase II custom-made MCP-PMT prototypes. The board connects each of the 64 output channels from J1 or J2 connectors on the interface board through a mated edge high-bandwidth connector[2] to a sub-miniature coaxial surface mount socket[3] (Figure 5.6). A U.FL-to-SMA adaptor[4] for connecting to an oscilloscope is required.
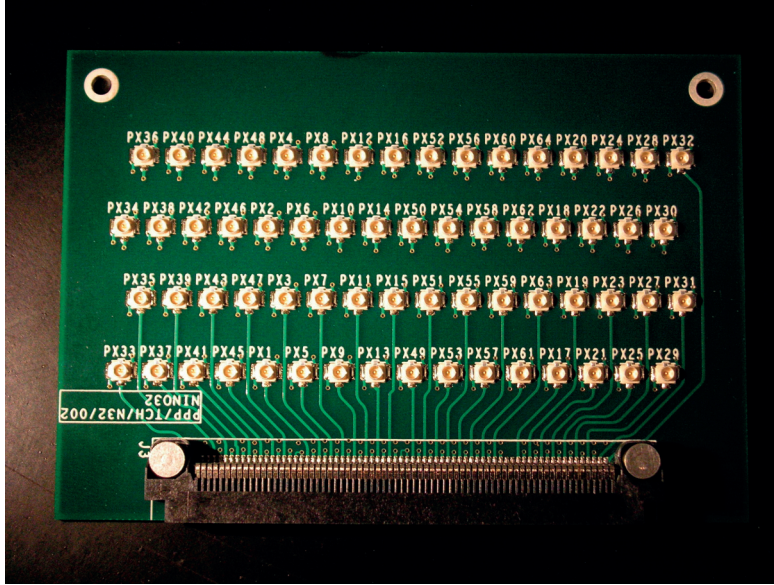
Figure 5.6: Photograph of the analogue board.

In the present study, the analogue board is connected to one of the high bandwidth connectors (J2) on the MCP interface board. All pins from the other connector (J1) are connected to ground. The laser spot is positioned in between the two central anode pads in column S1 (Figure 5.7 (left)). The channels corresponding to the four central pads on the analogue board are connected via the U.FL-to-SMA adaptor cable to a patch panel (see Appendix D for channel map details). The eight neighbouring channels are also connected and terminated with 50 Ω. Figure 5.7 (right) shows the rear-side of the MCP-PMT prototype tube and the analogue board

---

[2]High-bandwidth connector model ERF8-070 from Samtec.
[3]Hirose U.FL.
[4]U.FL to SMA adaptor model 1699231 from Farnell.

is mounted on dedicated mechanics.

Figure 5.7: Layout of laser alignment and electronics connectivity.

5.3.1 Laser light level and MCP gain calibrations

The MCP tube is operated at +3800 V. The four channels under study are read out with a fast oscilloscope[5]. The light intensity level, the amount of charge collected on each anode pad and the MCP gain are evaluated. The laser synchronization signal is used as trigger. Figure 5.8 shows the experimental set-up.
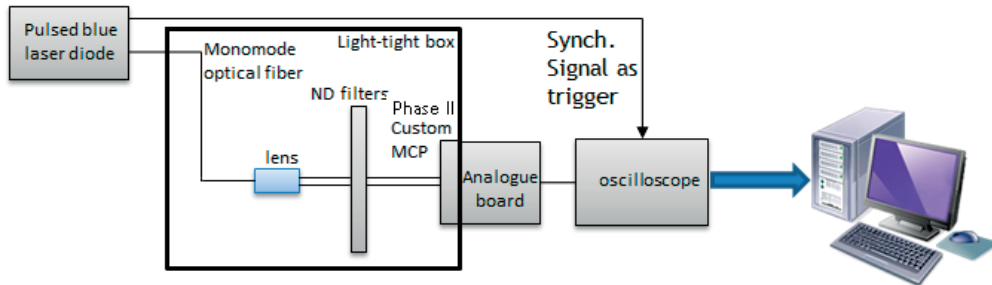
Figure 5.8: Experimental set-up for charge measurements using the analogue board.

Charge spectra are recorded. Each data point corresponds to the surface of the analogue pulses from the anode pads. An oscilloscope display of the analogue pulses at an operating overall voltage of +3800 V is shown in Figure 5.9 (left). The resulting charge spectra are reproduced in Figure 5.9 (right). The charge is spread over four pads at +3800 V, where the central pads get most of the charge. The average number of photoelectrons per pulse is found to be 0.24±0.02.

From the amount of charge collected on each pad the tube is calibrated in gain. Figure 5.10 (left) shows the charge spectrum from a central pad at +3800 V. The fit model consists of two

---

[5]Oscilloscope model Wave Runner 104MXi-A 1 GHz bandwidth 10 G/s from LeCroy.
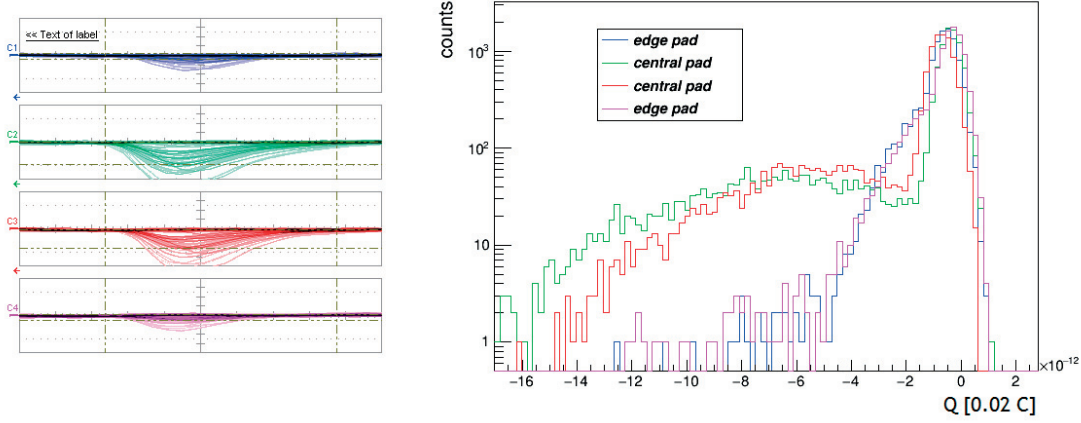
Figure 5.9: Scope display of analogue signals from four pads of the Phase II MCP-PMT proto-type. The scale of the x-axis goes from 116.5 ns to 121.5 ns and that of the y-axis goes from -8 mV to 8 mV (left). Charge spectra of the same four pads (right).

Gaussians describing the pedestal and the 1-photoelectron peaks. The charge collected by a central pad is ~90 fC. The contamination of a second photoelectron is small:

$$\frac{P_{0.24}(2)}{P_{0.24}(1)} = \frac{\mu}{2} = \frac{0.24}{2} = 12\% \tag{5.5}$$

which ensures that the operating regime is essentially with single photoelectrons.

The tube is operated at various voltages and the resulting characteristic gain-voltage curve is re-produced in Figure 5.10 (right). The overall MCP gain is calculated as the sum of the individual channel gains for the four calibrated channels and at +3800 V is found to be 1.6×10^6 electrons.
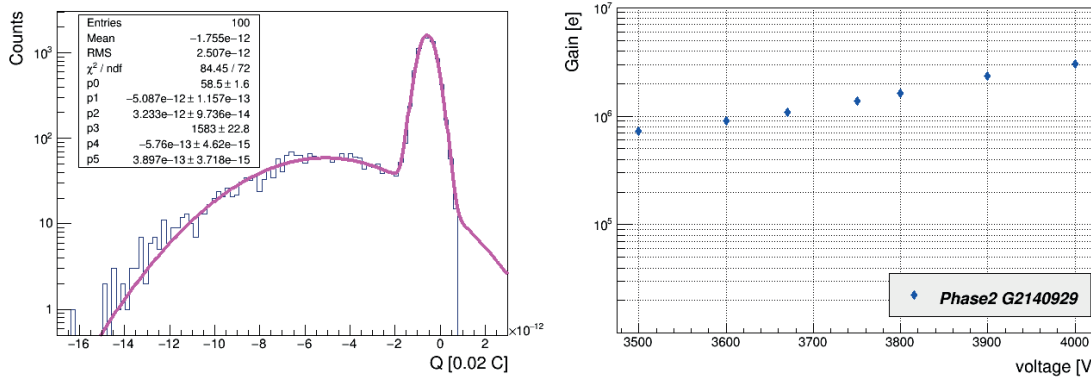
Figure 5.10: Charge spectrum for a central pad at +3800 V with an average charge of ~90 fC (left). Overall MCP gain as a function of the applied voltage for a Phase II MCP-PMT prototype (right).

5.3.2   Timing performance

In a first step and for comparison purposes the time response of a single pad is measured using the already introduced commercial fast amplifier and CFD while the other three pads are connected to the oscilloscope. The laser synchronization pulse and the CFD signal are connected to the START and STOP inputs, respectively, of the commercial TAC module (Figure 5.11 (left)). A typical time distribution is reproduced in Figure 5.11 (right). The main peak is fitted using Equation (3.9) since back-scattered photoelectrons populate the main peak due to the rather small MCP input gap of 0.204 mm, contributing to the asymmetric shape. A single Gaussian describes the laser relaxation pulse. A time resolution of 28.2 ps is obtained from a single pad. This value corresponds to the best timing performance that can be achieved.
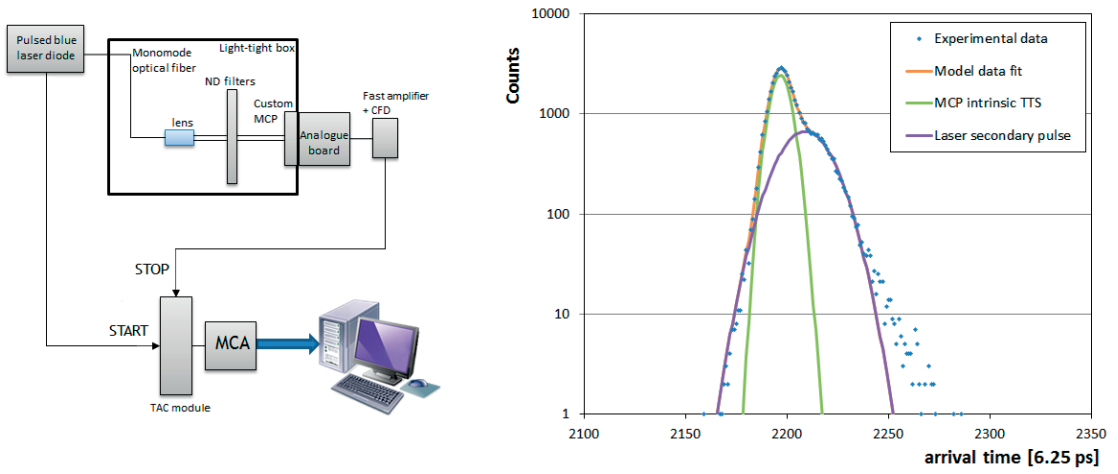
Figure 5.11: Experimental set-up for timing measurements using the analogue board with ORTEC CFD and TAC module (left). Time distribution from a single channel with a time resolution of 28.2 ps (right).

5.4   32-channel custom-made readout electronics

The second-generation readout electronics system is a modular and scalable design giving flexibility to instrument different photon detectors. This system has been calibrated in the laboratory with tests pulses. Since the Phase II MCP-PMT prototype uses the charge-sharing technique the collected charge is measured on several channels. The width of the NINO output signals depends on the input charge and thus the non-linear relation between pulse width and charge is evaluated.

5.4.1   Front-end NINO32 board

A FE NINO32 board incorporates two 32-channel NINO ASICs [85]. As in the previous generation the MCP-PMT analogue signals from single photoelectrons are amplified and discrimi-

nated by the NINO chips[6]. The width of the NINO output pulses is measured using the TOT technique according to a user-defined threshold that can be set by an on-board DAC. The DAC thresholds can be programmed either by on-board headers via an edge connector using a commercial SPI microcontroller[7] or by a FPGA on a HPTDC board (see next Subsection) when coupled to it. The design threshold adjustment is in the range 16-100 fC and is separately set for odd and even channels where two settings, positive and negative, are needed. The NINO32 chip has also a stretch functionality to meet the input requirements of the HPTDC.
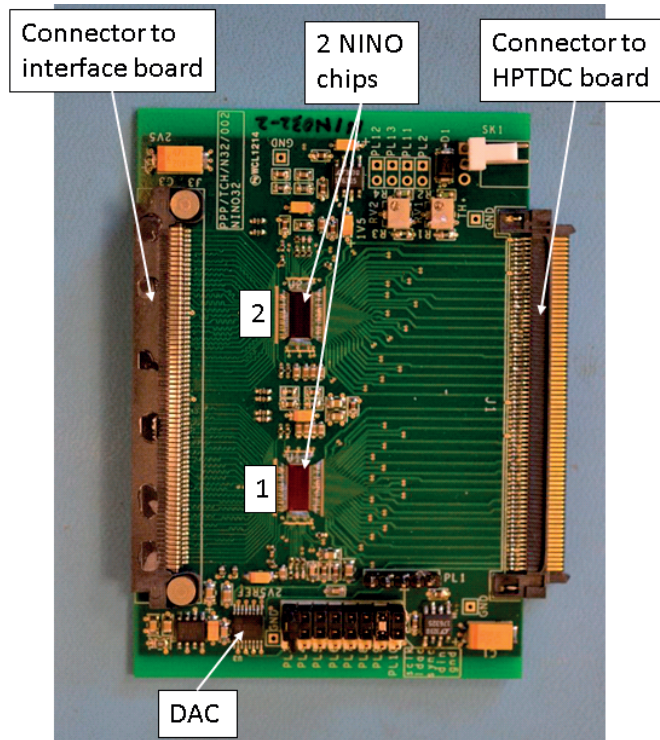
Figure 5.12: Photograph of the front-end NINO32 board incorporating two 32-channel NINO chips [51].

5.4.2   Time-to-digital conversion board (HPTDC32)

A time-to-digital conversion board called HPTDC32 is equipped with two HPTDC chips operated in HRM offering a 100 ps time bin precision for all 32 channels of each HPTDC chip. An on-board Xilinx Spartan 3AN FPGA [106] reads and buffers the HPTDC data. It also provides control, configuration and data formatting functions. The HPTDC configuration can be loaded through a readout board (see next Subsection) and programmed in to the corresponding HPTDC via a JTAG interface.

---

[6]In this case the 32-channel version type IRPICS2.

[7]Microcontroller model NXP LPC1768 from mbed, http://mbed.org.
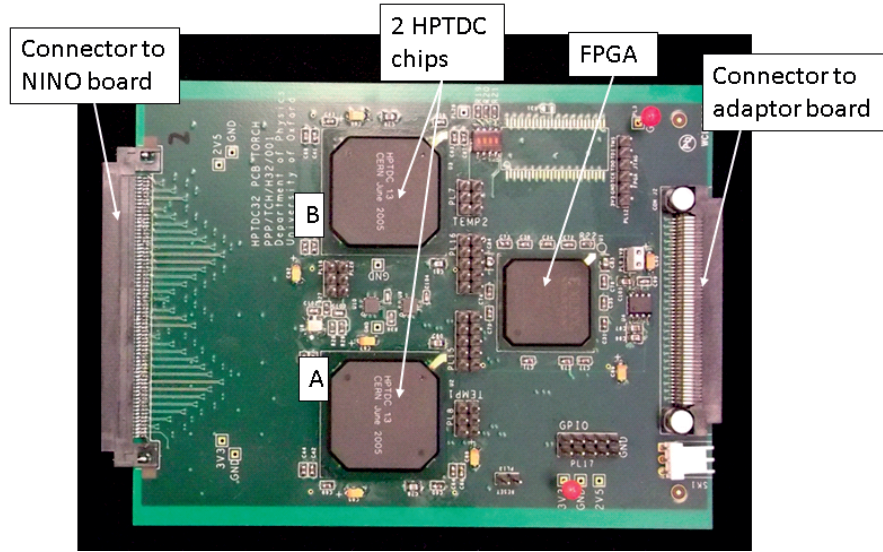
Figure 5.13: Photograph of the time-to-digital conversion board incorporating two 32-channel HPTDC chips controlled by a Spartan 3AN FPGA [51].

5.4.3 Adaptor and readout boards

An adaptor board routes the output of the HPTDC boards to a readout board. The connector layout is compatible with the interface board of both Phase II MCP-PMT prototypes and a 32×32 pads Planacon device. Power regulators are included on the adaptor board to supply 3.3 V and 2.5 V for the NINO32 and HPTDC32 boards, providing up to 9 A for both voltages.
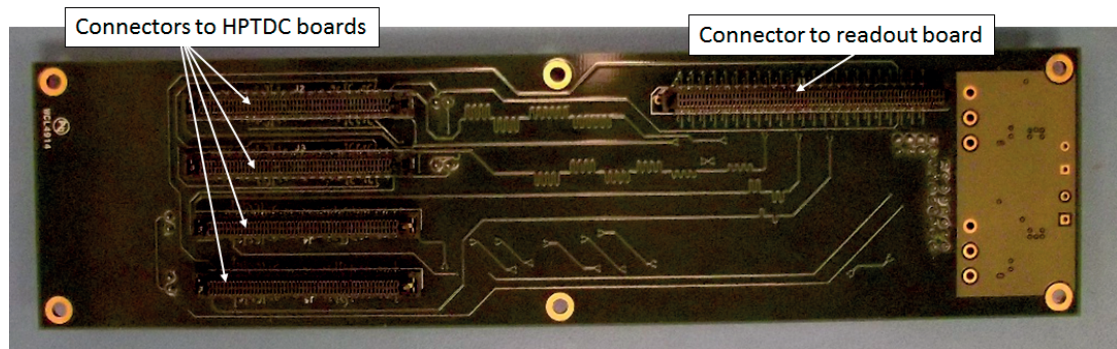
Figure 5.14: Photograph of the adaptor board incorporating one connector to a readout board and four connectors to HPTDC boards compatible with various photon detector layouts.

The readout board includes of a Xilinx Spartan 6 LX45T FPGA [107], a Gigabit Ethernet PHY chip, a 1 G-bit DDR3 RAM and low-jitter clock fan out ASICs [51]. It uses a single 5 V power supply, and all required voltages are regulated locally. The fan-out clock and trigger are received from a HDMI connector which is pin compatible with the AIDA Trigger Logic Unit (TLU) [108]. The TLU also allows the interface between TORCH electronics and e.g. a tracking

telescope or Cherenkov threshold counters during beam tests. The DAQ connection is done via a Gigabit Ethernet link using a Cat5 Ethernet cable to communicate with a DAQ PC that runs LabVIEW.
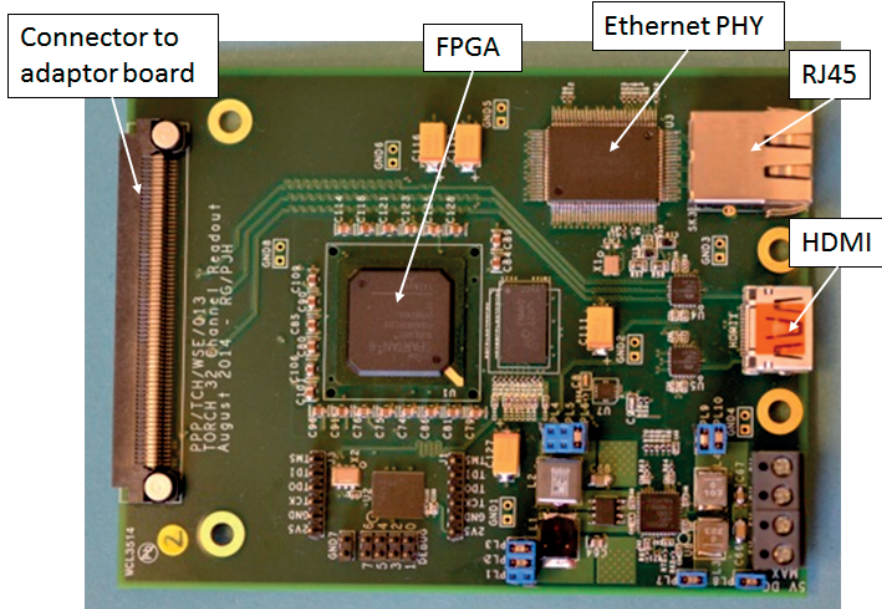
Figure 5.15: Photograph of the readout board [51].

5.4.4 Characterization of a front-end NINO32 board with test pulses

A NINO32 board with the stretch functionality OFF has been initially characterized with test pulses at CERN. Break-in and break-out boards have also been produced at Oxford to allow the testing of the NINO32 electrical performance. The experimental set-up is described in the following paragraphs and a picture is shown in Figure 5.16.

A pulse generator is used to send electrical pulses to individual NINO channels. A pulse with amplitude -200 mV is split in two by a power divider[8]. One half pulse is connected to a fast oscilloscope[9] as reference signal and the other half is sent to the electronics. Several high-bandwidth SMA attenuators[10] are used to inject a large range of pulse amplitudes. A simple circuit consisting of a 10 pF injection capacitor with 50 Ω termination is used to inject a given charge to a NINO channel via the break-in board.

The NINO32 board is powered with a high-precision and high-stability low-voltage power supply[11]. The NINO threshold setting is configured by the on-board DAC which is programmed

---

[8]SMA resistive power divider model 4901.19.A 50 Ω 6 dB 1 W DC-12.4 GHz from Suhner.

[9]Oscilloscope model Wave Runner 104MXi-A 1 GHz bandwidth 10 G/s from LeCroy.

[10]Low power attenuators models ref. R413803000 3 dB, ref. R413806000 6 dB, ref. R413810000 10 dB and ref. R413820000 20 dB 18 GHz from Radiall.

[11]Low-voltage power supply model TSX3510P from Aim TTI, Cambridgeshire PE29 7DR, UK.

using a commercial SPI microcontroller[12]. This device can be connected via flying wires to a pin connector either directly to the FE NINO32 board or to the break-out board. For these tests, the threshold for all odd and even channels of both NINO chips is set to 100 mV.

An active differential probe[13] is connected to the oscilloscope to record and digitize the LVDS output signals from the corresponding NINO channel via the break-out board.
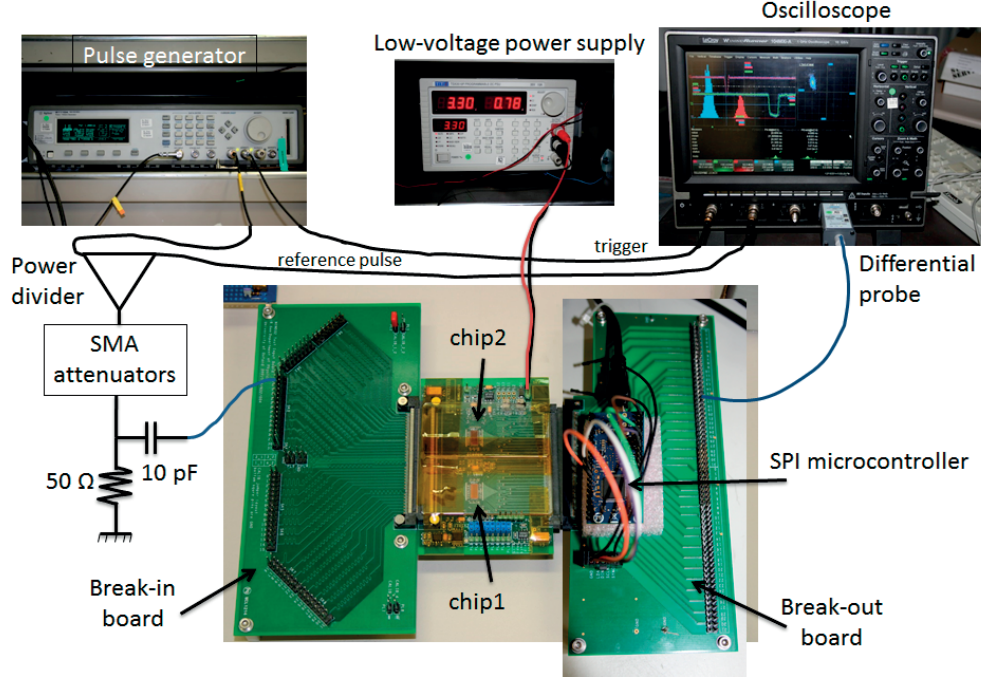
Figure 5.16: Experimental set-up for testing the NINO32 board with test pulses.

When testing the NINO32 board, it was noticed that the response of half of the channels (even) in chip 1 was unstable. This instability was identified to the NINO sensitivity to external light. When covering the board the channels response was as expected. Due to a mistake in the original NINO pinout table, the output polarity of the first five channels of each chip on the board is inverted.

Charge-to-width calibration with NINO stretch OFF

An input pulse V_{in}=-100 mV is attenuated by combining several attenuators of 3 dB, 6 dB, 10 dB and 20 dB allowing a large range of amplitudes which are calibrated in charge, Q. Figures 5.17 and 5.18 show two oscilloscope displays for the 20 dB attenuator. They show the reference pulse, the 20 dB attenuated pulse before the RC filter (blue coloured signal in Figure 5.17) and the pulse after the RC filter measured with the differential probe (green coloured signal

---

[12]Microcontroller model NXP LPC1768 from mbed, http://mbed.org.
[13]Active differential probe model AP034/10452 from LeCroy.

in 5.18). The pulse areas are measured and the amount of charge estimated.
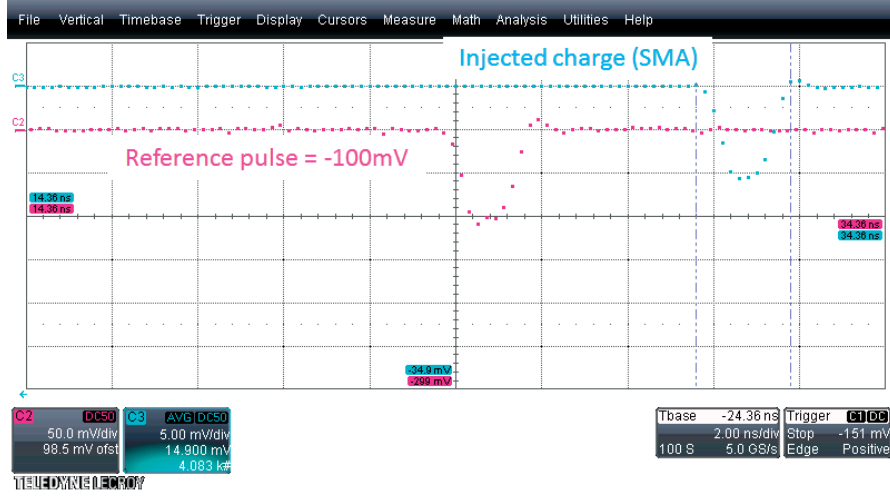
Figure 5.17: Oscilloscope display showing the reference pulse (upper trace) and the 20 dB attenuated pulse (lower trace) before the RC filter.
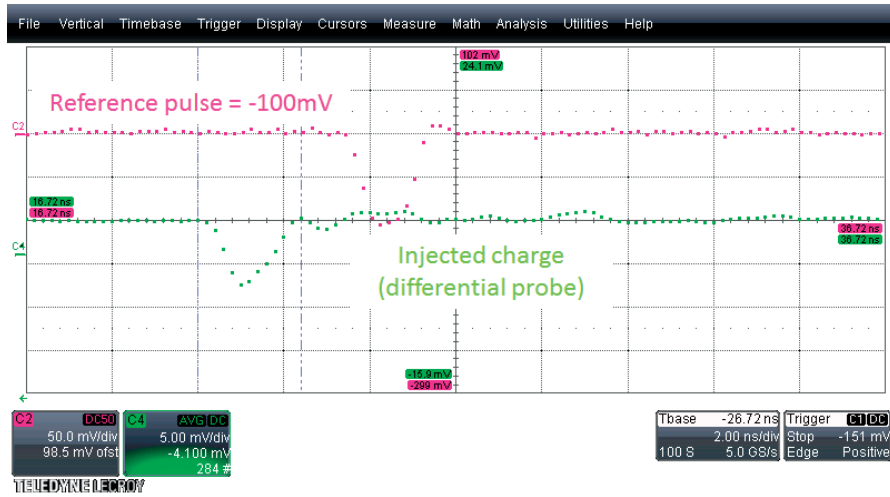
Figure 5.18: Oscilloscope display showing the reference pulse (upper trace) and the 20 dB attenuated pulse after the RC filter and measured with the differential probe (lower trace).

The charge of the reference pulse is calculated using a triangular approximation as

$$Q_{-100\,mV} = \frac{-100\,mV \times 2\,ns}{2 \times 50\,\Omega} = 2\,pC \tag{5.6}$$

The ratio between the input and attenuated pulses before the RC circuit satisfies the following relation

$$-att = 20 \times \log\left(\frac{V_{att}}{V_{in}}\right) \tag{5.7}$$

where att is the value of the attenuator in dB. The charges as a function of the attenuation level before and after the RC filter are shown in Figure 5.19.
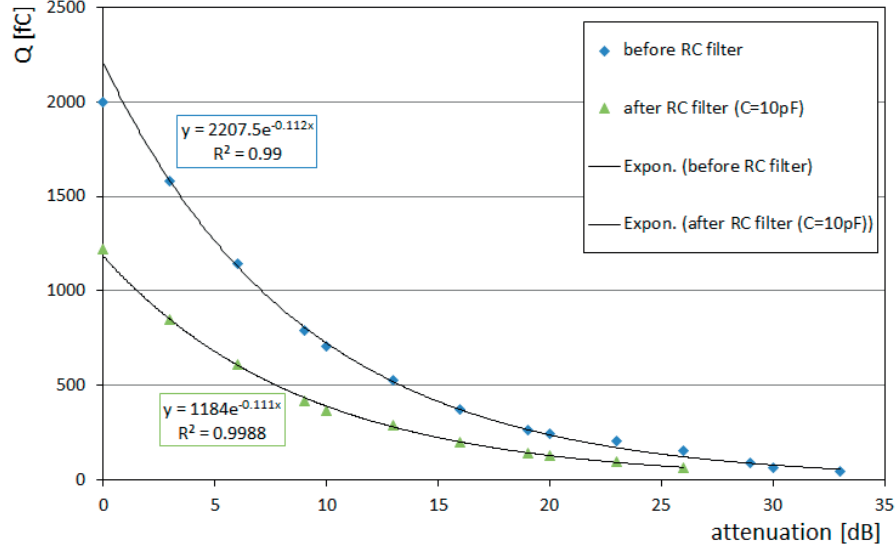
Figure 5.19: Amount of charge estimate from the pulses' surface before and after the RC filter using a fast oscilloscope.

These calibrated charges are injected into a NINO channel. The waveform of the NINO pulses are registered by the oscilloscope and transferred to a PC for off-line processing. The pulse width is measured also by the oscilloscope at a 50% level of the pulse amplitude for each value of the input charge. Figure 5.20 shows the waveforms of the NINO pulses for various injected charges and the 2D TOT plot of the pulse width as a function of the arrival time of the pulse. Since the stretch functionality is OFF, the pulse width varies in the range 2-6 ns. This figure also illustrates the time walk effect, smaller pulses are detected later than larger pulses. The pulse width and arrival time distributions for three specific input charges are reproduced in Figure 5.21.

The pulse width distributions are fitted with a Gaussian model. The relation between pulse width, w, and input charge, Q, is not linear and is reproduced in Figure 5.22. The measured data are then fitted using a four parameter model describing the charge response of a NINO channel. This model has been used for the TOT calibration of the TimePix chip [109] and is given by:

$$w(Q) = a \times Q + b - \frac{c}{Q - d} \tag{5.8}$$

where the parameters a and b describe the linear region of the curve (for large charges), parameter d is correlated with the threshold level and parameter c acts on the curvature.

The time walk effect is also observed by applying several threshold values to the NINO channels for a given input charge, as shown in Figure 5.23. The threshold values are indicated as the
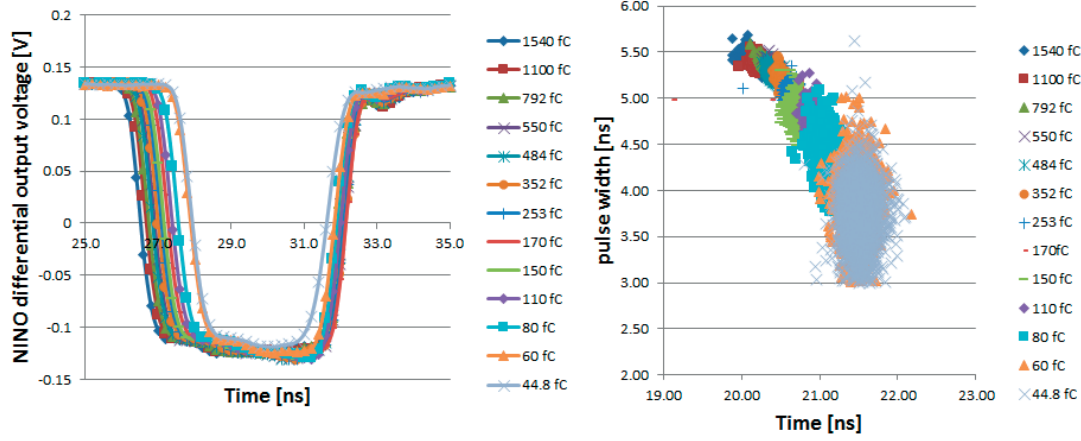
Figure 5.20: NINO pulses for different input charges (left). 2D TOT plot of pulse width as a function of arrival time for different input charges (right).
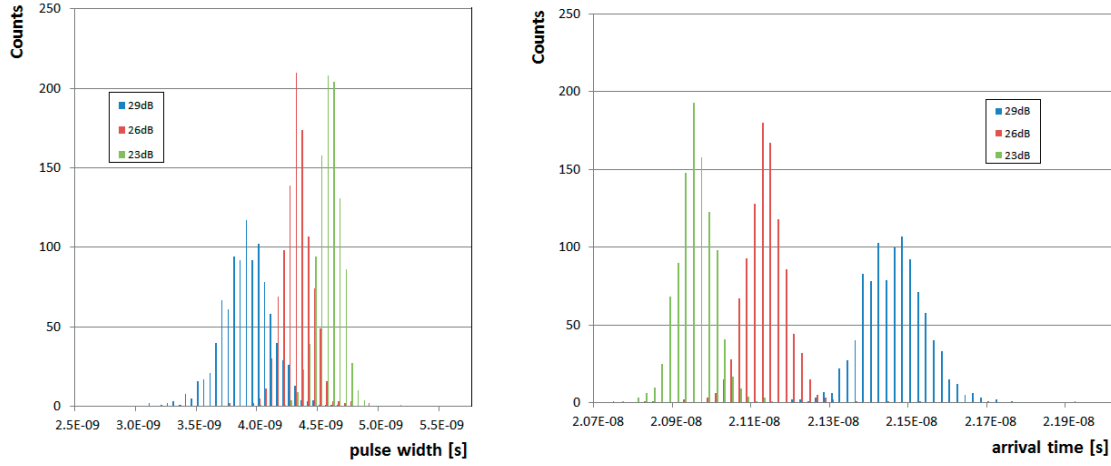
Figure 5.21: Pulse width distributions (left) and arrival time distributions (right) for three specific input charges.

difference between the positive and negative voltage settings. As the threshold difference increases only the largest signals are detected resulting in a smaller pulse width and a delayed detection time.

Time resolution

The time difference between the leading edge of the reference pulse (t_{ref}) and that of the NINO pulse (t_{nino}) is measured for the full range of charges. A 2D TOT plot for three specific input charges and a time distribution for a charge of 110 fC are reproduced in Figure 5.24. The arrival time distributions are fitted with a single Gaussian where the time resolution is defined as the standard deviation of the Gaussian and amounts to 42.9 ps for 110 fC.
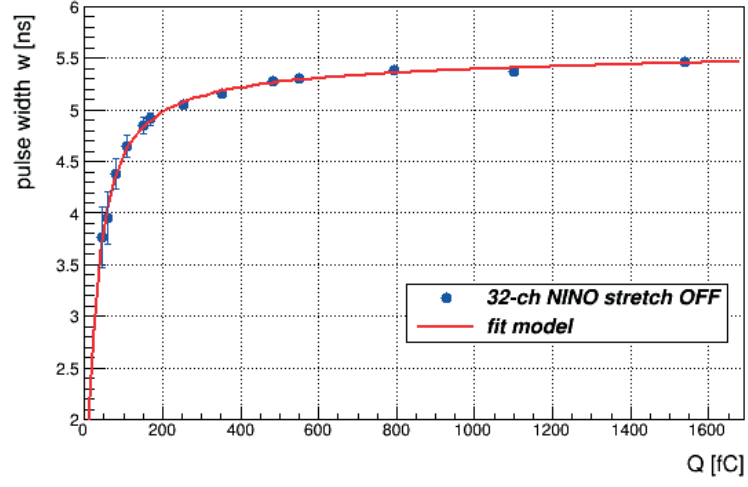
Figure 5.22: Measured pulse width as a function of the input charge for a single NINO channel with stretch OFF.
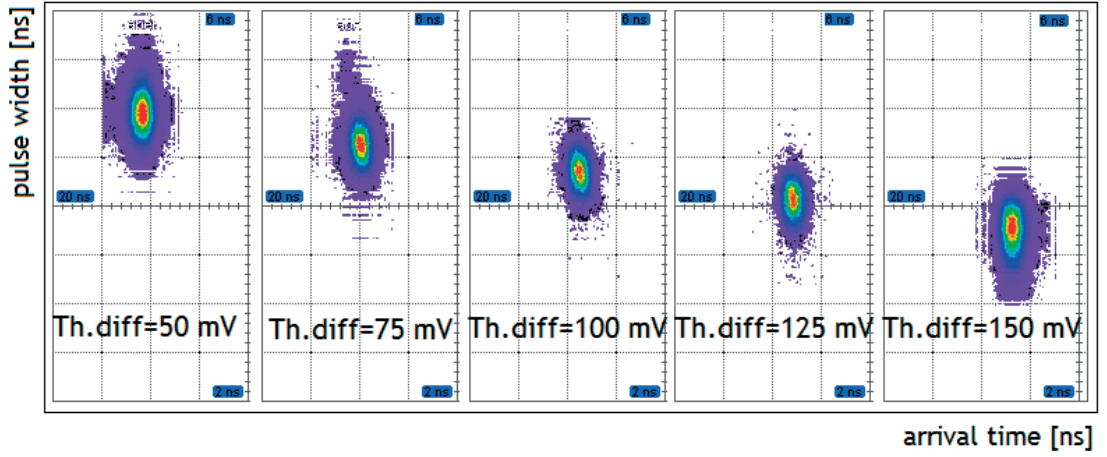
Figure 5.23: Pulse width as a function of arrival time for an input charge of 80 fC and at different NINO thresholds. The scale of the x-axis goes from 20 ns to 22 ns and that of the y-axis goes from 2 ns to 6 ns.

The contributions from the pulse generator and oscilloscope jitters are estimated to be 9.3 ps. Assuming a quadratic sum of these contributions the intrinsic resolution of the NINO channels are then evaluated. Data in Figure 5.25 are fitted using a model based on the one that has been applied in the calibration of the ALICE VZERO trigger system [110] and is given by the following equation:

$$\sigma = \sqrt{a + \frac{b}{Q^3}} \tag{5.9}$$

where a and b are the fit parameters.
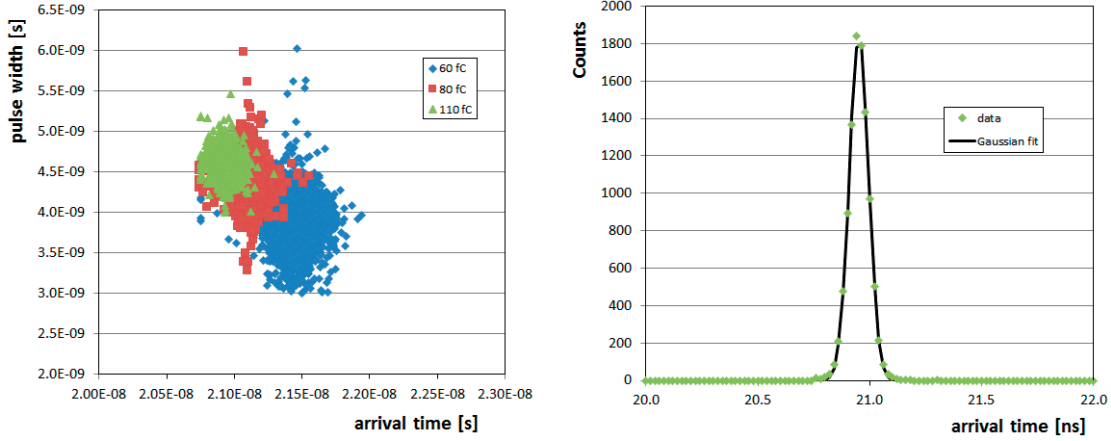
Figure 5.24: TOT plot for three different charges (left). Arrival time distribution for a charge of 110 fC with a time resolution of 42.9 ps (right).
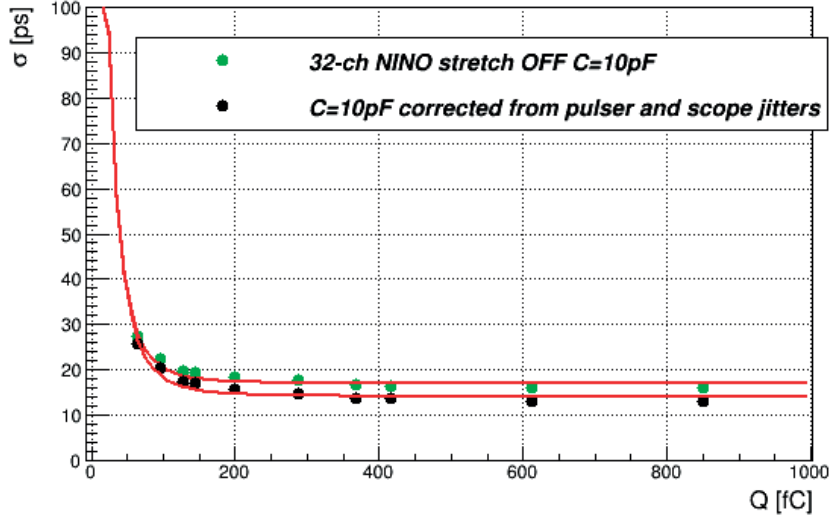
Figure 5.25: Time resolution on the leading edge of the NINO output pulse as a function of the input charge for a single NINO channel.

5.4.5   Characterization of full readout chain with test pulses

A similar procedure and set-up are used for the characterization of the full readout chain; break-in board, NINO32 board with stretch ON, HPTDC32 board and adaptor and readout boards are connected together (Figure 5.26). In this case a set of charges are generated by varying the amplitude of the signal from the pulse generator. A single configuration of attenuators of 26 dB is used. The injection capacitor is 10 pF. The power is supplied to the system via the 5 V at which the readout board is connected. The NINO thresholds are now configured via the FPGA on the HPTDC board. Three threshold settings are applied: ΔTH=50 mV, 100 mV and 200 mV. The HPTDCs are operated in 100 ps resolution mode with internal clock and are configured via the FPGA. A 30 ns-long trigger signal is injected on the HPTDC board and a

trigger for both HPTDC chips synchronized to the clock is generated by the FPGA firmware. A scaler[14] is also used to monitor the number of triggers input into the electronics.
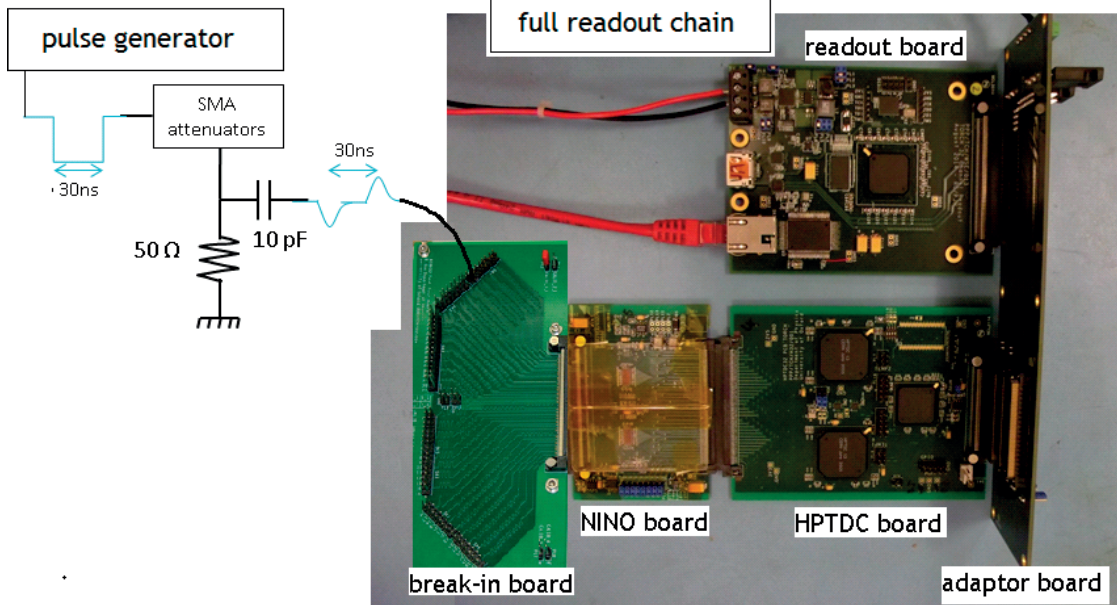
Figure 5.26: Experimental set-up for testing the full readout chain with test pulses.

Four NINO channels have been calibrated, one odd and one even from each NINO chip corresponding to channels 16 and 17 from NINO chip 1 and channels 14 and 15 from NINO chip 2 which are connected to those anode pads studied with the analogue board (Appendix D). The charge of the injected pulses is estimated, the charge-to-width is calibrated and the NINO threshold in amount of charge is evaluated. The charge-to-width calibration is a key information for further TORCH analyses such as the spatial resolution studies which will be covered later in the chapter.

Charge-to-width calibration with NINO stretch ON

Figure 5.27 (left) reproduces the charge values Q as a function of the amplitude of the non-attenuated pulses V. Data are fitted with a linear regression model, $Q = a \times V + b$ and the linear regression fit parameters are a=-0.527±0.006 and b=5.1±0.7. From the ratio between the charge and the amplitude of the attenuated pulse V' the value of the input capacitor C_{in} used in the RC filter can be obtained. Figure 5.27 (right) reproduces the charge values as a function of the amplitude of the attenuated pulses V'. Data are also fitted with a linear regression model, $Q = a' \times V' + b'$ and the linear regression fit parameters are a'=-10.2±0.4 and b'=4.1±3.4 giving a C_{in}=10.2 pF. The ideal response with a 10 pF capacitor is a straight line with slope -10.

---

[14]Quad scaler and preset counter/timer model N1145 from Caen.
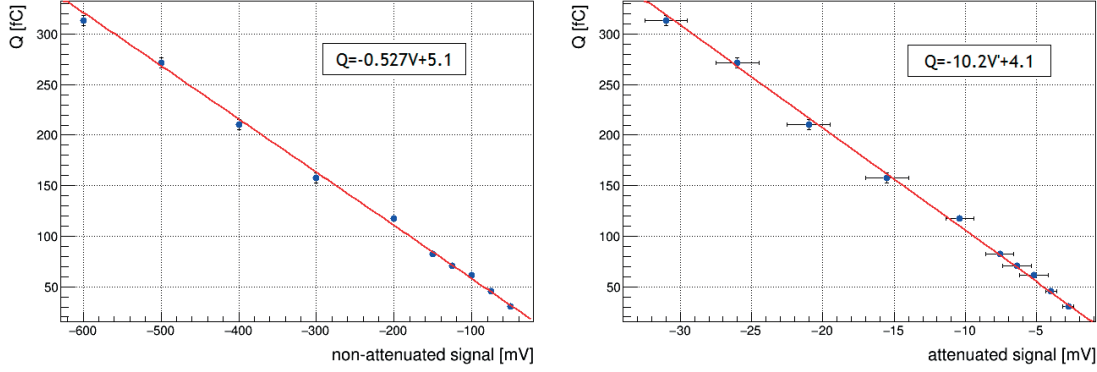
Figure 5.27: Estimated charge as a function of the amplitude of the non-attenuated pulses (left). Estimated charge as a function of attenuated pulses after the RC circuit (right).

The mean and the standard deviation values from the Gaussian fit of the pulse width distributions are obtained. The measured data for four NINO channels are reproduced in Figures 5.28 and 5.29 at a threshold setting of 100 mV. Data are fitted in all cases using Equation 5.8. Additional charge-to-width calibration curves are obtained for two different threshold settings of 50 mV and 200 mV and are reproduced in Appendix E.
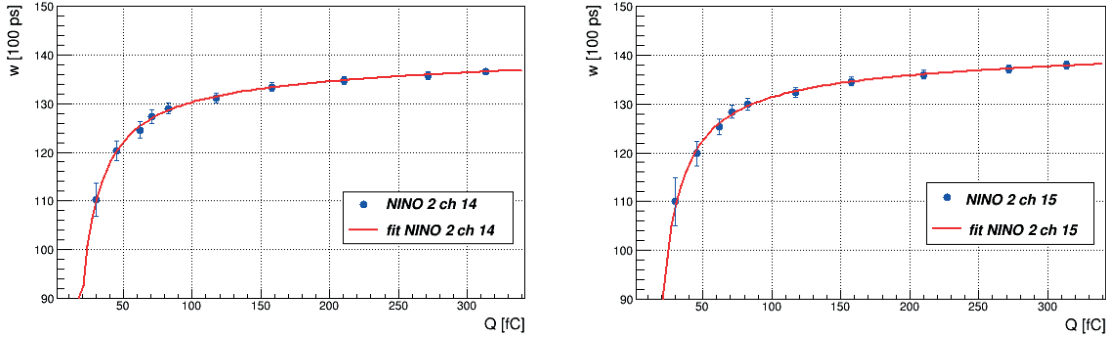
Figure 5.28: Charge-to-width calibration curves from channels 14 (left) and 15 (right) of NINO chip 2 at a threshold setting of 100 mV.

32-channel NINO threshold calibration

Since the number of triggers input into the electronics is known, the count efficiency, E_c is calculated as the ratio between the counts on the width distribution histogram and the number of triggers. Figures 5.30 and 5.31 display E_c as a function of the non-attenuated amplitude. Data are fitted using a four-parameter logistic function [111] which is used in many applications, a clear example is the Fermi-Dirac distribution. The analytical formula is given
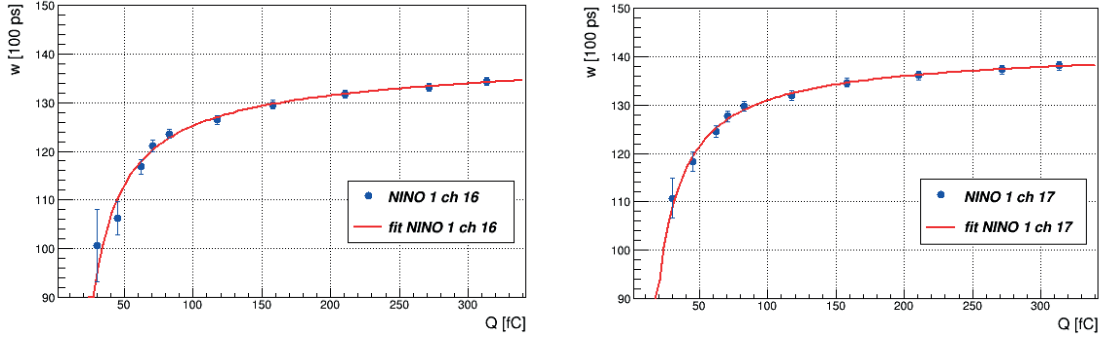
Figure 5.29: Charge-to-width calibration curves from channels 16 (left) and 17 (right) of NINO chip 1 at a threshold setting of 100 mV.

by:

$$E_c = p_0 + \frac{p_1 - p_0}{1 + \exp(-s(V - V_c))} \tag{5.10}$$

where p_0 is the minimum asymptote value, p_1 is the maximum asymptote value, s is the hill slope and V_c is the non-attenuated amplitude at 50% level. In the present case, p_0=0 and p_1=1, leading to the following simplified equation:

$$E_c = \frac{1}{1 + \exp(-s(V - V_c))} \tag{5.11}$$
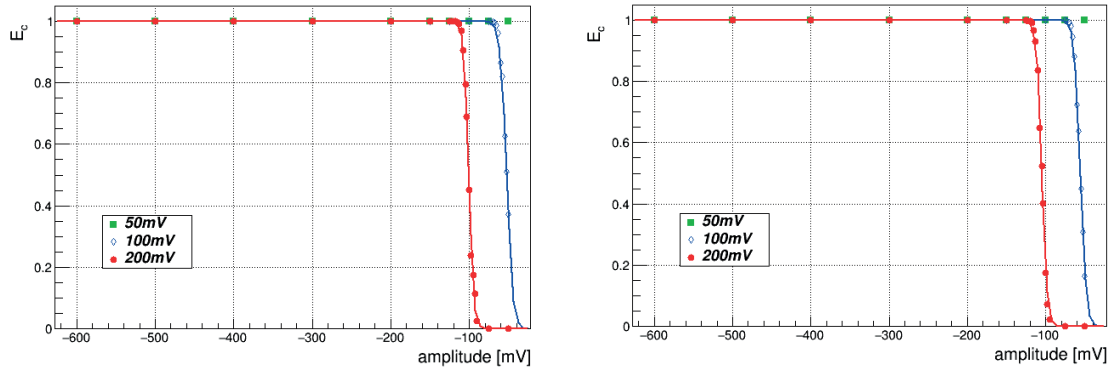
Figure 5.30: Count efficiency from channels 14 (left) and 15 (right) of NINO chip 2 as a function of the input pulse amplitude.

The NINO threshold is then evaluated at a 50% level of E_c. From the four-parameter function fit this value is provided by the parameter V_c in V units and is converted into charge by the linear regression fit from Figure 5.27 (left). The results are summarized in Table 5.2.
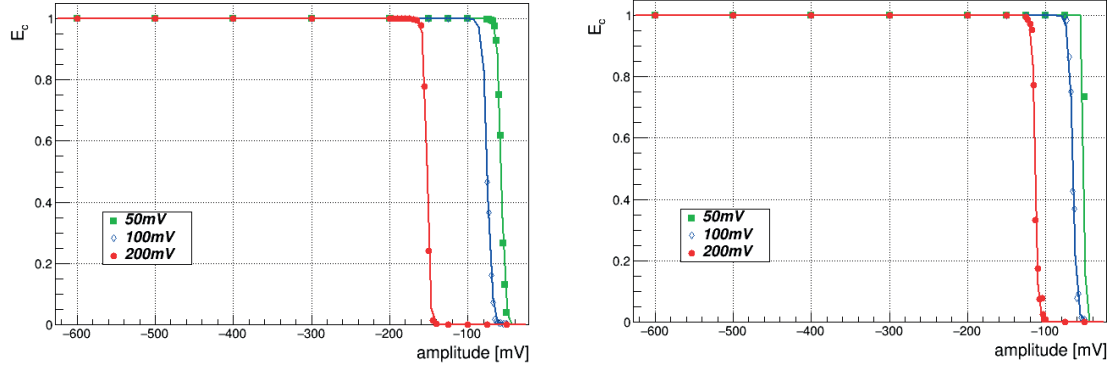
Figure 5.31: Count efficiency from channels 16 (left) and 17 (right) of NINO chip 1 as a function of the input pulse amplitude.

Table 5.2: NINO threshold estimate in amount of charge for four NINO channels.

ΔTH [mV]	NINO chip 2		NINO chip 1	
	ch 14	ch 15	ch 16	ch 17
50			35.3±0.4 fC	31.5±0.3 fC
100	32.9±0.4 fC	34.7±0.4 fC	44.8±0.5 fC	39.5±0.5 fC
200	58.3±0.7 fC	60.5±0.7 fC	85.5±0.9 fC	65.0±0.8 fC

It is seen that the same threshold setting applied to all channels corresponds to different threshold levels; channels on NINO chip 2 have lower threshold than those on NINO chip 1. In addition, even channels in chip 1 have significantly larger threshold. This will result in different channel response. Since the threshold setting is applied to odd and even channels and to both chips separately, optimal threshold values should be chosen in such a way to have an homogeneous response for all channels.

5.5 MCP-PMT prototype timing performance using a NINO32 board

A NINO32 board and a break-out board are now connected in place of the analogue board (connector J2 on the MCP interface board). Four differential probes are used to read out the output signals from the NINO channels using an oscilloscope. The NINO threshold setting of 100 mV is configured via the SPI microcontroller. In this configuration the time reference is provided by the signal from the single-channel MCP device coupled to the CFD. Figure 5.32 shows the experimental set-up used to measure the time response of the Phase II MCP-PMT prototype using the NINO32 board with the oscilloscope. A photograph of the MCP-electronics assembly is also shown.

Figure 5.32: Experimental set-up used for timing measurements with the NINO32 board.

5.5.1 Time walk calibration

The width of the NINO pulses and the time difference between the leading edge of the NINO pulse and that of the reference signal are measured. A 2D scatter plot of pulse width as a function of arrival time for a single NINO channel is reproduced in Figure 5.33 (left). The time walk calibration follows the same procedure already explained in Subsection 4.3.2. Time distributions before (blue) and after (red) time walk correction are shown in Figure 5.33 (right). Both distributions are fitted using Equation (3.9) and a single Gaussian accounting for the laser relaxation pulse. The time resolution improves from 90 ps to 65 ps after off-line correction for time walk effects.
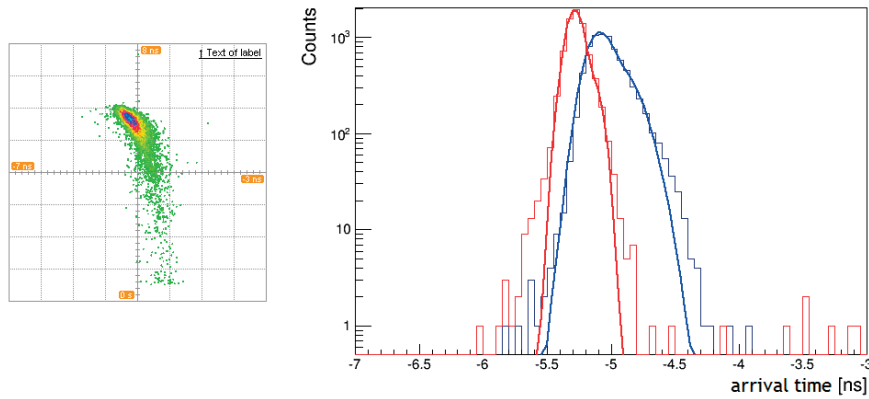
Figure 5.33: 2D scatter plot measured by the oscilloscope (left). Time distributions from a single channel using a NINO32 board and a break-out board with the oscilloscope (right). Blue colour curves correspond to the raw time distribution and its fitting model and red colour curves correspond to the corrected time distribution and its fitting model. The time resolution after time walk correction is found to be 65 ps.

5.6 MCP-PMT prototype performance using the full NINO-HPTDC readout electronics

A set of NINO32 and HPTDC32 boards instruments half of the tube and the other half of the channels are connected to ground. The NINO threshold setting is 100 mV. Both NINOs and HPTDCs are configured via the FPGA on the HPTDC board and the commands are loaded using a LabVIEW interface. The power is provided via the readout board. All boards are mounted on dedicated mechanics. The time reference signal provided by the single-channel MCP device coupled to the CFD is attenuated by 26 dB to match the input requirements of the NINOs and input into a reference channel via the MCP interface board (SMA connector P3 in Figure 5.35 (left)). Figure 5.34 shows the experimental set-up for the full readout chain configuration and a photograph of the electronics assembly outside the light-tight box. The back-plane adaptor board is not connected to allow viewing the rear part of the MCP tube and the other boards.
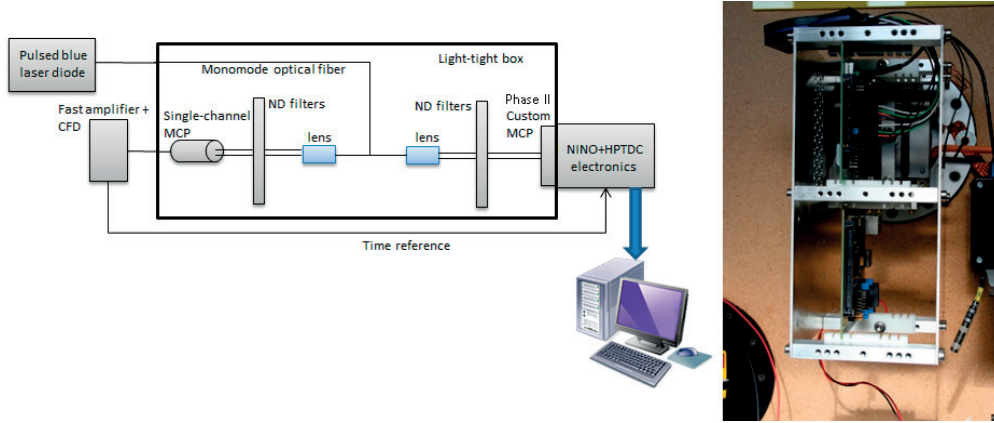
Figure 5.34: Experimental set-up used with the full NINO-HPTDC electronics.

As previously, the laser spot is positioned between the central MCP anode pads in column S1. Each NINO chip covers half of columns S0 and S1 (see Appendix D for details). A hit map at this laser position is reproduced in Figure 5.35 (right). The bottom channel in column S1 corresponds to the reference channel and these data are not used to build this histogram.

5.6.1 INL calibration of the HPTDC chip in HRM (100 ps time bin precision)

The same method as described in Subsection 4.3.1 is used to calculate the INL correction factor in HRM, INL'_j. In this HPTDC operating mode, the 25 ns time interval corresponds to 256 bins with a bin size of ~100 ps. Consequently, the fine time is defined as the bottom 8-bits from the time hits of the leading and trailing edges of the signals measured by the HPTDCs and is in the range 0-255. Figure 5.36 (left) shows the INL curve for a single channel. This distribution corresponds to a pad that collects a large amount of data. The projection onto the
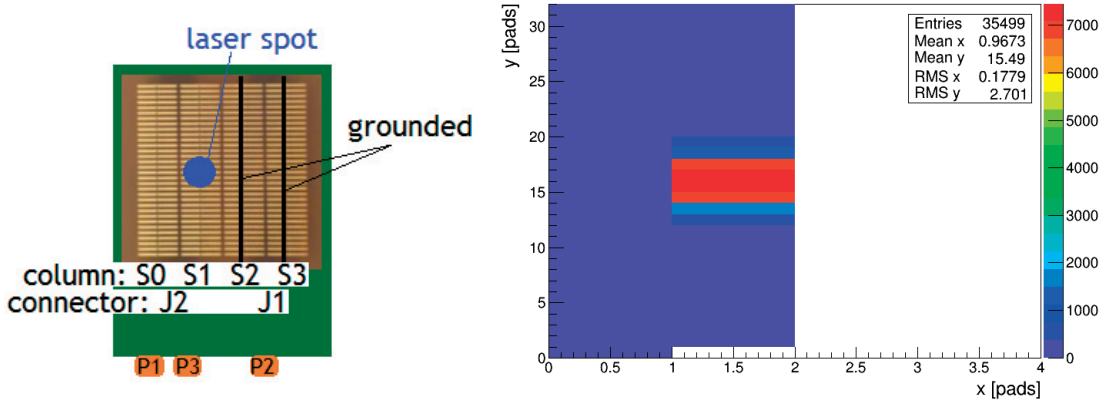
Figure 5.35: Layout of laser spot position (left). Corresponding hit map (right).

vertical axis is shown in Figure 5.36 (right). From the INL'_j values it is seen that the deviation from the ideal bin size is very small. The RMS value is 0.376 time bins which contributes to the time resolution as 37.6 ps if raw data are not corrected for the non-linearity of the HPTDCs.
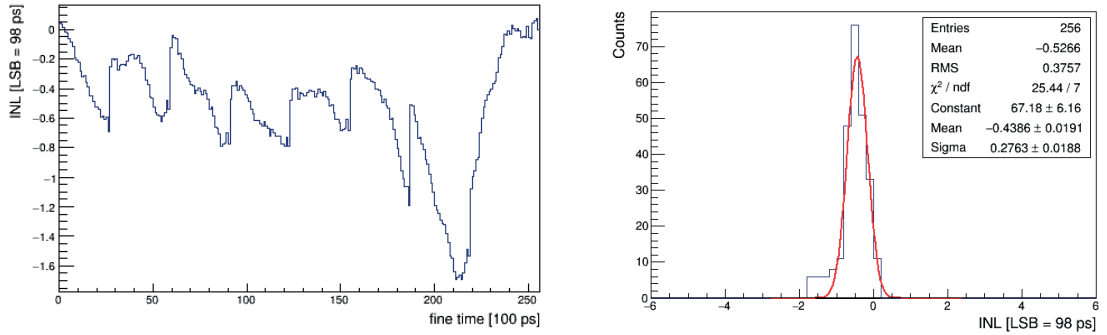
Figure 5.36: INL distribution (left). INL cumulative plot (right).

Raw data from a channel that receives the largest charge is corrected using Equation (4.5). No significant improvement in the time resolution is observed. In addition, there is a difficulty on applying this correction. For the current set-up configuration, all channels do not receive the same amount of charge, some channels more and some others less, and for a given data sample the CDT does not produce a high-statistics DNL histogram for all channels which is essential for a good INL correction. Consequently, it is decided to not apply this calibration at this stage. In Appendix F, 2D histograms of pulse width as a function of the arrival time show the effect of applying the INL correction in channels with low statistics.

5.6.2 Time walk correction

From a data sample recorded when the laser is positioned at the centre of a pad a 2D scatter plot of pulse width as a function of arrival time is built. Since the pad gets most of the photon charge only large signals are detected. The full shape of the 2D histogram is not seen at lower charges hindering the procedure to obtain the time walk calibration curve.

Following this observation, new data are recorded at several laser spot positions along the fine direction in steps of half a pitch of a pad. Moving the laser spot away from the pad will populate the low-charge region for that pad. This laser scan allows to populate the full range of charges in the 2D scatter plot. For a given NINO channel a 2D scatter plot is built by adding all 2D histograms from each laser spot position. This combined 2D histogram is used to generate the calibration curve as already explained in Subsection 4.3.2. Figure 5.37 (left) shows the various laser positions and Figure 5.37 (right) reproduces the resulting 2D scatter plot. The calibration curve is fitted using Equation (4.6) and is superposed on the plot.
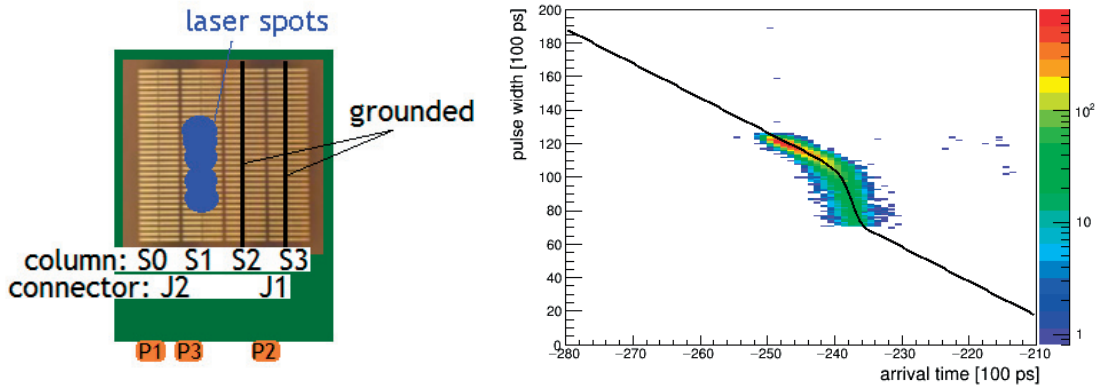
Figure 5.37: Layout of laser spot positions (left). 2D scatter plot of pulse width as a function of arrival time (right). The colour scale is logarithmic. The fitted calibration curve is superposed with the experimental data (black line).

Figure 5.38 (left) displays the time distributions before (blue) and after (red) time walk correction. The time resolution measured on the calibrated channel improves from 100 ps to 80 ps after time walk correction. This calibration curve will be applied to other channels assuming that their response is similar.

A photon cluster is formed by one or more than one channel that are hit by a photon in a given event. The residual time contribution to the leading edge time between hits in a photon cluster after data are corrected for time walk is evaluated as follows. A specific laser spot position, the centre of a channel, is considered. This channel gets the largest charge and consequently should be the earliest hit in the event before any correction. The time residuals, $leading_{res}$, are calculated as the time difference between the leading edge of the hit channel that gets the largest charge, $leading_{ch}$, and that of each hit channel that collects part of the photon charge

in the same cluster, $leading_i$, and is expressed by:

$$leading_{res} = \sum_{i=0}^{channels} (leading_{ch} - leading_i) \tag{5.12}$$

Figure 5.38 (right) illustrates the time residual distributions before (blue) and after (red) time walk correction. The same time walk calibration curve is applied to all channels. The raw distribution (blue) has a main peak centred at zero and two other small peaks for negative values. Peripheral channels that get less charge than the central channel populate the negative part of the distribution. After time walk corrections the time residual distribution dramatically improves. The resulting single peak (red curve) is fitted with a Gaussian. The residual time contribution to the leading edge time between hits in a photon cluster is defined as the standard deviation of the Gaussian and amounts to 115 ps, where non correlated fluctuations dominate.
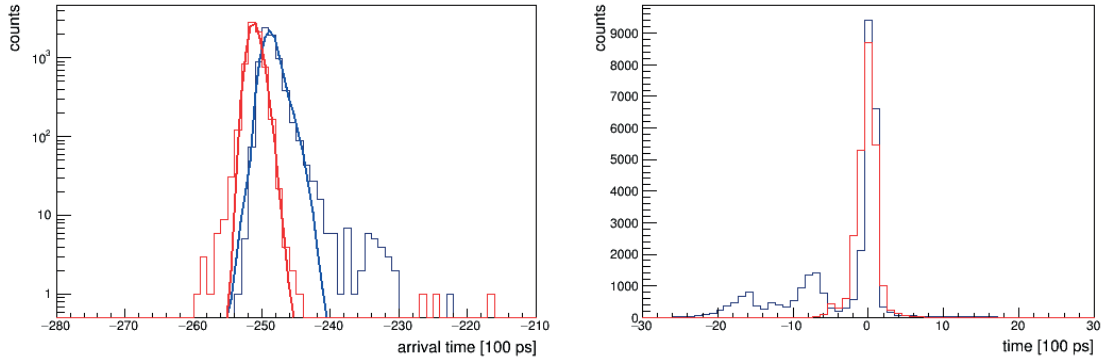
Figure 5.38: Time distributions before (blue) and after (red) time walk corrections (left). Time residuals in a photon cluster before (blue) and after (red) time walk corrections calculated with respect to the pad that gets the largest charge (right).

5.6.3 Electronics detection efficiency

The electronics detection efficiency (EDE) is estimated as follows. An average number of photoelectrons of 0.24 is used, from the value estimated from Poisson statistics and the charge spectra recorded using the analogue board and an oscilloscope (Subsection 5.3.1). Using Equation (4.8) the electronics detection efficiency is estimated to be 88%.

In order to further validate this hypothesis of $\mu=0.24$, the ratio between the counts detected by a NINO channel, c_{NINO}, and the number of sent triggers, $c_{triggers}$, is calculated using the following equation:

$$\frac{c_{NINO}}{c_{triggers}} = 1 - P'(0) \tag{5.13}$$

A set of measurements at different overall MCP voltages and at a NINO threshold setting

of 100 mV is performed. The ratio 1-P'(0) is calculated for each operating voltage and is reproduced in Figure 5.39.
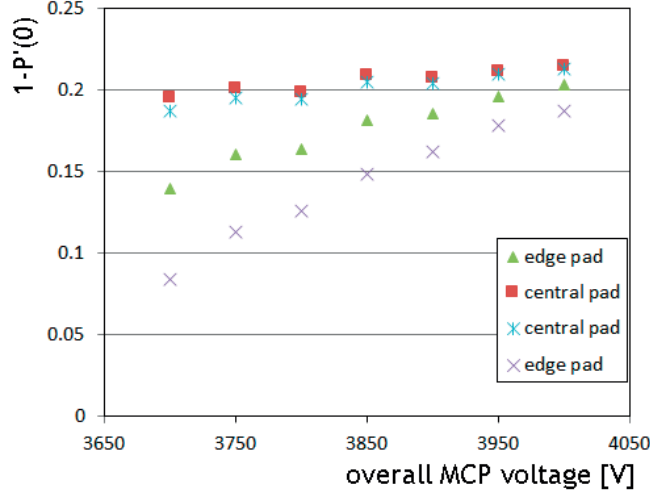
Figure 5.39: Normalized count rate, 1-P'(0), as a function of the overall MCP voltage for the four pads that collect part of the photon charge.

As the voltage increases, 1-P'(0) should asymptotically reach 1-P(0). At +3800 V, the efficiency is:

$$EDE = \frac{1 - P'(0)}{1 - P(0)} = \frac{0.182}{1 - P(0)} = 88\% \tag{5.14}$$

then, μ=0.23 resulting in a 4% error. Figure 5.39 shows the values of 1-P'(0) for the four channels that get charge and the values reach asymptotically 0.22.

5.6.4 Charge, MCP gain and electronics detection efficiency for single photoelectrons

The charge and the MCP gain have been estimated using the analogue board in Section 5.3. Using the TORCH electronics the charge, Q, collected on each pad is measured by the NINOs through the TOT and the resulting output pulse width, w, is input in the following equation:

$$Q = \frac{a \times d + w - b + \sqrt{(b - a \times d - w)^2 - 4a \times (-b \times d - c + d \times w)}}{2a} \tag{5.15}$$

which corresponds to the inverse function of Equation (5.8) from the charge-to-width calibration described in Subsection 5.4.5. Each NINO channel should use its specific charge-to-width calibration curve.

Figure 5.40 (left) illustrates the pulse width distributions of the four central channels in column S1. The pulse width is expressed in HPTDC time bins of 100 ps, resulting in 6 to 14 ns-long
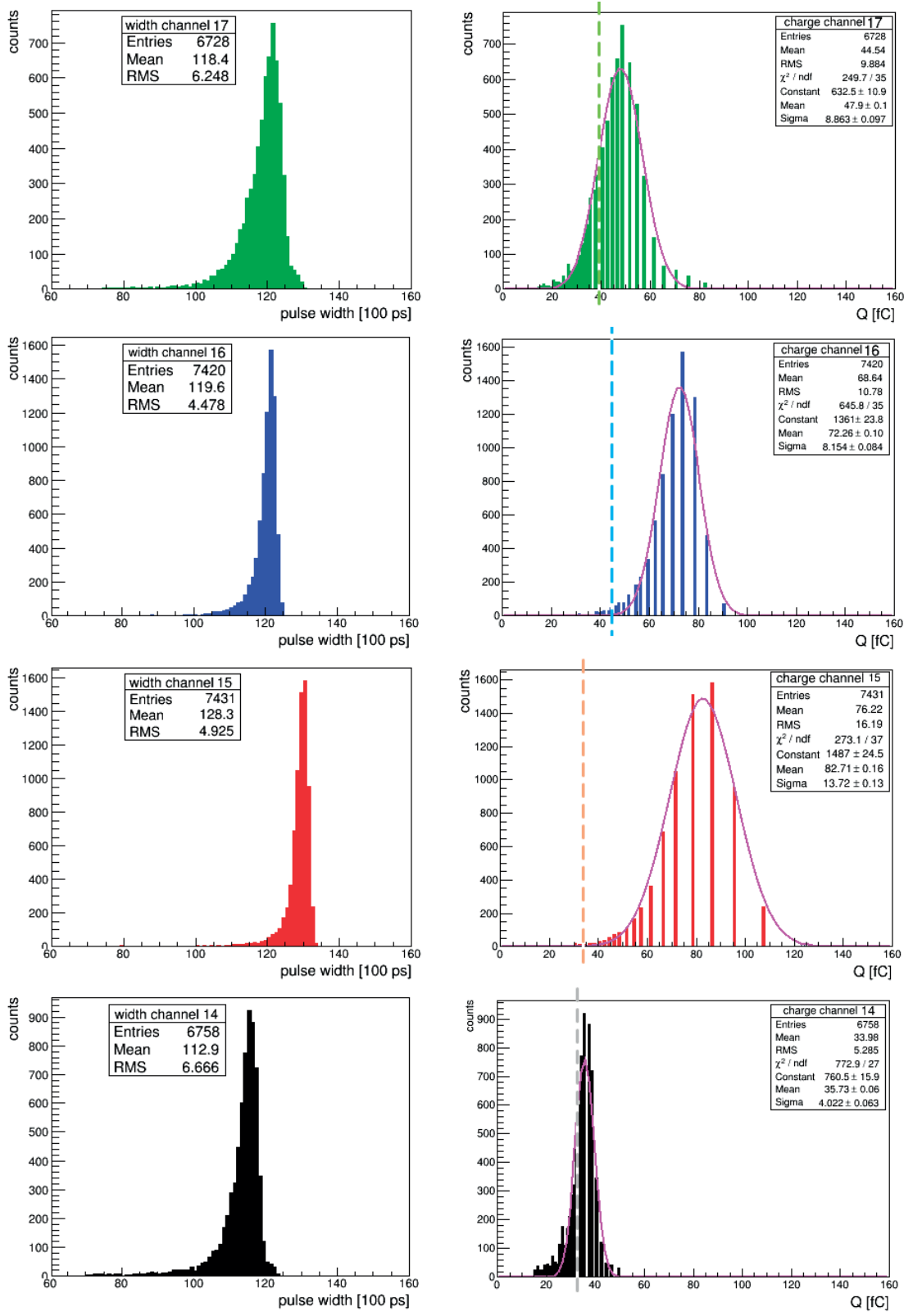
Figure 5.40: Pulse width distributions of four pads (left). Corresponding charge distributions of four pads and the corresponding NINO threshold cut (right).

NINO pulses at a threshold setting of 100 mV. Plots are displayed following the channel physical position at the centre of column S1: blue and red distributions correspond to the central channels and green and black to the adjacent channels. The corresponding charge distributions are illustrated in Figure 5.40 (right). Since the pulse width values are expressed in integer numbers of 100 ps bins the resulting charge distributions are discrete.

From these charge distributions the MCP gain is estimated and is found to be 1.5×10^6 which is consistent with that measured using the analogue board and the oscilloscope. Figure 5.41 shows the charge collected on four channels as a function of laser spot position. The colour of each data set at 0 mm corresponds to a width and charge distributions in Figure 5.40. Dashed lines indicate the area of the four pads, each of 0.828 mm size in the fine direction. Charge-sharing is visible. The centre position of each channel is -1.2 mm, -0.4 mm, 0.4 mm and 1.2 for line colors green, blue, red and black, respectively. The asymmetry of the curves is attributed to the channel efficiency (see Table 5.3).
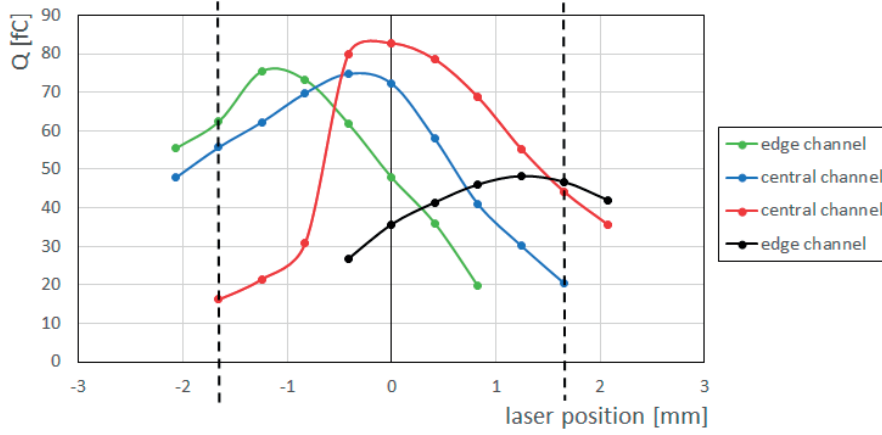
Figure 5.41: Individual channel charge as a function of laser spot position across 4 channels.

The single channel efficiency is also estimated. Using the NINO threshold values in amount of charge from Table 5.2 at a setting of 100 mV, a cut on the charge distributions in Figure 5.40 (right) is applied. Dashed lines correspond to the threshold value for each channel. The single channel efficiency values are tabulated in Table 5.3. Despite of the threshold on channel 14 of NINO chip 2 is the smallest value between the four channels, channel 14 is less efficient. The photon *cluster* efficiency is essentially 100%.

Table 5.3: Single channel efficiency values estimated from the charge distributions in Figure 5.40 (right) by applying the corresponding NINO threshold cut.

	channel 17	channel 16	channel 15	channel 14
NINO Threshold [fC]	39.5	44.8	34.7	32.9
single channel efficiency [%]	82.8	99.9	99.9	75.9

5.6.5 Spatial resolution

The photon position, y_c, is calculated using a centroid algorithm. For each photon cluster in an event, each hit position is weighted by the charge of that hit, q_i, as:

$$y_c = \frac{\sum_{i=0}^{channels} y_i \times q_i}{\sum_{i=0}^{channels} q_i} \qquad (5.16)$$

Figure 5.42 shows the centroid photon position (left) in units of channels for a laser spot position midway between channels 15 and 16, using the charge information, and the position residuals, y_{res_i}, (right) calculated as the difference between the centroid position and that of each hit in a cluster as given by:

$$y_{res_i} = y_c - y_i \qquad (5.17)$$

The standard deviation of a Gaussian fit of Figure 5.42 (left) gives the spatial resolution and amounts to 0.0248±0.0003 mm. This value is better than the resolution required by TORCH of 0.4 mm/$\sqrt{12}$=0.12 mm. Note that this spatial resolution is achieved at rather high gain of 1.6×10^6 electrons. The large peaks in Figure 5.42 (right) correspond to events when all four channels collected charge above threshold allowing a full centroid position calculation, and they are consistent with the physical position of each channel. The small continuous background is explained by events where q_i is not above threshold for all four channels. As expected, the spatial resolution at the channel boundary is improved when using the charge information rather than the pulse width (Figure 5.43).
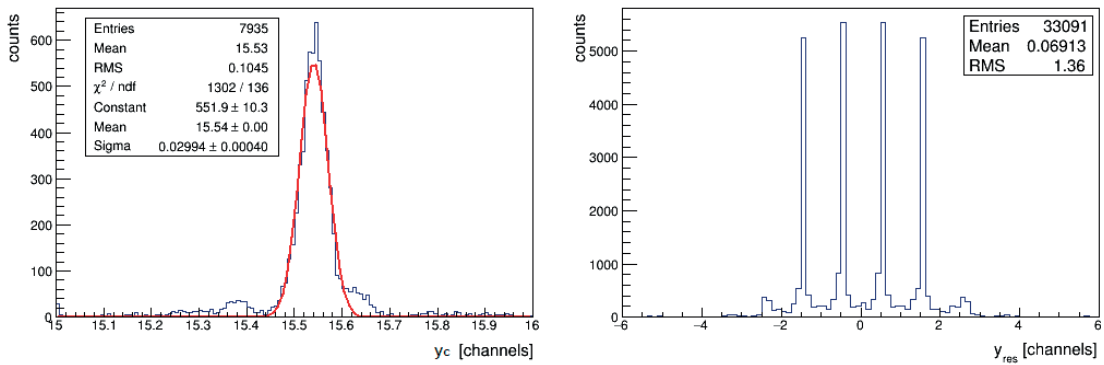
Figure 5.42: Centroid position of photon cluster using the charge information (left). Hit position residuals calculated with respect to the centroid position of the photon cluster (right).
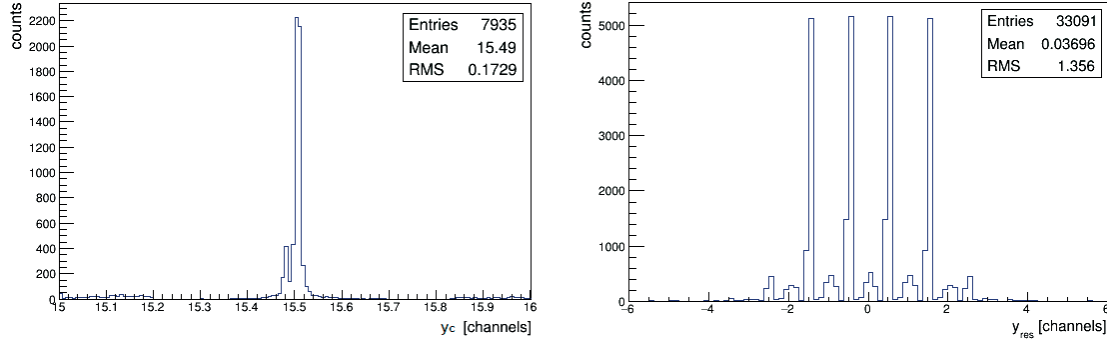
Figure 5.43: Centroid position of photon cluster using the pulse width information (left). Hit position residuals calculated with respect to the centroid position of the photon cluster (right).

5.6.6   Summary

The timing performance of custom-made MCP prototypes for TORCH is assessed with customized 32-channel NINO-HPTDC electronics. The resulting time resolution is 80 ps. The correction for non-linearity of the HPTDCs is not applied to the raw data. The INL calibration in HRM will need further investigation in the laboratory and is not included in this thesis. A possible protocol configuration would consider the illumination of the full active surface of the MCP prototype tube and record a high-statistics data sample. This will allow to obtain a INL calibration curve for all channels.

The time walk calibration of the NINOs is performed on a single channel and used to correct all other channels, assuming they have similar response. Charge-to-width calibration is performed on four channels, an odd and an even of each NINO chip. The threshold for each channel type is applied separately. The calibrations are applied to each type of channel assuming all odd and even channels on each chip behave similarly to the calibrated channels. Ideally, each NINO channel should be calibrated individually. Further study in the laboratory with an automatized set-up to perform these calibrations on all channels will also need to be investigated.

The obtained spatial resolution on the measurement of the photon cluster position includes contributions from the Phase II MCP-PMT prototype tube and the readout electronics. This spatial measurement in TORCH is important for the photon path reconstruction. The spatial resolution contributes to the error on the measurement of the photon propagation angle in the quartz.

Figure 5.44 shows the photon hit map and the centroid position for a laser spot position a few channels away from the central part of column S1. This effect is similarly seen if the laser is positioned in the mirrored bottom part of column S1. The required resolution for TORCH is also achieved when fitting the main peak with a single Gaussian.

There is still no clear understanding of these asymmetric spatial distributions that depend on
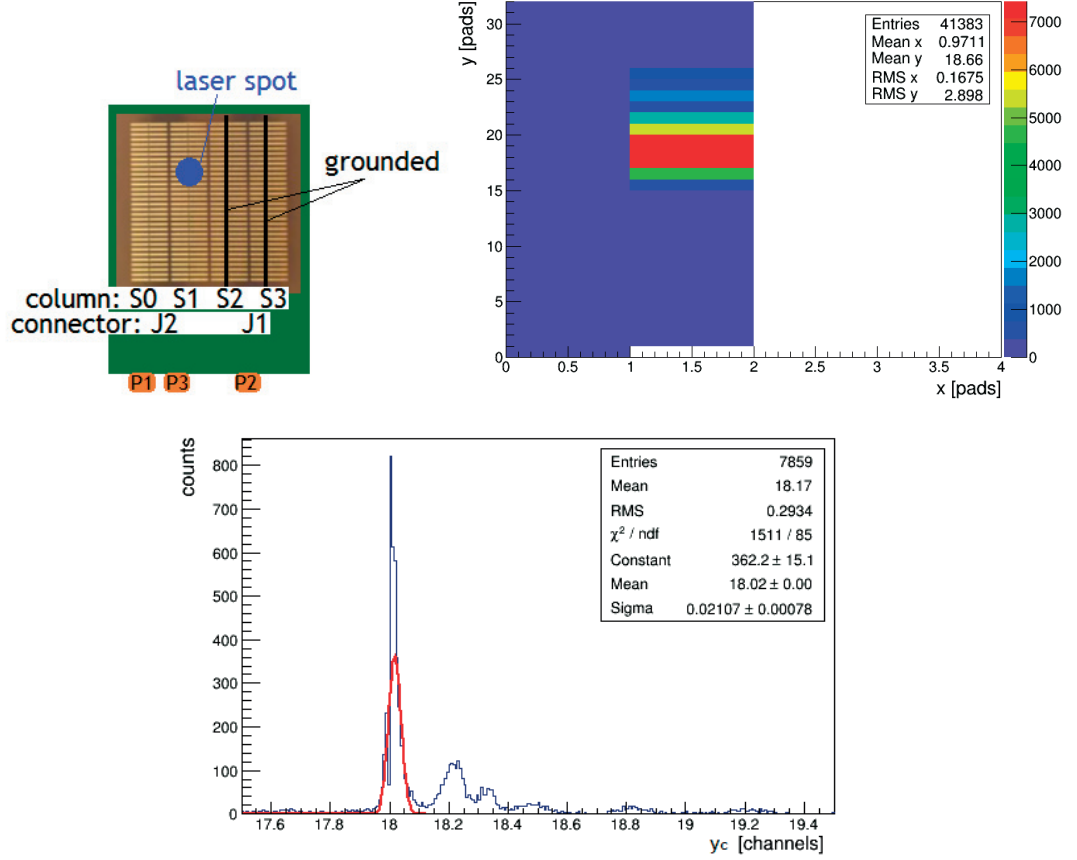
Figure 5.44: Laser spot position (top left). Associated photon hit map (top right). Centroid position of photon cluster resulting in an asymmetric distribution (bottom).

where the laser is positioned along the fine anode direction of the Phase II MCP-PMT tube. This asymmetry can possibly originate from:

- Phase II MCP-PMT prototype

- ACF coupling of MCP-PMT anode with interface PCB

- Crosstalk in the interface PCB

- NINO chip behaviour

- Crosstalk in TORCH electronics

6 Optical studies

A small-scale TORCH prototype module has been built (Figure 6.1 (left)). The quartz radiator plate consists of a rectangular piece of dimensions $10 \times 120 \times 350$ mm^3 with a wedge at the top end which simplifies the focusing block design and manufacturing and reduces the difficulties in the polishing. The focusing block with the cylindrical mirror, at the periphery of the radiator plate, has been designed to be coupled to two 2-inch square MCP photon detectors. Both optical components have been manufactured by Schott Switzerland[1]. Figure 6.1 (right) shows a photograph of the optical components mounted on a dedicated mechanical structure.
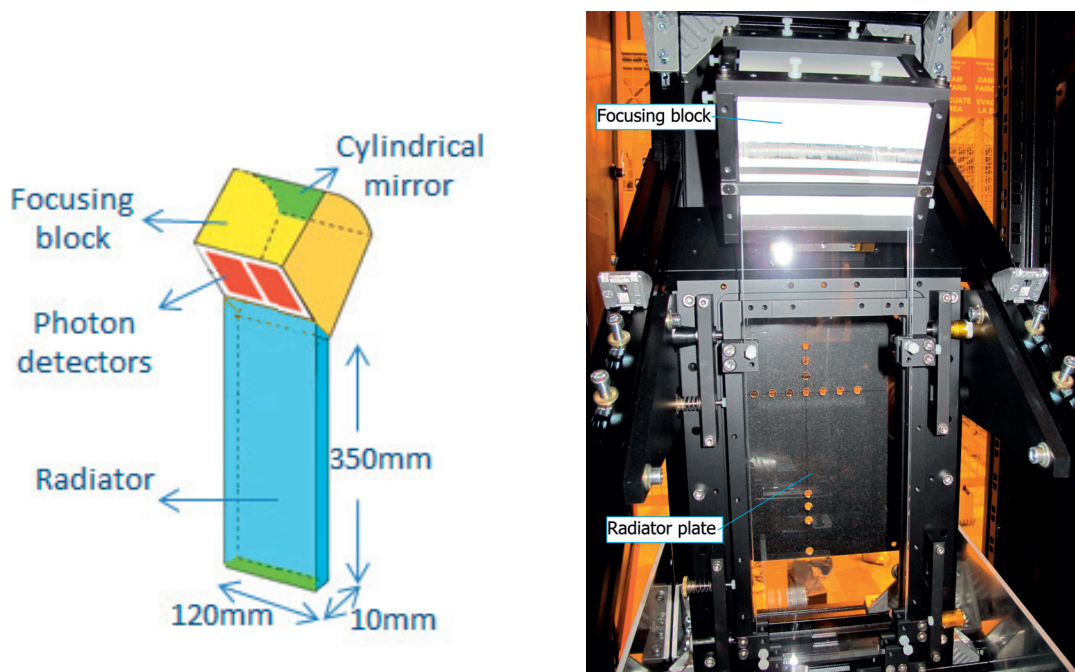
Figure 6.1: Drawing (left) and photograph (right) of the small-scale TORCH prototype module.

---

[1]SCHOTT Suisse SA, Yverdon-les-Bains, Switzerland. http://www.schott.com

6.1 Investigation of light transmission and scattering losses

A suitable gluing material between the optical elements of the TORCH prototype is required since the optical transmission of the glue and its photon energy cut off will have a significant impact on the number of detected Cherenkov photons and the TORCH performance.

This section covers the studies of the light transmission and scattering losses through various glass and glue samples. The aim of these measurements is to find a glue with optimal transmission in the UV region, since most of the Cherenkov photons are emitted in the UV (See Figure 1.6).

A dedicated set-up has been prepared for these tests (Figure 6.2). The light source is a continuous wave (cw) laser diode[2] emitting at 640 nm. Laser light is transported in a monomode fibre. A 12-bits charge coupled device (CCD) camera[3] controlled via a PC is mounted on an optical bench. The CCD parameters are adjusted in combination with ND filters to avoid light saturation.
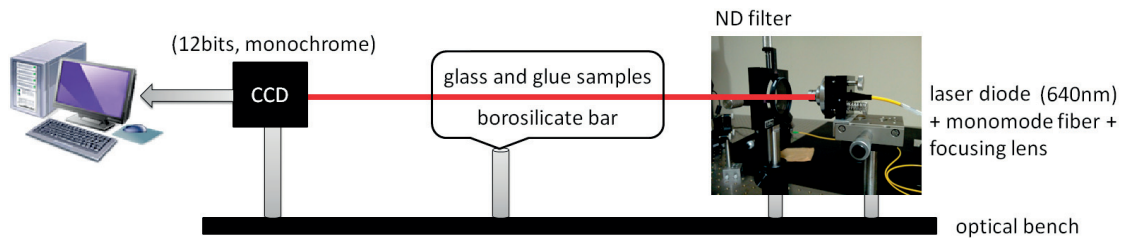
Figure 6.2: Set-up used for the systematic tests of light transmission through glass and glue samples.

6.1.1 Characterization of laser beam

A collimated laser beam has been characterized in terms of spot intensity and diameter. The beam profile is studied at various positions. For each position a raw image of the spot is recorded with the CCD camera and registered in the control PC. The image is converted into a portable pixmap (ppm) format for off-line analysis. A ROOT [112] script originally developed for analyses of light transmission through aerogel [29] has been adapted to analyse these ppm images.

Background calibration

A first approach for background subtraction is to use a small region in a non-illuminated area of the laser spot image and estimate the average background. However, it was observed that the background is non-uniform over the full CCD pixel surface.

---

[2]Laser diode model ZFSM Fibre from Z-Laser Optoelektronik GmbH, Freiburg, Germany.
[3]CCD camera model acA1600-20μm/uc from Basler AG, Ahrensburg, Germany.

Following this observation, a *dark* measurement without laser light is performed to calibrate the background level. Several dark raw images are recorded and show similar spectra. Along the horizontal axis, the intensity level varies. Figure 6.3 (left) shows a pixel map of a dark image illustrating the non-uniformity over the CCD surface and Figure 6.3 (right) shows the corresponding pixel intensity distribution. Figure 6.4 (left) illustrates an intensity profile of a laser spot image which also shows the background non-uniformity. This image is built using ImageJ software[4] and selecting an intensity range 0-1000 for the vertical axis. Figure 6.4 (right) shows the corresponding pixel intensity distribution. The background level depends on the gain of the CCD, a larger amplification factor results in a larger background level. This level does not depend on the CCD exposure time. For every measurement, a dark image is subtracted from each laser spot image.
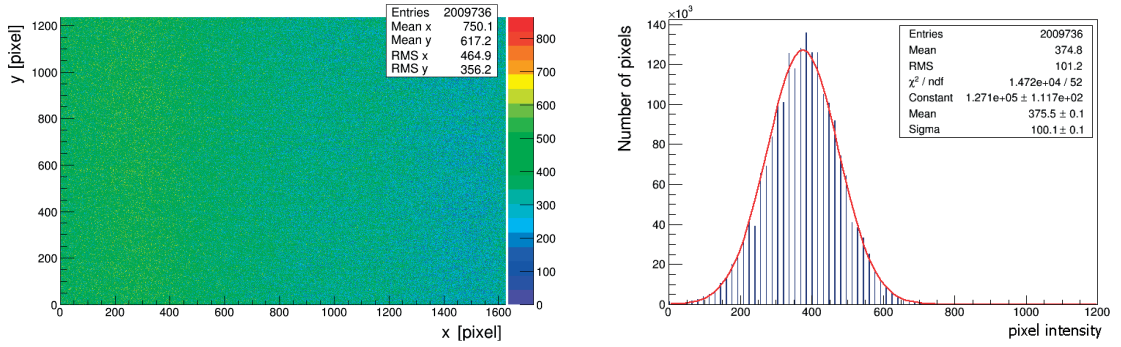
Figure 6.3: Pixel map of a dark image (left). Pixel intensity levels for a dark image (right).
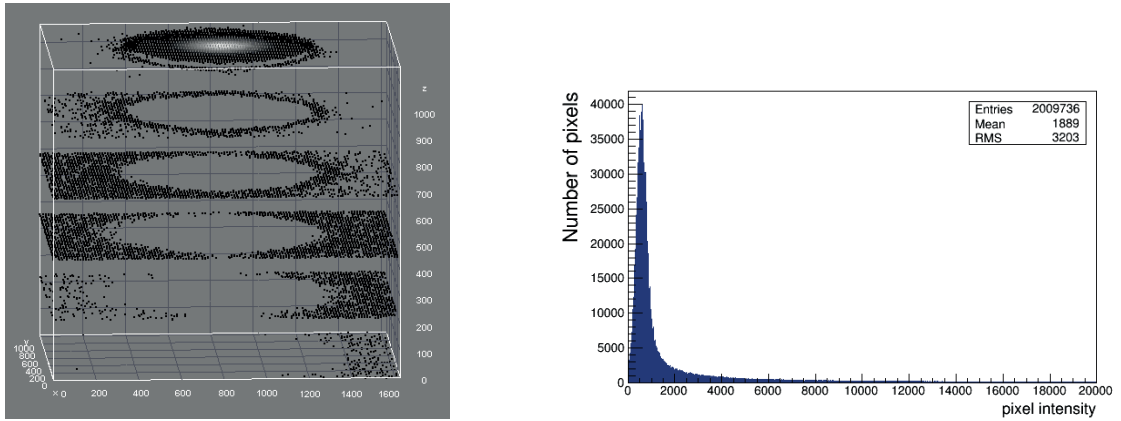
Figure 6.4: Intensity profile of a laser spot image. The various slices correspond to the number of pixels at a given intensity (left). Pixel intensity levels for a laser spot image (right).

---

[4]https://imagej.nih.gov/ij/

Procedure to determine centre of gravity and D_0 of laser spot

After background subtraction, the centre of gravity (COG) coordinates from the laser spot image is calculated by using each pixel coordinate (i,j) and its intensity level, $l_{i,j}$:

$$x_{COG} = \frac{\sum\limits_{i=0}^{x_w-1} \sum\limits_{j=0}^{y_w-1} i \times l_{i,j}}{\sum\limits_{i=0}^{x_w-1} \sum\limits_{j=0}^{y_w-1} l_{i,j}} \qquad\qquad y_{COG} = \frac{\sum\limits_{i=0}^{x_w-1} \sum\limits_{j=0}^{y_w-1} j \times l_{i,j}}{\sum\limits_{i=0}^{x_w-1} \sum\limits_{j=0}^{y_w-1} l_{i,j}} \qquad\qquad (6.1)$$

where x_w and y_w are the CCD dimensions in pixel units of size 4.4 μm along the x and y axes, respectively.

From the COG position, the intensity integral as the radial distance increases is compared to the total image intensity. A diameter D_0 is defined as to contain 95% of the total image intensity [113] and is calculated as:

$$D_0 = 2 \times R_0 \times 4.4\mu m \qquad\qquad (6.2)$$

where R_0 is the radius at 95% in pixel units. Figure 6.5 (left) shows the normalized light intensity as a function of radial distance in pixel units. Figure 6.5 (right) shows the processed laser spot image after background subtraction with its COG and D_0 determined. The COG position is indicated with a black marker and the region containing 95% of the total intensity is delimited by the pink coloured circle.
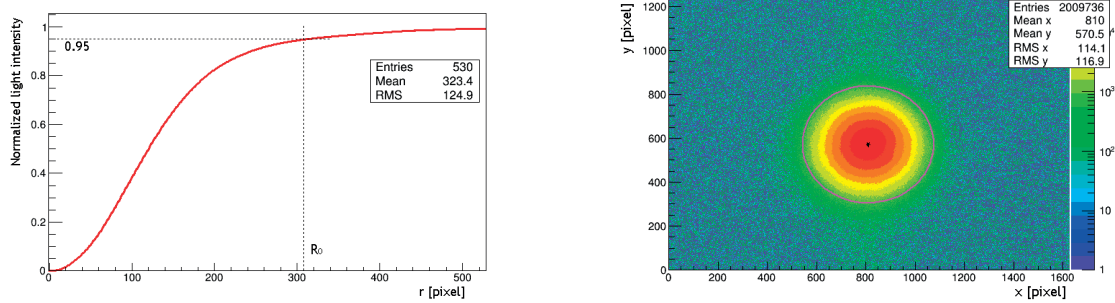
Figure 6.5: Intensity integral normalized to the total image intensity as a function of radial distance from the COG (right). The dashed line indicates the R_0 corresponding to 95% intensity. Laser spot image after background subtraction (left). COG is represented by the black marker and the pink circle has radius R_0.

Laser beam profile

With the knowledge of the COG position, the absolute intensity and D_0, the laser beam profile along the beam path can be parameterized. Figure 6.6 reproduces the projection of the D_0 in

pixel units on the x-axis as a function of the distance to the CCD camera in mm. The color scale corresponds to the pixel density inside D_0 on the y-axis. The variation of D_0 over a light path of ~1 m is 2.8%. The beam divergence is the angular measure of the increase in radius with distance from the optical aperture as the beam emerges and is found to be $2\times(0.07\pm0.01)$ °.

Once it has been determined that the laser beam is as parallel as possible in the direction of the light propagation, the laser is set to a reference position, 900 mm, where the smallest D_0 is measured and an image is acquired. For this reference measurement the COG_{ref}, the intensity I_{ref} and $D_{0\,ref}$ are calculated as previously described.
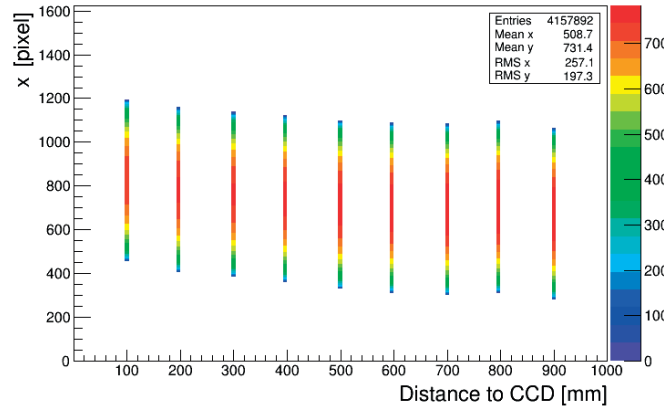
Figure 6.6: D_0 in pixel units as a function of laser distance to the CCD in mm.

Laser intensity stability tests

For the optical measurements described in next Subsection a laser intensity and D_0 stability is required. At the reference laser position, the laser intensity is monitored with a power metre for two hours. Figure 6.7 (left) shows the laser power as a function of time. Data fluctuation is found to be 1%. The laser stability is also monitored with the CCD camera. An image is recorded every 5 s. The total intensity in the image is calculated. The background is then subtracted and the actual total intensity is determined.

Figure 6.7 (right) shows the total intensity of a laser spot image before and after background subtraction. The fluctuation using this procedure is found to be 0.8% and the variation of D_0 is 0.5%. This measurement with the CCD also shows that the background corresponds to 14% of the total intensity from the raw image and if not subtracted can affect the determination of the COG and D_0.

6.1.2 Glass and optical glue samples

The optical quality of various glass and glue samples has been investigated [87]. The holding structure for the samples is installed in a rotary stage. Light transmission through single glass
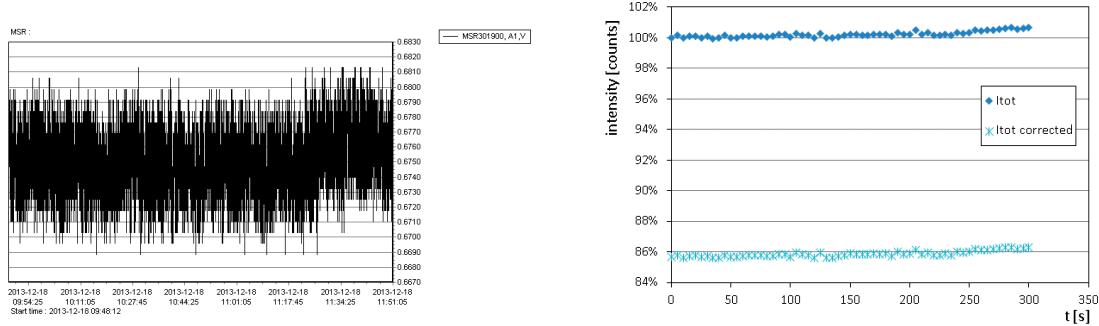
Figure 6.7: Laser intensity monitoring with the power metre (left) and with the CCD camera (right).

samples[5] and scattering effects have been studied. The results are compared with those where two glass samples are glued with various epoxy glues, EPO-TEK 305 and EPO-TEK 301-2, of different thicknesses. These epoxy glues are two-component materials [114, 115]. Figure 6.8 shows the photographs of the set-up configuration for a single glass sample (left) and a glued sample (right).
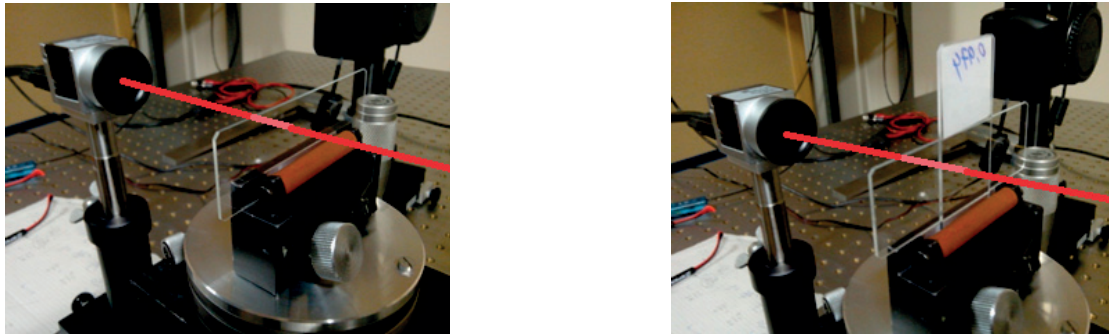
Figure 6.8: Photograph of set-up configuration for the light transmission studies through a single glass (left) and a glued glass sample (right).

Bubbles surface-ratio

To study the impact of a small air gap in a glued glass sample, bubbles were artificially created in the glue. An image taken with a microscope (Figure 6.9 (left)) is processed and a threshold in the intensity level of 215 is applied to the pixel intensity levels which are in the range 0-255. This threshold value was chosen to select the maximum number of pixels in the bubbles without considering pixels from other regions as bubbles. The areas with air bubbles, $l_{i,j}$>215, are set to zero and the pixels in other regions, $l_{i,j}$<215, to 255 (Figure 6.9 (right)). The bubbles

---

[5]Microscope slides from Thermo Scientific: http://www.thermoscientific.com/en/products/microscope-slides-specialty-glass.html.

surface-ratio, b_{s-r}, is determined as:

$$b_{s-r} = \frac{n_b}{n_{CCD}} \qquad (6.3)$$

where n_b is the number of pixels at zero intensity level and n_{CCD} is the total number of pixels in the CCD. For this sample at the given threshold of 215, b_{s-r} is found to be 21%.
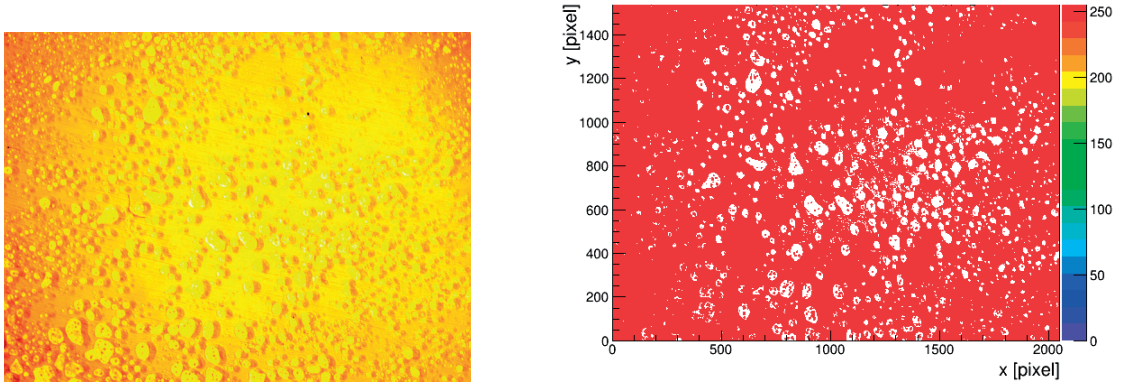
Figure 6.9: Microscope image of a glued glass sample with high bubble density (left). Processed image for a threshold cut in pixel intensity level (right).

Light transmission as a function of angle of incidence

The dependence of the transmission on the angle of incidence is shown in Figure 6.10. Fresnel equations [105] are used to describe experimental data and the effect of different interfaces; air-glass-glue-bubbles-glue-glass-air. As expected, no bulk absorption is observed at a wavelength of 640 nm. The theoretical transmittance, T=1-R, for non-polarized light through a single interface is calculated using Equations (G.1) and (G.4) at normal incidence and at $\theta \neq 0$, respectively.

The transmitted intensity at normal incidence for a single glass and glued glass sample is 90-92%. For all samples the light transmission is in agreement with that expected from Fresnel equations. When varying the angle of incidence from 0 to 50 ° the intensity loss for single glass is 4% and for all EPO-TEK 305 samples with different glue thickness and EPO-TEK 301-2 25 μm the intensity loss is 3%. The intensity loss in glued samples with respect to the single glass is 1-2%. Using Fresnel equations this loss corresponds to a 25% bubble density. In this case bubbles are not visible by eye but samples can contain micro-bubbles. In the case of the sample EPO-TEK 301-2 25 μm with bubbles, the intensity loss at normal incidence is ~15% corresponding to a bubble density of ~90%. The intensity loss depends on the bubble-surface ratio. A 100% bubble density is equivalent to a continuous and uniform air gap between the two glass samples. The intensity loss when varying the angle of incidence from 0 to 50 ° is 6%.

In addition to absorption effects, light can be scattered during its propagation through the

glass and the glue, resulting in an increase of the laser spot size. The difference in spot size before and after the sample determines the amount of scattered light. A spot diameter through a single glass sample of 2.39 mm was measured and was identical to that measured through a glued glass sample. Consequently, no measurable scattering effect was identified by using this method. However, for the sample EPO-TEK 302-1 25 μm with bubbles $D_{0\,bubbles}$ is 110%$D_{0\,ref}$ with an intensity loss of 6% with respect that from a single and other glued samples.
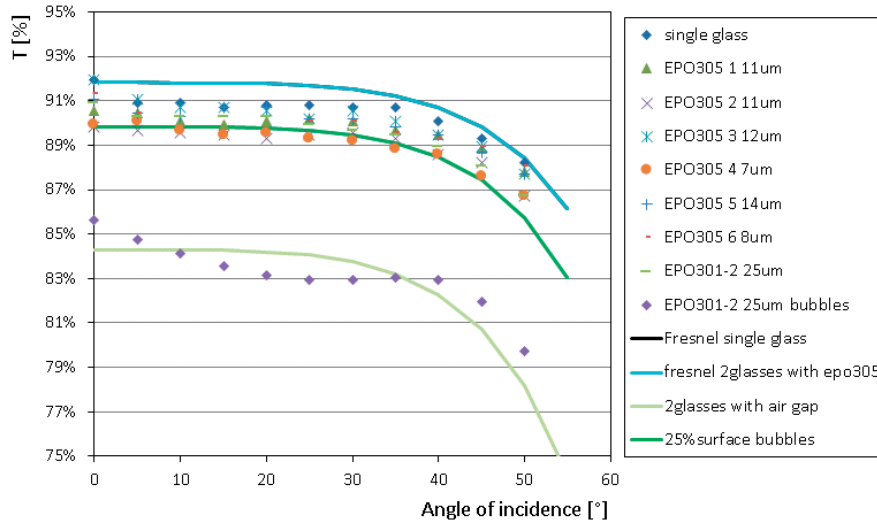
Figure 6.10: Transmission curves as a function of angle of incidence for various epoxy glued samples. The blue line corresponds to the expected values from Fresnel equations for a two glasses perfectly glued with EPO-TEK 305.

Light transmission as a function of wavelength

New square samples made of quartz (Spectrosil) were prepared with the same epoxy glues of 38 μm and 46 μm thicknesses for EPO-TEK 301-2 and EPO-TEK 305, respectively. Other glues have also been tested, in particular a two-component optical silicone, PACTAN 8030. Light transmission through the quartz and the glued samples was measured with a spectrophotometer[6] as a function of photon wavelength in the range 200-800 nm. Figure 6.11 reproduces the transmission curves for a single quartz specimen and various glued samples. EPO-TEK 305 shows better transmission in the UV region than EPO-TEK 301-2. PACTAN 8030 transmits even more in the UV, which makes it suitable for the TORCH detector.

Following these investigations, a 50 μm thickness of PACTAN 8030 was chosen for the coupling of the quartz radiator and focusing block. This silicone can be easily removed and after cleaning the quartz surfaces the light transmission measured with the spectrophotometer was 86% at 200 nm. The transmission for Spectrosil quartz before and after cleaning is shown in

---

[6]LAMBDA 650 UV/Vis Spectrophotometer from Perkin Elmer: http://www.perkinelmer.com/product/lambda-650-uv-vis-spectrophotometer-l650.

the inset of Figure 6.11.
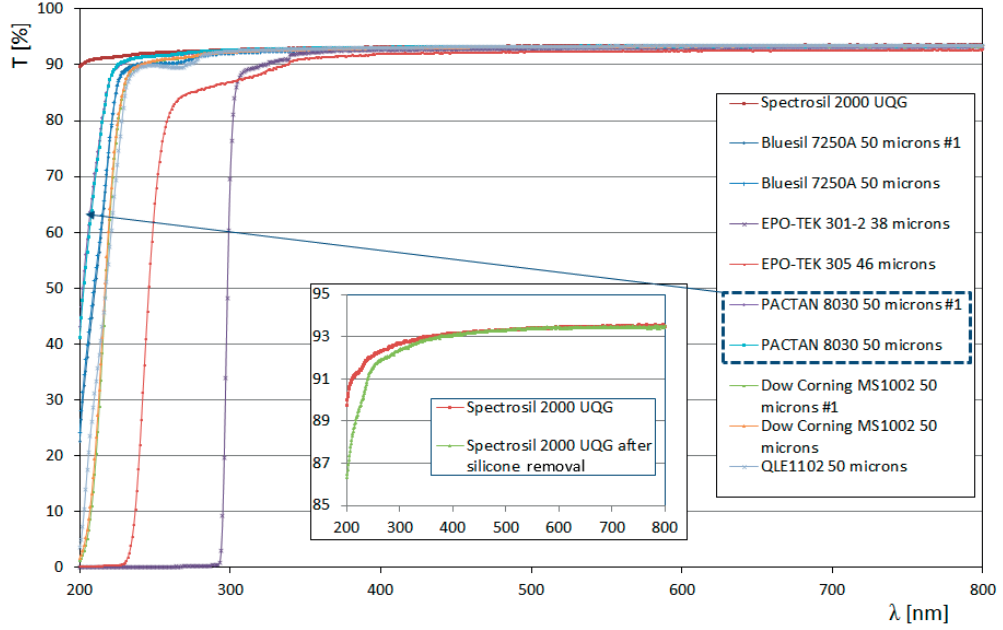
Figure 6.11: Transmission for Spectrosil quartz sample and different glues as a function of photon wavelength. Transmission for Spectrosil quartz before and after cleaning the sample when removing the silicone (inset).

6.2 TORCH optics simulation

This section covers simulation studies of the optical components of the small-scale TORCH prototype module using the Optica module from the Mathematica software [104]. The design parameters of the focusing block are used. The first modelled element is the cylindrical mirror which is designed as a cylindrical surface with the following coordinate:

$$x_m = r_m \cos\varphi \qquad y_m = l_m \qquad z_m = r_m \sin\varphi \qquad (6.4)$$

where r_m is the mirror radius, l_m is the mirror length and φ is the angular coordinate. All other components will be positioned with respect to the position of the mirror centre of curvature, c_m. The focusing block and the radiator are modelled. The focusing block surfaces can be chosen as reflective or non-reflective.

6.2.1 Focal plane studies

The focusing optics has been designed to couple perfectly to a 2 mm-thick MCP optical quartz window (i.e. with no air gap). The design is chosen to focus at the MCP photocathode deposited on the inside surface of the MCP quartz window. In the simulation the focal plane consists of a rectangular surface with its centre position coordinates (84.4744, 0, 107.7920)

137
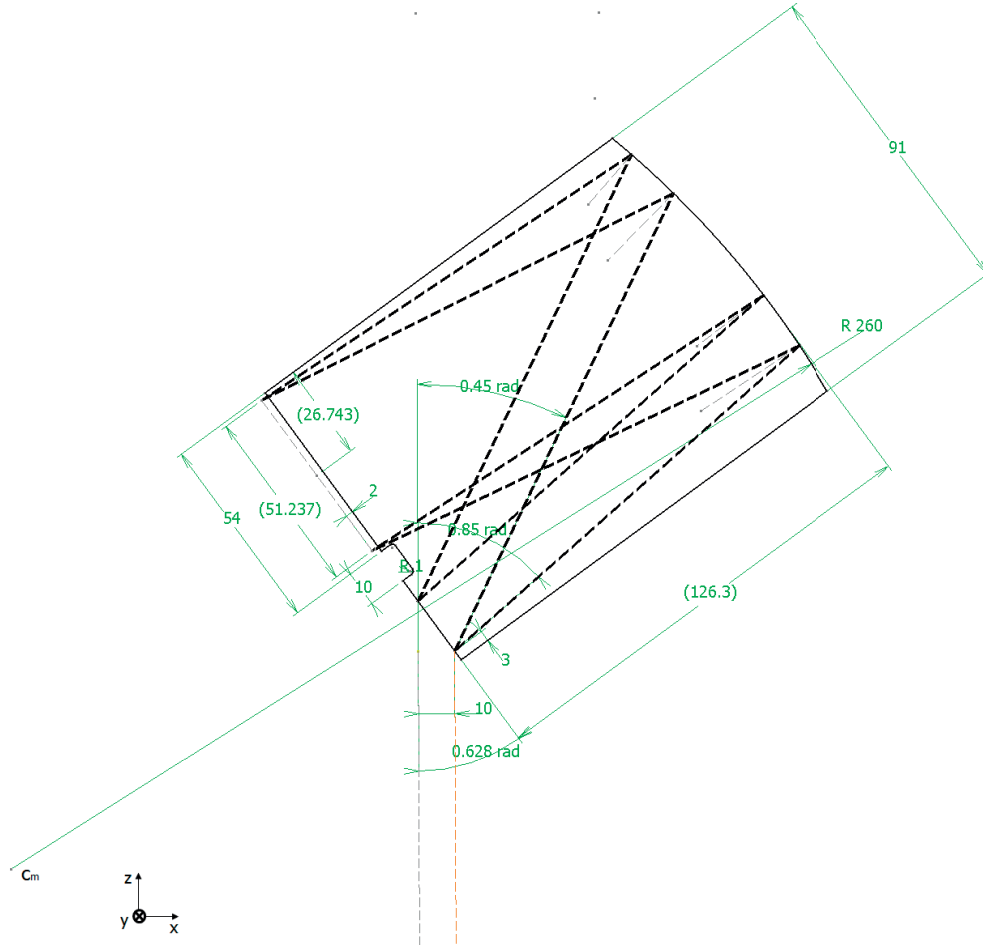
Figure 6.12: Drawing of the TORCH focusing block with design parameters provided by C. Frei.

in mm and rotated 36 ° with respect to the y-axis. Figure 6.13 (left) shows a side view of the simulated TORCH optics.

The focusing properties are studied by considering photons of λ=420 nm propagating only through the focusing block and reflected off the cylindrical mirror. Single rays are emitted at various θ_z angles in the range 0.45-0.85 rad and at different positions along the radiator wedge thickness. The spatial spread of the photons, σ_y, in the y_f direction at the focal plane is found to be 0.06 mm for θ_z values 0.45 rad and 0.85 rad, and 0.11 mm for 0.65 rad.

For each θ_z angle a focal point coordinate is defined. Figure 6.13 (right) shows the resulting focal points. The position of the focal plane is estimated by calculating the average position using the focal points corresponding to θ_z=0.45 rad and 0.85 rad and using all five focal points. Figure 6.13 (right) also shows the coordinates for the estimated positions of the focal plane which are compared with those of the design focal plane. Data are fitted with a second order
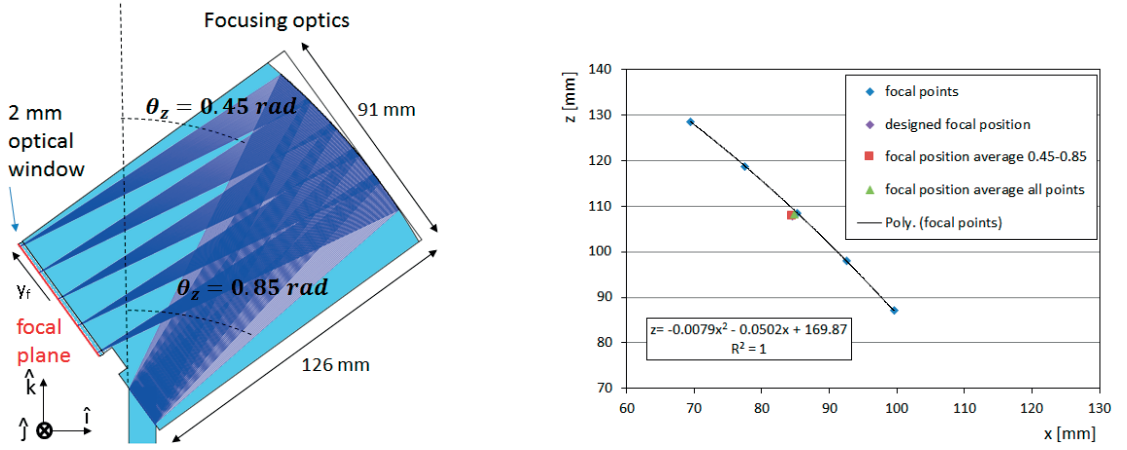
Figure 6.13: Side view of simulated TORCH optics with the design parameters (left). Focal points for each θ_z which define the focal plane surface (right). The design and estimated positions of the focal plane are also plotted.

polynomial function which shows that photons are more spread at θ_z=0.65 rad.

From this simulation the photon position at the focal plane, y_f, can be converted to the angle θ_z at the entrance of the focusing block through the following equation:

$$\theta_z = -0.0078 \times y_f + 0.6527 \qquad (6.5)$$

where y_f is in mm and θ_z in rad. A quadratic term of $-3\times10^{-6} \times y_f^2$ can be added to the linear calibration curve in order to include the aberration effect.

6.2.2 Air gap optimization

Two MCP-PMT photon detectors types will be coupled to the focusing optics; a commercial 32×32 pads Planacon tube with 1 mm-thick sapphire optical window and the Phase II MCP-PMT prototype with 9 mm-thick quartz optical window. The design of the Phase II MCP-PMT allows operating the photocathode at ground potential. In the case of the 32×32 pads Planacon the photocathode is operated at negative high voltage. This makes coupling the MCP-PMT optical window to the TORCH focusing optics more delicate. In order to be safe in terms of discharges an air gap between the focusing optics and the MCP-PMT optical window is preferred.

The optimal MCP-PMT position with respect to the exit surface of the optics has been investigated by looking at the photon spatial spread at the photocathode plane of the photon detectors. Photons are generated at different positions along the radiator plate thickness and focused via the cylindrical mirror at the focal plane. Various air gaps between the exit surface of the focusing block and the input face of the two MCP-PMT optical windows are considered. The model approximates the photocathode surface as a rectangle of dimensions 54×120 mm².

The spatial spread of photons at the photocathode plane as a function of the photon propagation angle in the radiator plate, θ_z, for several air gaps is shown in Figure 6.14 for sapphire (left) and quartz (right) MCP-PMT optical windows. The photon spread is found to be $\sigma_y < 0.12$ mm for the 1 mm-thick sapphire window and $\sigma_y < 0.45$ mm for the 9 mm-thick quartz window. For the sapphire window, the smaller air gaps (0, 0.25 and 0.5 mm) lead to a location of the photocathode plane closer to the exit surface of the focusing optics than the design focal plane. This results in a different response in the same θ_z range.
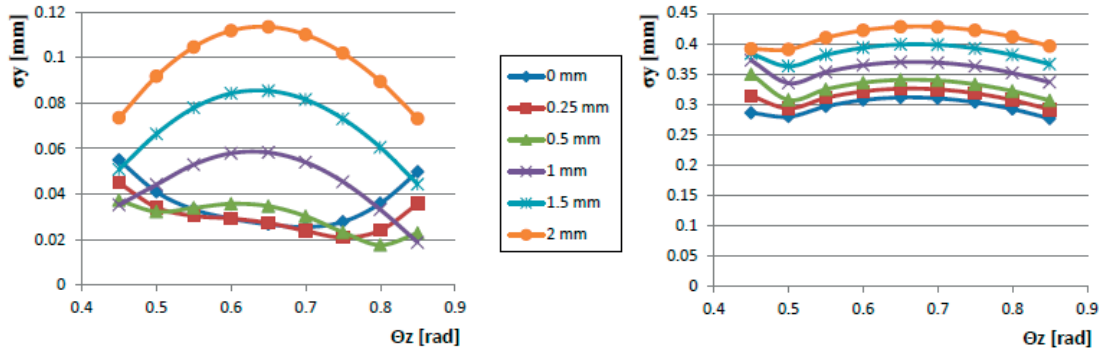
Figure 6.14: Photon spread, σ_y, at the photocathode plane as a function of photon propagation angle, θ_z. The various curves correspond to air gaps between the exit surface of the optics and the input face of the 1 mm-thick sapphire (left) and 9 mm-thick quartz (right) MCP-PMT optical windows. Note the different vertical scales.

Figure 6.15 (left) shows the spatial photon spread at the photocathode plane as a function of air gap thickness for $\theta_z = 0.7$ rad. The optimal position for the sapphire optical window is found to be at 0.25 mm away from the exit of the focusing block. For safety aspects, an air gap of 0.5 mm was chosen.

At this optimal air gap of 0.5 mm, for the quartz window rays are focused via the cylindrical mirror at the focal plane ~1.3 mm inside the optical window. The resulting photon spread at the exit of the optical window in the fine direction is $0.3 < \sigma_y < 0.35$ mm which degrades the spatial precision in the fine direction and therefore the reconstruction of the photon propagation angle.

The calibration curve for the photon position conversion into photon propagation angle for each MCP-PMT optical window is described by the following equations:

$$\theta_{z\,sapphire} = -0.000003\,y_f^2 - 0.007809\,y_f + 0.651332 \tag{6.6}$$

$$\theta_{z\,quartz} = -0.000005\,y_f^2 - 0.007830\,y_f + 0.659141 \tag{6.7}$$

The reconstructed photon propagation angle θ_z(rec) for each optical window is calculated

using the previous equations. The distribution resulting from the difference between the photon angle θ_z(true) and the reconstructed angle for both optical windows is reproduced in Figure 6.15 (right).
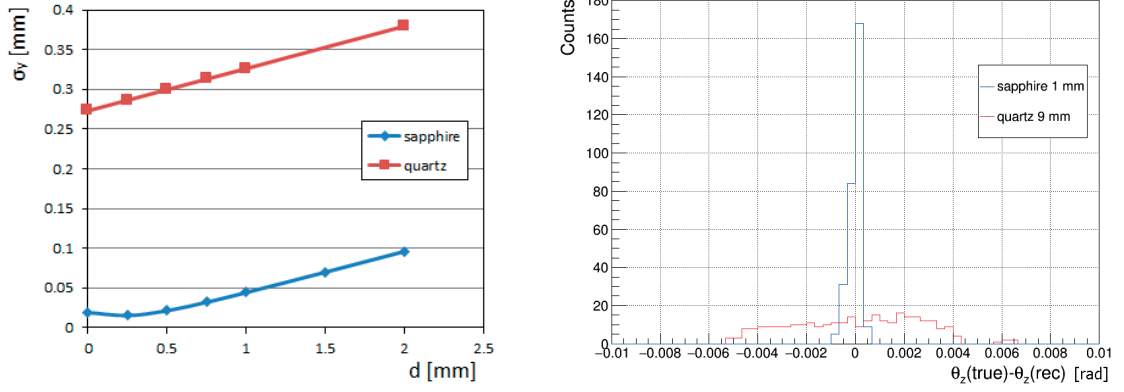
Figure 6.15: Photon spread at the photocathode plane as a function of air gap between the exit surface of the focusing block and the input surface of the MCP-PMT optical window at a fixed θ_z angle 0.7 rad (left). Distribution of the difference between the θ_z(true) and the θ_z(rec) for sapphire and quartz windows (right).

The spatial resolution achieved by the Phase II MCP-PMT and electronics in the laboratory (Subsection 5.6.5) contributes to the precision σ_{θ_z} on the measurement of θ_z as 0.19 mrad. However, the contribution to σ_{θ_z} from a photon spread of 0.35 mm through the optics and optical window is 2.7 mrad. The sum in quadrature of these two values, 2.7 mrad, is to be compared with the 1 mrad precision required for TORCH. The reconstruction of the photon propagation angle is consequently dominated by the optical window thickness. The final photon detectors for TORCH will have smaller window thickness and have matching focal and photocathode planes.

6.2.3   TORCH module performance with Cherenkov photons

The pattern of Cherenkov photons at the photocathode plane for the optimal MCP position has been studied. A cone of light rays that simulates Cherenkov photons of λ=420 nm is generated in the quartz radiator plate. The half-angle of the emission cone is obtained from Equation (1.8). The simulation corresponds to saturated tracks (β=1) and $n_{fused\,silica}$ at a given λ is provided by the *RefractiveIndex* function in Optica. A set of photon emission points along the track path through the quartz plate are studied. Figure 6.16 illustrates the pattern of Cherenkov photons at the photocathode plane for a track crossing the radiator plate at normal incidence close to its bottom edge. The left and right plots in Figure 6.16 correspond to without and with reflective surfaces for the focusing block, respectively. If we compare Figure 6.16 (left) and (right), the missing photons in the pattern in (left) correspond to photons that hit the focusing block surface but are not reflected and therefore not arriving at the photocathode.

The difference in photon spread and pattern displacement due to the MCP window thickness is clearly observed.
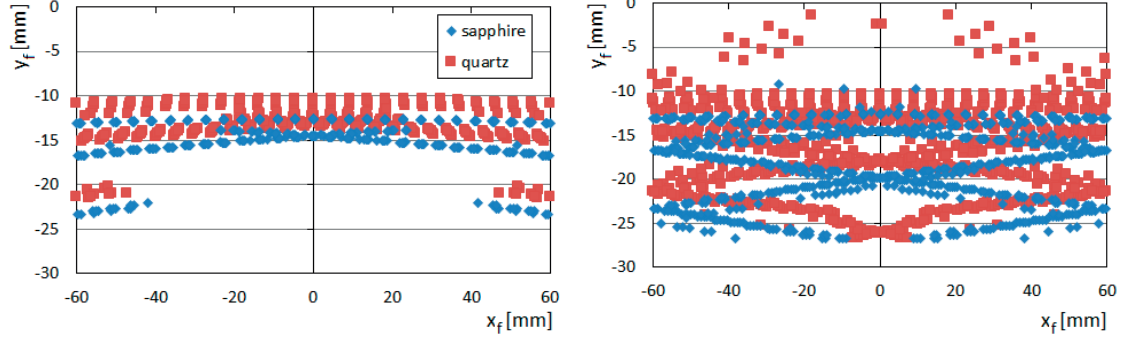
Figure 6.16: Cherenkov photons pattern at the photocathode plane without (left) and with (right) reflective surfaces for the focusing block for two MCP-PMT optical windows.

Various track positions (top and bottom of the radiator) and angles of incidence (0, 5, 10 and 15 °) are also investigated. Figure 6.17 reproduces the photon pattern considering only direct Cherenkov photons for two track positions at different track angles. The left plot in Figure 6.17 corresponds to a track hitting the quartz plate close to its top edge. The right plot in Figure 6.17 corresponds to a track hitting the quartz plate close to its bottom edge. In the latter case reflections at the side surfaces of the quartz radiator appear in the pattern. In both cases the change on the track angle results in a displacement of the photon pattern at the photocathode plane.
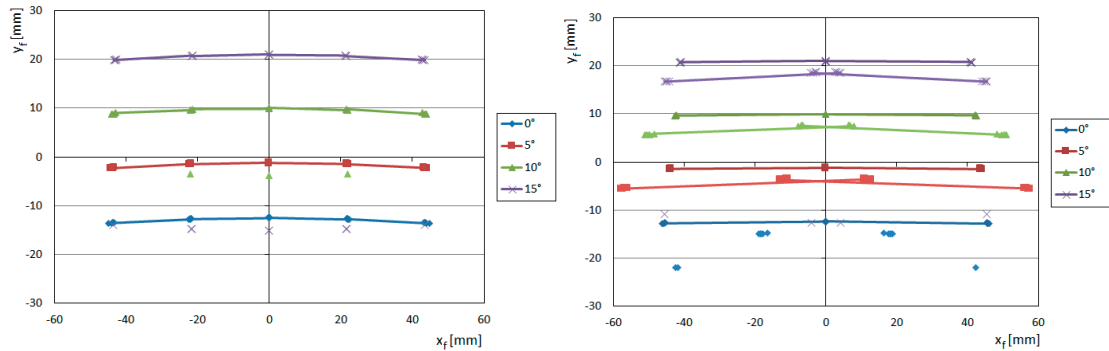
Figure 6.17: Photon pattern at the photocathode plane for four track angles from a track crossing point closer to the top edge of the radiator plate (left) and from a track crossing point closer to the bottom edge of the radiator plate (right).

6.3 Summary

Light transmission through glass and glue samples has been carried out using a collimated CW laser and a CCD camera. The light intensity recorded in a laser spot has been determined from background-subtracted images. The laser spot position has been characterized by applying a centre-of-gravity algorithm. The laser spot diameter has been defined as to contain 95% of the total image intensity. The transmission dependence on the angle of incidence has been investigated. The transmission loss in glued samples with respect to a single glass sample is 1-2%. No measurable change of laser spot diameter has been observed.

The optical transmission of the samples has been measured with a spectrophotometer. Given that Cherenkov light peaks in the UV, the glue with the best UV transmission has been selected for the coupling of the optical components of the TORCH prototype module.

A ray tracing software has been used for simulating the TORCH optics. The focal plane of the focusing element has been studied. For Phase II MCP-PMT prototypes equipped with a 9 mm-thick optical window photons are spread σ_y<0.45 mm at the photocathode plane which will degrade the measurement of the photon propagation angle θ_z. This large spread is due to a mismatch between the focal and photocathode planes. For a Planacon photon detector with a 1 mm-thick optical window this spread is smaller than 0.12 mm.

The pattern of Cherenkov photons at the photocathode plane has been studied. Different categories of Cherenkov photons are observed; e.g. arriving directly, with one reflection, with two reflections, etc. For Phase II MCP-PMT prototypes, photons arriving directly and with one reflection overlap partially due to the above mentioned mismatch.

7 Charged-particle beam tests

The small-scale TORCH prototype module has been characterized in a charged-particle beam instrumented with a Phase II MCP-PMT photon detector and the 32-channel NINO-HPTDC electronics [103]. Tests have been performed at the H8 beam line at the CERN SPS facility. Two test campaigns have been undertaken in May and July 2015.

7.1 Small-scale TORCH prototype module

7.1.1 Simulation of test beam configuration

The first tested configuration consists of the small-scale TORCH prototype module as described in Chapter 6. The Phase II MCP-PMT prototype, with 9 mm-thick quartz window, is positioned 0.5 mm away from the exit surface of the focusing optics. Since this MCP is a quarter size of the final prototype tube, the covered surface at the exit of the focusing block is 1/8 of the total surface. The tube is positioned in the central part (Figure 7.1) and the anode active area is 26.5×26.5 mm^2. From Figure 6.17, Cherenkov photons arriving directly from a track hitting the radiator plate at normal incidence will be detected at the bottom edge of the photocathode plane (blue coloured line). Consequently, it has been decided to tilt the TORCH prototype module by 5 ° which will displace the photon pattern at the centre of the MCP tube (red coloured line).

The photon trajectories for three Cherenkov angles corresponding to a photon wavelength of 300, 420 and 640 nm are simulated. The simulation considers saturated tracks and the track position corresponds to the centre of the radiator plate. Cherenkov photons are generated at five emission points along the track path through the quartz plate. The resulting Cherenkov photon pattern at the photocathode plane is reproduced in Figure 7.2 (left). In addition to the mismatch of focal and photocathode planes, the resulting smeared photon pattern is also due to chromatic dispersion where Cherenkov photons of different wavelength propagate with different speed in the quartz. TORCH uses the measured Cherenkov angle of each photon to correct for this dispersion. Direct photons are detected in the middle of the photocathode
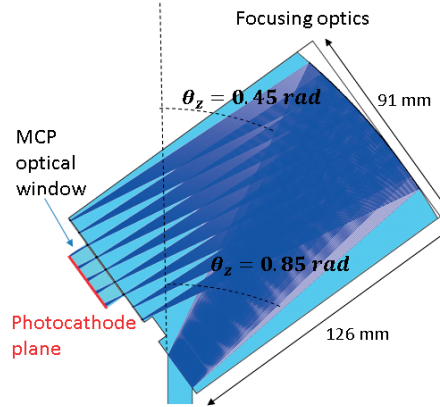
Figure 7.1: Side view of the focusing block simulated using Optica. Rays are generated at thirty emission points and at nine θ_z angles in the range 0.45-0.85 rad. The simulation includes refraction effects at the exit of the focusing block.

plane, at y~0. The position in x direction corresponds to different θ_x angles in the quartz plate plane. Photons that are reflected once off at the surface of the focusing block populate the region -1 mm<y<-6 mm together with photons reflected at the side surfaces of the radiator plate. The spread in x direction is explained by the different emission points along the track path in the quartz. Photons reflected twice (larger θ_x) are seen at the bottom edge of the photocathode plane. In this simulation, for each photon wavelength, the different categories of photons (direct, first reflected and second reflected) are well separated and θ_z is reconstructed and plotted in Figure 7.2 (right). However, in TORCH the photon wavelength is a priori unknown. As it is seen direct photons with λ=640 nm superpose with first reflected photons with λ=300 nm. This hinders the Cherenkov photon reconstruction.
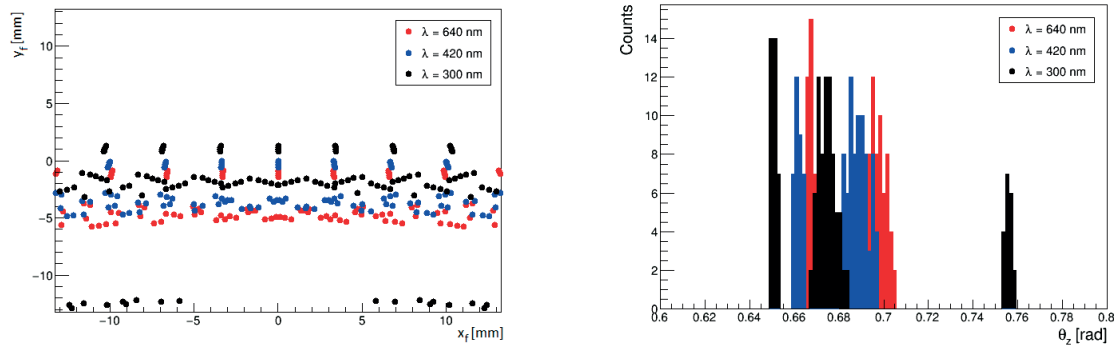
Figure 7.2: Cherenkov photons pattern at the photocathode plane for a Phase II MCP-PMT prototype for the nominal test beam configuration (left). Distribution of the reconstructed θ_z for each photon wavelength (right).

A 3D-view of the simulated small-scale TORCH prototype is shown in Figure 7.3. A specific track and Cherenkov angle configuration is illustrated. The red square indicates the photo-

cathode plane and the area covered by the Phase II MCP-PMT prototype.
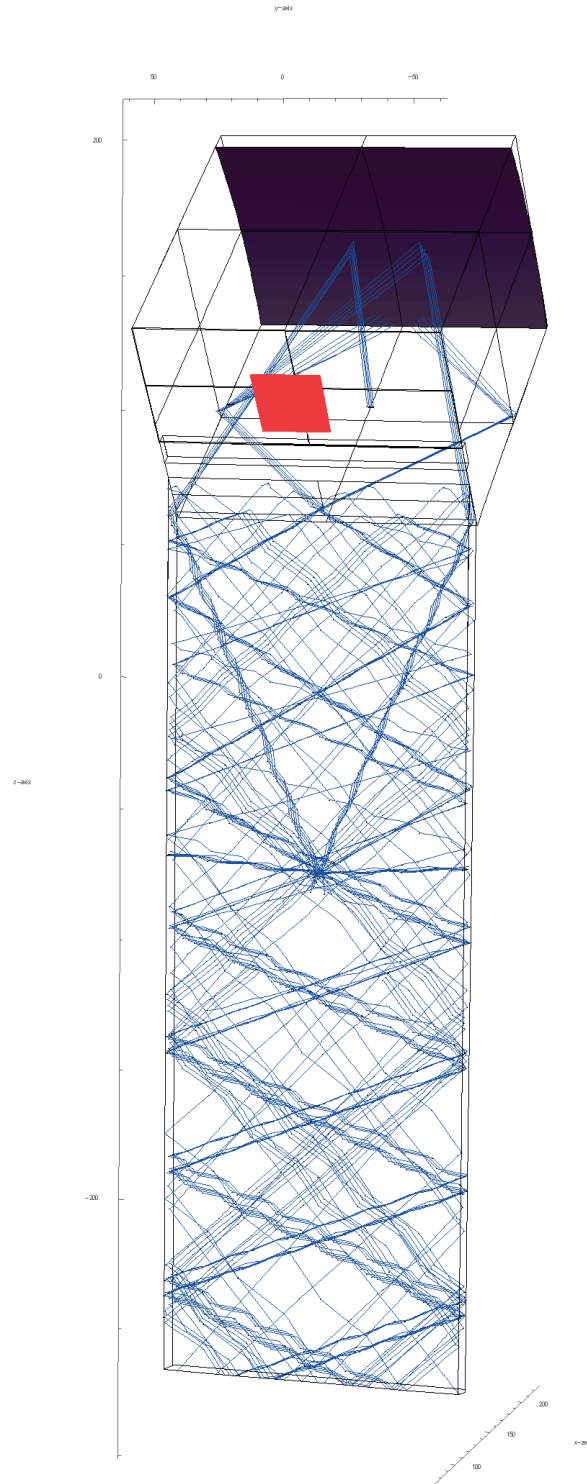
Figure 7.3: Simulated small-scale TORCH prototype module equipped with a Phase II MCP-PMT prototype. The red square region corresponds to the active area of the photon detector.

7.1.2 Preparatory tests in the laboratory

The TORCH prototype has first been characterized in the laboratory. The prototype was assembled and mounted inside a dedicated light-tight housing. The Phase II MCP-PMT device was half instrumented with NINO-HPTDC readout electronics and was mounted on a translation chariot (Figure 7.4) mechanically coupled to the focusing block. Collimated laser light was injected in the quartz radiator from its bottom edge and propagated via total internal reflection to the focusing block and there reflected off the cylindrical mirror. Figure 7.5 (left) is a photograph of the laser pattern at the exit of the focusing block and the footprint of the MCP area instrumented with electronics. Figure 7.5 (right) displays the corresponding hit map.
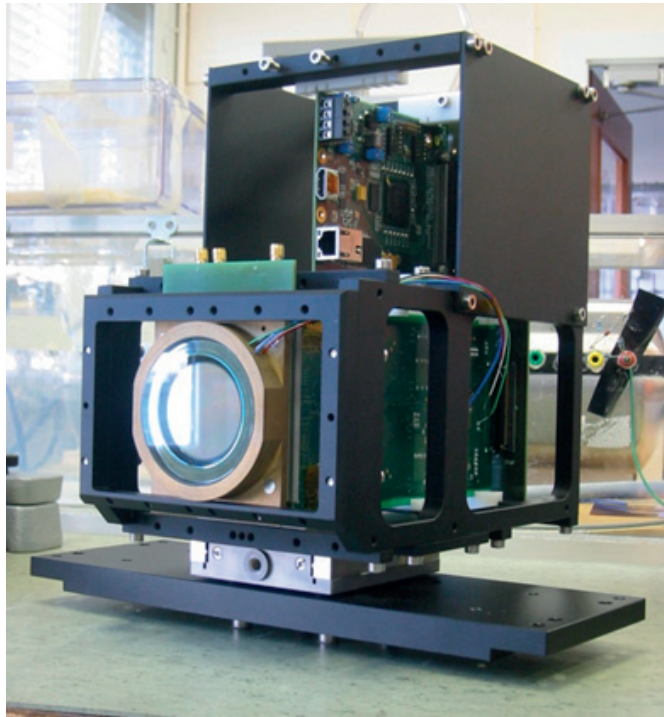
Figure 7.4: Photograph of mechanical structure holding a Phase II MCP-PMT prototype and a set of NINO-HPTDC electronic boards.

A specific code has been written to arrange and decode the raw data from the two HPTDCs and a ROOT [112] file containing the data for each event is created. Data quality has also been investigated in the laboratory. At a NINO threshold of 100 mV, 5% of the events contain hits where the trailing edge of the pulse was not registered. Consequently, for these hits the pulse width cannot be measured and the charge cannot be used to perform charge-sharing calculation. Channels that are more affected are those that collected less charge. The missing trailing edge is attributed to a low-amplitude signal providing a short NINO pulse that the HPTDC is not able to digitise the trailing edge. Two additional checks were performed:

- By decreasing the NINO threshold to 60 mV, channels collected more hits, as expected.
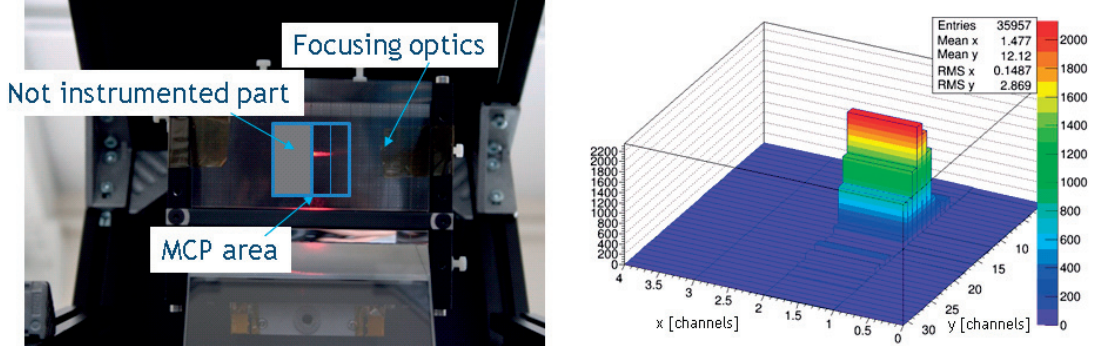
Figure 7.5: Laser arrangement of the small-scale TORCH prototype module together with the Phase II MCP-PMT prototype and NINO-HPTDC electronics (left) and the resulting channel hit map (right).

However, the number of hits with equal number of leading and trailing edges was reduced and the number of hits with missing trailing edge was increased.

- By increasing the laser rate from 1 kHz to 100 kHz, at the same laser tune setting of 60%, channels collected less hits and the number of events with zero hits increased. Laser intensity is affected when the rate is increased resulting in a hit drop on the reference channel and the illuminated channels.

Other effects such as the rate capability, photoelectron back-scattering, crosstalk, data bandwidth, HPTDC busy state, empty HPTDC buffers have not been investigated in this work.

7.1.3 Performance in a charged-particle beam

The TORCH layout at the SPS-H8 experimental area is shown in Figures 7.6, 7.7 and 7.8. The tests were performed with a high-momentum (180 GeV/c) charged-particle beam essentially populated with protons. A pixel telescope from the LHCb VELO group [116] was used to provide particle track information and the coincidence signal from two scintillators in the VELO telescope provided the trigger signal. Two sets of data taking runs were performed; stand-alone runs and runs using the AIDA TLU [108] to synchronise the telescope with the TORCH electronics.

TORCH electronics require a start time to perform timing measurements. The time reference signal was provided by direct Cherenkov photons generated in a borosilicate bar (8×8×100 mm^3) with blackened surfaces coupled to a single-channel MCP, read out with a fast amplifier and CFD (see also Section 7.2). This reference signal was input into a test channel of the NINO-HPTDC electronics. The borosilicate bar provides a start time and was installed in a small light-tight box mounted on the outer stage of the VELO telescope infrastructure and located ~1 m upstream from the TORCH prototype. This station was aligned with respect to the beam axis using the telescope translation and rotation stage system. The alignment

procedure can be found in Appendix H.
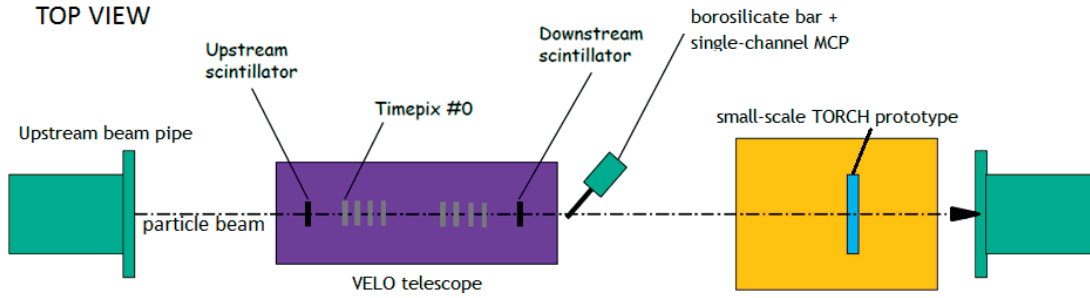
Figure 7.6: A schematic of the test beam infrastructure at the CERN SPS-H8.
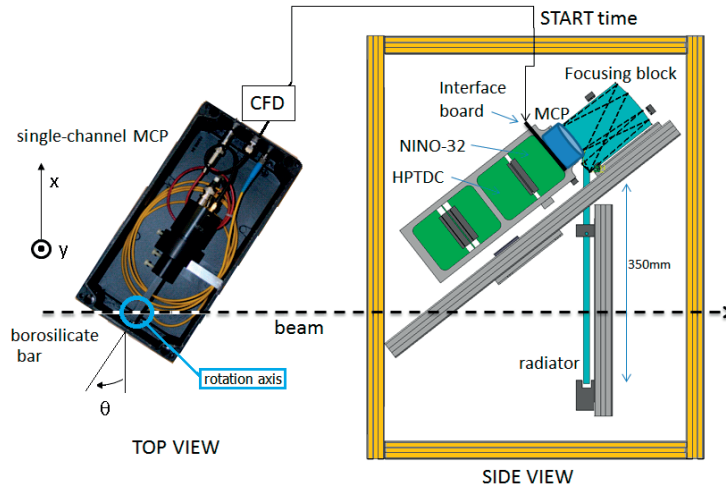
Figure 7.7: A schematic of the TORCH test beam infrastructure at the CERN SPS-H8.

Preliminary results

The user interface of the TORCH data acquisition system is based on LabVIEW. Data were recorded for various TORCH configurations and NINO thresholds (Appendix I). The TORCH prototype installed on a "DESY" table (Figure 7.8) could be translated horizontally and vertically. The nominal configuration corresponded to the beam crossing the quartz plate at its centre in both horizontal and vertical directions. The radiator was tilted by 5 °. Preliminary results at this nominal configuration are reported.

A hit map from the TORCH raw data is reproduced in Figure 7.9 (left). Channel with coordinates (2,31) corresponds to the test channel and provides the time reference. The corresponding data is masked for visibility. Each count on this histogram corresponds to a hit on a channel having both leading and trailing edge information. A code has been written for off-line analysis. For each event, the time information of the leading edge is corrected for time walk effects using the
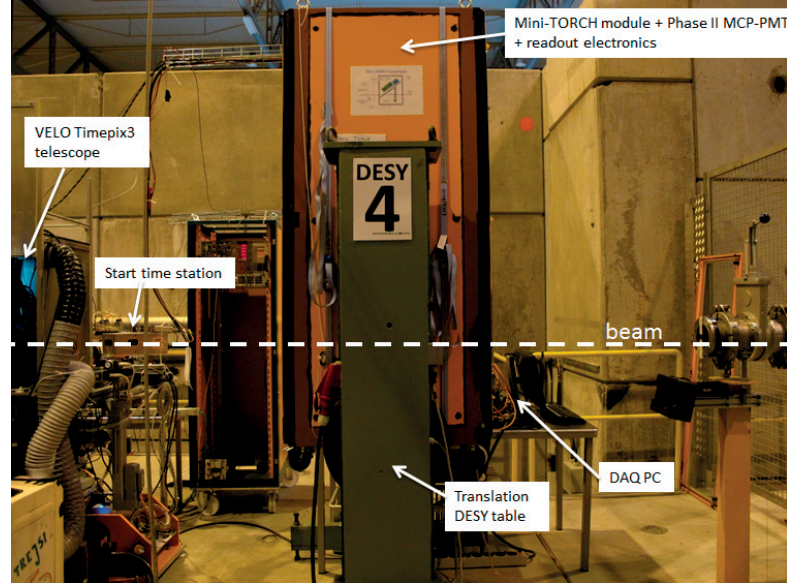
Figure 7.8: Photograph of the TORCH test beam infrastructure at the CERN SPS-H8.

calibration curve described in Subsection 5.6.2. This calibration curve is used for global time walk corrections assuming all channels behave similarly. Subsequently, a clustering algorithm is applied. Hits belonging to a photon cluster must satisfy one of the two following conditions:

- The hit channels of a photon cluster are in the same column with a maximum difference in row position of 4 channels maximum and with a maximum time difference between leading edges after time walk corrections of 3 time bin units of 100 ps.

- The hit channels of a photon cluster are in the same row with a maximum difference in column position of 1 channel and with a maximum time difference between leading edges after time walk corrections of 3 time bin units of 100 ps.

The maximum of 3 time bin units is based on the knowledge that the timing residuals measured in the laboratory are 1.15 time bin units (Subsection 5.6.2). A larger time window is allowed since the same time walk corrections are applied to all channels assuming they behave similarly.

Once the photon clusters are identified, a centroiding algorithm is applied to calculate the photon cluster position (see Subsection 5.6.5). This clustering results in an improved visibility of the photon patterns. The corresponding hit map after clustering is reproduced in Figure 7.9 (right). Each count on this histogram corresponds to a photon cluster. The position residuals within a photon cluster are calculated using Equation 5.17 and the distribution is reproduced in Figure 7.10.

The time distribution of a single channel is shown in Figure 7.11. A time resolution of 220 ps is achieved for single photons after time walk corrections. This resolution represents the

single-channel response with no reconstruction. Consequently, this value of 220 ps includes contributions from:

- Chromatic dispersion

- Emission point error

- Track position

- Time reference

- Electronics.
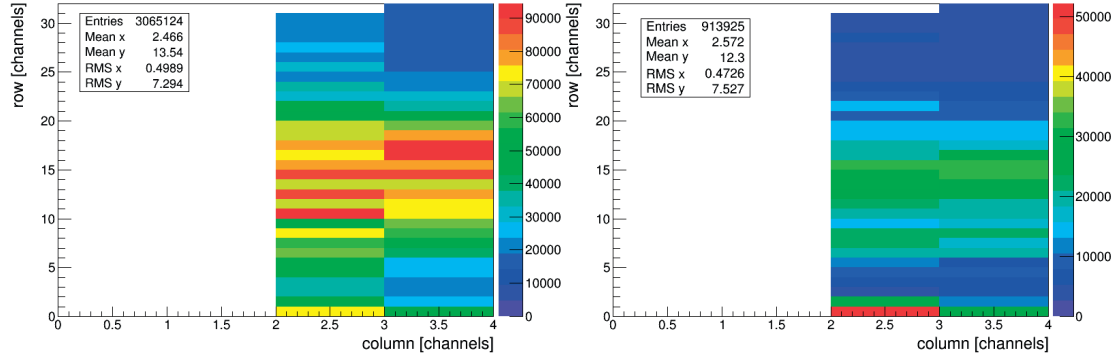
Figure 7.9: Raw (left) and clustered (right) TORCH photon hit map at the photocathode plane.
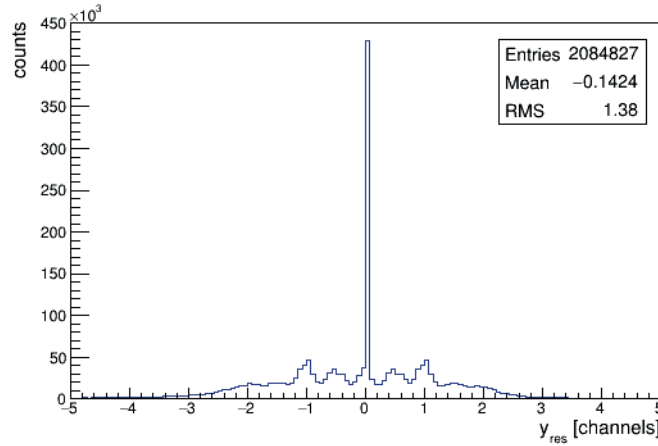
Figure 7.10: Hit position residuals calculated with respect to the centroid position of the photon cluster.

The electronics contribution to the time resolution is measured using the two NIM output signals from the CFD and delaying one with respect to the other (Figure 7.12 (left)). Both signals are injected into the test channel of the NINO-HPTDC electronics. The electronics jitter can be inferred from the distribution of the time difference between the leading edge of
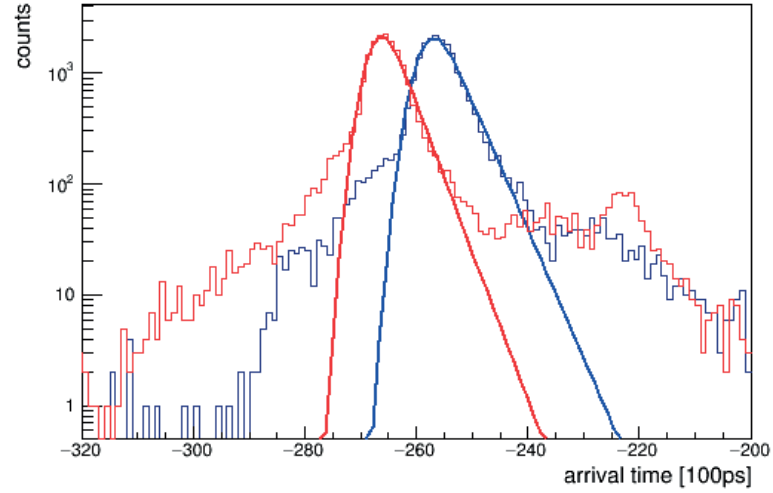
Figure 7.11: Time distributions before (blue) and after (red) time walk correction from a single channel measured with the TORCH prototype module in a charged-particle beam. An offset in time is introduced for graphical display.

each signal (Figure 7.12 (right)). The jitter of 59.1 ps, already scaled by $1/\sqrt{2}$, is dominated by the HPTDC time bin precision of 100 ps and is currently not a significant contribution to the overall measured time resolution.
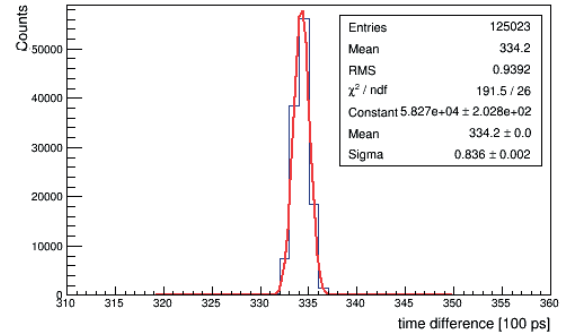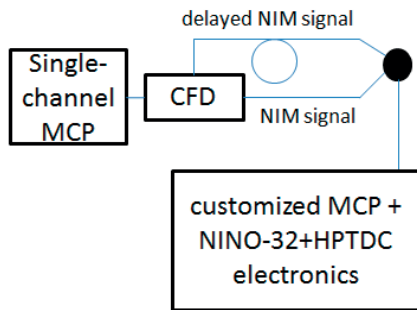
Figure 7.12: Set-up for measuring the electronics jitter (left). Time difference between two NIM output signals measured by the NINO-HPTDC electronics with a combined σ=83.6 ps (right).

The time projection histograms represent the photon time information as a function of its position at the photocathode plane. The expected patterns from simulation using Geant4 reported in [52] are reproduced in Figure 7.13 (top). The different colour points referred to different categories of Cherenkov photons; direct (red points), first reflected (blue and green points) and second reflected (blue and black points). The simulated time projections assuming a 100 ps photon smearing are reproduced in Figure 7.13 (bottom). The corresponding plots using TORCH data also reported in [52] are reproduced in Figure 7.14.
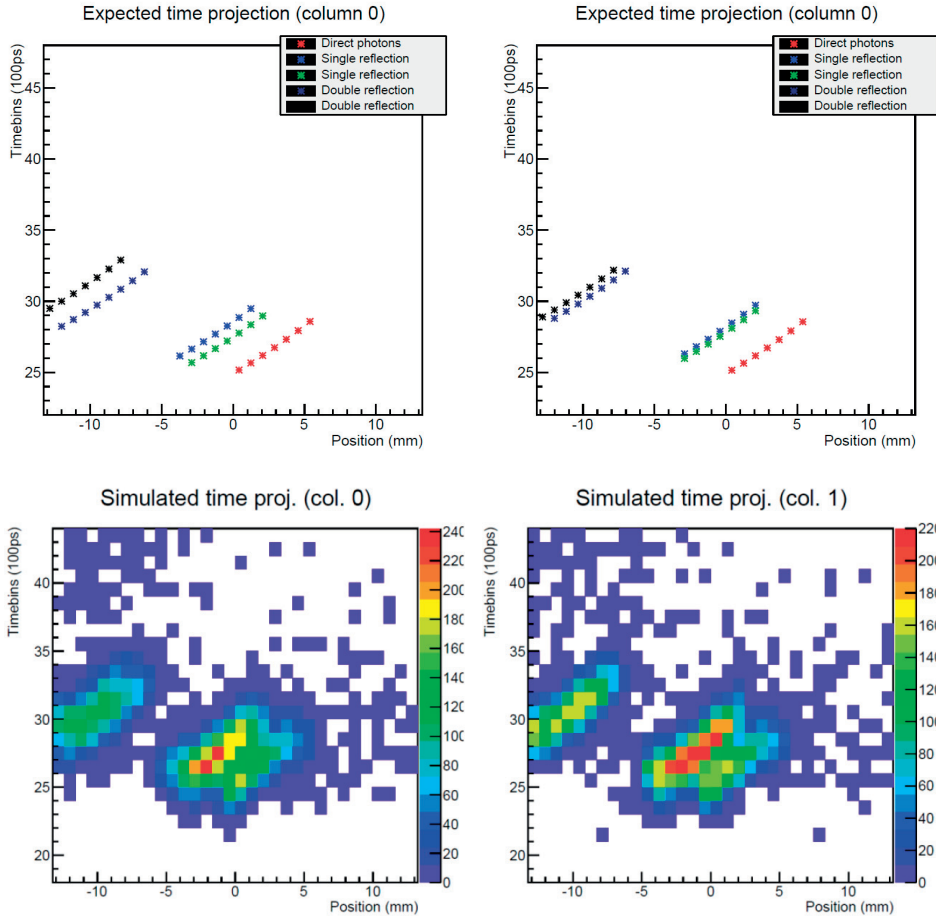
Figure 7.13: Simulated time projection patterns for columns S0 (left) and S1 (right). The bottom plots correspond to a 100 ps photon smearing [52].
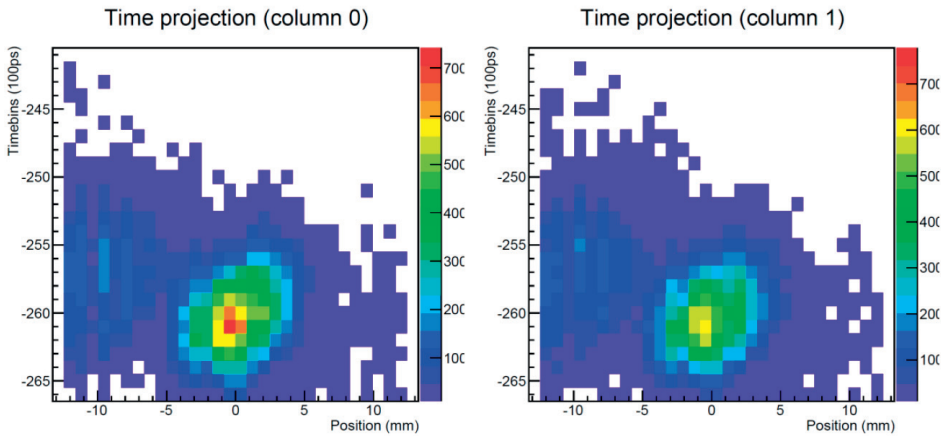
Figure 7.14: TORCH time projection patterns for columns S0 (left) and S1 (right) [52].

The separation of different categories of Cherenkov photons is affected by the mismatch of the focal and photocathode planes (see Chapter 6).

In addition, the time walk calibration curve was obtained from the response of a single NINO channel and the charge-to-width calibration was performed in four NINO channels. Both electronics calibrations have been applied for global correction assuming all channels behave similarly. From the laboratory tests it has been shown that each NINO channel requires its own calibration for both time walk and charge-to-width conversion. The NINO threshold settings are applied to odd and even channels independently, which increases the number of settings combinations for the channel response optimization.

Another important remark in the channel-to-channel behaviour is illustrated in Figures 7.15 and 7.16. These figures show 2D scatter plots of pulse width as a function of arrival time for all 32-channels of both NINO chips. It is observed that on each chip the first 16 channels behave differently from the other 16 channels. Those channels from both chips within a blue or an orange frames have similar response. Blue and orange colours also indicate the corresponding column of the MCP anode pads, S0 and S1, respectively. This different behaviour in pulse width vs arrival time can be attributed to different track lengths on the interface board of the Phase II MCP-PMT device (See Figure 5.2 (right)).

7.2 Start time station

During a second beam test, two similar start time stations have been used in conjunction to determine the contribution of a single start time station to the overall time resolution achieved with the TORCH prototype. Photon yield and time jitter of these timing stations have been measured.

7.2.1 Performance in a charged-particle beam

Figure 7.17 shows the configuration of the two-station system. The second station (T2) has been calibrated in the laboratory to operate at the same gain of 1.5×10^5 electrons as the first station (T1) used in the previous beam test.

The two-station system was mounted on the telescope infrastructure and x-y and rotation scans were performed to align the system with respect to the beam (Appendix J). Each timing station was first instrumented with a charge pre-amplifier to record a pulse height spectrum (PHS) and estimate the photon yield.

The average detected photon yield of each station was found to be 1.7 photoelectrons (T1) and 1.6 photoelectrons (T2). The recorded PHS are shown in Figure 7.18 for the T1 station (left) and the T2 station (right).

For the timing measurements, each timing station was coupled to an amplifier/CFD and the output signals were delayed with respect to each other. Both signals were input to a commercial TAC module and time jitter distributions were recorded using a multi-channel analyser. The coincidence signal from the two scintillators of the pixel telescope was used as
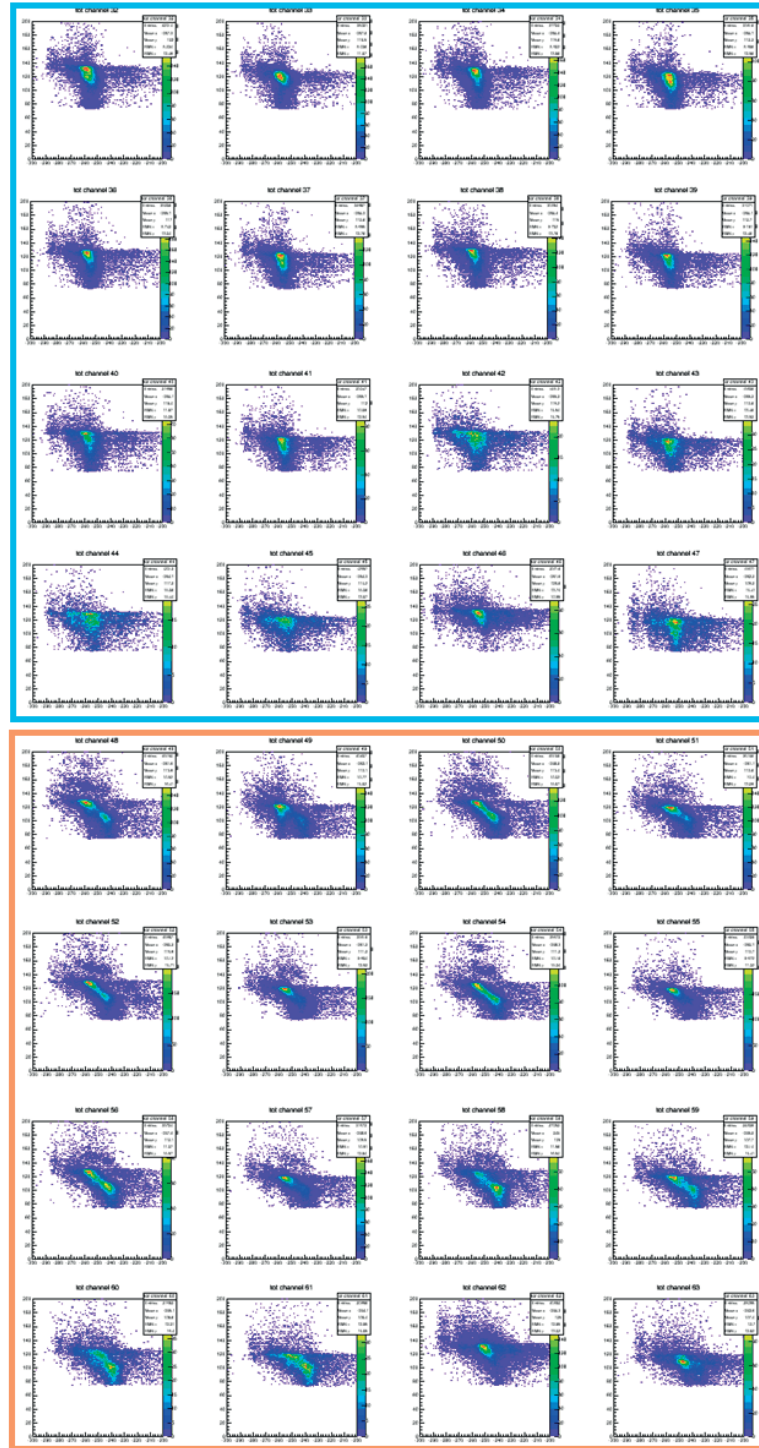
Figure 7.15: 2D TOT plots of pulse width as a function of arrival time for 32-channels of NINO chip 1. The first 16 channels (blue square) are connected to column S0 of Phase II anode pads and the other 16 channels (orange square) are connected to column S1 of Phase II anode pads.
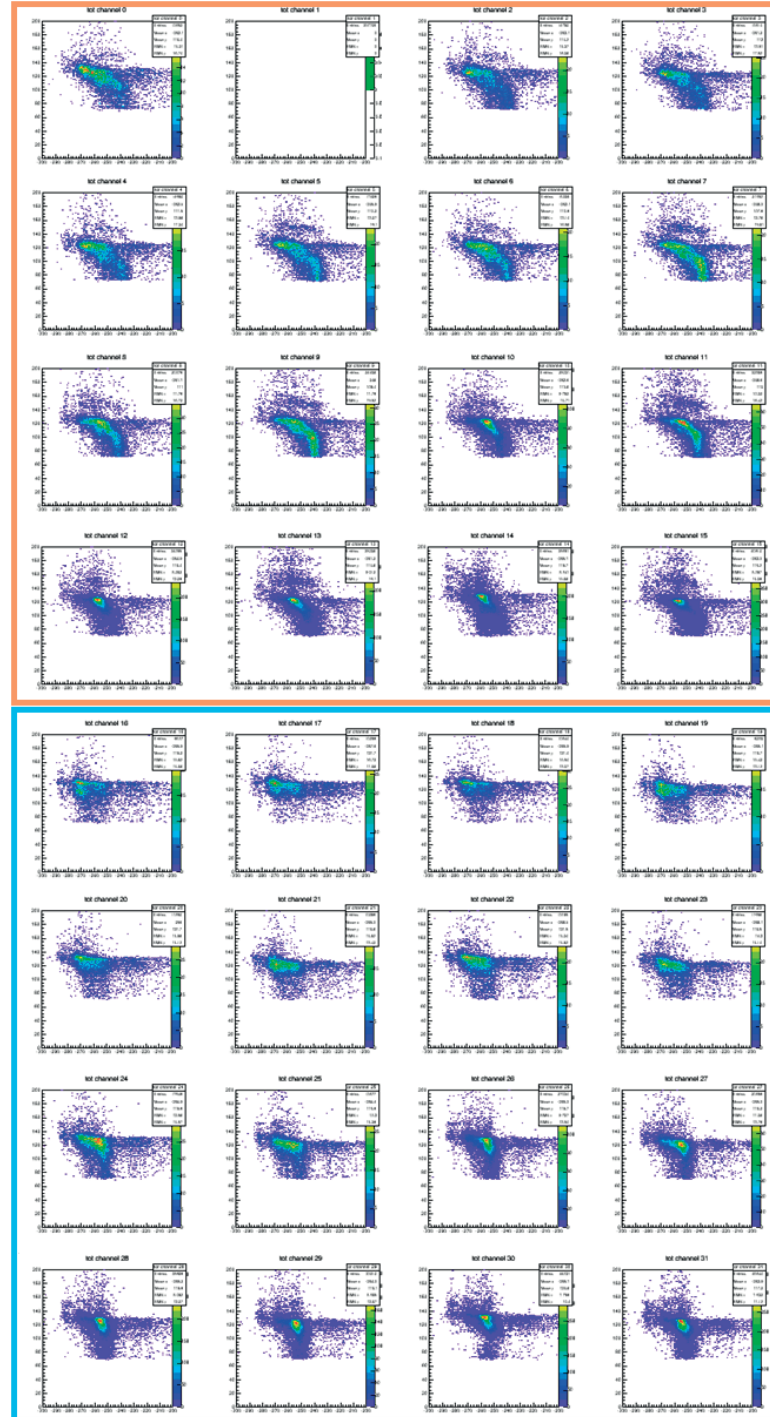
Figure 7.16: 2D TOT plots of pulse width as a function of arrival time for 32-channels of NINO chip 2. The first 16 channels (orange square) are connected to column S1 of Phase II anode pads and the other 16 channels (blue square) are connected to column S0 of Phase II anode pads. Channel 1 is the time reference channel where the data are not displayed.
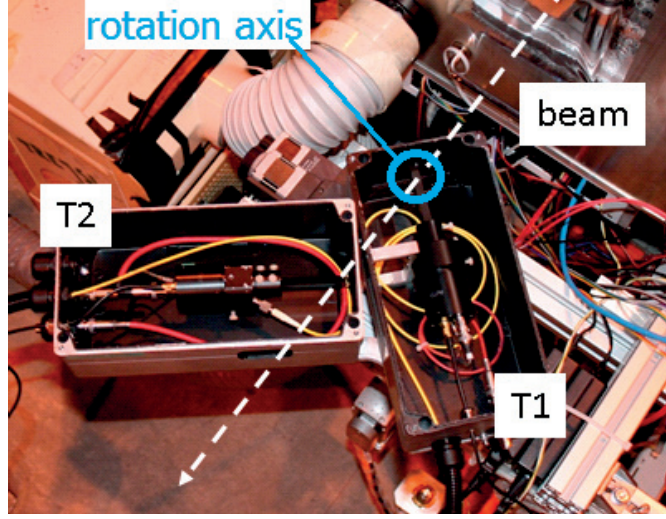
Figure 7.17: Configuration of the two-station system in the beam test.
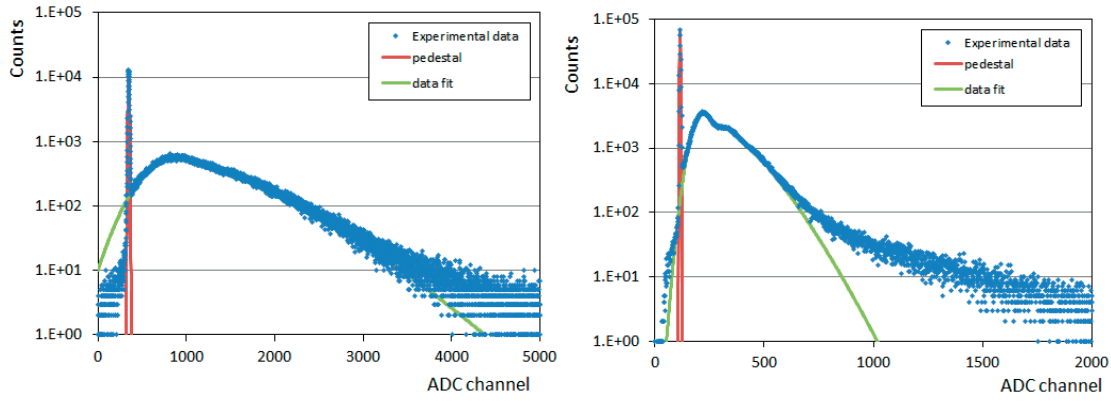
Figure 7.18: PHS (logarithmic vertical scale) recorded with a charge pre-amplifier from T1 (left) and T2 (right) stations. The measured average photon yield are μ_1=1.7 photoelectrons and μ_2=1.6 photoelectrons.

a trigger. The time difference distribution in Figure 7.19 is fitted with a Gaussian; the time resolution of a single station is given by the standard deviation of the Gaussian scaled by $1/\sqrt{2}$. This resolution is found to be 48.1 ps. The structure outside the Gaussian is attributed to Cherenkov photons emitted at different points along the borosilicate bar length due to the beam size ~1 mm.

A second configuration of the borosilicate Cherenkov radiators was tested in which unblackened bars were installed in place of the previous blackened bars. In this configuration, the average detected photon yield of each station was found to be 8.5 photoelectrons (T1) and 8.7 photoelectrons (T2) (Figure 7.20). The low-amplitude peak in T2 is attributed to triggered tracks that do not cross the full thickness of the radiator bar. The position of the first photoelectron peak in the right plot is constrained by that of the low-amplitude peak. The corresponding
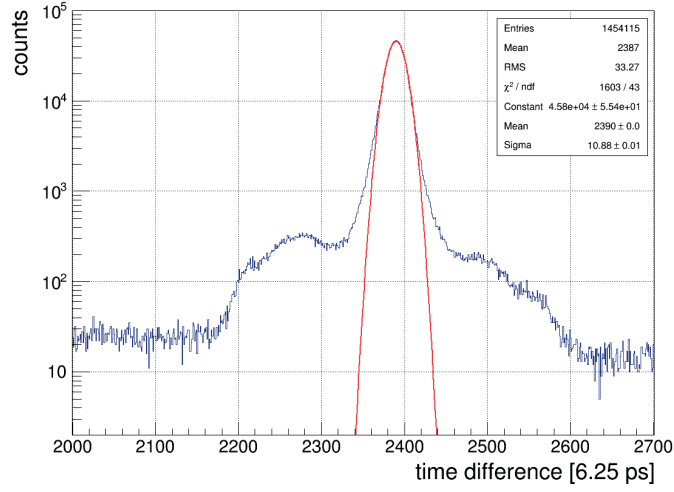
Figure 7.19: Time difference distribution (logarithmic vertical scale) of borosilicate bars with blackened surfaces with a σ=68 ps.

single-station time resolution (Figure 7.21) was found to be 31.8 ps (already scaled by $1/\sqrt{2}$). This configuration provides a better time reference for the TORCH prototype and is now the baseline option for future beam tests.
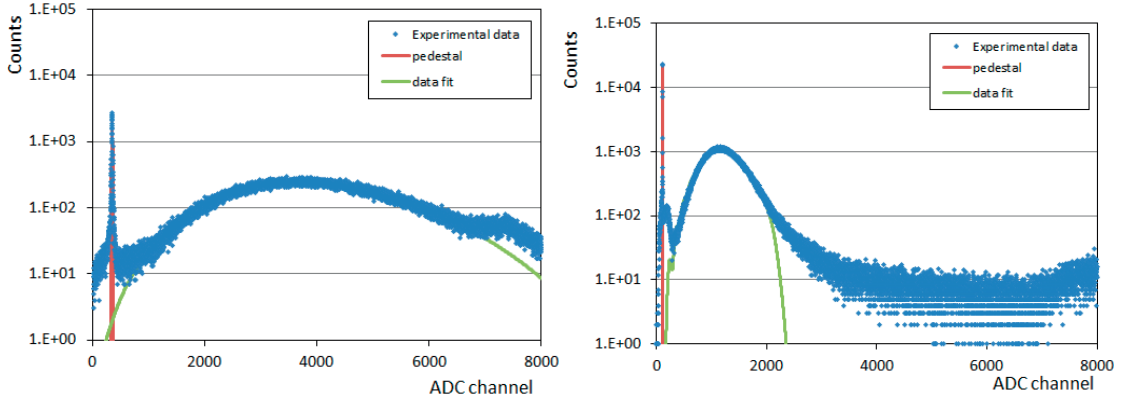
Figure 7.20: PHS (logarithmic vertical scale) recorded with a charge pre-amplifier from T1 (left) and T2 (right) stations with unblackened bars. The measured average photon yield are μ_1'=8.5 photoelectrons and μ_2'=8.7 photoelectrons. Both multi-channel analyser saturate at the end of the operating range.

7.3   Summary

A first test beam campaign has been devoted to the study of a small-scale TORCH prototype module. Raw data recorded with the NINO-HPTDC electronics are corrected for time walk effects. Since the charge from a photon is spread over several channels at the anode of the
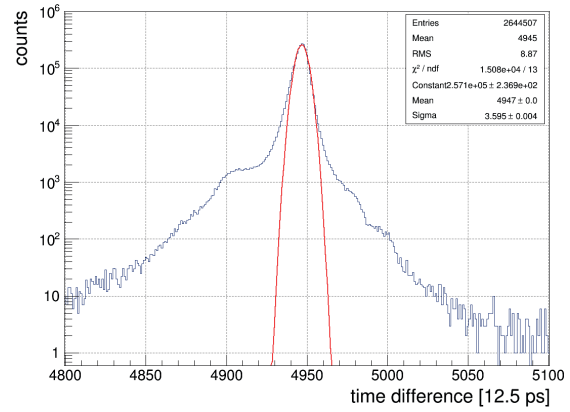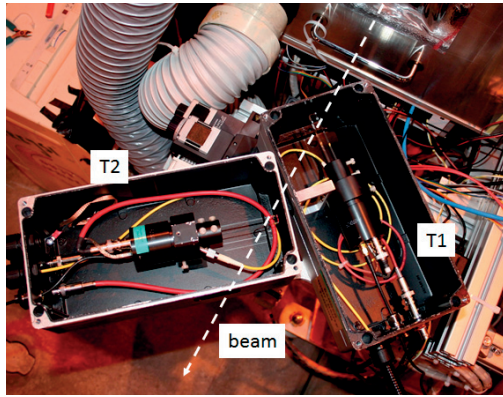
Figure 7.21: Configuration of the two-station system with unblackened borosilicate bars (left). Corresponding time difference distribution (logarithmic vertical scale) with a σ=44.9 ps (right).

Phase II MCP-PMT prototype, a clustering algorithm is applied. The position of each cluster is calculated using a centroid algorithm and the charge information from each hit. The residual pixel position with respect to the cluster centroid is calculated. The residual distribution corresponds to the point spread function of the MCP-PMT prototype. The RMS value of 1.38 channels in Figure 7.10 is very close to that achieved with laser data in the laboratory for well calibrated channels (Figure 5.42). The RMS value is in good agreement with simulation. The time resolution of the start time station has been assessed in a second beam test campaign and is 48.1 ps.

8 Conclusion

TORCH, a novel high-precision time-of-flight detector for particle identification at low momentum, is presented in this thesis. Work on photon detectors, readout electronics, optics and beam tests carried out during the TORCH R&D programme is reported.

The first part of the thesis covered the investigation of the operation and performance of Micro-Channel Plate (MCP) photon detectors. A calibration system with a stable laser illumination operating in single photoelectron regime was prepared for this work. Commercial single-channel MCP devices have been characterized using standard electronics demonstrating a time resolution of 38.9 ps for single photoelectrons. Analytical models have been proposed for the description of the measured time distributions and the effects of back-scattered photo-electrons, laser and readout electronics. In multi-photon regime the time resolution is 18.3 ps, which makes these MCP-PMTs suitable as a good time reference for lab tests.

Ageing tests performed by our industrial partner (Photek Ltd.) have shown that Phase I MCP-PMT prototypes for TORCH reached the target value of 5 C/cm^2 with acceptable degradation in performance. The use of Atomic Layer Deposition (ALD) technology allowed to achieve the same gain with significantly lower operating voltage, reducing the damage of the photocathode due to ion bombardment. These tubes feature a time resolution of better than 30 ps at a gain of 3×10^5 with an electronics efficiency of 90% for single photoelectrons. This resolution is already better than the TORCH requirement. These tubes have a small photocathode-MCP gap of 200 μm and consequently, the photoelectron back-scattering effects are mitigated. However, this small gap is difficult to achieve for square tubes.

Commercial and custom MCP photon detectors with segmented anode have been investigated using two versions of custom multi-channel electronics (NINO-HPTDC). Their performance has been qualified in the laboratory with emphasis in the single photoelectron regime. Software has been developed to decode and analyse the data from the readout electronics. Raw data from the 8×8 pads Planacon MCP-PMT and the Phase II MCP-PMT prototype read out by the NINO-HPTDC electronics required various corrections. For the non-linearity in the time bins of the HPTDC chips, an algorithm has been implemented for off-line corrections. A

procedure to correct the time walk of the NINO chips and an analytical model to describe the calibration data points have been developed. These calibration studies have contributed to the development of the readout electronics.

The Planacon device has been operated at a low gain of 6×10^5 compliant with the lifetime aspects. After non-linearity and time walk corrections, the time resolution has significantly improved from 88 ps to 68 ps, a value close to the TORCH requirement. In this device the MCP input gap of 4.5 mm results in signal from the back-scattered photoelectrons delayed by ~1.5 ns from the prompt photoelectrons. Consequently, these late photoelectrons will not be useful for the timing reconstruction in TORCH.

Phase II custom MCP-PMT prototypes with fine anode segmentation have been operated at a gain of 1.6×10^6 at which the electron charge cloud is spread over four anode pads. Tests with commercial electronics have demonstrated a time resolution down to 28.2 ps on a single channel. With the NINO-HPTDC electronics, no significant improvement in the time resolution has been observed when correcting for the non-linearity in the 100 ps resolution mode of the HPTDC. A time resolution of 80 ps for a single channel has been achieved after time walk corrections. Using a charge-sharing technique a spatial resolution of 0.025 mm has been measured, a value that is better than the TORCH requirement. For this purpose, an additional calibration of the NINO chips has been performed, an analytical model has been developed and a centre of gravity algorithm has been applied.

The optical quality of various glass and glue samples has been investigated and a gluing material suitable for the coupling of the TORCH optical components has been chosen, which transmits 86% of light at a wavelength of 200 nm. Design parameters of TORCH optics have been verified in simulation. The spread of Cherenkov photons at the photocathode plane of two different photon detectors has been evaluated. From simulation, a 9 mm-thick MCP optical window coupled to the TORCH optics has shown a degradation in the measurement of the propagation angle of Cherenkov photons due to an optical mismatch between the focal and photocathode planes. The final MCP-PMT prototypes for TORCH will have thinner optical window to reduce this effect. The simulated photon spread for a 1 mm-thick MCP optical window is smaller than 0.12 mm.

The performance of a small-scale TORCH prototype module incorporating a Phase II MCP-PMT prototype has been assessed with a charged-particle beam. The system has been pre-calibrated in the laboratory. A clustering algorithm for the photon hits has been developed. Time walk corrections are applied globally to all hit channels in a photon cluster, assuming all channels have similar behaviour. However, further channel-to-channel calibrations with an automated set-up are required. A total time resolution of 220 ps for a single channel has been achieved after time-walk corrections. The electronics contribution of 59.1 ps is dominated by the HPTDC time bin of 100 ps. In a dedicated beam test the start time jitter was found to be 48.1 ps. Both are not currently significant in the overall measured time resolution. Different categories of Cherenkov photons; e.g. arriving directly, with one reflection, two reflections

etc., hit different positions of the photocathode plane at different times, which have to be corrected.

Test of the TORCH prototype with a 32×32 pads Planacon MCP-PMT with a low-momentum charged-particle beam is foreseen for late summer 2016. The final MCP-PMT prototypes suitable for TORCH are being manufactured. They will combine the lifetime and granularity requirements in a square-shape with an active area of 80%. The MCP input and output gaps must be minimised in the design.

A Datasheets of the commercial 8×8 pads Planacon MCP photon detector

Photon Detector

XP85012

PLANACON®

25μm MCP-PMT
8x8 Anode
53 mm Square

Applications
- ✓ Specialized Medical Imaging
- ✓ Cherenkov – RICH, TOF, TOP, DIRC
- ✓ High Energy Physics Detectors
- ✓ Homeland Security
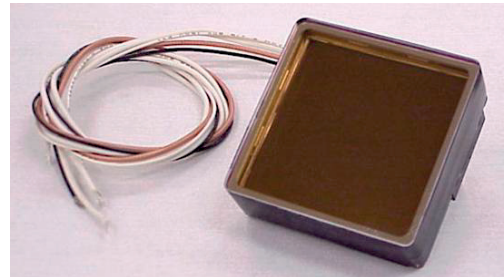
Description

Description	
Window options	Schott 8337B or equivalent, UVFS (-Q)
Photocathode	Bialkali
Multiplier structure	MCP chevron (2), 25 μm pore, 40:1 L:D ratio
Anode structure	8×8 array, 5.9 / 6.5 mm (size / pitch)
Active area	53×53 mm
Package open-area-ratio	80%

Photocathode characteristics	Min	Typ	Max	Unit
Spectral range:	200		650	nm
Maximum sensitivity at		380		nm
Sensitivity:				
Luminous *	50	60		μA/lm
Blue *	7.5	8.5		μA/lmF
Radiant, at peak		70		mA/W
Quantum Efficiency		22		%

Characteristics	Min	Typ	Max	Unit
Overall Voltage for 10^5 Gain *		1800	2400	V
Total anode dark current @ 10^5 gain *		2	10	nA
Rise time		0.6		ns
Pulse width		1.8		ns

Typical spectral response

Recommended Voltage Divider (not included)

CAUTION: POWER GROUND CONNECTION AND UNUSED ANODES MUST BE CONNECTED TO GROUND FOR SAFETY AND PROPER TUBE OPERATION

Typical gain curve

Characteristic measured and recorded on the test ticket of each tube

166

Photon Detector

XP85012

XP85012/A1

TOP VIEW SIDE VIEW BOTTOM VIEW

59.0±0.3
53 SQ
ACTIVE AREA

11	12	13	14	15	16	17	18
21	22	23	24	25	26	27	28
31	32	33	34	35	36	37	38
41	42	43	44	45	46	47	48
51	52	53	54	55	56	57	58
61	62	63	64	65	66	67	68
71	72	73	74	75	76	77	78
81	82	83	84	85	86	87	88

600 NOM

Mass: ~128g

27.9±0.9
25.4±0.9

4
2

12.9 TYP

32

4 3 2 1

4X 32 PIN CONNECTOR
(2mm PITCH)

CONN 4	CONN 3	CONN 2	CONN 1
18 GND	16 GND	14 GND	12 GND
GND 17	GND 15	GND 13	GND 11
28 GND	26 GND	24 GND	22 GND
GND 27	GND 25	GND 23	GND 21
38 GND	36 GND	34 GND	32 GND
GND 37	GND 35	GND 33	GND 31
48 GND	46 GND	44 GND	42 GND
GND 47	GND 45	GND 43	GND 41
58 GND	56 GND	54 GND	52 GND
GND 57	GND 55	GND 53	GND 51
68 GND	66 GND	64 GND	62 GND
GND 67	GND 65	GND 63	GND 61
78 GND	76 GND	74 GND	72 GND
GND 77	GND 75	GND 73	GND 71
88 GND	86 GND	84 GND	82 GND
GND 87	GND 85	GND 83	GND 81

A CATHODE BIAS (WHITE, Ø1.8)
B MCP INPUT BIAS (WHITE, Ø1.8)
C MCP OUTPUT BIAS (WHITE, Ø1.1)
D MCP Output Signal (COAX)
E POWER GROUND (BLACK)

A B C D E

Internal Connection Schematic – XP85012/A1 *

CATHODE BIAS
2X 22 kΩ
MCP INPUT BIAS
0.01 µF
MCP OUTPUT SIGNAL
MCP OUTPUT BIAS
4X 200 Ω
1 MΩ
4X 0.01 µF
POWER GROUND
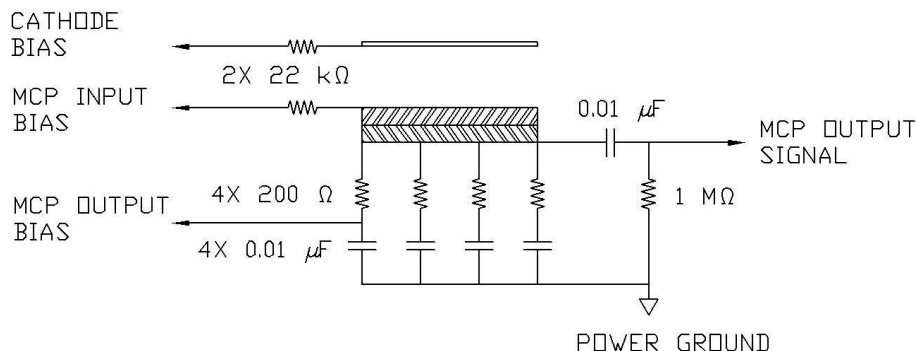
Limiting values**	Min	Max	Unit
Cathode to MCP_{in} voltage		500	V
MCP_{in} to MCP_{out} voltage		2000	V
MCP_{out} to Anode voltage		500	V
Overall HV when using recommended voltage divider		2400	V
Total anode current under uniform illumination		3	µA
Ambient temperature:			
Operating Temperature	0	+50	°C
Storage Temperature (for extended periods)	-15	+50	°C

* Custom or unfurnished external connections are available upon request.
** Warning: Continuous operation at maximum ratings may result in shorter product life or unreliable performance.

B Test input circuitry on 8-channel front-end NINO-HPTDC board (FE5)

The test input circuitry has been studied and calibrated in the laboratory. The NIM signal from the CFD is attenuated by a 13 dB attenuator corresponding to a pulse amplitude of -200 mV. The CFD output pulse width is 5 ns. The injected charge and the input capacitor are calculated. The time reference signal is input into a dedicated NINO channel.

Figure B.1 shows a picture of the FE NINO-HPTDC board with the test input and output cabling. Figure B.2 shows the injection circuitry (left) and an oscilloscope display of the test input signal via the differential probe (right).
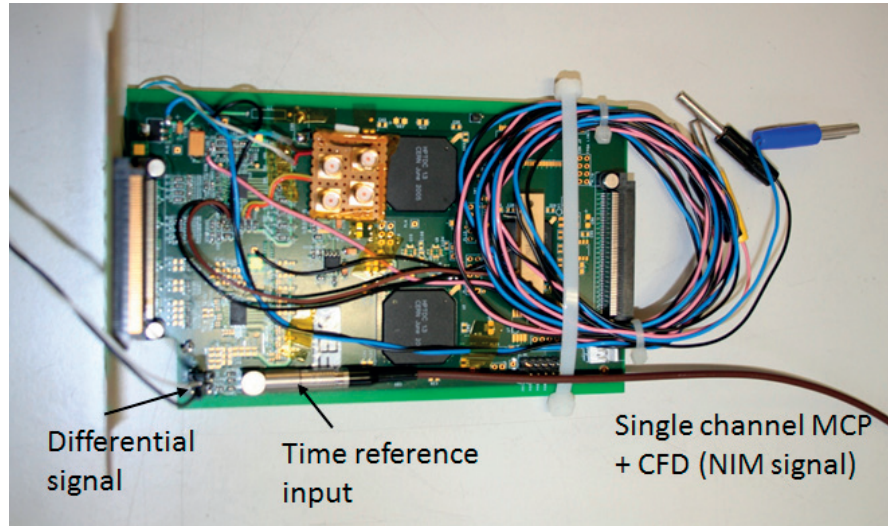
Figure B.1: Photograph of the front-end NINO-HPTDC board (FE5) showing the injection of a time reference signal via a LEMO connector and the differential output.

The input charge is estimated from the pulse surface and is calculated as:

$$Q = \frac{58\,mV \times 4.4\,ns}{100\,\Omega} = 2.6 \pm 0.4\,pC \tag{B.1}$$

and the capacitor is then calculated as

$$C = \frac{2.6\,pC}{200\,mV} = 13.0 \pm 3.6\,pF \tag{B.2}$$

The estimated value of the input capacitor is larger than 10 pF and is attributed to the influence of parasitic capacitance.
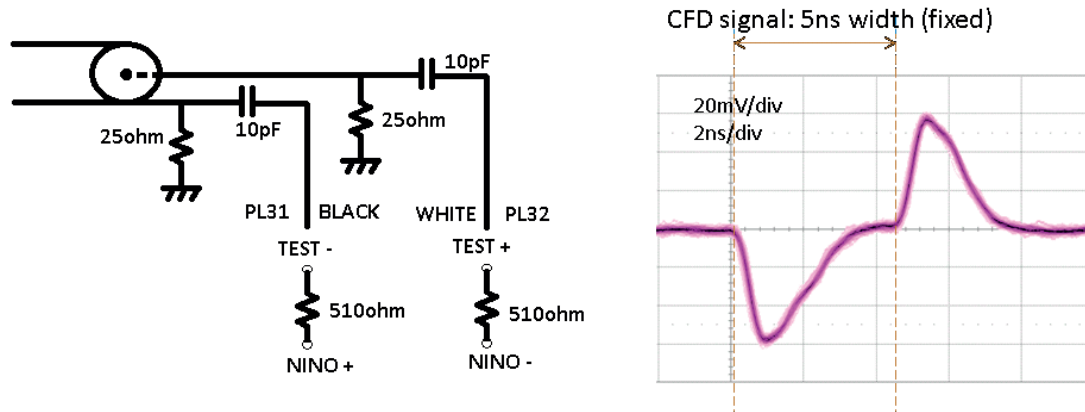
Figure B.2: Injection circuitry on the test input of the front-end NINO-HPTDC board (FE5) (left). Charge measured with scope on the test input of the front-end NINO-HPTDC board (FE5) (right).

C Investigations of the test input circuitry on the Phase II MCP-PMT interface board

In order to time the arrival of photons a time reference signal (start time) is required. In the laboratory the time reference is provided by the laser multi-photon signal (μ ~7 photoelectrons) detected from the single-channel MCP tube coupled to the CFD and is input into a dedicated NINO channel. The first version of TORCH electronics (8-channel NINO) includes a test input, whereas the new generation electronics (32-channel NINO) does not provide any. Therefore, a test input has been incorporated on the interface board which is coupled to the Phase II MCP-PMT prototypes. The test input circuitry has been studied and calibrated. The NIM signal from the CFD is attenuated by a 13 dB attenuator corresponding to a pulse amplitude of -200 mV. The CFD output pulse width is 5 ns. The injected charge and the input capacitor are calculated.

The single test input on the interface board, TIME REF, is fanned out in two, TIME REF0 and TIME REF1, to input the reference signal via a 2.2 pF capacitor into both front-end boards connected to J1 and J2. This is illustrated in Figure C.1 where the injection circuitry is represented.

In addition to the tests with the NIM signal from the CFD, this circuitry is studied with test pulses from the pulse generator. A 20 ns-long pulse with an amplitude of -100 mV and a rise time of 0.8 ns is generated. Two configurations have been studied:

- Interface board coupled to a break-out board

- Interface board coupled to a NINO32 board and a break-out board

C.1 Interface board coupled to a break-out board

Although the break-out board has not been made for this purpose it can be connected directly to the interface board for the charge and injection capacitor estimate. In this configuration, the pinout is not compatible with the NINO channel pinout from both connectors on the
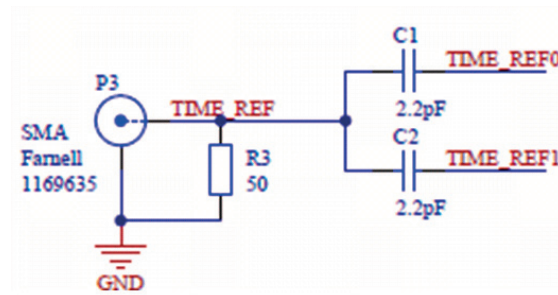
Figure C.1: Injection circuitry on the interface board of Phase II MCP-PMT prototypes (Photek Ltd.).

interface board. The time reference is only seen through one connector (J1), that corresponds to TIME REF0. The output signal is read out from the pins, LDAC (+) and DIN (-), on the break-out board for which their actual functionality is to program the NINO thresholds via the SPI microcontroller. A differential probe is used to monitor the injected charge on an oscilloscope. Figure C.2 shows a photograph of the set-up. Figure C.3 shows two oscilloscope displays for the injection of test pulses from the pulse generator and NIM signal from the CFD. The charge and the injection capacitor results are summarized in Table C.1.
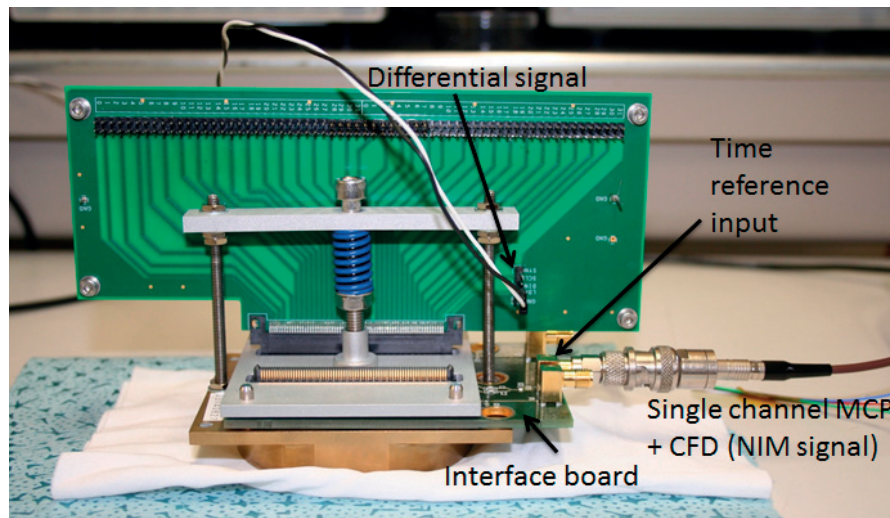
Figure C.2: Photograph showing the injection of a time reference signal via the interface board and the output signal is read out via the break-out board.

C.2 Interface board coupled to a NINO32 board and a break-out board

In this configuration, both time references TIME REF0 and TIME REF1 can be seen through both connectors on the interface board, J1 and J2 respectively. Figure C.4 shows a photograph
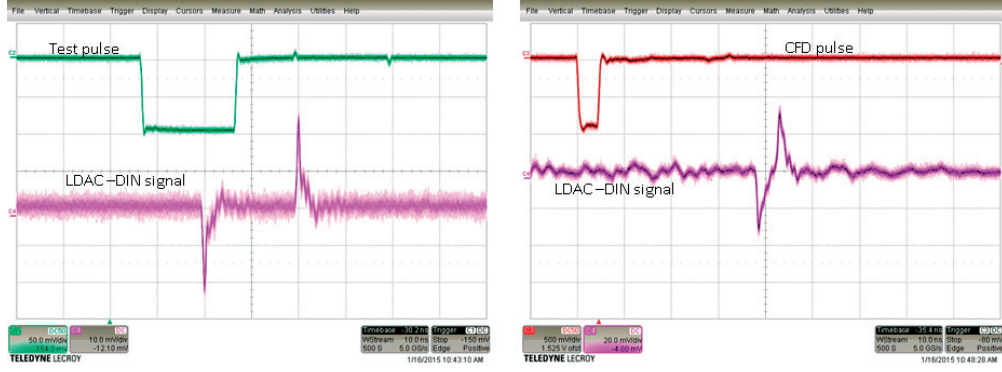
Figure C.3: Oscilloscope displays showing a test pulse and a NIM signal injection into the interface board of the Phase II MCP-PMT prototype.

Table C.1: Charge and injection capacitor estimate for the interface board of two Phase II MCP-PMT prototypes.

Signal	Tube G2140929		Tube G21140827	
	Q [fC]	C [pF]	Q [fC]	C [pF]
test pulse	261±28	2.6±0.5	NA	NA
NIM signal CFD	552±32	2.8±0.5	609±35	2.5±0.4

of the set-up. Each time reference signal is injected into one channel of a NINO chip on a board, TIME REF0 corresponds to chip 1 channel 31 and TIME REF1 corresponds to chip 2 channel 0. Figure C.5 shows two oscilloscope displays for the test pulse and for the NIM signal from the CFD. The NINO pulses are also shown. The time resolution of a NINO channel can be determined from the difference between the leading edge of the NINO pulse and that of the reference pulse, t_{ref}-t_{nino}. Results are summarized in Table C.2. The time resolution values are corrected for the jitter contributions from the pulser and/or the NIM signal and the oscilloscope.

Table C.2: Time resolution for test pulses and NIM signal from the CFD. NINO channels 31 from chip 1 and 0 from chip 2 are studied. The contributions from the jitter of the pulser or laser and oscilloscope are subtracted in quadrature to the resulting time resolutions.

Time resolution (σ) [ps]	Tube G2140929	
	test pulse	jitter from pulser+oscilloscope
chip 1 channel 31	16.6 → 14.5	$11.5/\sqrt{2}$=8.1
chip 2 channel 0	18.3 → 16.4	
	NIM signal CFD	jitter from laser+oscilloscope
chip 1 channel 31	40.6 → 29	$40.1/\sqrt{2}$=28.4
chip 2 channel 0	41.2 → 29.8	
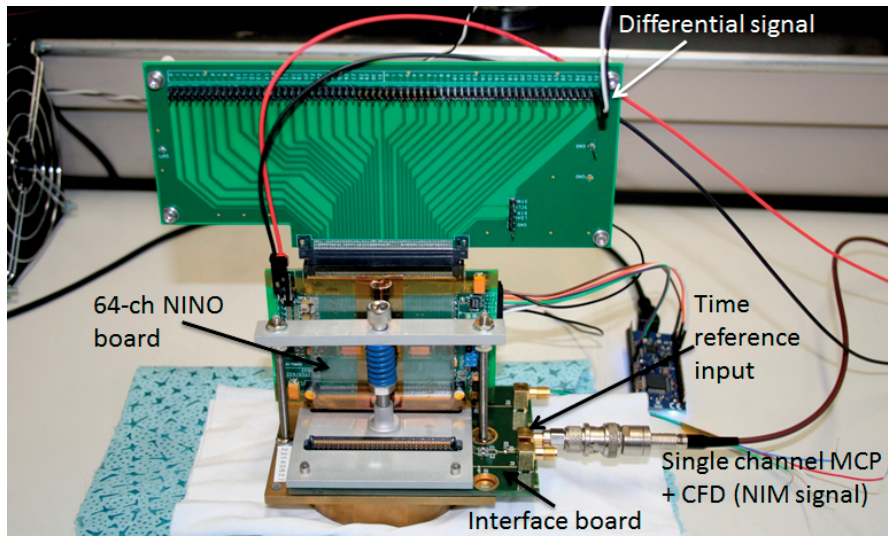
Figure C.4: Photograph showing the injection of a time reference signal via the interface board coupled to the 32-channel NINO board and the output signal is read out via the break-out board on a NINO channel.
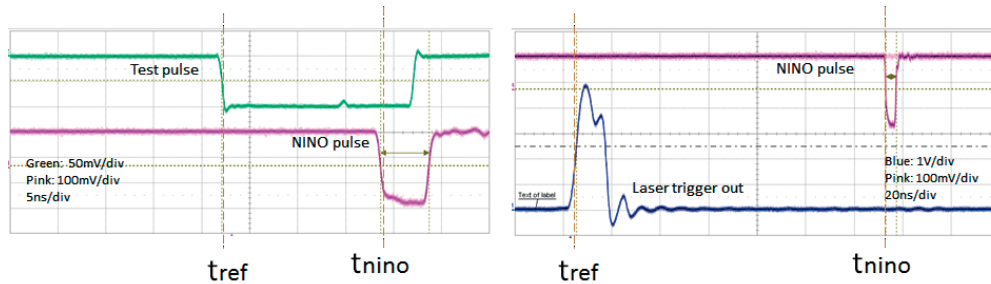
Figure C.5: Oscilloscope displays for the time resolution measurements using a test pulse and a NIM signal from the CFD.

C.3   HPTDC operating resolution mode

The HPTDCs used in the new generation of electronics are operated in HRM of 100 ps bin precision in order to provide 32 channels per chip. A test in VHRM could be performed to see the contribution to the time resolution from the HPTDC time bin.

The time reference signal is input into NINO chip 1 channel 31 (J1 connector) and NINO chip 2 channel 0 (J2 connector). Due to a PCB design error HPTDC channels are swapped by pairs with respect to NINO channels (0-1,2-3,...), the HPTDC channels where the reference signal is injected are TDC A channel 30 and TDC B channel 1, respectively. HPTDC channels 1 and 30 are not active in the 25 ps resolution mode. Consequently, the current electronics design does not allow the use of a time reference as injected through the interface board in 25 ps resolution mode and no timing performance can be assessed in this configuration.

D Phase II MCP-PMT prototype pad map

Figure D.1: Anode pads mapping for the Phase II MCP-PMT prototypes. The conversion tables MCP anode pads into electronics channels are attached.

Table D.1: Conversion table 1 of MCP anode pad into electronics channel.

J1	J2	UFL	NINO CHIP 1	HPTDC A
15	16	49	0	1
14	17	50	1	0
13	18	51	2	3
12	19	52	3	2
11	20	53	4	5
10	21	54	5	4
9	22	55	6	7
8	23	56	7	6
7	24	57	8	9
6	25	58	9	8
5	26	59	10	11
4	27	60	11	10
3	28	61	12	13
2	29	62	13	12
1	30	63	14	15
0	31	64	15	14
15	16	17	16	17
14	17	18	17	16
13	18	19	18	19
12	19	20	19	18
11	20	21	20	21
10	21	22	21	20
9	22	23	22	23
8	23	24	23	22
7	24	25	24	25
6	25	26	25	24
5	26	27	26	27
4	27	28	27	26
3	28	29	28	29
2	29	30	29	28
1	30	31	30	31
Time ref0	31	32	31	30

Table D.2: Conversion table 2 of MCP anode pad into electronics channel.

J1	J2	UFL	NINO CHIP 2	HPTDC B
31	Time ref1	33	0	1
30	1	34	1	0
29	2	35	2	3
28	3	36	3	2
27	4	37	4	5
26	5	38	5	4
25	6	39	6	7
24	7	40	7	6
23	8	41	8	9
22	9	42	9	8
21	10	43	10	11
20	11	44	11	10
19	12	45	12	13
18	13	46	13	12
17	14	47	14	15
16	15	48	15	14
31	0	1	16	17
30	1	2	17	16
29	2	3	18	19
28	3	4	19	18
27	4	5	20	21
26	5	6	21	20
25	6	7	22	23
24	7	8	23	22
23	8	9	24	25
22	9	10	25	24
21	10	11	26	27
20	11	12	27	26
19	12	13	28	29
18	13	14	29	28
17	14	15	30	31
16	15	16	31	30

E Charge-to-width calibration curves at different NINO threshold settings
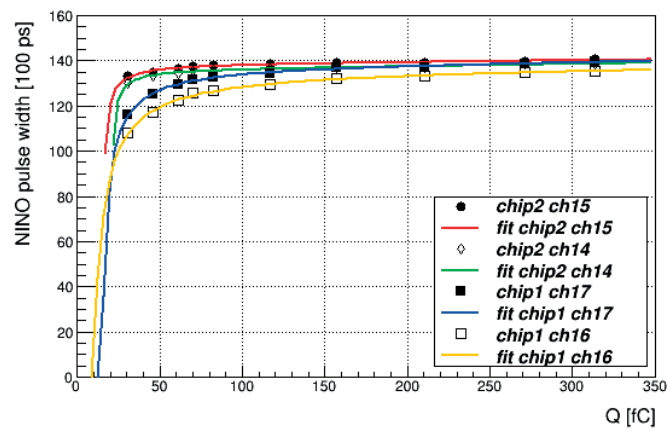
Figure E.1: Charge-to-width calibration curves from four NINO channels at a threshold setting of 50 mV.
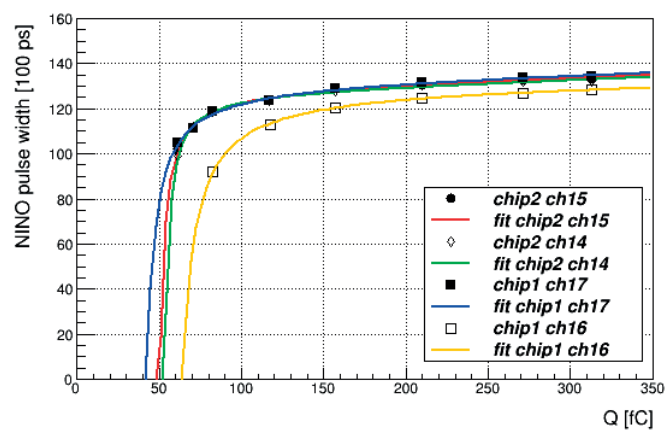
Figure E.2: Charge-to-width calibration curves from four NINO channels at a threshold setting of 200 mV.

F INL correction in HRM
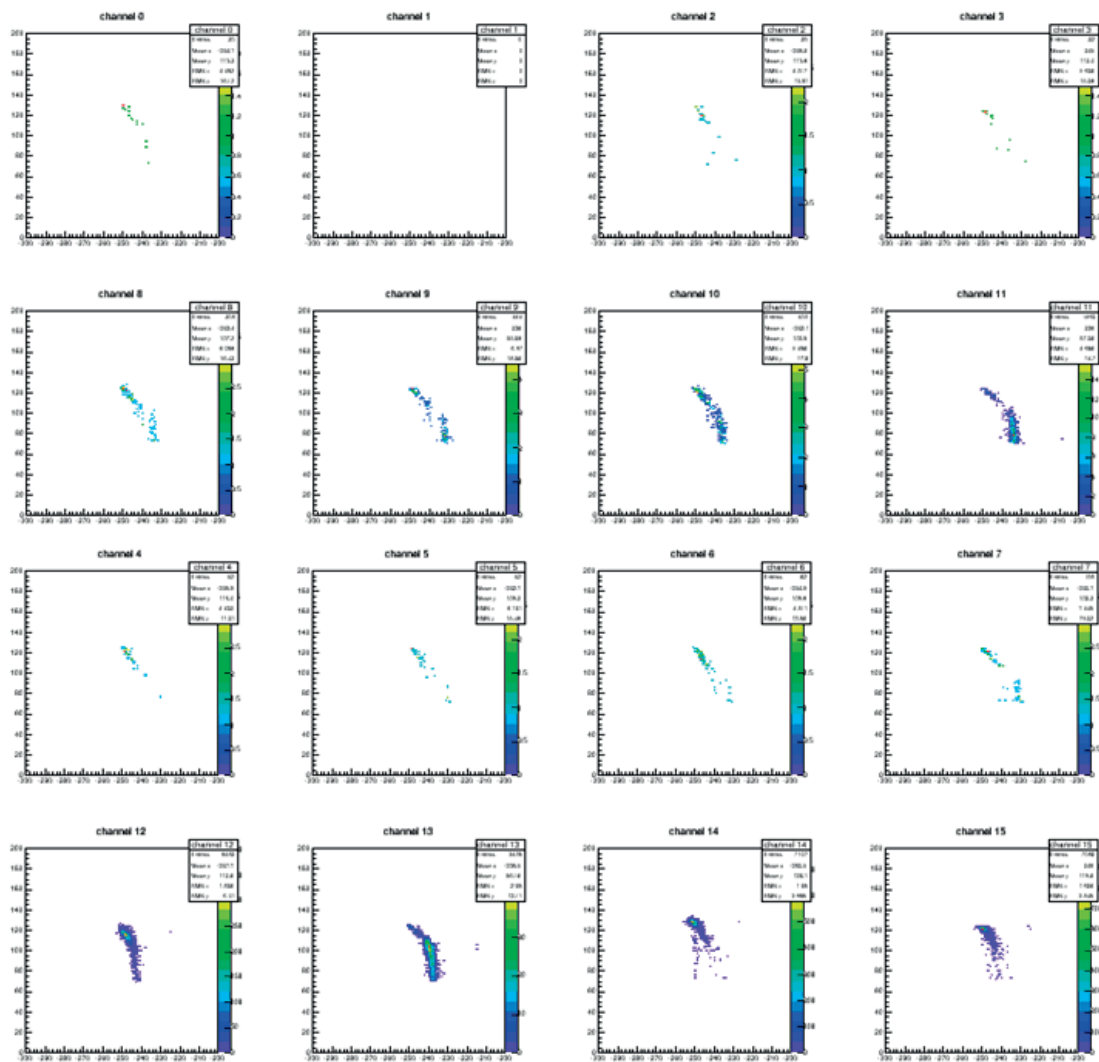
Figure F.1: 2D TOT plot for 16 channels of the NINO chip 2 before INL correction.
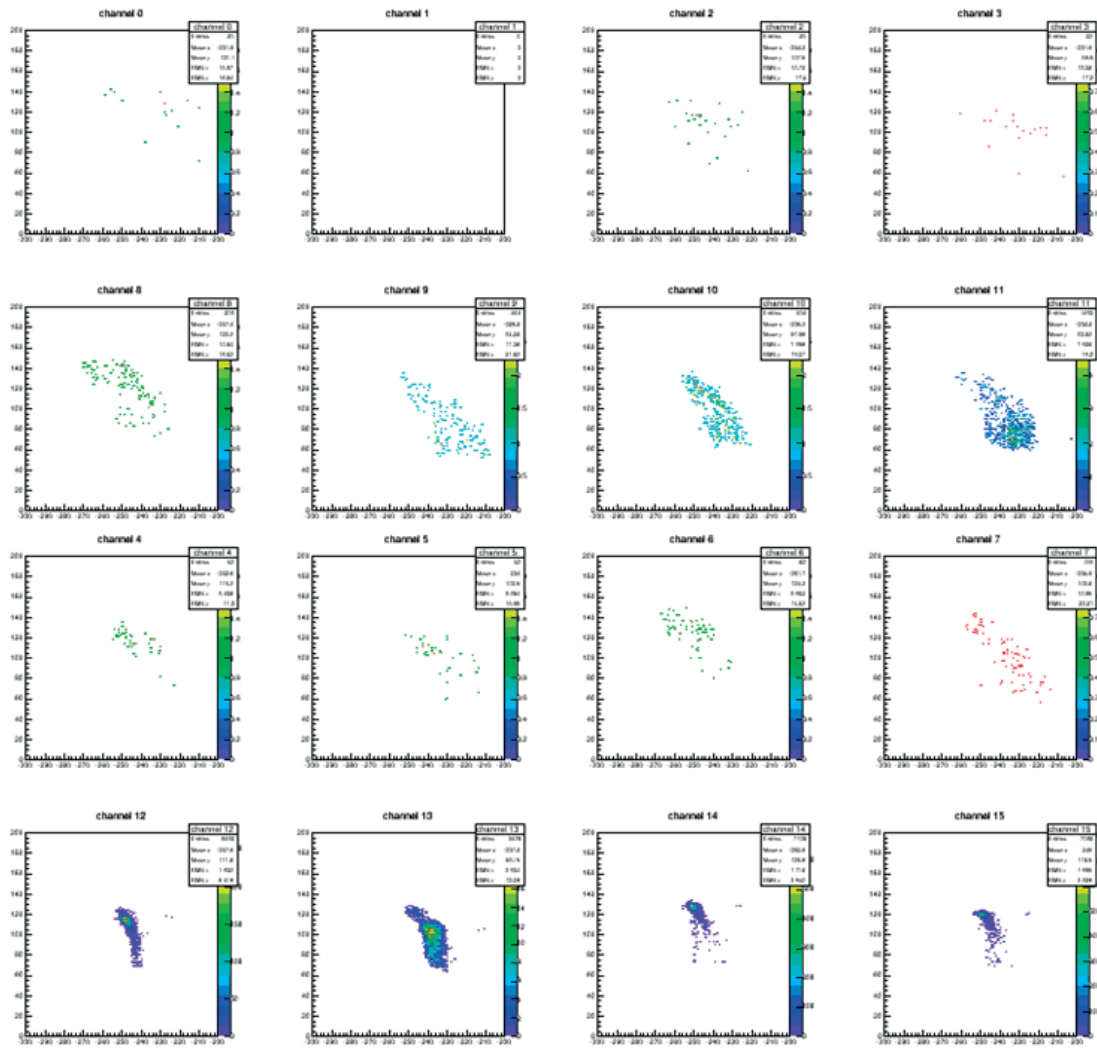
Figure F.2: 2D TOT plot for 16 channels of the NINO chip 2 after INL correction.

G Light transmission studies in borosilicate bars

Light transmission through borosilicate glass samples is studied. These samples have been used in beam tests (Chapter 7) [88, 103] and they are in the form of 100 mm-long bars with a cross-section of $8{\times}8$ mm^2.
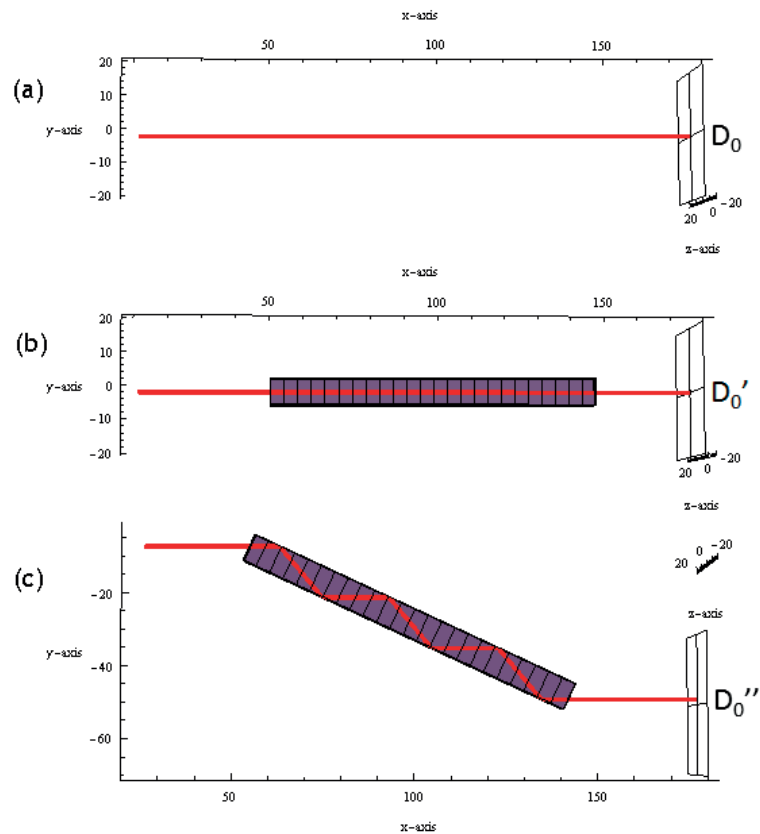
Figure G.1: Simulated configurations for the borosilicate bar measurements: direct transmission (b) and total internal reflection (c).

G.1 Light transmission and scattering losses

Light transmission through the bars, any change in the spot profile and possible scattering effects are investigated. The total image intensity and D_0 are calculated and compared to those corresponding to the reference measurement, I_{ref} and $D_{0\,ref}$, (configuration (a) in Figure G.1).

In configuration (b), laser light is normal to the entrance face of the bar and any distinction between the parallel, $R_\parallel$, and perpendicular, $R_\perp$, components of the reflectance, R, vanishes. From *Fresnel equations* [105], R' at normal incidence is calculated as:

$$R' = R_\parallel = R_\perp = \left(\frac{n_1 - n_2}{n_1 + n_2}\right)^2 = 4.1\% \tag{G.1}$$

where in the present case n_1=1.0 is the refractive index of air and n_2=1.51 is the refractive index of borosilicate glass at 640 nm.

The expected intensity at the exit of the bar is $91.8\%I_{ref}$, since ~2×R' of the light incident normally will be reflected back at the entrance and exit faces of the borosilicate bar. From the analysis of a CCD image the intensity through the bar is $90.6\%I_{ref}$ and D_0' is $104\%D_{0\,ref}$.

Another important effect for TORCH is the total internal reflection (TIR) at the inner surfaces of the radiator plate. This effect is investigated by rotating the borosilicate bar and moving the CCD camera accordingly with the laser spot displacement (configuration (c) in Figure G.1). An image is recorded every even number of reflections up to 6. The same procedure is used to calculate the transmitted intensity and D_0".

In configuration (c), the angle of incidence is 41 °. From *Fresnel equations*:

$$R_\parallel = \left|\frac{n_1\cos\theta_1 - n_2\cos\theta_2}{n_1\cos\theta_1 + n_2\cos\theta_2}\right|^2 = 8.2\% \tag{G.2}$$

$$R_\perp = \left|\frac{n_1\cos\theta_2 - n_2\cos\theta_1}{n_1\cos\theta_2 + n_2\cos\theta_1}\right|^2 = 1.4\% \tag{G.3}$$

where θ_1 is the angle of incidence in air and θ_2 is the angle of refraction in the borosilicate bar. R" for non-polarized light is given by:

$$R'' = \frac{R_\parallel + R_\perp}{2} = 4.8\% \tag{G.4}$$

The expected intensity at the exit of the bar after 6 TIR is $90.4\%I_{ref}$, twice R" due to reflections at the entrance and exit faces of the borosilicate bar. From the analysis of a CCD image the intensity after 6 TIR is $89.2\%I_{ref}$ and D_0" is $102\%D_{0\,ref}$. No measurable intensity loss and light scattering are observed with this method.

G.2 Total internal reflection coefficient of a borosilicate bar

In configuration (c) in Figure G.1 where laser light undergoes TIR, a method used in [117] is applied to determine the total internal reflection coefficient, $\mathcal{R}$, of these borosilicate bars. The technique consists of measuring four light intensities (I_0, I_1, I_2 and I_3) as shown in Figure G.2. It is necessary to move the CCD by hand to find the corresponding laser spot for I_1 and I_3.
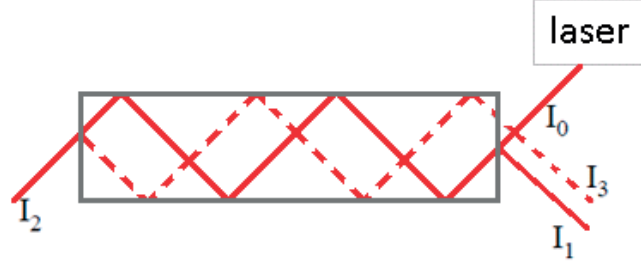
Figure G.2: A schematic layout of the set-up to measure the internal reflection coefficient of borosilicate bars [117].

The four measured intensities are related as follows:

$$\left((I_0 - I_1)\frac{1}{x} - I_2\right)\frac{1}{x} = I_3 \tag{G.5}$$

where $1/x$ is the fraction of the light transmitted as it propagates down the bar one time. This leads to a second order polynomial expression from which the value of $1/x$ can be calculated. The fraction $1/x$ may be written as a combination of reflection losses and bulk attenuation:

$$x^{-1} = \mathcal{R}^N \exp\left(-\frac{L}{\Lambda}\sqrt{1 + \left(\frac{bN}{L}\right)^2}\right) \tag{G.6}$$

where N is the number of TIR, L is the borosilicate bar length, b is the borosilicate bar width and Λ is the bulk attenuation length. Here, the value of Λ for fused silica at 633 nm is used and amounts to 2.1×10^6 mm. The internal reflection coefficient is found to be 1.0±0.2. The resulting level of precision using this method is attributed to laser intensity fluctuations. An improvement in the accuracy will require a more sophisticated and automated set-up which includes several CCDs or photodiodes as in [117] to measure the various intensities simultaneously.

H Alignment of the single start time station

The start time station was aligned with respect to the beam axis using the VELO telescope translation and rotation stage system. Following a pre-alignment with a laser, the initial coordinates (x, y, θ) were (26 mm, 41 mm, 49 °), respectively.
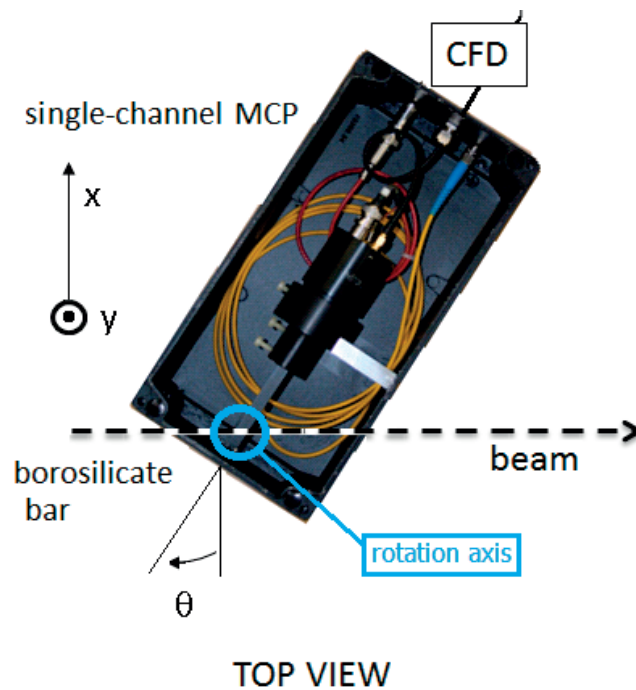
Figure H.1: Start time station geometry in beam test configuration.

For each position, the ratio of counts from the test channel over the number of triggers was calculated. Figure H.2 shows coarse and fine scans in the x (left) and y (right) directions. Displacements in the positive x direction correspond to moving the station away from the beam axis which results in a count drop. When moving the station closer to the beam axis the count ratio was increasing. To keep the single-channel MCP at a safe distance from the beam

axis, the original x position was kept unchanged. The offset correction in the y direction was -2 mm. Figure H.3 shows coarse and fine rotation scans. The optimal angle was -8 ° from the initial value. The complementary angle, 90 °- θ, was consistent with the Cherenkov angle in borosilicate glass, ~49 °. The coordinates for the optimal alignment were found to be (26 mm, 39 mm, 41 °). The count ratio on the test channel was further improved by reducing the CFD threshold level.
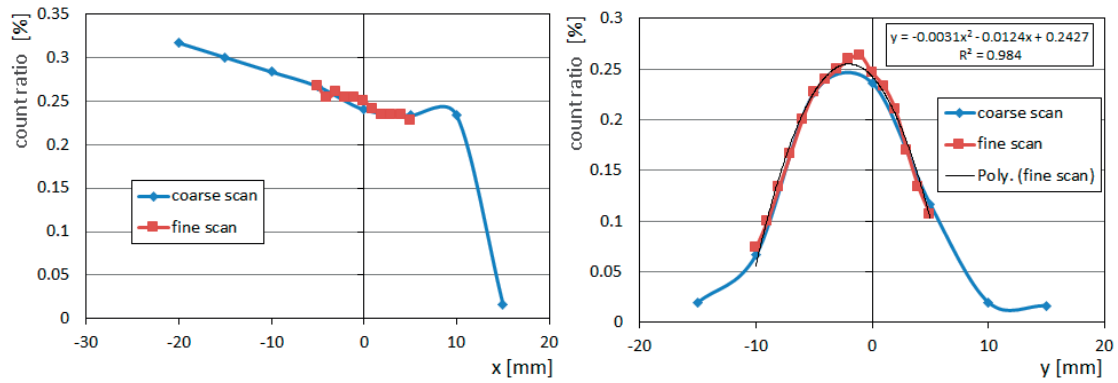
Figure H.2: Start time station scans in the x (left) and y (right) transversal directions with respect to the beam axis.
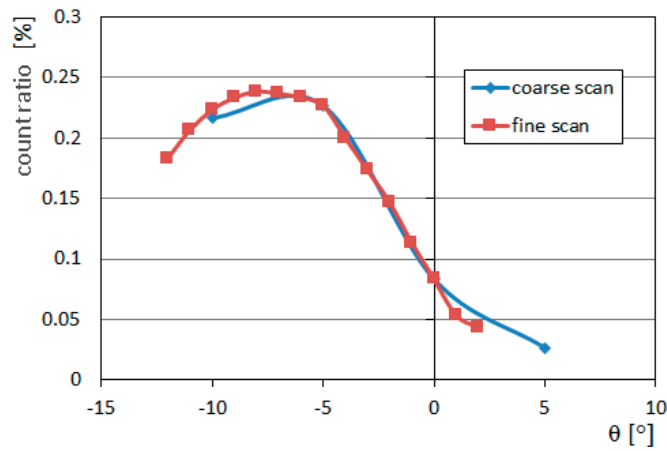
Figure H.3: Start time station rotation scan.

I NINO threshold optimization

The NINO threshold settings were optimized by monitoring the response of all channels. The initial settings were 100 mV, the value that was previously used in the laboratory. In Chapter 5 it was estimated that the same threshold setting resulted in a different actual threshold for each NINO channel. Since the threshold settings are configured separately for odd and even channels for both NINO chips on a board, several combinations were tried. Figure I.1 shows a screen display of the DAQ software with channel count histograms (top plots) for both NINO chips. On the left display it is observed that odd and even channels respond differently and on the right display, for an optimized threshold setting, the response has been homogenized[1]. Three NINO threshold settings were chosen: 50, 100 and 200 mV.
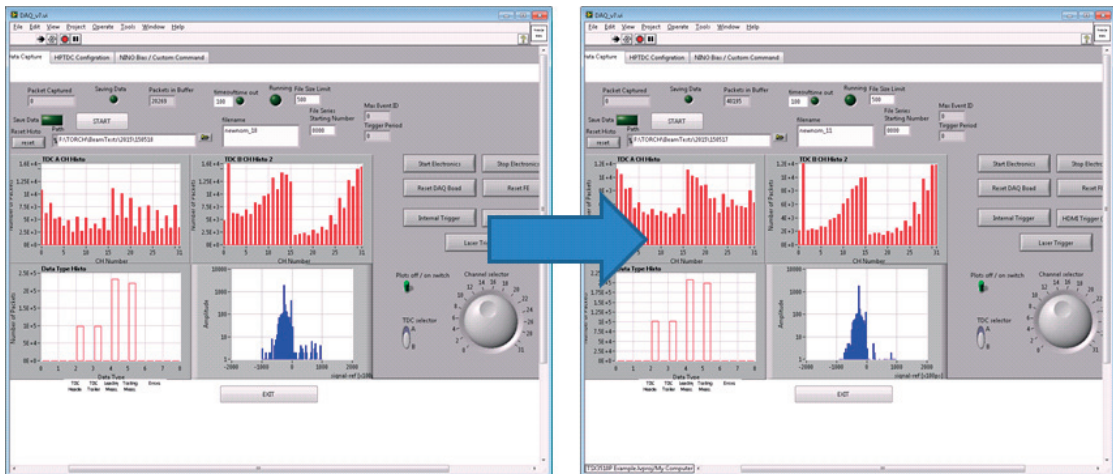
Figure I.1: Screen display of DAQ software showing the channel hit response with NINO threshold used in the laboratory (left) and the optimized setting in test beam (right).

---

[1]Note that due to the PCB layout error, odd and even channels are swapped by pairs on the LabVIEW display.

J Alignment of the two-station system

The two-station system was aligned with respect to the beam axis using the VELO pixel telescope translation and rotation stage system. The initial coordinates (x, y, θ) were (26 mm, 39 mm, 41 °), respectively. For each specific position, the ratio of counts on the pedestal over the number of total counts in the pulse height spectrum was calculated for both stations. Figures J.1 and J.2 show the measured points for XY and θ scans. The coordinates for the optimal alignment were found to be (27 mm, 41 mm, 41 °).
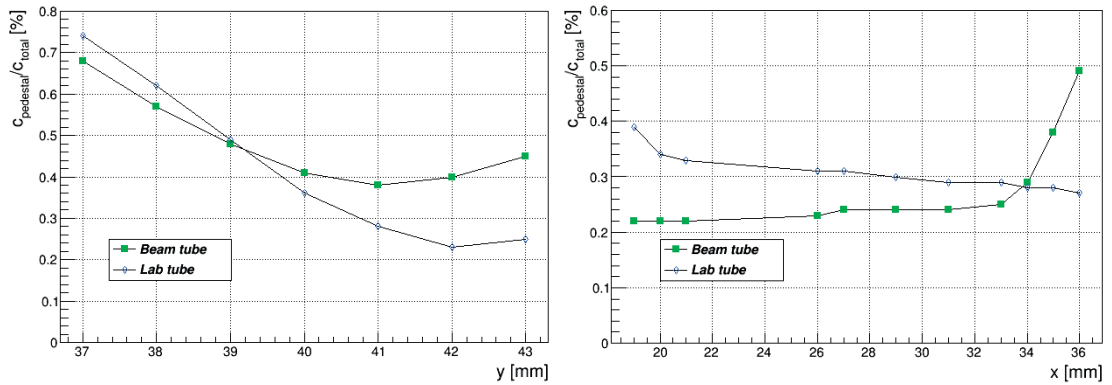
Figure J.1: Two-station system scans in the y (left) and x (right) transversal direction with respect to the beam axis.

Figure J.2: Two-station system rotation scan.
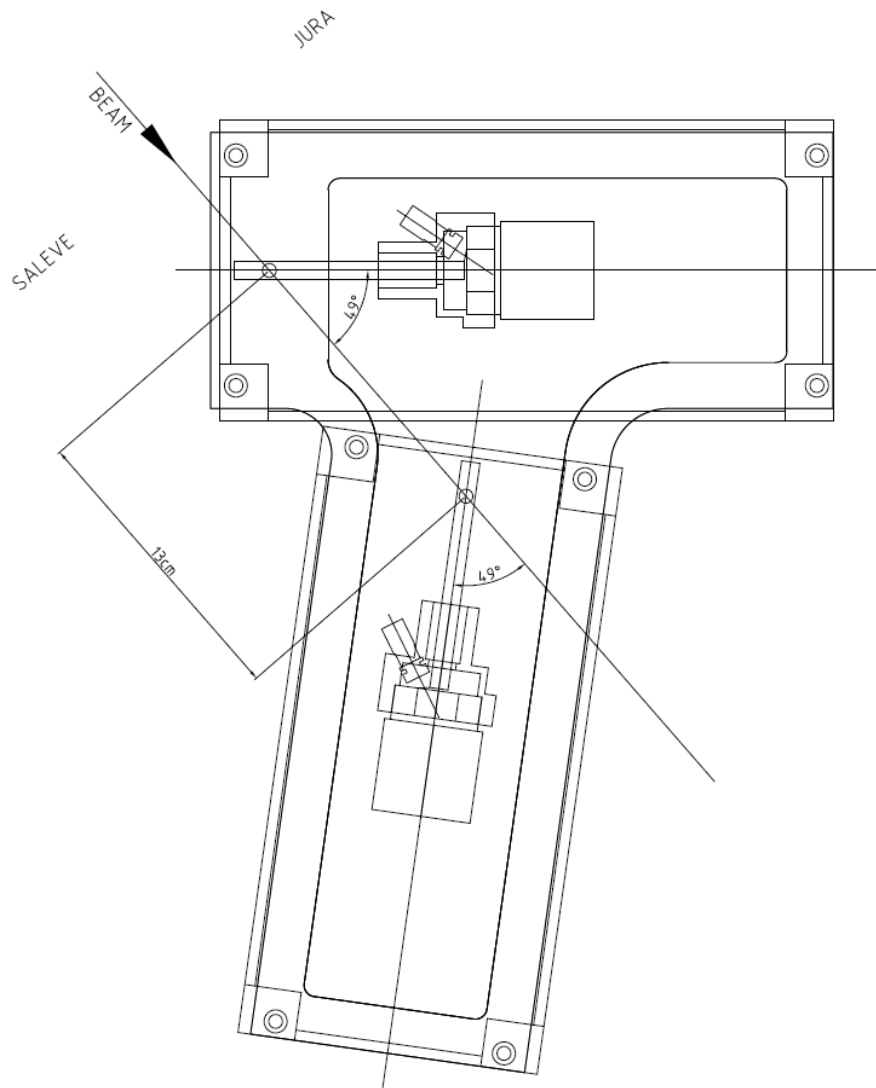
Figure J.3: Two-station system geometry provided by D. Piedigrossi.

Bibliography

[1] C. Lippmann. *Particle identification.* Nucl. Instr. and Meth. A **666** (2012) 148-172.

[2] P. Križan. *Overview of particle identification techniques.* Nucl. Instr. and Meth. A **706** (2013) 48-54.

[3] J. Va'vra. *PID Techniques: Alternatives to RICH Methods.* Nucl. Instr. and Meth. A **639** (2011) 193-201.

[4] E. Nappi. *Charged Particle Identification via Ionization Energy Loss and Time-of-Flight Measurements.* AIP Conf. Proc. *674* (2003) 18.

[5] The ALICE Collaboration. *The ALICE experiment at the CERN LHC.* JINST **3** (2008) S08002.

[6] L. Evans et al. *LHC Machine.* JINST **3** (2008) S08001.

[7] *CERN.* http://home.web.cern.ch/.

[8] The ALICE Collaboration. *ALICE Technical Design Report of the Time-of-flight system.* CERN-LHCC-2000-012.

[9] P. Antonioli. *The ALICE time-of-flight system.* Nucl. Phys. Proc. Suppl. B **125** (2003) 193-197.

[10] A. Akindinov et al. *The multigap resistive plate chamber as a time-of-flight detector.* Nucl. Instr. and Meth. A **456** (2000) 16-22.

[11] F. Anghinolfi et al. *NINO: an ultra-fast and low-power front-end amplifier/discriminator ASIC designed for the multigap resistive plate chamber.* Nucl. Instr. and Meth. A **533** (2004) 183-187.

[12] M. Mota, J. Christiansen, et al. *A flexible multi-channel high-resolution time-to-digital converter ASIC.* IEEE Trans. Nucl. Sci. **2** (2000) 9/155-159.

[13] J. Christiansen. *HPTDC High Performance Time to Digital Converter.* version **2.2** (2004) for HPTDC version 1.3. https://edms.cern.ch/file/599848/2.2/hptdc_manual_ver2.2.pdf.

Bibliography

[14] A. Akindinov et al. *Performance of the ALICE Time-of-flight detector at the LHC.* Eur. Phys. J. Plus **128** (2013) 44.

[15] E. D. Palik. *Handbook of Optical Constants of Solids.* Academic Press (1998).

[16] J. V. Jelley. *Cerenkov Radiation And Its Applications.* Pergamon Press, London (1958).

[17] P. A. Cherenkov. *Visible light from clear liquids under the action of gamma radiation.* C. R. (Doklady) Akad. Sci. URSS **2** (1934) 451-454.

[18] *Generating Cerenkov Radiation.* http://mxp.physics.umn.edu/s04/projects/ s04cherenkov/theory.htm.

[19] J.D. Jackson. *Classical electrodynamics.* Third Edition John Wiley & Sons, Inc.

[20] I. Frank and I. Tamm. *Coherent Visible Radiation of Fast Electrons Passing Through Matter.* Dokl. Akad. NaukSSSR **14** (1937) 109.

[21] *The Nobel Prize in Physics 1958.* http://www.nobelprize.org/nobel_prizes/physics/ laureates/1958/.

[22] J. Litt and R. Meunier. *CERENKOV COUNTER TECHNIQUE IN HIGH-ENERGY PHYSICS.* Ann. Rev. Nucl. Sci. **23** (1973) 1-44.

[23] J. Seguinot and T. Ypsilantis. *Photo-ionization and Cherenkov ring imaging.* Nucl. Instr. and Meth. **142** (1977) 377-391.

[24] Particle data group, J. Beringer, et al. *Review of particle physics.* Phys. Rev. D **86** (2012).

[25] The LHCb Collaboration. *The LHCb detector at the LHC.* JINST **3** (2008) S08005.

[26] The LHCb Collaboration. *LHCb RICH Technical Design Report.* CERN-LHCC-2000-037.

[27] A.F. Danilyuk, V.L. Kirillov, et al. *Recent results on aerogel development for use in Cherenkov counters.* Nucl. Instr. and Meth. A **494** (2002) 491-494.

[28] Y. Sallaz-Damaz, L. Derome, et al. *Characterization study of silica aerogel for Cherenkov imaging.* Nucl. Instr. and Meth. A **614** (2010) 184-195.

[29] D.L.Perego. *The LHCb RICH silica aerogel performance with LHC data.* Nucl. Instr. and Meth. A **639** (2011) 234-237.

[30] M. Boostels, F. Hahn, S. Haider, R. Lindner, and O. Ullaland. *LHCb RICH Gas System Proposal.* LHCb-2000-079.

[31] F.C.D. Metlica and LHCb Collaboration. *Development of light-weight spherical mirrors for RICH detectors.* Nucl. Instr. and Meth. A **595** (2008) 197-199.

[32] T. Gys. *The pixel hybrid photon detectors for the LHCb-rich project.* Nucl. Instr. and Meth. A **465** (2001) 240-246.

[33] K. Wyllie et al. *Silicon detectors and electronics for pixel hybrid photon detectors.* Nucl. Instr. and Meth. A **530** (2004) 82-86.

[34] T. Gys. *Status and perspectives of vacuum-based photon detectors for single photon detection.* Nucl. Instr. and Meth. A **595** (2008) 136-141.

[35] R. Forty and O. Schneider. *RICH pattern recognition.* LHCb-98-040.

[36] The LHCb RICH Collaboration. *Performance of the LHCb RICH detector at the LHC.* Eur. Phys. J. C **73** (2013) 2431.

[37] B. Ratcliff. *The B Factory Detector for PEP-II: a Status Report.* SLAC-PUB-5946.

[38] I. Adam, R. Aleksan, et al. *The DIRC Particle Identification System for the BaBar Experiment.* Nucl. Instr. and Meth. A **538** (2005) 281-357.

[39] K. Inami et al. *Development of a TOP counter for the Super B factory.* Nucl. Instr. and Meth. A **595** (2008) 96-99.

[40] T. Abe et al. *Belle II Technical Design Report.* KEK Report 2010-1.

[41] P. Schoenmeier et al. *Disc DIRC endcap detector for PANDA@FAIR.* Nucl. Instr. and Meth. A **595** (2008) 108-111.

[42] The LHCb Collaboration. *LHCb Particle identification Upgrade Technical Design Report.* CERN-LHCC-2013-022.

[43] M.J. Charles and R. Forty. *TORCH: Time of flight identification with Cherenkov radiation.* Nucl. Instr. and Meth. A **639** (2011) 173-176.

[44] The LHCb Collaboration. *Letter of Intent for the LHCb Upgrade.* CERN-LHCC-2011-001.

[45] R. Forty. *The TORCH project.* JINST **9** (2014) C04024.

[46] *ERC-2011-AdG, 291175-TORCH.* http://cordis.europa.eu/projects/rcn/103813_en.html.

[47] L. Castillo García. *Testing micro-channel plate detectors for the particle identification upgrade of LHCb.* Nucl. Instr. and Meth. A **695** (2012) 398-402.

[48] S. Agostinelli, J. Allison, et al. *GEANT4 - a simulation toolkit.* Nucl. Instr. and Meth. A **506** (2003) 250-303.

[49] J. Allison et al. *Geant4 developments and applications.* IEEE Transactions on Nuclear Science **53** No. 1 (2006) 270-278.

[50] R. Gao, R. Cardinale, L. Castillo García, et al. *Development of precision Time-Of-Flight electronics for LHCb TORCH.* JINST **9** (2014) C02025.

[51] R. Gao, N. Brook, L. Castillo García, et al. *Development of scalable electronics for the TORCH time-of-flight detector.* JINST **10** (2015) C02028.

Bibliography

[52] M. Van Dijk. *Design of the TORCH detector: A Cherenkov based Time-of-Flight system for particle identification.* PhD thesis, University of Bristol, 2016. https://cds.cern.ch/record/2154410?ln=en.

[53] A. Einstein. *Concerning an Heuristic Point of View Toward the Emission and Transformation of Light.* Annalen der Physik **17** (1905): 132-148.

[54] *The Nobel Prize in Physics 1921.* http://www.nobelprize.org/nobel_prizes/physics/laureates/1921/.

[55] W.B. Colson, J. McPherson, and F.T. King. *High-gain imaging electron multiplier.* Rev. Sci. Instr. Vol. **44** Issue 12 (1973) 1694-1696.

[56] S. Korpar, P. Križan, et al. *Timing and cross-talk properties of BURLE multi-channel MCP PMTs.* Nucl. Instr. and Meth. A **595** (2008) 169-172.

[57] A. H. Sommer. *Multi-alkali photo-cathodes.* IRE Trans Nucl Sci **3** Issue 4 (1956) 8-12.

[58] W. E. Spicer. *Photoemissive, Photoconductive, and Optical Absorption Studies of Alkali-Antimony Compounds.* Phys. Rev. **112** (1958) 114.

[59] W. E. Spicer and A. Herrera-Gómez. *Modern Theory and Applications of Photocathodes.* Proc. SPIE **2022** Photodetectors and Power Meters, 18 (1993).

[60] K. Nakamura, Y. Hamana, Y. Ishigami, and T. Matsui. *Latest bialkali photocathode with ultra high sensitivity.* Nucl. Instr. and Meth. A **623** (2010) 276-278.

[61] I. P. Csorba. *Image tubes.* Howard W. Sams & Co. Inc (1985).

[62] T. Gys. *Micro-channel plates and vacuum detectors.* Nucl. Instr. and Meth. A **787** (2015) 254-260.

[63] Joseph Ladislas Wiza. *Microchannel plate detectors.* Nucl. Instr. and Meth. A **162** (1979) 587-601.

[64] J. G. Timothy. *Microchannel plates for photon detection and imaging in space.* ISSI Scientific Reports Series **9** (2010), p. 365.

[65] Photek. *Image Intensifier User Guide.* Electrodes and End Spoiling section. http://www.photek.co.uk/pdf/technical-papers/Intensifier_ManualDS2.pdf.

[66] N. Kishimoto et al. *Lifetime of MCP-PMT.* Nucl. Instr. and Meth. A **564** (2006) 204-211.

[67] T. Jinno et al. *Lifetime-extended MCP-PMT.* Nucl. Instr. and Meth. A **629** (2011) 111-117.

[68] D. R. Beaulieu et al. *Nano-engineered ultra-high-gain microchannel plates.* Nucl. Instr. and Meth. A **607** (2009) 81-84.

[69] A. Lehmann et al. *Improved lifetime of microchannel-plate PMTs.* Nucl. Instr. and Meth. A **766** (2014) 138-144.

196

[70] A. Lehmann et al. *Lifetime of MCP-PMTs.* 2016 JINST **11** C05009.

[71] T. M. Conneely, J.S. Milnes, and J. Howorth. *Extended lifetime MCP-PMTs: Characterisation and lifetime measurements of ALD coated microchannel plates, in a sealed photomultiplier tube.* Nucl. Instr. Meth. A **732** (2013) 388-391.

[72] L. Castillo García. *Systematic studies of micro-channel plate tubes model PP0365G from Photonis.* LHCB-PUB-2013-017.

[73] *Handbook of Kodak Photographic Filters.* Eastman Kodak Company (1990).

[74] ORTEC. *Modular Pulse-Processing Electronics catalogue.* Section on preamplifiers. http://www.ortec-online.com/download/ORTEC-Catalog-Modular-Electronics-Section.pdf.

[75] ORTEC. *Modular Pulse-Processing Electronics catalogue.* Section on amplifiers. Same as Ref. [74].

[76] ORTEC. *Modular Pulse-Processing Electronics catalogue.* Section on fast timing discriminators. Same as Ref. [74].

[77] K. Carnes. *Constant Fraction Discriminators.* (2003). http://jrm.phys.ksu.edu/Resource/Pubs/CFD/CFD.doc.

[78] ORTEC. *1-GHz Amplifier and Timing Discriminator.* model 9327. http://www.ortec-online.com/download.asbx?AttributeFileId=71ec09fa-b9ea-45ef-94e7-6603ea255854.

[79] ORTEC. *Modular Pulse-Processing Electronics catalogue.* Section on time-to-amplitude converters. Same as Ref. [74].

[80] I. G. McWilliam and H. C. Bolton. *Instrumental peak distortion.* Analytical Chemistry, Vol. 41, No. 13, November (1969) 1755-1762.

[81] Y. Tanaka. *A Study on Performance of Micro Channel Plate Detectors for the TORCH System within the LHCb Upgrade.* CERN Summer Student internal report, September (2011).

[82] M. A. Furman and M. T. F. Pivi. *Probabilistic model for the simulation of secondary electron emission.* Phys. Rev. ST Accel. Beams **5** (2002) 124404.

[83] M. A. Furman and M. T. F. Pivi. *Erratum: Probabilistic model for the simulation of secondary electron emission.* Phys. Rev. ST Accel. Beams **16** (2013) 069901.

[84] T. Gys, L. Castillo García, J.Fopma, et al. *Performance and lifetime of micro-channel plate tubes for the TORCH detector.* Nucl. Instr. and Meth. A **766** (2014) 171-172.

[85] M. Despeisse et al. *Multi-Channel Amplifier-Discriminator for Highly Time-Resolved Detection.* IEEE Trans Nucl Sci **58** Issue 1 (2011) 202-208.

Bibliography

[86] L. Castillo García. *Timing performance of a MCP photon detector read out with multi-channel electronics for the TORCH system.* Astroparticle, Particle, Space Physics and Detectors for Physics Applications, **8** (2014) 633.

[87] L. Castillo García, N. Brook, et al. *Micro-channel plate photon detector studies for the TORCH detector.* Nucl. Instr. and Meth. A **787** (2015) 197-202.

[88] R. Cardinale. *The RICH detectors for the LHCb experiment and a study of charmless three-body B decays.* PhD thesis, Università degli Studi di Genova, 2013. CERN-THESIS-2013-293.

[89] T. Gys. *CERN Summer Students' workshop: Time-Of-Flight.* 2013-2014.

[90] M. Mota. *Design and Characterization of CMOS High-Resolution Time-to-Digital Converters.* PhD thesis, Technical University of Lisbon, 2000. http://paulo.moreira.free.fr/microelectronics/padova/thesisManuelMota.pdf.

[91] W. Gao et al. *Integrated High-Resolution Multi-Channel Time-to-Digital Converters (TDCs) for PET Imaging.* Biomedical Engineering, Trends in Electronics, Communications and Software (2011) Chapter 16.

[92] J. Schambach. *Proposed STAR Time of Flight Readout Electronics and DAQ.* Computing in High Energy and Nuclear Physics (2003) 1-10.

[93] J. Doernberg. *Full-speed testing of A/D converters.* IEEE Journal of Solid-State Circuits, Vol. 19, No. 6, pp. 820-827, Dec. 84.

[94] Z. Sang et al. *A non-linearity correction method for fast digital multichannel analyzers.* Physics Procedia **37** (2012) 1594-1599.

[95] D. McDonald. *Calibration of the STAR Time-of-Flight Detector for Particle Identification.* Master's thesis, Rice University, 2010. https://scholarship.rice.edu/handle/1911/70345.

[96] J. H. Ricketts and G. A. Head. *A five-parameter logistic equation for investigating asymmetry of curvature in baroreflex studies.* Am J. Physiol. (Regulatory Integrative Comp. Physiol. 46) **277** (1999) 2 R441-R454.

[97] P. Križan et al. *Tests of the Burle 85011 64-anode MCP PMT as a detector of Cherenkov photons.* Nucl. Instr. and Meth. A **567** (2006) 124-128.

[98] A. Lehmann et al. *Studies of MCP properties.* JINST **4** (2009) P11024.

[99] T. M. Conneely, N. Brook, et al. *The TORCH PMT: a close packing, multi-anode, long life MCP-PMT for Cherenkov applications.* JINST **10** (2015) C05003.

[100] ShinEtsu Polymer. *MT-type of inter-connector.* webpage accessed April 2015.

[101] J.S. Milnes, T. M. Conneely, et al. *The TORCH PMT, a close packing, multi-anode, long life MCP–PMT for Cherenkov applications.* Nucl. Instr. Meth. A **766** (2014) 183-184.

[102] T. M. Conneely, J.S. Milnes, and J. Lapington. *Simulation studies of a novel, charge sharing, multi-anode MCP detector.* PoS (TIPP2014) 306.

[103] L. Castillo García, N. Brook, et al. *Development, characterization and beam tests of a small-scale TORCH prototype module.* 2016 JINST **11** C05022.

[104] *Optica Software.* http://www.opticasoftware.com/.

[105] E. Hecht. *Optics.* 4th Edition (2002) Pearson Education Inc. publishing as Addison Wesley.

[106] *Spartan-3 FPGA data sheet.* http://www.xilinx.com/support/documentation/data_sheets/ds557.pdf.

[107] *Spartan-6 FPGA data sheet.* http://www.xilinx.com/support/documentation/data_sheets/ds160.pdf.

[108] *AIDA mini TLU.* http://www.ohwr.org/projects/fmc-mtlu/wiki.

[109] J. Jakubek. *Precise energy calibration of pixel detector working in time-over-threshold mode.* Nucl. Instr. Meth. A **633** S1 (2011) S262-S266.

[110] ALICE Collaboration. *Performance of the ALICE VZERO system.* JINST **8** (2013) P10016.

[111] J. Newell, U. Genschel, and N. Zhang. *Media Discontinuance: Modeling the Diffusion "S" Curve to Declines in Media Use.* Journalism publications and other works, Paper 1 (2014).

[112] *ROOT website.* http://root.cern.ch/.

[113] M. Laub. *Development of opto-mechanical tools and procedures for the new generation of RICH-detectors at CERN.* PhD thesis, 2001. LHCb-2001-130.

[114] *EPO-TEK 305 technical data sheet.* http://www.epotek.com/site/administrator/components/com_products/assets/files/Style_Uploads/305.pdf.

[115] *EPO-TEK 301-2 technical data sheet.* http://www.rikei.co.jp/epo-tek/pdf/05/301-2.pdf.

[116] K. Akiba et al. *The Timepix Telescope for high performance particle tracking.* Nucl. Instr. and Meth. A **723** (2013) 47-54.

[117] J. Cohen-Tanugi et al. *Optical properties of the DIRC Fused Silica Cherenkov Radiator.* SLAC-PUB-9735 (2003).

Lucía Castillo García

Physicist

464 B 002 Rue du Breu
01710 Thoiry (France)
📞 +41 (0) 76 238 91 18
✉ lcastillogarcia@hotmail.com
30 years old, Spanish

Education

Sept. 2012 – May 2016 **PhD in Physics**, *Ecole Polytechnique Fédérale de Lausanne (EPFL)*, Switzerland.
Study of a prototype module of a precision time-of-flight detector for particle identification at low momentum. Thesis director: Prof. T. Nakada

2004 – 2011 **Physics Degree**, *Universidad de Granada*, Spain.
First 2 years studied at Universitat de Barcelona.

2009 – 2010 **Physics Erasmus exchange programme**, *EPFL*, Switzerland.
Attended courses at level of Bachelor and Master of Science in Physics.

Research activities

since 2010 **Member of LHCb Collaboration**.

2015 **Reviewer**, *Reviewer of a research article in Applied Optics OSA journal*.

TORCH project: *ERC-2011-AdG, 291175-TORCH*

Innovative DIRC-style time-of-flight detector for particle identification proposed for the upgrade of LHCb experiment, [*NIM A **639** (2011) 173-176*, *JINST **9** (2014) C04024*].

2012 – 2015 **CERN Doctoral Student**, *CERN*, Geneva, Switzerland. Supervisor: T. Gys.

- Operation of commercial and custom made micro-channel plate photon detectors and investigation of their spatial and timing properties
- Use of analytical models to describe physical phenomena in a photon detector
- Characterization, calibration and contribution to the development of fast multi-channel custom made readout electronics
- Study of scattering effects and transmission properties of glass and optical glue samples
- Simulation of optical components of a TORCH prototype using a ray tracing software
- Prototype development and commissioning in test-beam campaigns involving important activities: pre-characterization in the laboratory, operation of data acquisition and monitoring software, development of analysis software and data analysis
- Oral communication skills expressed in regular presentations in TORCH Collaboration meetings and participating at international conferences, schools and workshops
- Writing reports and scientific papers

2010 – 2011 **CERN Technical Student**, *CERN*, Geneva, Switzerland. Supervisor: T. Gys.

- Characterization of micro-channel plate photon detectors: laboratory tests, data acquisition, data analysis, regular presentations and participation at an international conference

Publications

Main author

5 **Development, characterization and beam tests of a small-scale TORCH prototype module**, *DIRC2015 proceedings*, *2016 JINST **11** C05022*.

Spatial properties of customized MCP photon detectors are investigated using multi-channel read-out electronics. Results from the characterization of small-scale TORCH prototype with a charge-particle beam are discussed.

4 **MCP photon detectors studies for the TORCH detector**, *NDIP2014 proceedings*, *Nucl. Instr. and Meth. A **787** (2015) 197-202*.

Commercial and customized MCP photon detectors are characterized in the laboratory. The focusing quality is verified by simulation.

3 **Timing performance of a MCP photon detector read out with multi-channel electronics for the TORCH system**, *14thICATPP proceedings*, *Astroparticle, Particle, Space Physics and Detectors for Physics Applications, **8** (2014) 633*.

A commercial MCP photon detector is characterized using customized multi-channel electronics and the photo-electron efficiency is estimated.

2 **Systematic studies of micro-channel plate tubes model PP0365G from Photonis**, *LHCb public note, LHCB-PUB-2013-017*.

The probability of back-scattered photo-electrons at the input surface of a MCP is studied for various MCP photon detectors.

1 **Testing micro-channel plate detectors for the particle identification upgrade of LHCb**, *NDIP2011 proceedings*, *Nucl. Instr. and Meth. A **695** (2012) 398-402*.

A commercial MCP photon detector is characterized using single-channel electronics and spatial properties are investigated.

Direct contribution

4 **Performance and lifetime of micro-channel plate tubes for the TORCH detector**, *Nucl. Instr. and Meth. A **766** (2014) 171-172*.

Contribution to photon detector characterization.

3 **LHCb PID Upgrade Technical Design Report**, *CERN-LHCC-2013-022*.

Contribution to Appendix 2.7 on photon detector and read-out electronics performance.

2 **R&D status for the LHCb TORCH project**, *JINST **6** (2011) C10004*.

Contribution to photon detector characterization.

1 **Letter of Intent for the LHCb Upgrade**, *CERN-LHCC-2011-001*.

Contribution to Chapter 7, Section 7.2 on photon detector characterization.

Other publications

2012 – 2015 **I have been co-author of other 9 research papers, 2 of them to be published**.

Conferences, schools and workshops

Talks

11 – 13 November 2015 **DIRC2015, Workshop on fast Cherenkov detectors**, *Rauischholzhausen*, Germany.
Development, characterization and beam tests of a small-scale TORCH prototype module.

30 June – 4 July 2014 **NDIP2014, International Conference on New Developments In Photodetection**, *Tours*, France.
MCP photon detectors studies for the TORCH detector.

23 – 27 Sept. 2013	**14th ICATPP, Conference on Astroparticle, Particle, Space Physics, Detectors for Physics Applications**, *Como*, Italy.
	Timing performance of a MCP photon detector read out with multi-channel electronics for the TORCH system.

April 2014	**CERN Doctoral Students Assembly**, *Geneva*, Switzerland.
	Optical properties studies of glass samples for prototyping a TORCH detector module, *CERN-Poster-2014-419*.
27 – 31 May 2013	**3rd EIROforum School on Instrumentation**, *CERN*, Geneva.
	TORCH: Time-of-flight detector for low momentum PID, *CERN-Poster-2014-423*.
4 – 8 July 2011	**NDIP2011, International Conference on New Developments In Photon detection**, *Lyon*, France.
	Testing micro-channel plate detectors for the particle identification upgrade of LHCb.

Other

2013 - 2014	**CERN Time-Of-Flight Workshop**, *Geneva*, Switzerland.
	Preparation and contribution to two Time-Of-Flight Workshops for Summer Students at CERN

Software skills

Programming	**C/C++**	Data analysis	**Mathematica, ROOT**
Editors	**MS Office, LATEX**	Design	**LabVIEW**
Other	**Windows, Linux**		

Languages

Spanish	**Native**	Catalan	**Bilingual Proficiency**
English	**Professional Proficiency**	French	**Professional Proficiency**

Academic experiences

2009	**High school support near two young children**, Granada, Spain.
2006	**School support near a young child**, Barcelona, Spain.
2003 – 2004	**Librarian in a High School**, Barcelona, Spain.
2002 – 2003	**High school support near two young children**, Barcelona, Spain.

Work experiences

2006	**Employee in a haberdashery**, Barcelona, Spain.
2003 – 2006	**Employee in a take-away shop**, Barcelona, Spain.
2003 – 2004	**Employee in a department store**, Barcelona, Spain.
Dec. 2001/02	**Volunteer in a Christmas fair for children**, Barcelona, Spain.

Other interests

- First prize of Catalonia in the "I tu què en penses?" contest for the Study of drugs effects on young people
- Driving license